DETERMINISTICALLY ENGINEERED, HIGH POWER DENSITY ENERGY STORAGE DEVICES ENABLED BY MEMS TECHNOLOGIES

A Dissertation
Presented to
The Academic Faculty

by

Andac Armutlulu

In Partial Fulfillment
of the Requirements for the Degree
Doctor of Philosophy in the
School of Chemical and Biomolecular Engineering

Georgia Institute of Technology
December 2014

DETERMINISTICALLY ENGINEERED, HIGH POWER DENSITY ENERGY STORAGE DEVICES ENABLED BY MEMS TECHNOLOGIES

Approved by:

Dr. Sue Ann Bidstrup Allen, Advisor
School of Chemical and Biomolecular Engineering
Georgia Institute of Technology

Dr. Tom Fuller
School of Chemical and Biomolecular Engineering
Georgia Institute of Technology

Dr. Mark G. Allen, Advisor
School of Electrical and Computer Engineering
Georgia Institute of Technology

Dr. Hang Lu
School of Chemical and Biomolecular Engineering
Georgia Institute of Technology

Dr. Dennis Hess
School of Chemical and Biomolecular Engineering
Georgia Institute of Technology

Dr. Meilin Liu
School of Materials Science and Engineering
Georgia Institute of Technology

Date Approved: August 11, 2014

Anne ve babama…

ACKNOWLEDGEMENTS

First and foremost, I would like to thank my advisors, Dr. Sue Ann Bidstrup Allen and Dr. Mark G. Allen, for their continuous guidance, advice, and support over the course of my PhD studies, and for accepting me as their academic child.

I was very fortunate to have Dr. Dennis Hess, Dr. Tom Fuller, Dr. Hang Lu, and Dr. Meilin Liu as my committee members, whom I confidently consider to be the best in their respective fields, and who have been an academic inspiration to me throughout these years. As well, I must acknowledge my unofficial academic advisor Dr. Lawrence Bottomley for treating me like his own student and providing me with both technical and non-technical support whenever needed.

Many thanks go to both previous and current members of the MSMA group, with whom I have had the honor to work alongside. In particular: Richard Shafer, for making the lab run smoothly; Dr. Seong-Hyok Kim, for his excellent mentorship; Dr. Preston Galle, for his endless support; and Purnima Sharma, for all the administrative support.

I would like to present my sincere gratitude and appreciation to Dr. Turkan Haliloglu and Dr. Oner Hortacsu for their guidance and for making this long but rewarding PhD journey possible for me.

I am grateful to Dr. Seda Keskin Avci, Dr. Emmanuel Haldoupis, and Dr. Sung Gu Kang for helping me get started with my PhD adventure. I am also appreciative of my *Italiano* friends Alessio, Andrea, and Gabriele for making me feel home in this far-away continent; and my dearest study group members Carine, Christine, Deepraj, Jose, Nitesh, and Wilmarie.

Last but not least, I owe a special debt of gratitude to my beloved parents, in particular my father, Dr. Ismail Hakki Armutlulu, for their endless love and unconditional support from as far back as I can remember.

TABLE OF CONTENTS

		Page
ACKNOWLEDGEMENTS		iv
LIST OF TABLES		viii
LIST OF FIGURES		x
SUMMARY		xix
CHAPTER		
1	INTRODUCTION	1
	1.1 Motivation	1
	1.2 Selection of the Appropriate Energy Storage System	2
	1.3 Fundamental Principles and Design Considerations	3
	1.4 Structures Designed for High-Power Applications from the Literature	9
	1.5 Contributions of This Work	16
	1.6 Thesis Outline	17
	1.7 References	20
2	DESIGN AND FABRICATION OF MEMS-ENABLED MULTILAYER STRUCTURES	23
	2.1 Sequential Multilayer Deposition	23
	2.2 Mold Preparation	50
	2.3 Etching of the Sacrificial Layers	60
	2.4 Surface Area Characterization	67
	2.5 References	70
3	ZINC-AIR MICROBATTERIES	74
	3.1 Background and Motivation	74

3.2 Fabrication Process 77

3.3 Performance Characterization of the Microbatteries 92

3.4 Conclusions 97

3.5 References 99

4 NICKEL HYDROXIDE-BASED ELECTRODES 101

4.1 Background and Motivation 101

4.2 Design and Modeling of the Electrodes 102

4.3 Fabrication of the Multilayer Current Collector 117

4.4 Synthesis of $Ni(OH)_2$ 130

4.5 Performance Characterization of the Electrodes 142

4.6 Modeling of the Fabricated Electrodes 157

4.7 Performance Projections Using the Models 160

4.8 Conclusions 164

4.9 References 168

5 ELECTRODES FOR LITHIUM-ION BATTERIES 173

5.1 Background and Motivation 173

5.2 Choice of Materials 176

5.3 Fabrication of the Electrodes 182

5.4 Design and Modeling of the Electrodes 187

5.5 Performance Characterization of the Electrodes 205

5.6 Modeling of the Fabricated Electrodes 211

5.7 Conclusions 212

5.8 References 216

6 MEMS-ENABLED ELECTROCHEMICAL CAPACITORS 219

6.1 Background and Motivation 219

6.2 NiO- and $Ni(OH)_2$-based Electrodes 227

6.3 Fabrication of the Electrodes 231

6.4 Performance Characterization of the Electrodes 251

6.5 Conclusions 259

6.6 References 262

7 CONCLUSIONS AND FUTURE WORK 267

7.1 Summary and Conclusions 267

7.2 Suggestions for Future Work 270

7.3 References 281

APPENDIX A: MATLAB CODES 282

VITA 285

LIST OF TABLES

Page

Table 1.1: Ionic conductivities of various commonly used electrolytes in batteries 5

Table 1.2: Common electrode materials used in batteries along with their ionic diffusivities and electronic conductivities 6

Table 2.1: Compositions of the Ni and Cu plating baths 28

Table 2.2: Comparison of various polymer pairs used in the fabrication of multilayer structures 37

Table 2.3: The specifications for the laser used in the ablation process 41

Table 2.4: Plasma specifications for the removal of the sacrificial polymer layers 44

Table 3.1: The composition of Cu immersion and Zn electroplating baths 79

Table 4.1: Concentration profiles of H^+ within the $Ni(OH)_2$ active material as a function of time at various thicknesses 107

Table 4.2: Concentration profiles of the OH^- ions in the electrolyte located inside the channels with a width of 300 μm 113

Table 4.3: Modeling results for various channel dimensions 114

Table 4.4: Comparison of the electrodeposition methods for $Ni(OH)_2$/NiOOH 137

Table 5.1: The composition of the NiSn electroplating bath 186

Table 5.2: Concentration profiles of Li within the NiSn active material as a function of time at various thicknesses 192

Table 5.3: Concentration profiles of the Li ions in the electrolyte located inside the channels 197

Table 5.4: Impact of the width between the etching holes (i.e., L) on the other dimensions and capacity of the multilayer electrode with a total thickness of 300

μm 200

Table 6.1: Selected types of materials for electrochemical capacitors 224

Table 6.2: Performance of various $Ni(OH)_2$-based electrochemical capacitors 229

Table 6.3: Performance comparison of various NiO-based electrochemical capacitors 230

LIST OF FIGURES

Page

Figure 1.1: Simplified Ragone plot showing the specific power vs. specific energy of various energy storage systems 3

Figure 1.2: Demonstration of the kinetics and transport phenomena within three main components of a conventional battery electrode 4

Figure 1.3: Cu pillars fabricated through Al_2O_3 templates 11

Figure 1.4: Schematic of the assembly of Si-coated carbon black particles into spherical granules 12

Figure 1.5: Schematic describing morphological changes in Si after electrochemical cycling 14

Figure 1.6: High-power electrodes enabled by inverted opal structures 16

Figure 2.1: Comparison of lateral and vertical high-aspect-ratio structures 24

Figure 2.2: Conceptual rendering of the robotically-assisted sequential electroplating setup for the fabrication of the metallic multilayer structures 26

Figure 2.3: Multilayer Ni structures following the removal of Cu layers 29

Figure 2.4: Fabrication sequence for the partially-etched multilayer structures 33

Figure 2.5: Fabrication sequence for the anchor-supported structures 34

Figure 2.6: Fabrication sequence for the anchor-supported multilayer polymer structures 36

Figure 2.7: Fabrication sequence for the partially etched multilayer polymer structures 37

Figure 2.8: SEM images of the multilayer polymer structures based on 3 pairs of Unity/POSS 38

Figure 2.9: Optical and SEM images of the polymer-based multilayer structure with 3 pairs of Avatrel/POSS layers 42

Figure 2.10: POSS layers following the thermal removal of Avatrel at 405 ^{o}C 43

Figure 2.11: Optical images showing the top view of the high-density array of holes enabled by laser ablation 45

Figure 2.12: SEM images of the multilayer POSS/Avatrel structures following partial plasma etching of Avatrel layers 46

Figure 2.13: Fabrication scheme for the vertical high-aspect-ratio structures 49

Figure 2.14: SEM images of the partially etched SU-8 mold and multilayer Ni/Cu structure following partial etching of the Cu layers 53

Figure 2.15: Schematic illustration of removal of SU-8 molds with the help of a strong adhesive tape 54

Figure 2.16: Conceptual rendering of the SU-8 removal process via boiling water 54

Figure 2.17: Optical images showing the top view of the AZ molds in the form of varying number of cylindrical pillars all built on a footprint of 1 cm^2 56

Figure 2.18: Optical images showing the top view of the AZ molds in the form of varying number of rectangular pillars all built on a footprint of 1 cm^2 57

Figure 2.19: Thick AZ mold with rectangular pillar array 58

Figure 2.20: Thick AZ mold with cylindrical pillar array 59

Figure 2.21: Uneven etching distribution across the multilayer structures due to the accumulation of the higher-density etch products on the bottom 61

Figure 2.22: Illustration of the PMMA platforms used for the Cu etching 62

Figure 2.23: Optical images showing the backside of the Cu/Ni-coated glass substrate following various durations of Cu etching 64

Figure 2.24: Potentiodynamic curves for Cu and Ni in 0.1 M H_2SO_4 solution 66

Figure 3.1: A simplified schematic demonstrating the key features of a Zn-air cell 75

Figure 3.2: Alternative fabrication process for Zn/Cu pairs 78

Figure 3.3: Multilayer structure fabricated by sequential deposition of electroplated Zn and electrolessly plated Cu layers 80

Figure 3.4: Multilayer Zn/Cu structures following the anodization process 81

Figure 3.5: Fabrication sequence for the Zn-air batteries 82

Figure 3.6: SEM images showing the multilayer structure after photoresist removal 83

Figure 3.7: Schematic description of the release process of the air bridges during the sacrificial etching of Cu layers 84

Figure 3.8: Surface profiles of Zn films deposited at two different current densities 87

Figure 3.9: Multilayer Ni backbone before and after Zn electroplating 88

Figure 3.10: Enlarged view of the Zn film electroplated at 10 A dm^{-2} 89

Figure 3.11: Conceptual rendering of the battery assembly 90

Figure 3.12: Zn-air battery prior to performance characterization 91

Figure 3.13: Experimental setup for the characterization of the discharge performance of the multilayer Zn electrodes 93

Figure 3.14: Discharge profiles of the Zn-air microbattery based on multilayer Zn anode under various electrical loads 93

Figure 3.15: Areal energy densities of various microbatteries as a function of discharge current 94

Figure 3.16: Multilayer Ni backbone following the discharge of the microbattery at high rates 96

Figure 4.1: Electrode model assuming an infinitely wide plane sheet of thickness L 104

Figure 4.2: Model of the KOH electrolyte between two adjacent layers of the multilayer electrode 110

Figure 4.3: Capacity as a function of the distance between the etching holes (L) for a multilayer electrode with a total thickness of 300 μm, Ni layer thickness of 1.5 μm, and active material film thickness of 0.1 μm 115

Figure 4.4: Optimum dimensions for the $Ni(OH)_2$ film thickness and the inter-layer spacing for a channel with a width of 300 μm 116

Figure 4.5: Patterns of the multilayer structures (top row) and their corresponding anchors (bottom row) 118

Figure 4.6: Anchor-supported multilayer Ni structure based on rectangular-spiral pattern following the selective etching of the Cu layers 121

Figure 4.7: Anchor-supported multilayer Ni structure based on parallel-line pattern following the selective etching of the Cu layers 122

Figure 4.8: AZ 125 nXT mold for thick multilayer structures 126

Figure 4.9: Substrates following the electrodeposition of the multilayer structures 127

Figure 4.10: Optical images showing the thick multilayer structure with the NR-21 film deposited and patterned on it prior to the electrodeposition of the Ni anchors 129

Figure 4.11: Etching holes of a multilayer structure electroplated through AZ mold 130

Figure 4.12: Process flow for the template-free growth of the $Ni(OH)_2$ nanosheets on the multilayer Ni structures and the optical images of the resulting electrodes following varying durations of growth 134

Figure 4.13: SEM images showing the multilayer Ni structure before and after the template-free growth of the $Ni(OH)_2$ for 10 hours 136

Figure 4.14: Schematic of the experimental setup illustrating the cathodic electrodeposition of $Ni(OH)_2$ 140

Figure 4.15: Multilayer Ni backbone 141

Figure 4.16: Capacity and discharge profiles of the electrodes with varying number of

layers 143

Figure 4.17: Areal capacities of two multilayer electrodes with different number of laminations and interlayer distance 144

Figure 4.18: Discharge profile of a 90-layer electrode based on template-free grown $Ni(OH)_2$ 145

Figure 4.19: Power performance of a 25-layer electrode charged at 10 C and discharged at various rates ranging from 2 to 90 C 147

Figure 4.20: Discharge profiles of a 90-layer electrode 149

Figure 4.21: Zn anode after 200 cycles at high charge and discharge rates 150

Figure 4.22: Discharge profile of a 100-layer electrode at various charge and discharge cycles tested in a three-electrode-cell configuration by charging and discharging at 20 C and 10 C, respectively 151

Figure 4.23: Normalized capacity of a 100-layer electrode charged in three steps at various rates and discharged at 4 C for over 80 cycles 152

Figure 4.24: Sidewall of a multilayer structure following more than 100 charge and discharge cycles 153

Figure 4.25: Bottommost layer separated from the rest of the multilayer electrode to confirm conformal coating of the active material 154

Figure 4.26: Discharge profile of a $Ni(OH)_2$ electrode at 2.4 C composed of a stack of 3 90-layer electrodes 156

Figure 4.27: Theoretical capacity retention vs. experimental data of a 100-layer electrode with a 1-μm-thick active material at various charge rates 159

Figure 4.28: Model projections of the areal capacity of a 300-μm-thick $Ni(OH)_2$ electrode as a function of the individual Ni layer thickness 161

Figure 4.29: Model projections of the areal capacity of a 300-μm-thick $Ni(OH)_2$

electrode as a function of the $Ni(OH)_2$ film thickness 161

Figure 4.30: Theoretical power and energy density of the electrodes as a function of the $Ni(OH)_2$ film thickness and the Ni layer thickness 163

Figure 4.31: Ragone plot comparing the gravimetric power and energy densities of the 25-layer $Ni(OH)_2$ electrode (point A) and the modeled electrode with the optimized dimensions (point B) to the existing energy storage systems 166

Figure 4.32: Ragone plot comparing the volumetric power and energy densities of the 25-layer $Ni(OH)_2$ electrode (point A) and the modeled electrode with the optimized dimensions (point B) to the existing energy storage systems 167

Figure 5.1: Illustration of the electrochemical processes inside a Li-ion battery cell composed of a carbonaceous negative material (anode) and a metal oxide positive material (cathode) 174

Figure 5.2: Electrode materials and electrolytes studied for Li-ion batteries 175

Figure 5.3: (A) SEM image of the sidewall after MnO_2 deposition, (B) XPS spectrum of the electrodeposited MnO_2 film 183

Figure 5.4: (A) Schematic of the triple plating setup utilized for the fabrication of NiSn electrodes, (B) electroplating sequence of the layers using the triple plating setup 185

Figure 5.5: (A) XRD pattern of the NiSn film, (B) SEM image showing the cross-sectional view of the Ni layers sandwiched between the NiSn active material films 187

Figure 5.6: Electrode model assuming an infinitely wide plane sheet of thickness L 188

Figure 5.7: Model of the electrolyte between two adjacent layers of the multilayer electrode 194

Figure 5.8: Optimum dimensions for the NiSn film thickness and the inter-layer spacing for the multilayer electrode 199

Figure 5.9: Theoretical areal capacity of a 300-μm-thick NiSn electrode as a function of

the distance between its etching holes 201

Figure 5.10: Theoretical areal capacity of a 300-μm-thick NiSn electrode as a function of the individual Ni layer thickness 202

Figure 5.11: Theoretical areal capacity of a 300-μm-thick NiSn electrode as a function of the NiSn layer thickness 203

Figure 5.12: Theoretical power and energy density of the electrodes as a function of the NiSn film thickness and the Ni layer thickness: (A) gravimetric density, (B) volumetric density 204

Figure 5.13: Discharge profiles of the MnO_2 electrode charged at various rates and discharged at 5 C 206

Figure 5.14: (A) Lithiation profile of a NiO electrode at a rate of 0.1 C, (B) cycling performance of a NiO electrode consisting of a stack of three 90-layer structures 208

Figure 5.15: Electrochemical characterization of the NiSn electrodes 210

Figure 5.16: Theoretical capacity retention vs. experimental data of a 90-layer electrode with a 0.2-μm-thick active material at various charge rates 211

Figure 5.17: Ragone plot comparing the gravimetric power and energy densities of a 90-layer NiSn electrode (point A) and the modeled electrode with the optimized dimensions (point B) to the existing energy storage systems 214

Figure 5.18: Ragone plot comparing the volumetric power and energy densities of a 90-layer NiSn electrode (point A) and the modeled electrode with the optimized dimensions (point B) to the existing energy storage systems 215

Figure 6.1: Schematic representation of the double-layer region on the electrode 220

Figure 6.2: Fabrication sequence for the lateral high-aspect-ratio parallel plate current collectors 231

Figure 6.3: Top view of a multilayer Cu current collector 232

Figure 6.4: CV profiles of Tl on Cu and Ni electrodes 234

Figure 6.5: (A) Schematic illustration of the electrodes with various surface areas used in the UPD calibration experiments and (B) calibration plot showing the total charge stripped vs. the surface area of the electrodes 236

Figure 6.6: CV profiles of the electrodes in 1 M KOH solution 239

Figure 6.7: Cross-sectional view of a Cu layer sandwiched between Ni/$Ni(OH)_2$ films 240

Figure 6.8: Conceptual rendering illustrating the cross-sectional view of the vertical high-aspect-ratio concentric cylinder electrodes 241

Figure 6.9: High-aspect ratio SU-8 pillars with two different aspect ratios 243

Figure 6.10: 17x17 array of SU-8 pillars coated with 125 pairs of Ni/Cu layers fabricated on a footprint of 1 cm^2 244

Figure 6.11: Top view of a multilayer pillar structure following the mechanical lapping process 246

Figure 6.12: Conceptual rendering showing the top view of the growth pattern of the electrodeposited Cu and Ni layers on the rectangular SU-8 pillars 247

Figure 6.13: SEM image showing the top view of the multilayer pillar structure after the selective Cu etching step 248

Figure 6.14: Cross-sectional view of a multilayer pillar after the etching process 250

Figure 6.15: Electrochemical characterization of the $Ni(OH)_2$ electrodes based on lateral high-aspect-ratio structures 253

Figure 6.16: Ragone plot showing the relationship between the specific power and energy of a $Ni(OH)_2$-based electrochemical capacitor electrode 256

Figure 6.17: CV profiles at 20 mV s^{-1} 258

Figure 6.18: Ragone plot comparing the performance of the fabricated electrodes to the

existing energy storage systems 260

Figure 7.1: Optical image showing the top view of the photoresist mold 271

Figure 7.2: Etching holes formed via laser ablation process 272

Figure 7.3: Conceptual rendering of the fabrication process for the interdigitated electrodes 275

Figure 7.4: Laser-cut interdigitated electrodes based on vertical high-aspect-ratio concentric cylinders 275

Figure 7.5: Fabrication scheme for the vertical high-aspect-ratio channels 279

SUMMARY

This study focuses on the design, fabrication, and characterization of deterministically engineered, three-dimensional architectures to be used as high-performance electrodes in energy storage applications. These high-surface-area architectures are created by the robotically-assisted sequential electrodeposition of structural and sacrificial layers in an alternating fashion, followed by the removal of the sacrificial layers. The primary goal of this study is the incorporation of these highly laminated architectures into the battery electrodes to improve their power density without compromising their energy density. MEMS technologies, as well as electrochemical techniques, are utilized for the realization of these high-power electrodes with precisely controlled characteristic dimensions. Diffusion-limited models are adopted for the determination of the optimum characteristic dimensions of the electrodes, including the surface area, the thickness of the active material film, and the distance between the adjacent layers of the multilayer structure.

The contribution of the resultant structures to the power performance is first demonstrated by a proof-of-concept Zn-air microbattery which is based on a multilayer Ni backbone coated with a conformal Zn film serving as the anode. This primary battery system demonstrates superior performance to its thin-film counterpart in terms of the energy density at high discharge rates. Another demonstration involves secondary battery chemistries, including $Ni(OH)_2$ and Li-ion systems, both of which exhibit significant cycling stability and remarkable power capability by delivering more than 50% of their capacities after ultra-fast charge rates of 60 C. Areal capacities as high as 5.1 mAh cm^{-2}

are reported. This multilayer fabrication approach is also proven successful for realizing high-performance electrochemical capacitors. $Ni(OH)_2$-based electrochemical capacitors feature a relatively high areal capacitance of 1319 mF cm^{-2} and an outstanding cycling stability with a 94% capacity retention after more than 1000 cycles.

The improved power performance of the electrodes is realized by the simultaneous minimization of the internal resistances encountered during the transport of the ionic and electronic species at high charge and discharge rates. The high surface area provided by the highly laminated backbone structures enables an increased number of active sites for the redox reactions. The formation of a thin and conformal active material film on this high surface area structure renders a reduced ionic diffusion and electronic conduction path length, mitigating the power-limiting effect of the active materials with low conductivities. Also, the highly conductive backbone serving as a mechanically stable and electrochemically inert current collector features minimized transport resistance for the electrons. Finally, the highly scalable nature of the multilayer structures enables the realization of high-performance electrodes for a wide range of applications from autonomous microsystems to macroscale portable electronic devices.

CHAPTER 1

INTRODUCTION

1.1 Motivation

Over the past two decades, the widespread miniaturization of portable electronic equipment from smart phones to various multimedia tools has led to the need for similarly scaled energy storage systems. In addition to such macroscale applications, there has also been enormous progress in the development of microdevices, encompassing autonomous microsensors and microactuators. The rate of technological advancement in both macro- and microscale electronic device industry, however, has been more rapid than that of compatible and suitably sized energy storage technologies which are necessary to power these devices. The vast majority of these energy storage systems utilized in the portable electronic devices are composed of batteries.

Considering the currently available battery chemistries, a drastic improvement in the battery performance in terms of capacity, which determines the operation duration of the mobile device on a single charge of the battery, is not anticipated in the near future. Unless a completely new battery chemistry with an extremely high energy density is developed, the only way to achieve longer operation times is through increasing the mass of the active material present within the battery, which is incompatible with the current shrinking trend of the portable electronic devices. However, improvements can be achieved in the rate of the energy, i.e. the power, which these batteries can deliver. For example, a battery with which a mobile device can operate continuously for one hour would be considered to have a relatively low capacity performance. But this relatively short life of the battery can easily be overlooked if the battery is capable of being fully charged in 1-2 minutes with a minimal forfeit in its capacity.

The study reported herein focuses on developing rationally designed and deterministically engineered structures to be used as electrodes in energy storage applications, which address the need for high energy density systems with rapid charging capabilities. In addition to the intrinsic properties of the active materials, proper micro- and macrostructural design is also required for the realization of high-performance electrodes. To achieve this, electrochemical, as well as microfabrication techniques enabled by microelectromechanical systems (MEMS) technologies have been utilized. The utilization of such technologies enables the fabrication of high-performance and highly scalable power sources for a wide variety of applications, ranging from autonomous microsystems to macroscale portable electronics.

1.2 Selection of the Appropriate Energy Storage System

In order for a high-power energy storage system to be practically useful for the aforementioned portable electronic devices, it should be able to store a significant amount of energy (>10 mWh), which can be achieved by utilizing several energy storage systems [1]. The simplified Ragone plot in Figure 1.1 shows some of these conventional energy storage systems along with their specific power and energy density.

It should be noted that there is a trade-off between the two key attributes, namely power and energy density, of the given energy storage systems. However, the ideal energy storage system that is expected to satisfy the goals of our research, must possess both high energy and power density, and thus, needs to be located on the top right region of the plot. Based on the energy storage technologies shown in Figure 1.1., capacitors and fuel cells require higher orders of magnitudes improvement in their respective energy and power densities when compared to batteries, to meet the demands that constitute the main motivation behind this research.

Therefore, the primary focus of our research will be on batteries. In order to achieve that encircled performance in Figure 1.1, the specific power of the batteries has to be improved without compromising their energy density.

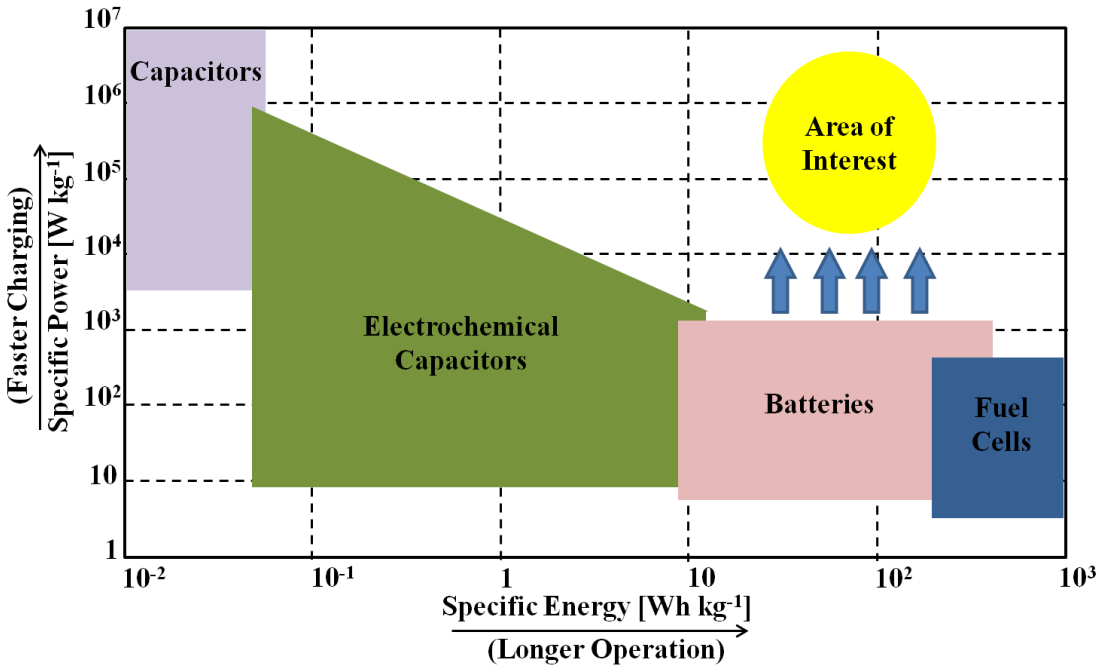

Figure 1.1: Simplified Ragone plot showing the specific power vs. specific energy of various energy storage systems [2]

1.3 Fundamental Principles and Design Considerations

The energy density of an electrochemical cell is defined as the amount of ultimately extractable energy stored in a given volume of the system. Hence, it can be improved in a simplistic way by increasing the packing density, or in other words, the amount of the electrochemically active material per given volume of that system. The power density, on the other hand, is a measure of the rate of energy transfer to and from the cell.

The key element that determines the power density of an electrochemical system is the rate at which ionic and electronic species are transported from one electrode to the other. During the transport process of ions and electrons, certain inherent resistances

pertaining to mass transfer and kinetics are encountered, which make up the total internal resistance of the electrochemical system. To overcome these resistances during the charging process of an electrochemical system, for example, high amounts of currents may be required, resulting in significantly increased voltage at the electrode. However, such high voltages may cause deleterious effects on the chemical and mechanical stability of the electrode material, leading to profoundly reduced capacities. Therefore, to avoid such effects, all of the inherent resistances must be minimized simultaneously in order to realize high-power systems.

Conceptual rendering of a simplified conventional battery electrode can be seen in Figure 1.2 which illustrates the kinetics and transport phenomena that happen during the charge and discharge of the battery electrode. As shown in Figure 1.2, all of the kinetics and transport phenomena take place in three main components of the battery: (1) the electrolyte, where the diffusion of liquid-state ions take place between two electrodes; (2) the active material, that hosts the kinetics, as well as the solid-state ion diffusion and electron conduction; and (3) the current collector, responsible for the delivery of the electrons to and from the active material.

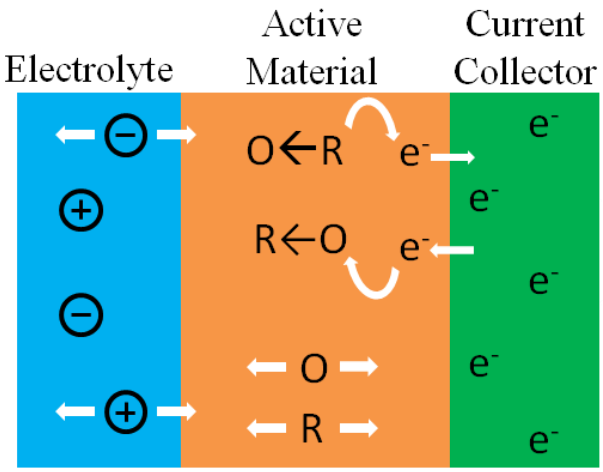

Figure 1.2: Demonstration of the kinetics and transport phenomena within three main components of a conventional battery electrode

The factors that affect the performance of a battery electrode can be classified in two categories: intrinsic and extrinsic factors. Both of these factors play an essential role in the transport process of ionic and electronic species and are investigated separately.

1.3.1 Intrinsic Factors Affecting the Electrode Performance

Intrinsic factors, such as the diffusivity and conductivity of the system components, depend on the choice of materials to be utilized within the system.

1.3.1.1 Diffusivity

Two types of diffusion take place within the cell: solid-state and liquid-state diffusion. The former type involves the transport of the ions in the active material, whereas the latter type is associated with the ion transport within the electrolyte. In special systems where solid electrolytes are utilized, such as lithium polymer batteries, the liquid-state ion transport is not available [3]. Ionic conductivities in the liquid-state electrolytes are several orders of magnitude higher than those of solid-state electrolytes. Therefore, liquid electrolytes are not as often a limiting factor for high-power batteries. Solid electrolytes, on the other hand, exhibit comparable diffusivities to the active materials which render them an inadequate choice for energy storage applications demanding fast charging and discharging. A comparison of the ionic conductivities for commonly used liquid and solid electrolytes can be found in Table 1.1.

Table 1.1: Ionic conductivities of various commonly used electrolytes in batteries

Phase	Electrolyte	Ionic Conductivity ($S\ cm^{-1}$)	Reference
Liquid	1 M $LiClO_4$ in EC/DMC	$8.4x10^{-3}$	[4]
	1 M $LiPF_6$ in EC/DMC	$10.7x10^{-3}$	[4]
	KOH (30 w.%)	$5x10^{-1}$	[1]
Solid	Li-ion conducting polymer	10^{-8}	[4]
	Glass (LiPON)	10^{-4}-10^{-7}	[4]

It has been reported that in most of the systems involving liquid electrolytes, the main cause of the decrease in extractable energy at high charge and discharge rates is pertaining to the overpotential associated with the diffusivity of the solid-state ions within the active material, rather than the liquid-state ions in the electrolyte [5]. This means that the solid-state diffusion within the active material is the main contributor to the transport resistance and thus, the rate limiting step for the majority of chemistries. Therefore, for high-power applications, liquid electrolytes along with active materials with high diffusion coefficients is preferred. A comparison of the diffusion coefficients for commonly-used active materials in batteries can be found in Table 1.2.

Table 1.2: Common electrode materials used in batteries along with their ionic diffusivities and electronic conductivities

Electrodes	**Material**	**Ion Diffusivity ($cm^2\ s^{-1}$)**	**Electron Conductivity ($S\ cm^{-1}$)**	**Reference**
Cathode	$Ni(OH)_2$	10^{-8} - 10^{-11} (H^+)	$2.5x10^{-5}$	[7]
	$LiMn_2O_4$	10^{-13} (Li^+)	$2\text{-}5x10^{-5}$	[7]
	$LiFePO_4$	10^{-8} - 10^{-14} (Li^+)	10^{-9} - 10^{-10}	[7]
Anode	Graphite	10^{-7} - 10^{-12} (Li^+)	10^{2} - 10^{4}	[4]
	PAN-based carbon fiber	10^{-11} - 10^{-14} (Li^+)	10^{1} - 10^{2}	[4]

1.3.1.2 Conductivity

Another type of intrinsic factor that contributes to the transport resistance within cell is the conductivity of the system components. Electrons that are delivered to the active material through current collector need to be transported to the electrode-electrolyte interface, where the oxidation and reduction reactions take place during the charge and discharge processes of the battery electrode. The current collector is only responsible for electron delivery to and from the active material. Hence, no ionic transport takes place in this component of the electrode. As a result of this, the only contribution to the overall resistance originating from this component of the electrode is

through its electrical resistance. This can be easily alleviated by incorporating highly conductive metals (e.g., Cu, Ni, Al) into current collectors.

However, the active materials, particularly for cathodes, are generally in the form of oxides or other less conductive compounds which suffer from high electrical resistance as shown in Table 1.2. This electrical resistance encountered by the electrons during their transport within the active material has been shown to cause a potential drop across the electrode, which has an adverse effect on the power performance of the system, particularly at high currents [6]. Therefore, along with the improvement of the diffusion coefficients, enhancement of the conductivity of the active material should also be sought to realize high-power electrodes.

1.3.2 Extrinsic Factors Affecting the Electrode Performance

Extrinsic factors, including the surface area, diffusion and conduction path lengths, play also a major role in the performance of the electrode. These factors primarily rely on the size and geometry of the system components.

1.3.2.1 Surface Area

The surface area is one of the key parameters affecting the power performance of a battery. It corresponds to the contact area between the active material and the electrolyte, where the oxidation and reduction reactions take place. In order to deliver a high number of charges in a short period of time, the amount of these reactions has to be maximized. This can be achieved by increasing the surface area of the electrode that is in contact with the electrolyte. This results in the increase in the number of active sites hosting the oxidation and reduction reactions, which in turn minimizes the loss originating from the electrode polarization and thus, enhances the power density of the electrode.

1.3.2.2 Diffusion Path Length

According to Fick's law of diffusion, the characteristic time constant for diffusion, τ, scales with the square of the diffusion path length, L, and the reciprocal of the diffusivity, D, as shown in Equation 1.1. Therefore, it can be deduced that reducing the diffusion path length is much more effective in improving the power performance of the system than increasing the diffusivity of the active material by the same amount, since the time constant is proportional to the square of the diffusion path length.

$$\tau = \frac{L^2}{D} \tag{1.1}$$

For example, the characteristic time for Li ions to diffuse through a 1-μm-thick active material with a diffusion coefficient of 10^{-10} cm^2 s^{-1} is 100 seconds. In the case of slow charge rates, the charge time would be much longer than the characteristic diffusion time of Li ions. As a result, a significant concentration gradient of the Li ions does not develop across the active material. However, when the charging rates are significantly increased, Li ions may not find sufficient time to diffuse through the active material which leads to the formation of a severe concentration gradient, and thus, a voltage gradient in the electrode that contributes to the overpotential of the cell [5].

1.3.2.3 Conduction Path Length

As mentioned earlier, similar principles apply to the conduction phenomenon, where the potential drop becomes higher as the distance that the electrons travel increases. This can be simply expressed by Ohm's law:

$$\nabla\Phi = -\frac{i \cdot L}{\kappa} \tag{1.2}$$

where $\nabla\Phi$, i, L, and κ stand for potential drop (V), current density (A cm^{-2}), conduction path length (cm), and conductivity (S cm^{-1}), respectively. Because of these reasons, minimization of the diffusion and conduction path lengths is necessary to improve the power density of the systems.

1.3.3 Design Considerations

In summary, a high-power system that is expected to meet the demands mentioned earlier needs to have a minimized transport resistance during high charge and discharge rates. The minimization can be achieved through simultaneous optimization of the aforementioned individual parameters that determine the overall cell resistance. For the optimum design, parameters such as diffusivity, conductivity, and surface area have to be maximized, while the diffusion and conduction path lengths are minimized. Developing active materials with enhanced intrinsic properties requires intensive research which is beyond the scope of this study. Hence, the focus will be on the design and fabrication of high-power electrodes that are composed of structures with optimized extrinsic properties utilizing the most suitable existing active materials for high-power applications.

1.4 Structures Designed for High-Power Applications from the Literature

Systems comprising of active materials in the form of nanoparticles realized by various nanostructuring concepts have demonstrated outstanding performance in terms of energy densities and cycle life of the electrodes [5, 8]. Yet, these systems usually do not allow direct control over the connectivity of different phases within the electrode [5]. Structuring the electrodes in a deterministic way permits control over not only the amount of the active material in terms of mass or volume, but also the aforementioned critical dimension such as surface area, as well as diffusion and conduction path lengths that determine the ultimate performance of the electrode. As a result, numerous efforts

have focused on developing structures engineered in a deterministic way [5, 9, 10]. The key challenge to realize this goal involves establishing cost-effective fabrication methodologies.

Although there is a wide variety of battery chemistries with high-power capabilities, such as $Ni(OH)_2$-based systems, the recent efforts in the literature mainly focus on Li-ion batteries, since they possess the highest energy density. The electrode structures designed for high-power applications can be classified into two main groups: high-power anodes and high-power cathodes. In our study, the former one is of more importance for the Li-ion batteries discussed in Chapter 5, whereas the latter one will be the only focus for the $Ni(OH)_2$-based systems covered in Chapter 4.

1.4.1 Electrodes for High-Power Anodes

One of the earliest examples of deterministically engineered electrodes for high power applications involves arrays of metal structures in the form of pillars that serve as a backbone for the active materials. In previous work, Cu pillars were fabricated via anodized Al_2O_3 (AAO) templates which support anode active materials of Fe_3O_4 and NiSn [11, 12]. The schematic illustrating this process and the SEM images of the resultant electrodes are shown in Figure 1.3. The Fe_3O_4 anode has been shown to maintain 80% of its total capacity at a discharge rate of 8 C for more than 100 cycles [12]. The charge and discharge rates for batteries are typically expressed as C rates, where the x-C rate equals the rate at which the electrode is completely charged or discharged in x^{-1} hours. Similarly, the NiSn anode has been reported to demonstrate a capacity of 200 mAh g^{-1} at a discharge rate of 10 C, which corresponds to nearly 50% of its 1 C capacity [11].

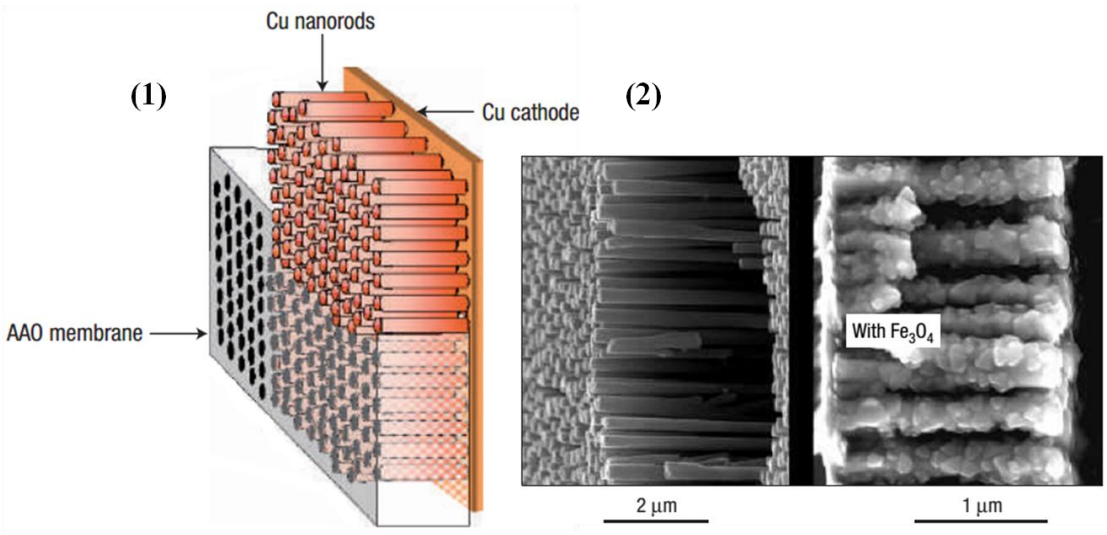

Figure 1.3: Cu pillars fabricated through Al_2O_3 templates: (1) schematically illustrated fabrication process for Cu nanorods, (2) their SEM images before and after active material deposition [12]

Another study using a similar pillar array configuration involves Sn/SnO nanowires with a length of 2 μm supported on self-organized TiO_2 nanotubes, that serve as high power anodes for Li-ion batteries [13]. These electrodes have been reported to enable areal capacities of 95 and 140 μAh cm^{-2} (675 mAh g^{-1}) and deliver 70 and 85% of their initial capacity over 50 cycles under rates of 4C and 2C. In another study with a similar approach, arrays of Ni nanocones that are conformally coated with Si serving as the active material have been reported to yield a capacity of 1250 mAh/g at a discharge rate of 2 C, which refers to approximately 50% of the 0.2 C rate [14]. Using the same principle but slightly different geometries, Li-ion anodes composed of Cu-Si nanocables coated with a thin layer of Al_2O_3 have been fabricated and tested under the current density of 14 A g^{-1} demonstrating a capacity of 790 mA g^{-1}, which corresponds to 43% of the capacity at 0.3 A g^{-1} [15].

A different hierarchical bottom-up approach comprises annealed carbon black as the supporting backbone which is first coated by Si nanoparticles through chemical vapor deposition (CVD) and then assembled into rigid spherical granules enabling a high-power

anodes with a capacity of 870 mAh g^{-1} at 8 C, which is 45% of that at C/20 [16]. Schematic showing the assembly of Si-coated carbon black particles can be seen in Figure 1.4.

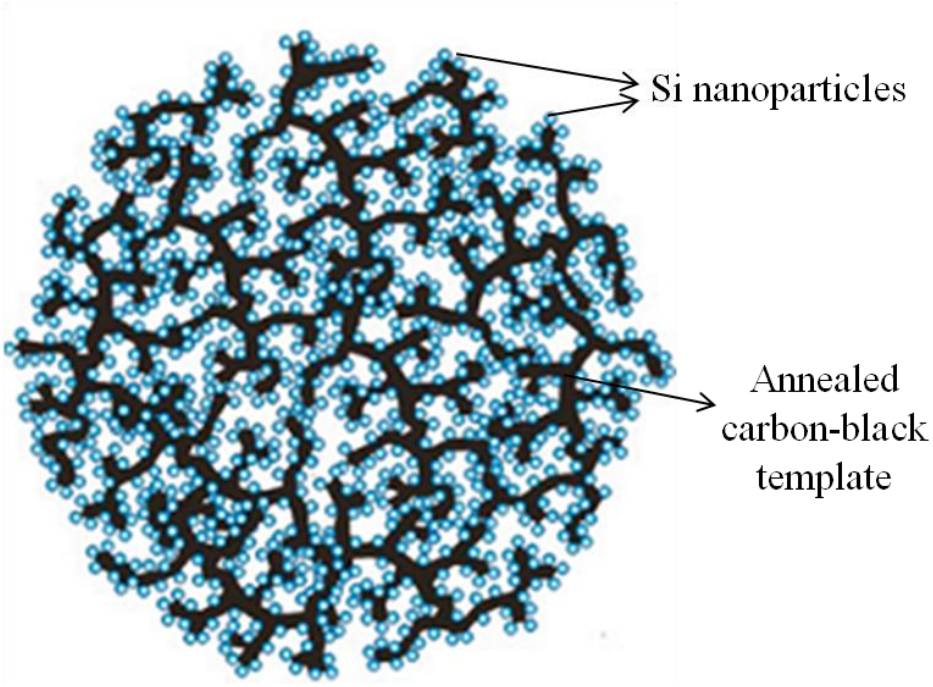

Figure 1.4: Schematic of the assembly of Si-coated carbon black particles into spherical granules [16]

Even higher charge/discharge rates of up to 40 C have been enabled via C-Al-Si anodes in the form of nanoscoops (i.e., a cone-shaped carbon nanorod base topped with a thin film of Al and a nanoscale Si "scoop") that minimize the mismatch at the interfaces and exhibit gradual volume change during lithiation process, yielding an average capacity of 429 mAh g^{-1} at 40 C, corresponding to 35% of its 1 C capacity [17]. A relatively lower specific capacity of 160 mAh g^{-1} but higher stability and discharge rate has been reported in a work comprising nanostructured anodes that are composed of $Li_4Ti_5O_{12}$ which are capable of retaining more than 90% of its 1 C capacity at a discharge rate of 20 C [18].

Besides the electrodes with stabilizing backbone structures, anodes featuring high rate performance and high cycle life have also been obtained by engineering the free volume required for their expansion during lithiation without utilizing any supporting scaffold [5]. This way, the stress buildup in the anode is alleviated and premature failure of the battery is prevented. These anode materials generally possess morphologies of nanotubes and nanowires or involve nanoporous and mesoporous structures. For example, arrays of mesoporous Co_3O_4 nanowires demonstrated a capacity of 700 mAh g^{-1} at a rate of 1 C and were able to deliver 50% of this capacity when the rate was increased to 50 C [19]. In another study, Si nanowires have been reported to have an extraordinarily high specific capacity of 3214 mAh g^{-1} at a discharge rate of C/20 and they were demonstrated to preserve more than 67% of that capacity when the discharge rate was increased to 1 C [20]. Another type of Si-based high-performance anodes in the form of 3D porous particles has been fabricated by thermal annealing and etching processes, where the resultant structures have reportedly delivered a capacity of 2158 mAh g^{-1} at 3 C discharge rate, which corresponds to 81% of the 1 C discharge rate [21]. Sol-gel derived and ordered mesoporous α-Fe_2O_3 thin-film electrodes have been demonstrated to deliver ~45% of their C/5 discharge capacity when discharged at 3 C [22]. Ultra-long Ge nanotubes prepared by using the Kirkendall effect (i.e., motion of the boundary layer between two metals as a result of the difference in diffusion rates) have been reported to enable exceptionally high charge capacitance retention among all metallic anodes by delivering a charge capacity of 580 mAh g^{-1} at 20 C, which refers to 60% of its 0.5 C charge capacity [23].

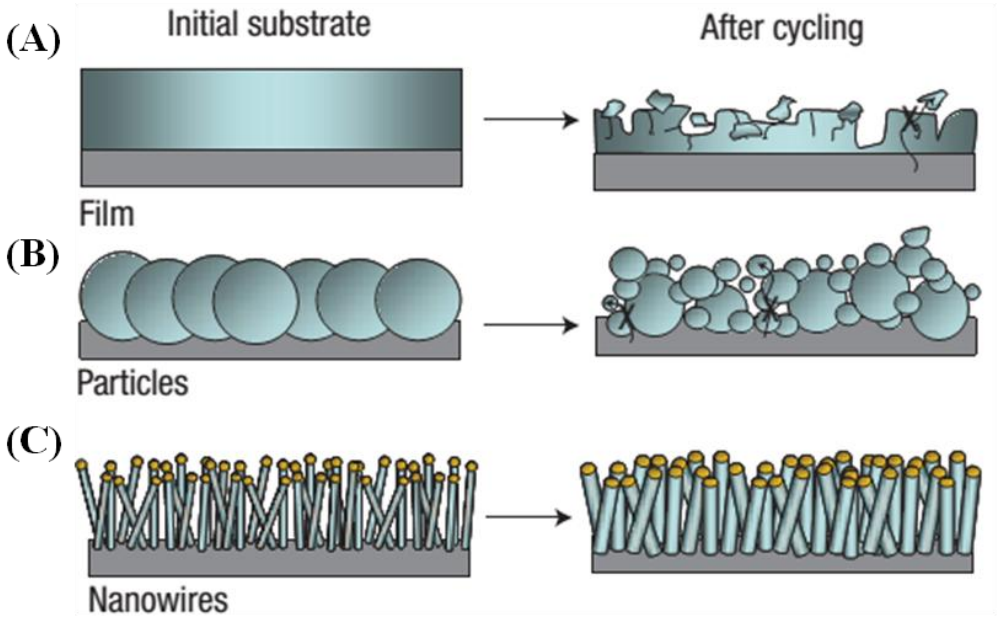

Figure 1.5: Schematic describing morphological changes in Si after electrochemical cycling: (A) breaking of Si films, (B) pulverization of Si particles, and (C) no damage in nanowires [20]

1.4.2 Electrodes for High-Power Cathodes

In addition to the anode materials, numerous studies have been carried out with regards to deterministically engineered high power cathode materials as well. Some of these structures include porous monolithic composites, self-ordered crystalline-glass mesoporous nanocomposites, and inverted opal structures [5]. Materials used in cathode electrodes, in general, possess less specific capacity than their anode counterparts. However, for high-power applications, they have been shown to be superior enabling charge and discharge rates of more than 1000 C while maintaining their significant portion of low rate energy [24]. In contrast to metallic and carbonaceous anodes with high conductivities, cathode materials are usually made of metal oxides and thus, possess lower conductivities.

So far, inverted opal structures (i.e., matrices with highly ordered 3D architecture of interconnected cavities) have been the most promising candidate for high-power

battery electrodes. An inverse opal electrode made of lithiated MnO_2 has been reported to enable 70 C discharge rate, at which it has been able to retain more than half of its capacity at 1.8 C discharge rate [25]. Similarly, another inverted opal electrode consisting of $LiFePO_4$ has yielded a capacity of 160 mAh g^{-1} at a discharge rate of 0.1 C and demonstrated a capacity retention of 72% when discharged at 5 C [26]. These two cathode materials owe their high rate performances to their short ionic diffusion lengths, as well as high surface area. Yet, the limiting factor for achieving even more improved power rates for both structures has been reported to be the long conduction paths for electrons which are at least 3 orders of magnitude longer than the ionic diffusion path lengths [5].

To alleviate the issues pertaining to the low electrical conductivities of the cathode materials, opal electrode designs have been improved by making use of a conductive inverted scaffold, which is first fabricated and subsequently coated with a thin layer of active material [5]. In this way, both the ionic diffusion and electron conduction path lengths have also been minimized. This approach can be considered as analogous to the metal nanofoams, which also serve as a conductive scaffold for the active materials they host [27]. However, the inverted scaffold concept not only provides a more uniform electrode structure, but also results in better control over the characteristic dimensions of the electrode.

A study focusing on demonstrating the contribution of this inverted conductive scaffold approach involves a carbon-based inverted opal structure coated with a thin layer of V_2O_5 gel as the active material. This structure has been tested at discharge rates as high as 5 A g^{-1} and shown to retain approximately 80% of its capacity at 0.1 A g^{-1} discharge rate [28]. In this approach, the main limitation to having higher energy densities originates from the relatively thick conductive scaffold that increases the total weight of the electrode, and thus reduces the energy density. Another study with the same motivation involves MnO_2 and $Ni(OH)_2$ chemistries where a conductive Ni scaffold of

94% porosity has been utilized and significantly higher discharge rates have been able to be achieved [7]. This electrode has been coated first with lithiated MnO_2 and shown to retain 76% and 38% of its capacity when discharged at 185 C and 1114 C, respectively. Then, the same electrode has been tested by utilizing $Ni(OH)_2$ chemistry where the capacity retention has been observed to be 75% of its 1 C rate when it has been discharged at a rate of 1017 C. Thus, it has been demonstrated that a significant increase in the power density can be obtained while maintaining large energy density retentions.

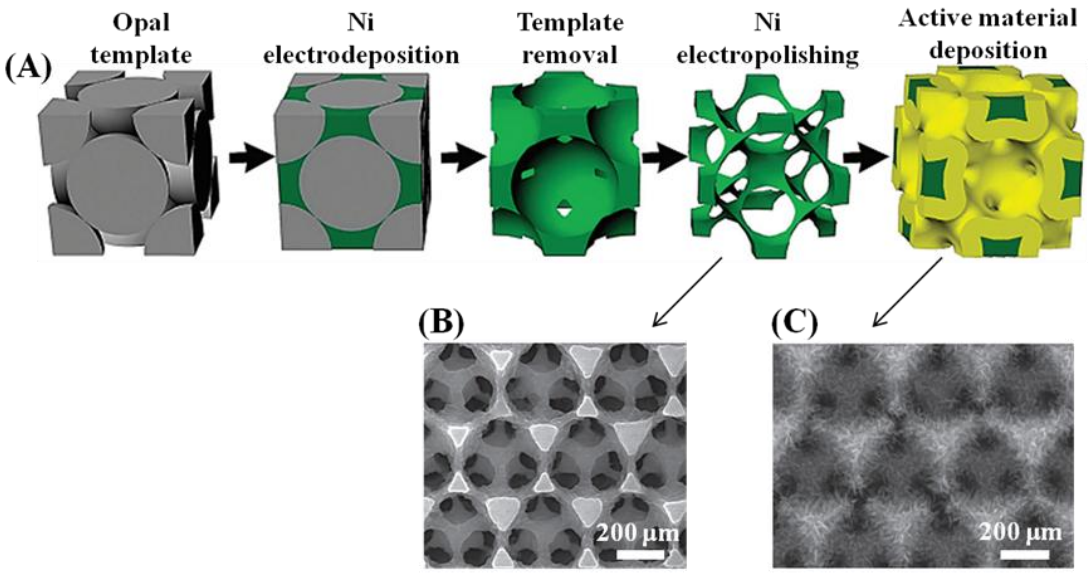

Figure 1.6: High-power electrodes enabled by inverted opal structures: (A) fabrication sequence, (B) SEM image of the current collector, and (C) current collector coated with active material [7]

1.5 Contributions of This Work

All of the approaches summarized in section 1.4 have proven quite successful in relation to the goals of our study. In general, the resultant electrodes reportedly exhibited improved capacity retentions at high charge and discharge rates. However, the reported electrodes involve microscale structures, and the capacities they demonstrated (e.g., 10-100 µWh) are far from being practically useful for portable electronic devices. It is also

not clear whether these electrodes would be capable of exhibiting the same power performance, when they are scaled up to sizes suitable for macroscale applications which require significantly more energy (e.g., >10 mWh).

The study reported herein involves rationally designed and deterministically engineered 3D structures with precisely controlled dimensions that address the aforementioned critical factors affecting the high-power capability and ultimately determine the performance of the electrochemical systems. Cost-effective and straightforward methods comprising electrochemical techniques and MEMS technologies have been utilized for the fabrication and characterization of the scalable, well-ordered, and high-surface-area structures that are suitable for use as electrodes in a variety of applications, ranging from autonomous microsystems to macroscale portable electronics.

These versatile structures are based on a large number of relatively thin layers of two different materials, one being sacrificial while the other is structural, fabricated through a temporary mold in an alternating sequence with the help of an automated robotic system. The final structure is obtained by the selective removal of the sacrificial material, leaving behind a large number of separate layers of the structural material to be coated with the electrochemically active material. Details about the fabrication process and performance of these structures are available in the forthcoming chapters of this study.

1.6 Thesis Outline

The body of this thesis is divided into seven chapters. Chapter 1 is the introductory section starting with the motivation behind the study reported herein. After indicating the devices of interest for high-power energy storage applications, a discussion on the fundamentals and design considerations is presented. It is followed by a detailed literature survey regarding the high-power electrodes studied thus far and our

contribution by introducing deterministically engineered multilayer structures to the high-power energy storage applications.

Chapter 2 presents various fabrication approaches utilized in this study to realize the multilayer structures. A detailed description of the methods and techniques, used to achieve and characterize these well ordered structures, as well as information regarding the chemicals used in these processes is provided.

Chapter 3 demonstrates the first proof-of-concept electrodes for primary Zn-air batteries enabled by utilizing these multilayer structures. A detailed description of the fabrication process of the electrodes is given along with their performance characterization.

Chapter 4 presents the first use of the multilayer structures for secondary battery chemistries by demonstrating $Ni(OH)_2$-based electrodes. Various methods with regards to active material deposition are discussed and the reasoning behind choosing this particular chemistry is explained. Two different fabrication approaches are reported in detail for low- and high-capacity applications. Finite-element-method (FEM) simulations performed to determine the optimum dimensions for the electrode is described in detail. Also, the high-power performance of the $Ni(OH)_2$-based electrodes is discussed and compared to the modeling results.

Chapter 5 covers the high-power Li-ion electrodes based on the rationally designed and deterministically engineered multilayer structures that meet the ultimate capacity goal of this study. Some background information pertaining to the anodes and cathodes used in Li-ion systems are given. Fabrication and characterization processes of the electrodes with the optimum dimensions designed by the FEM simulations are discussed.

The applicability of the deterministically engineered structures to electrochemical capacitors is presented in Chapter 6. Detailed background information regarding the

electrochemical capacitors is provided. $Ni(OH)_2$- and NiO-based electrochemical capacitors with significant capacitance values are reported.

Chapter 7 is devoted to the concluding summary of the whole study. The overall contributions of this study are presented. Also, some recommendations pertaining to future research are provided.

1.7 References

[1] T. B. Reddy, *Linden's Handbook of Batteries* vol. 4: McGraw-Hill New York, 2011.

[2] M. Winter and R. J. Brodd, "What are batteries, fuel cells, and supercapacitors?," *Chemical Reviews,* vol. 104, pp. 4245-4270, 2004.

[3] B. Scrosati, F. Croce, and S. Panero, "Progress in lithium polymer battery R&D," *Journal of Power Sources,* vol. 100, pp. 93-100, 2001.

[4] M. Park, X. Zhang, M. Chung, G. B. Less, and A. M. Sastry, "A review of conduction phenomena in Li-ion batteries," *Journal of Power Sources,* vol. 195, pp. 7904-7929, 2010

[5] P. V. Braun, J. Cho, J. H. Pikul, W. P. King, and H. Zhang, "High power rechargeable batteries," *Current Opinion in Solid State and Materials Science,* vol. 16, pp. 186-198, 2012.

[6] C. Delacourt, L. Laffont, R. Bouchet, C. Wurm, J.-B. Leriche, M. Morcrette, *et al.*, "Toward understanding of electrical limitations (electronic, ionic) in $LiMPO_4$ (M= Fe, Mn) electrode materials," *Journal of the Electrochemical Society,* vol. 152, pp. A913-A921, 2005.

[7] H. Zhang, X. Yu, and P. V. Braun, "Three-dimensional bicontinuous ultrafast-charge and-discharge bulk battery electrodes," *Nature Nanotechnology,* vol. 6, pp. 277-281, 2011.

[8] M.-K. Song, S. Park, F. M. Alamgir, J. Cho, and M. Liu, "Nanostructured electrodes for lithium-ion and lithium-air batteries: the latest developments, challenges, and perspectives," *Materials Science and Engineering: R: Reports,* vol. 72, pp. 203-252, 2011.

[9] J. W. D. Long, Bruce; Rolison, Debra R.; White, Henry S, "Three-dimensional battery architectures," *Chemical Reviews (Washington, DC, United States),* vol. 104, pp. 4463-4492, 2004.

[10] T. S. Arthur, D. J. Bates, N. Cirigliano, D. C. Johnson, P. Malati, J. M. Mosby, *et al.*, "Three-dimensional electrodes and battery architectures," *MRS Bull,* vol. 36, pp. 523-531, 2011.

[11] J. Hassoun, S. Panero, P. Simon, P. L. Taberna, and B. Scrosati, "High-rate, long-life Ni–Sn nanostructured electrodes for lithium-ion batteries," *Advanced Materials,* vol. 19, pp. 1632-1635, 2007.

[12] P.-L. Taberna, S. Mitra, P. Poizot, P. Simon, and J.-M. Tarascon, "High rate capabilities Fe_3O_4-based Cu nano-architectured electrodes for lithium-ion battery applications," *Nature Materials,* vol. 5, pp. 567-573, 2006.

[13] G. F. Ortiz, I. Hanzu, P. Lavela, P. Knauth, J. L. Tirado, and T. Djenizian, "Nanoarchitectured TiO_2/SnO: a future negative electrode for high power density Li-ion microbatteries?," *Chemistry of Materials,* vol. 22, pp. 1926-1932, Mar 2010.

[14] S. C. Zhang, Z. J. Du, R. X. Lin, T. Jiang, G. R. Liu, X. M. Wu, *et al.*, "Nickel nanocone-array supported silicon anode for high-performance lithium-ion batteries," *Advanced Materials,* vol. 22, pp. 5378-+, Dec 2010.

[15] F. F. Cao, J. W. Deng, S. Xin, H. X. Ji, O. G. Schmidt, L. J. Wan, *et al.*, "Cu-Si nanocable arrays as high-rate anode materials for lithium-ion batteries," *Advanced Materials,* vol. 23, pp. 4415-+, Oct 2011.

[16] A. Magasinski, P. Dixon, B. Hertzberg, A. Kvit, J. Ayala, and G. Yushin, "High-performance lithium-ion anodes using a hierarchical bottom-up approach," *Nature Materials,* vol. 9, pp. 353-358, Apr 2010.

[17] R. Krishnan, T. M. Lu, and N. Koratkar, "Functionally strain-graded nanoscoops for high Power Li-ion battery anodes," *Nano Letters,* vol. 11, pp. 377-384, Feb 2011.

[18] K. Amine, I. Belharouak, Z. H. Chen, T. Tran, H. Yumoto, N. Ota, *et al.*, "Nanostructured anode material for high-power battery system in electric vehicles," *Advanced Materials,* vol. 22, pp. 3052-3057, Jul 2010.

[19] Y. G. Li, B. Tan, and Y. Y. Wu, "Mesoporous CO3O4 nanowire arrays for lithium ion batteries with high capacity and rate capability," *Nano Letters,* vol. 8, pp. 265-270, Jan 2008.

[20] C. K. Chan, H. Peng, G. Liu, K. McIlwrath, X. F. Zhang, R. A. Huggins, *et al.*, "High-performance lithium battery anodes using silicon nanowires," *Nature Nanotechnology,* vol. 3, pp. 31-35, Jan 2008.

[21] H. Kim, B. Han, J. Choo, and J. Cho, "Three-dimensional porous silicon particles for use in high-performance lithium secondary batteries," *Angewandte Chemie-International Edition,* vol. 47, pp. 10151-10154, 2008.

[22] K. Brezesinski, J. Haetge, J. Wang, S. Mascotto, C. Reitz, A. Rein, *et al.*, "Ordered mesoporous alpha-Fe2O3 (Hematite) thin-film electrodes for application in high rate rechargeable lithium batteries," *Small,* vol. 7, pp. 407-414, Feb 2011.

[23] M. H. Park, Y. Cho, K. Kim, J. Kim, M. L. Liu, and J. Cho, "Germanium nanotubes prepared by using the Kirkendall effect as anodes for high-rate lithium

batteries," *Angewandte Chemie-International Edition*, vol. 50, pp. 9647-9650, 2011.

[24] C. J. Patrissi and C. R. Martin, "Improving the volumetric energy densities of nanostructured V 2 O 5 electrodes prepared using the template method," *Journal of the Electrochemical Society*, vol. 148, pp. A1247-A1253, 2001.

[25] D. Tonti, M. J. Torralvo, E. Enciso, I. Sobrados, and J. Sanz, "Three-dimensionally ordered macroporous lithium manganese oxide for rechargeable lithium batteries," *Chemistry of Materials*, vol. 20, pp. 4783-4790, 2008.

[26] C. M. Doherty, R. A. Caruso, B. M. Smarsly, and C. J. Drummond, "Colloidal crystal templating to produce hierarchically porous LiFePO4 electrode materials for high power lithium ion batteries," *Chemistry of Materials*, vol. 21, pp. 2895-2903, 2009.

[27] M. Yao, K. Okuno, T. Iwaki, M. Kato, S. Tanase, K. Emura, *et al.*, "LiFePO4-based electrode using micro-porous current collector for high power lithium ion battery," *Journal of Power Sources*, vol. 173, pp. 545-549, 2007.

[28] H. Yamada, K. Tagawa, M. Komatsu, I. Moriguchi, and T. Kudo, "High power battery electrodes using nanoporous V2O5/carbon composites," *The Journal of Physical Chemistry C*, vol. 111, pp. 8397-8402, 2007.

CHAPTER 2

DESIGN AND FABRICATION OF MEMS-ENABLED MULTILAYER STRUCTURES

2.1 Sequential Multilayer Deposition

The work presented in this study focuses on the development of rationally designed and deterministically engineered, highly laminated structures to be utilized as electrodes in electrochemical energy storage applications. These structures are based on sequential deposition of alternating layers of structural and sacrificial materials, followed by the selective removal of the sacrificial layers. Both metallic and polymeric materials were utilized in the fabrication process. The resultant versatile architectures are highly scalable, and the way they are designed enables them to possess high surface area on a small footprint. These structures also feature precisely designed characteristic dimensions on the order of hundreds of nanometers and overall thicknesses on the order of hundreds of micrometers.

Two categories of highly-laminated multilayer structures are investigated: structures with lateral high-aspect-ratio and vertical high-aspect-ratio, which are schematically shown in Figures 2.1.A and 2.1.B, respectively. The former involves structures with a high aspect ratio in the in-plane dimension over their thickness, whereas the structures based on the latter one possess a high out-of-plane to width ratio. As shown in Figure 2.1.A, the lateral high-aspect-ratio structures are deposited using a photoresist mold, confining the in-plane surface area. In contrast, the mold-free fabrication of vertical high-aspect-ratio structures enables an increase in surface area in both the vertical and radial directions as demonstrated in Figure 2.1.B.

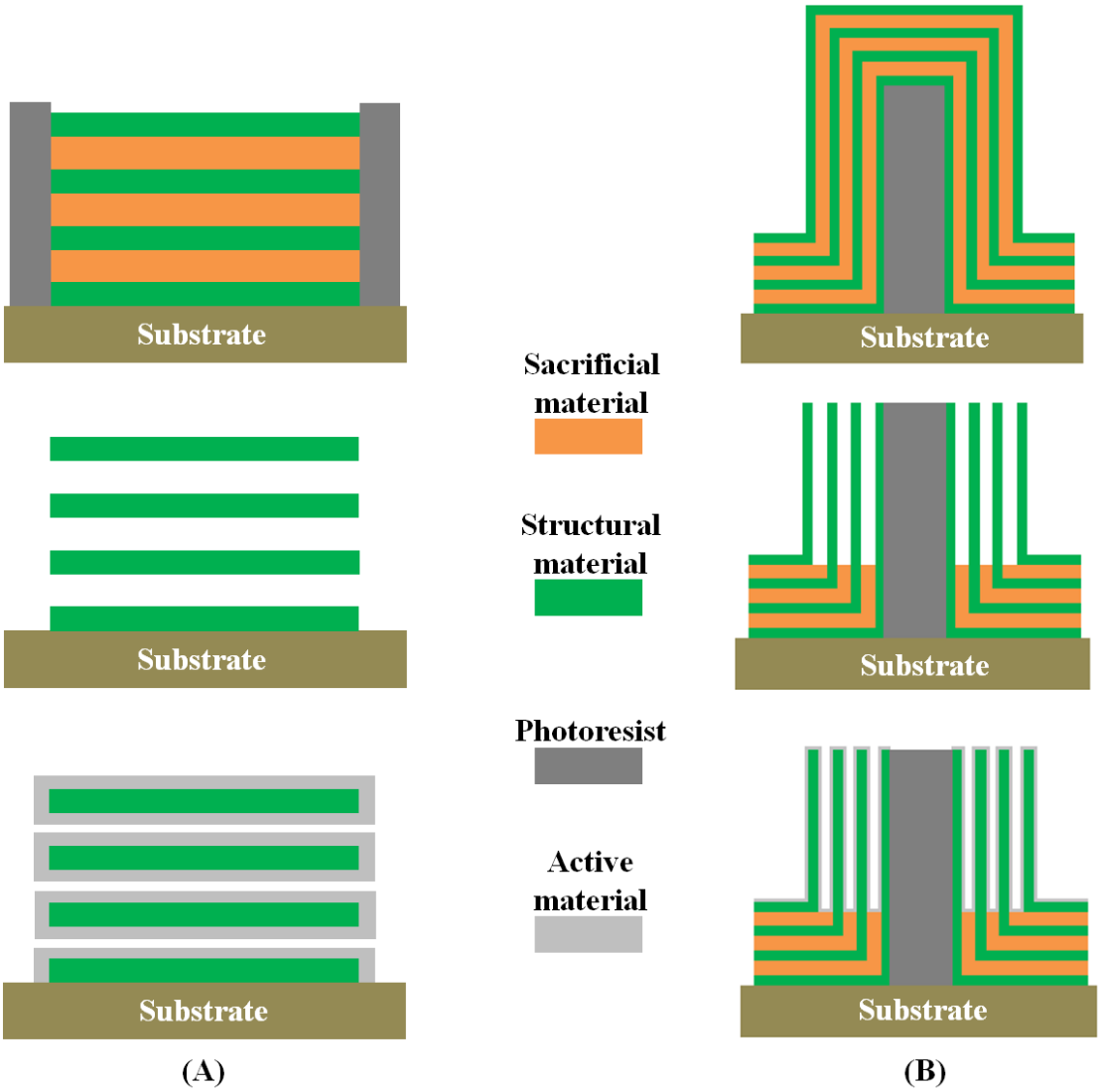

Figure 2.1: Comparison of lateral and vertical high-aspect-ratio structures

The vertical high aspect ratio approach demonstrates a subtle way of obtaining high-surface-area multilayer structures which requires neither molds nor anchors in their fabrication process. The drawback of these pillar structures, however, is the long diffusion path lengths for the liquid-state ions of the electrolyte. As can be seen in Figure 2.1.B, in order for the ions to reach to the active material located at the very bottom of the electrode, they have to diffuse all the way from the very top surface of the pillars that is in contact with the bulk of the electrolyte. In that sense, it is analogous to the lateral high-

aspect ratio structures without any etching holes where the diffusion of the ions to the center part of the layers would only be possible from the perimeter of the structure. In the case of lateral high-aspect-ratio structures, on the other hand, the diffusion path lengths of the liquid-state ions can be easily controlled by rearranging the positions of the photoresist mold (i.e., etching holes).

Since one of the goals of this study is to enable high-power electrodes by minimizing the diffusion path lengths for both solid- and liquid-state ions, the utilization of vertical high-aspect-ratio structures in high-power applications would be against the premise of this study. If, however, the amount of liquid ions within the vertical channels is sufficient to meet the demand of the solid electrode, then there would be no need for the ions to travel long distances. Batteries with significantly thick active material films may require large amounts of ions to be delivered to the bulk of the active material. Yet, systems involving surface-limited reactions, such as electrochemical capacitors, require smaller amounts of ions. Therefore, these vertical high-aspect-ratio structures have only been utilized as electrodes for electrochemical capacitors which will be covered in detail in Chapter 6.

More details pertaining to the fabrication of the lateral and vertical high-aspect-ratio structures will be revealed in sections of 2.1.1 and 2.1.2, respectively. The former type of structures will further be classified into three categories: partially etched metallic structures (Chapter 2.1.1.1), anchor-supported metallic structures (Chapter 2.1.1.2), and polymer-based multilayer structures (Chapter 2.1.1.3).

2.1.1 Lateral High-Aspect-Ratio Structures

In the case of metallic structures, a robotically-assisted electroplating setup has been utilized to fabricate the multilayer structures with alternating layers through a standard photoresist mold enabled by photolithography techniques. By adjusting the current density and electrodeposition time, structures composed of sub-micron-thick

individual layers were able to be realized whose total thicknesses reach up to several hundreds of microns. These structures eventually offer a high surface area that is more than a hundred times as large as the footprint area they are built on. The conceptual rendering of the experimental setup enabling the fabrication of these metallic multilayer structures can be seen in Figure 2.2.

Almost all of the lateral high-aspect ratio multilayer structures demonstrated in this study were fabricated on either a 4-inch Si wafer or a rectangular glass substrate (75 mm x 50 mm). In either case, Ti/Cu/Ti seed layers were sputtered onto the one side of the substrate (DC sputterer, CVC). For the sputtering process, high-purity Cu and Ti targets with respective diameters of 3 and 8 inches were used. Sputtering was preferred over other metallization techniques (e.g., evaporation) for two main reasons: (1) faster deposition rates enabled by the sputtering process; (2) the availability of a multi-target sputtering tool that enables the sequential deposition of different metals without the need for interrupting the process to change the targets.

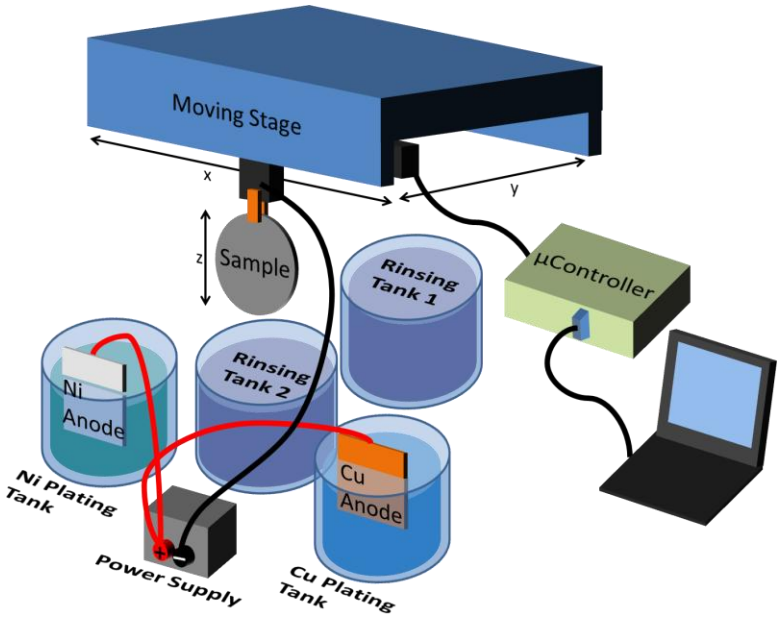

Figure 2.2: Conceptual rendering of the robotically-assisted sequential electroplating setup for the fabrication of the metallic multilayer structures

First, an approximately 500 nm Ti layer, which serves as the adhesion promoter between the substrate and the subsequent Cu layer, is sputtered at a power of 350 W for 10 minutes. Second, an approximately 2-μm-thick Cu layer is sputtered onto the Ti layer at 1000 W. This Cu layer serves as the initiation point (i.e., seed layer) of the electroplating process. On top of Cu layer, another 500-nm-thick Ti layer was sputtered under the same conditions as the first one. The reported thickness values for the sputtered layers were measured by a surface profiler (Tencor P15). The purpose of the last Ti layer is to prevent the underlying Cu layer from getting oxidized, especially in cases where the samples undergo high-temperature treatment, such as pre- and post-exposure bakes for the photoresist films. To prevent the oxidation of the deposits, as well as the targets, the whole sputtering process for both Ti and Cu layers was performed in 100% Ar environment under a pressure of 6 mTorr.

Once the metallization of the substrates is completed, the fabrication process for the deposition of the molds is initiated. This will be discussed in detail later in section 2.2. First, the emphasis will be on the sequential deposition of the multilayer structures.

All of the metallic multilayer backbone structures described in this study are based on the utilization of Ni/Cu pairs. Except in the case of electrochemical capacitors covered in Chapter 6, Cu and Ni have served as the sacrificial and structural materials, respectively.

Before the use of each electroplating bath, the plating solutions were filtered by passing through a 0.6-μm filter paper. After each use, they were stored in well-sealed containers, and a small amount of nitrogen gas was bubbled in the containers to keep the baths free of dissolved oxygen. The composition of the lab-made Ni and Cu plating baths can be found in Table 2.1.

Table 2.1: Compositions of the Ni and Cu plating baths [1]

Compounds	Ni Plating Bath	Cu Plating Bath
$NiSO_4.6H_2O$	350-400 g	
$CuSO_4.5H_2O$		200-250 g
H_2SO_4 (98%)		20-25 ml
H_3BO_3	35-40 g	
Saccharin	3 g	
DI water	1 L	1 L
pH	1.5-3	0.5-1

For all of the applications discussed in this study, the same Ni bath has been utilized for the electrodeposition of the Ni layers. However, except for the fabrication of the multilayer structures for the Zn-air batteries which will be discussed in Chapter 3, a commercial Cu plating solution (Clean Earth Cu-Mirror, Grobet) has been preferred over the sulfate-based Cu bath given in Table 2.1. The reason behind switching to the commercial plating solution is to obtain smoother layers by reducing the surface roughness of the deposits. Although surface roughness can be considered as a desired attribute for energy storage applications because of its contribution to the increased surface area, for applications comprising of ultra-thin layers, smoother deposits would enable better control over the dimensions of the structures. Figure 2.3 shows the difference between two multilayer structures fabricated by using two different Cu plating solutions. For the multilayer structures with a relatively low number of layers (e.g., 10), the surface roughness was not observed to constitute a severe problem. However, as the number of layers was increased, the roughness was found to be more problematic.

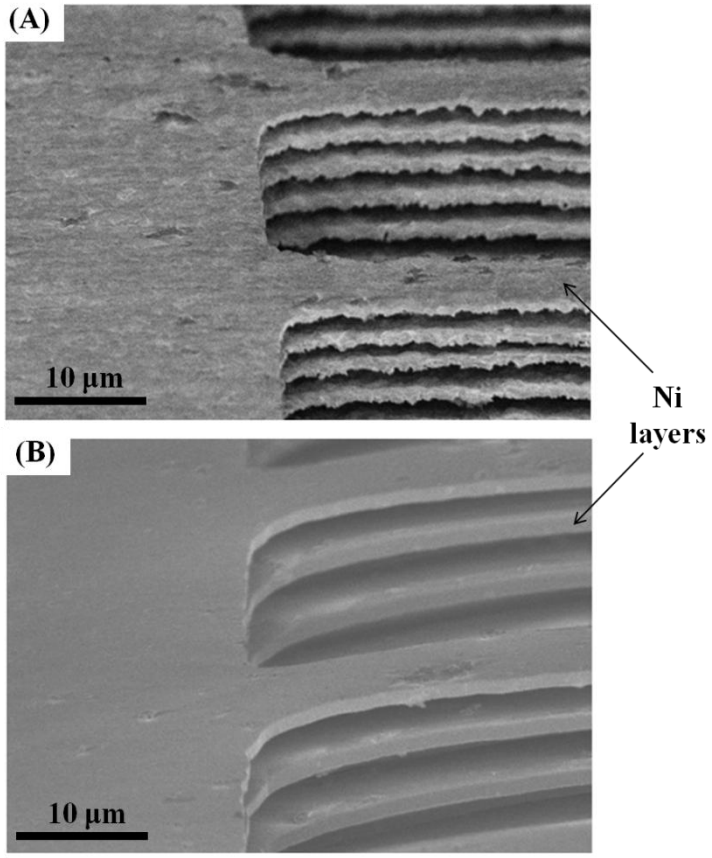

Figure 2.3: Multilayer Ni structures following the removal of Cu layers prepared by: (A) sulfate-based Cu plating solution, (B) commercial Cu plating solution with additives

Immediately before the electroplating of alternating Ni and Cu layers, the sample was immersed in diluted hydrofluoric acid (HF) solution ($HF:H_2O = 1:50$) to remove the topmost Ti layer on the regions of the substrate that were not covered by the photoresist mold. Once the underlying Cu layer was exposed, the sample was taken out from the HF solution and rinsed in DI water. To avoid the oxidation of the newly exposed Cu surface, the robotic plating process was started immediately.

The robotic plating process starts with the electroplating of the Ni layer in its corresponding all-sulfate bath for a given amount of time. The electrodeposition is carried out under galvanostatic conditions where a high-purity Ni sheet is utilized as the anode, and the current density is set to values ranging from 10 to 20 mA cm^{-2}. During the electroplating process, the Ni plating solution is stirred with a magnetic bar at a moderate

speed. This stirring effect enables removal of some of the high number of bubbles that form on the surface of the substrate during the Ni electrodeposition process, particularly when high current densities are applied.

Next, the robotic arm removes the sample from the Ni bath, and the excess solution on the sample is allowed to drip off from the substrate for three seconds. The sample is immersed in the first rinsing bath and then the second rinsing bath both of which contain deionized (DI) water. To ensure a thorough cleaning of the substrate, the arm moves the sample horizontally in the x-direction inside the rinsing baths for a total duration of 15 seconds each. Having two separate rinsing baths minimizes the cross-contamination between the Ni and Cu plating solutions. The time the sample spends in the air is minimized by rapid movements of the robotic arm, in order to prevent the freshly deposited layer from becoming oxidized, especially after the electrodeposition of the Cu layer.

Following the rinsing process, the arm quickly immerses the sample in the Cu plating bath, and the electroplating is performed for the given amount of time at the same current density as in the case of Ni. No agitation is performed in the case of Cu electrodeposition. A high-purity Cu sheet of the same geometric surface area as the sample is utilized as the anode. Prior to electrodeposition process, the Cu sheet is smoothed with a high-grade (600) sand paper and then cleaned with acetone/methanol/IPA mixture. Next, the Cu sheet is immersed in a diluted HCl solution ($HCl:H_2O = 1:4$) to remove the oxide layer on the Cu surface and then thoroughly rinsed with DI water followed by a blown nitrogen treatment.

For long-lasting plating processes (e.g., > 24 hours), the Cu anode was observed to be severely degraded due to the highly corrosive plating bath. As a result of this degradation, large amount of precipitates, which were suspected to negatively impact the quality of the deposits, were found on the bottom of the plating bath container. To avoid the precipitation of the degradation products, the Cu anode was kept wrapped in a

microporous filter paper throughout the plating process. A similar situation was not observed with the Ni anode.

This deposition sequence is repeated for as many times as the desired number of pairs of Cu/Ni layers. During the long-lasting electroplating processes where more than 25 pairs of Cu/Ni layers are deposited, the rinsing baths are refreshed every 25 pairs. Also, during such long-lasting electroplating processes, a significant decrease was observed in the amount of the plating solution, which stems from the evaporation of the water from the bath. Depending on the temperature in the lab, decreases in the volume of the plating bath by as high as 20% happened to be observed after 24-hour-long plating. The effects of these losses on the deposit quality could be quite severe as this indicates a significant change in the concentration of the bath. To compensate these losses, high-purity DI water was regularly added to the baths after each deposition of 25 pairs of Cu/Ni layers.

Once the electroplating process is completed, the photoresist mold is stripped from the substrate. Depending on the type of the multilayer structure, either the Cu etching process (see section 2.3), or the deposition of the second photoresist layer is initiated. The former process is pursued for the partially etched structures, which will be discussed in section 2.1.1.1. The latter process involves the anchor-supported multilayer structures, which can be found in section 2.1.1.2.

2.1.1.1 Partially Etched Structures

Three different types of fabrication approaches have been adopted for the realization of the lateral high-aspect-ratio structures. In this first approach, the etching process is initiated immediately after the removal of the photoresist mold. This fabrication sequence is shown in Figure 2.4. Cu layers are partially etched by using a Cu etchant providing an infinite selectivity of Cu over Ni. Details regarding the etchant will be discussed in section 2.3.

As can be seen from Figure 2.4, the more Cu that is removed, the more Ni surface area is exposed. On the other hand, it is also crucial to preserve a certain amount of Cu in order to provide both electrical connection between the Ni layers, as well as mechanical support to prevent the Ni structure from collapsing. To shorten the etching time, the layers contain a number of etching holes (see Figure 2.3). The presence of these etching holes enables the advancement of the etching from multiple points within the structures and thus, a faster removal of Cu layers. Increasing the number of etching holes results in a faster processing, but at the expense of decreasing the total surface area of the electrode structure.

The multilayer metallic structures fabricated according to this approach have been utilized as current collectors in Zn-air battery applications (see Chapter 3). The main advantage associated with this approach is that, compared to anchor-supported structures illustrated in Figure 2.5, it is based on a much simpler fabrication sequence which involves a single photolithography process. Also, since only partial etching is performed, the duration of the etching process is much shorter. However, due to the diffusion-related non-uniformity issues taking place in the prolonged etching processes, which will be discussed in detail in section 2.3, the partial etching approach is not recommended for structures which have a large area confined within the outer perimeter (i.e., footprint). Hence, the structures fabricated via this approach were built on relatively small footprints (e.g., 2-3 mm^2).

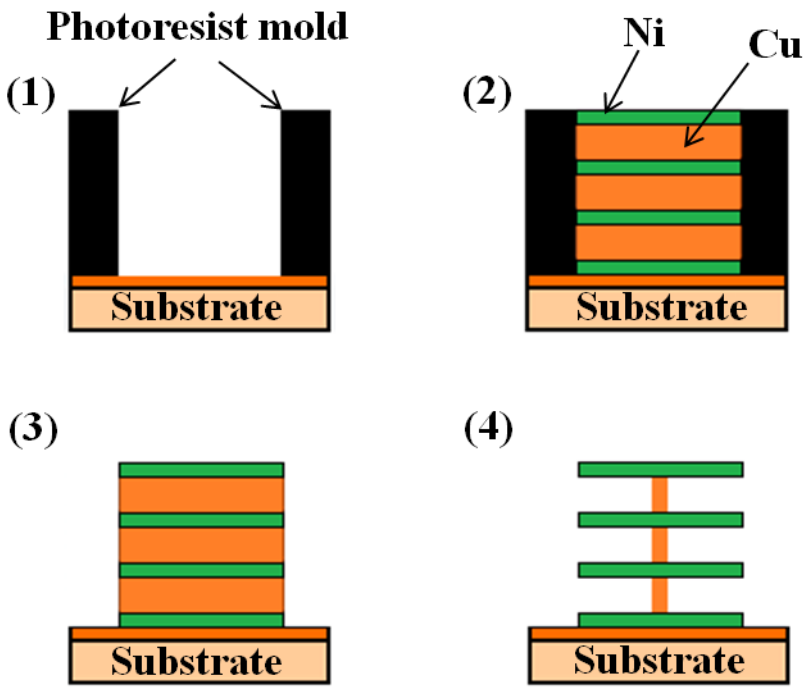

Figure 2.4: Fabrication sequence for the partially-etched multilayer structures: (1) development of the photoresist mold on a metal-coated substrate, (2) deposition of Ni and Cu layers in an alternating fashion, (3) removal of the photoresist mold, and (4) partial etching of sacrificial Cu layers

2.1.1.2 Anchor-Supported Structures

To overcome the issues originating from partial etching process and also, to enable structures with higher surface areas, methods to fabricate anchor-supported structures have been developed. The fabrication sequence for this approach is summarized in Figure 2.5.

Unlike the case of the partially etched structures, the removal of the photoresist after the sequential electroplating process is followed by the deposition of the second photoresist layer, which serves as a mold for the anchors. The anchors are then electroplated onto specific regions of the sidewalls of the multilayer structures by using the plating bath of the structural material (i.e., Ni) so that they do not dissolve in the etching process. Upon completion of the anchor electroplating, the second mold is stripped and the sample is immersed in the Cu etchant for the selective and complete

removal of the Cu layers. To ensure the complete removal, the etching durations were significantly increased (> 10 hours).

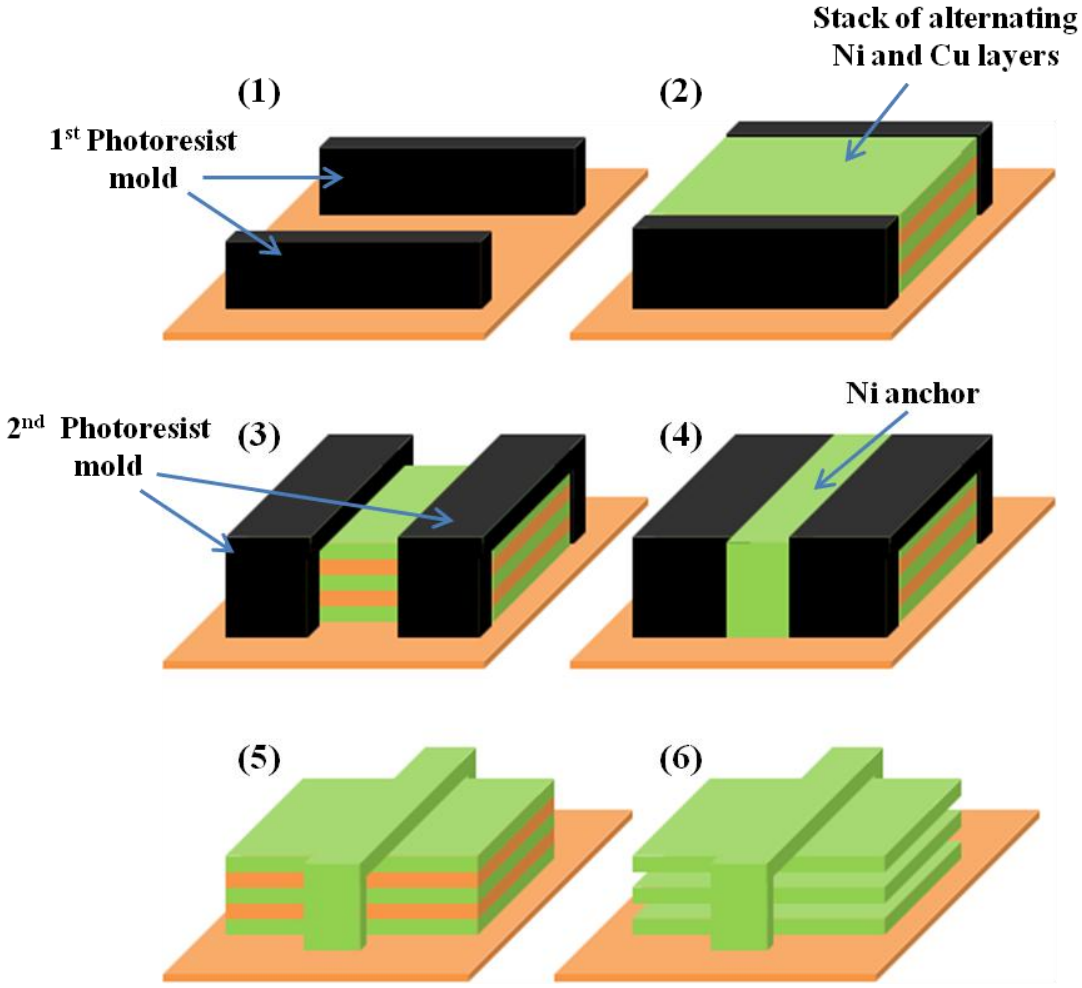

Figure 2.5: Fabrication sequence for the anchor-supported structures: (1) development of the photoresist mold on a metal-coated substrate, (2) electroplating of sequential Ni and Cu layers, (3) deposition of the second mold, (4) electroplating of Ni anchors, (5) removal of the second photoresist, and (6) selective and complete removal of the sacrificial Cu layers

This approach enables the realization of the maximum theoretical surface area of the multilayer structures by allowing the complete exposure of both sides of the individual Ni layers. This is achieved at the expense of the total fabrication time, since the etching duration is significantly increased. The resultant structures have been utilized

as current collectors for secondary battery chemistries, as well as electrochemical capacitors, which will be discussed in Chapters 4, 5, and 6.

2.1.1.3 Polymer-Based Structures

The same multilayer fabrication approach has been applied to polymer structures as well. There are three main motivations behind this route: (1) Using polymer structures would enable much lighter backbone materials than metals for a given mass and/or volume, which opens up the possibility for higher energy and power densities; (2) in contrast to metals that only have a small group of electrodepositable members, there is a wide variety of polymers that can be studied; and (3) unlike the metal electroplating, where highly corrosive (e.g., acidic Cu plating bath) and relatively toxic electroplating baths (e.g., cyanide-based baths), as well as hazardous chemicals may be utilized, the fabrication of the polymer structures is a more environmentally friendly process.

Similar to previously described metal-based approaches, two different polymers are used in the fabrication process, one being sacrificial while the other one is structural, and they are deposited in an alternating sequence. One of the major differences between the processing of the metal-based and polymer-based structures is that no mold is required for the latter one, which introduces simplicity to the process. Since no mold is utilized for the polymer structures, their final shape is obtained by the laser-micromachining, which is applied upon completion of the deposition of multilayer structures. The other major difference is the deposition technique utilized in both approaches. Metal-based structures are deposited electrochemically, while the polymers in this study undergo sequential spin-coating process.

As in the case of metallic multilayer structures, two fabrication approaches were pursued for the polymer-based structures: anchor supported and partially etched structures. Figure 2.6 and 2.7 illustrate the fabrication sequence of the former and latter approaches, respectively.

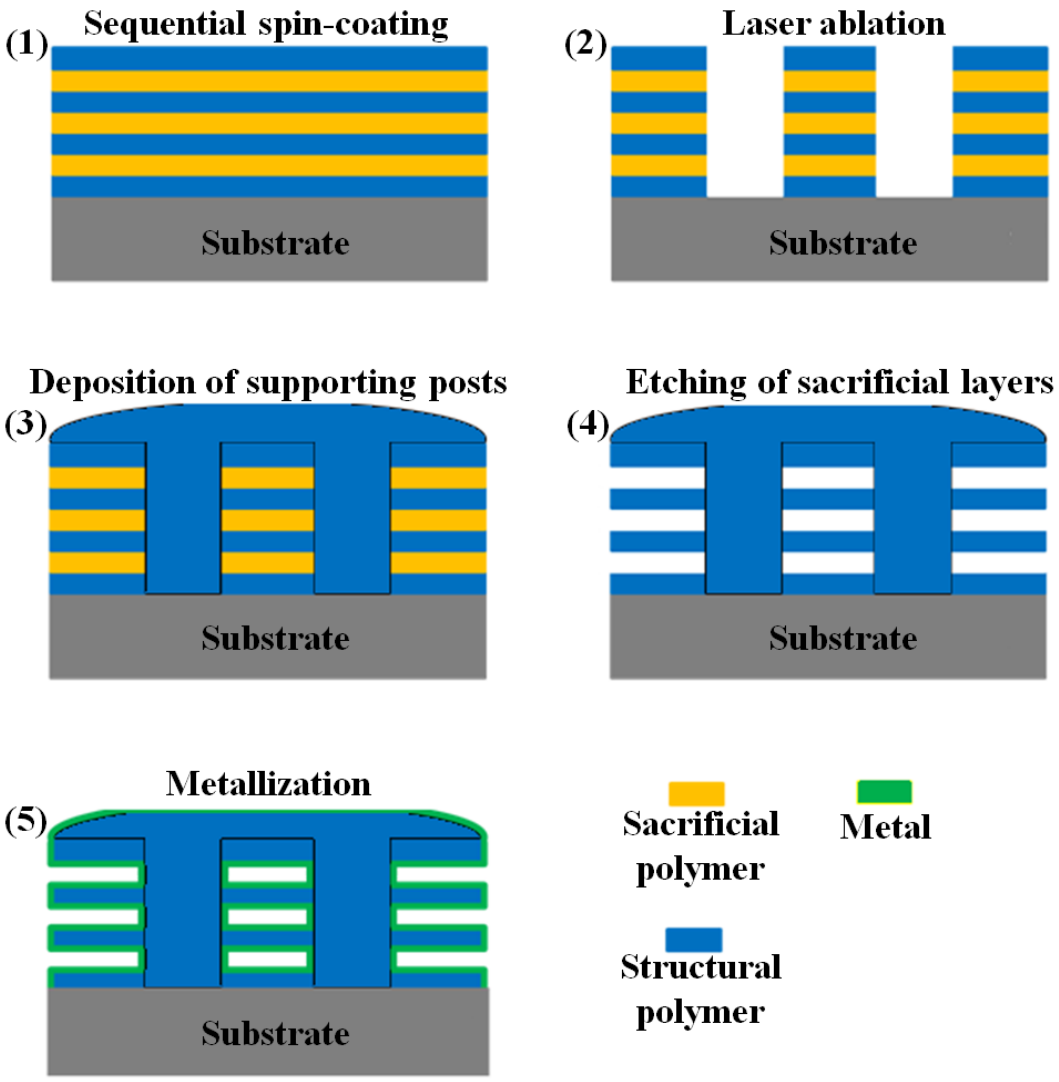

Figure 2.6: Fabrication sequence for the anchor-supported multilayer polymer structures: (1) sequential spin-coating of structural and sacrificial polymer layers, (2) laser ablation to open holes for the supporting posts, (3) deposition of the structural polymer in the laser-ablated holes, (4) removal of the sacrificial layers, and (5) metallization of the multilayer structure

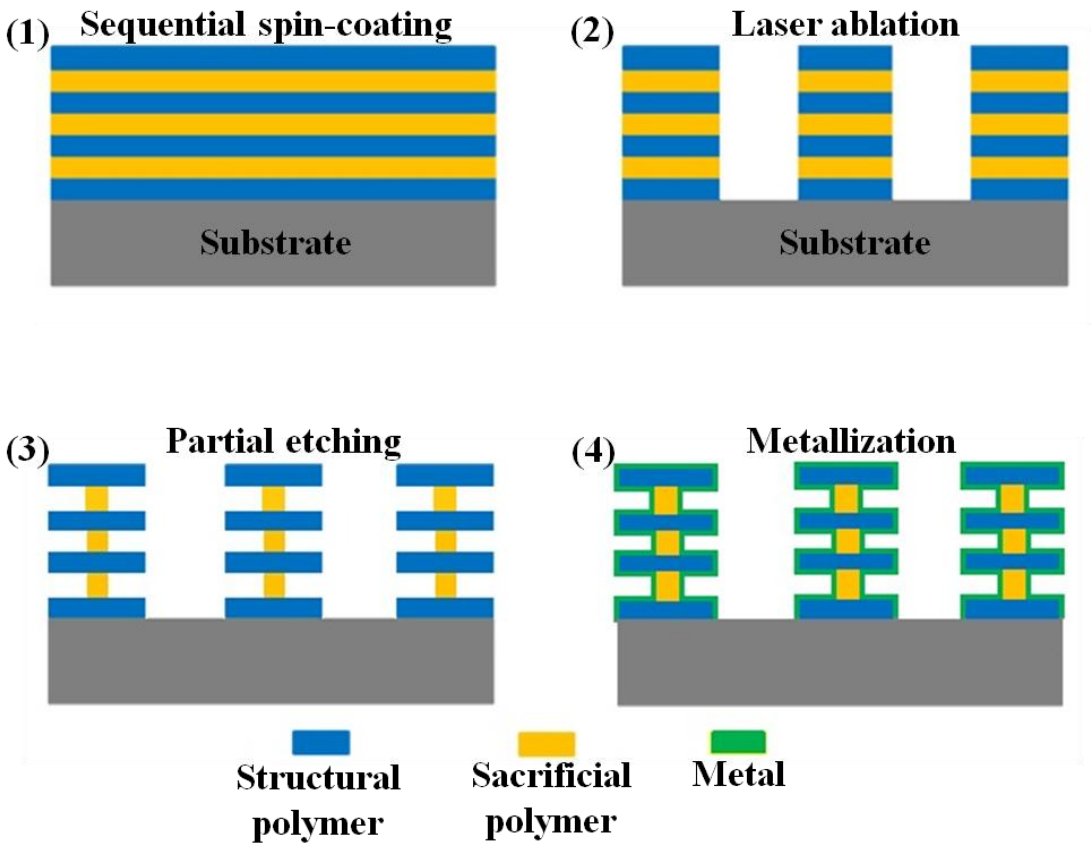

Figure 2.7: Fabrication sequence for the partially etched multilayer polymer structures: (1) sequential spin-coating of structural and sacrificial polymer layers, (2) laser ablation to open holes for the supporting posts, (3) removal of the sacrificial layers, and (4) metallization of the multilayer structure

Table 2.2: Comparison of various polymer pairs used in the fabrication of multilayer structures

Polymer Pair	Sacrificial Layer	Adhesion Quality	Ablation Quality	Etching Method
Unity/POSS	Unity	Good	Poor	Thermal or wet
Unity/SU-8	Unity	Poor	Good	Thermal or wet
POSS/SU-8	POSS	Good	OK	Wet
Avatrel/SU-8	Avatrel	OK	Poor	Wet
Avatrel/POSS	Avatrel	Good	Good	Plasma

Several polymer pairs have been studied most of which are listed in Table 2.2. Among these alternatives, a photodefinable polynorbornene-based polymer (Avatrel 2585P, Promerus) and a photodefinable epoxy-functionalized polymer (photodefinable

epoxycyclohexyl polyhedral oligomeric silsesquioxane (POSS)) pair with its good adhesion and ablation qualities were found to be the best candidate for the fabrication of the multilayer structures.

Another polynorbornene-based polymer (Unity 2203, Promerus) was also paired with POSS. Unity/POSS pair demonstrated a good adhesion quality as shown in Figure 2.8.A. However, its ablation process was problematic as it requires higher energy and longer duration to ablate through. Also, tapered side walls were observed in the ablated holes of Unity/POSS pair, which can be seen in Figure 2.8.B.

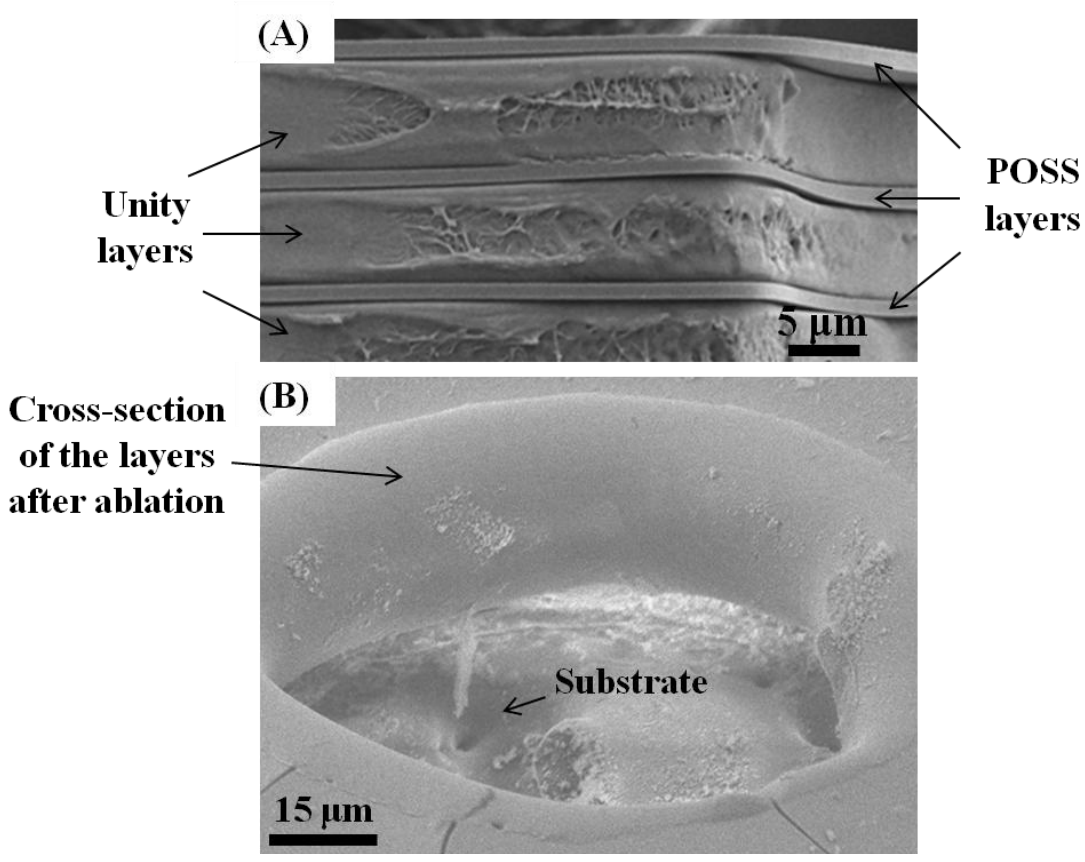

Figure 2.8: SEM images of the multilayer polymer structures based on 3 pairs of Unity/POSS: (A) cross-sectional view of the sidewall following the dicing process, (B) sidewall of the hole following the laser ablation process

The Unity/SU-8 pair, on the other hand, requires much less power to ablate, as well as formed clean and non-tapered side wall profile in the ablated holes. The main drawback is the poor adhesion quality between the layers, which results in non-uniform deposition of the layers. Similar to Unity/SU-8 pair, Avatrel/SU-8 pair has poor ablation qualities too, but a slightly better adhesion quality between the layers.

Taking all these aspects into account, Avatrel/POSS has been suggested as the most promising pair of polymers to study for these applications. In this scenario, POSS and Avatrel make up the structural and sacrificial layers of the multilayer structures, respectively. A proof-of-concept structure consisting of 3 pairs of POSS and Avatrel layers was fabricated.

As in the case of metal-based structures, Si wafer or glass was preferred as substrates on which the multilayer structures were deposited. Figure 2.6 and 2.7 illustrate the conceptual rendering of the fabrication processes for the polymer multilayer structures. The fabrication sequence starts with the spin-coating of the POSS layer on the Si substrate. A two-step spinning process was performed where the spin speed was set to 500 rpm for 10 seconds and then increased to 3500 for 30 s. Following the spinning, a soft-bake was performed on a hotplate at 105 °C for 3 minutes. Next, a flash UV exposure was carried out for 40 seconds where the wavelength and the power density of the UV light were 365 nm and 5 mW cm^{-2}, respectively. Immediately after the exposure, the sample was placed on a hotplate at 105 °C for 3 minutes to perform the post-exposure bake. It was found that the baking steps are quite critical. If not performed properly, the solvent from the subsequently deposited layer was observed to dissolve and thus deform the previously deposited layer. In order to minimize the total duration of the whole process, no waiting time was allowed between the steps. The thickness of the POSS layer enabled under the given conditions was found to be ~6 μm by using a surface profiler (Tencor P15).

Following the deposition of the POSS layer, the Avatrel layer was spin-coated as the next layer. As in the case of POSS, a two-step spinning process was performed. Initially, the spin speed was set to 500 rpm for 10 seconds and then increased to 1000 rpm for 30 seconds. Soft-bake, UV-exposure, and post-exposure bake steps were carried out under exactly same conditions as the POSS layers. The final Avatrel layer was measured to have a thickness of 2 μm. Upon completion of the Avatrel deposition, the whole process up to this point was repeated two more times to finalize the fabrication of the polymer-based multilayer structure with three pairs of layers.

Ideally, the Avatrel layers were meant to be slightly thicker than the POSS, since they were planned to serve as sacrificial layers. Therefore, the spinning speed for the Avatrel was much smaller than that of POSS. Nevertheless, the POSS layers in the resultant structure were found to be approximately 3 times as thick as the Avatrel layers, as can be seen in Figure 2.9. This resulted from the high viscosity of POSS, which can be subject to change by modifying the amount of solvent in the polymer.

The sequential deposition of the Avatrel/POSS layers was followed by the laser ablation process. As shown in the fabrication sequence in Figure 2.6, the ablation process enables the formation of the holes in the multilayer structure which were meant to be filled with the structural polymer, i.e. POSS, to provide mechanical support following the removal of the sacrificial polymer. The specifications of the laser had to be optimized to enable an adequate ablation. Table 2.3 summarizes the optimized parameters for the ablation process.

Table 2.3: The specifications for the laser used in the ablation process

Laser type	**UV Excimer**
Wavelength	248 nm
Mask Diameter	0.4 mm
Demagnification	x5
Laser Energy	200 mJ
Discharge High-Voltage	17.7 kV
Transmission	50%
Number of Pulses	60

Using the optimized parameters of the laser, an array of 10x10 holes were etched on a footprint of 3.24 mm^2, which can be seen in Figure 2.9. The diameters of these holes are 75 μm and have a center-to-center distance of 180 μm. As can be seen from the high-resolution scanning electron microscopy (SEM) image in Figure 2.9, the individual POSS and Avatrel layers can easily be distinguished indicating a good ablation capability. Some polymer residues originating from the redeposition of the molten polymers immediately after the ablation can also be noticed on the surface of the Si substrate.

Based on the fabrication sequence given in Figure 2.6, the holes were filled by pouring POSS onto the ablated multilayer structure, which was followed by soft-bake, UV exposure, and post-exposure bake steps under the same conditions as before. The next step involves complete removal of the sacrificial layers in the multilayer structures. To the best of our knowledge, there is not an appropriate wet etchant that would selectively remove Avatrel over POSS. Also, for this kind of polymer-based processes, wet etching may easily result in the stiction of the structural layers to each other following the removal of the sacrificial layers, which causes substantial deformations in the resulting structure. Therefore, thermal and plasma etching were considered as alternative removal techniques for the sacrificial polymers.

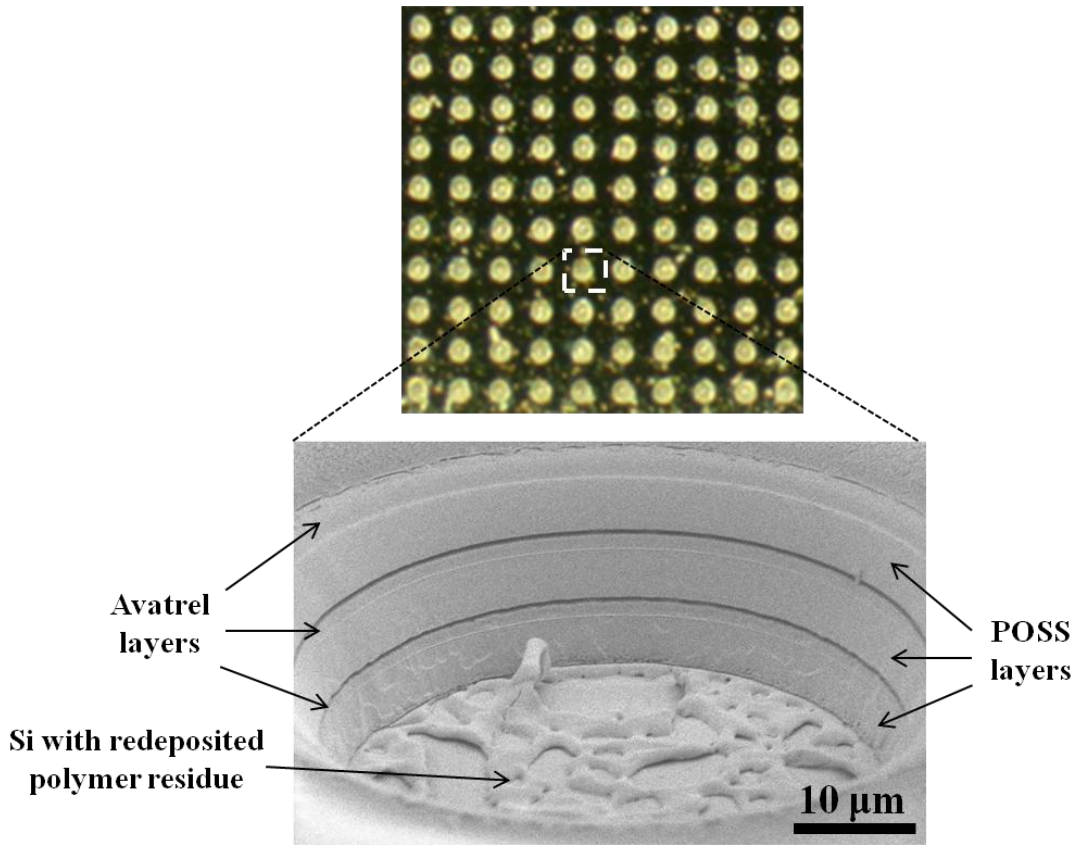

Figure 2.9: Optical and SEM images of the polymer-based multilayer structure with 3 pairs of Avatrel/POSS layers: (A) optical image showing the top view of a 10x10 hole array after laser ablation, (B) SEM image showing the cross-section of a laser-ablated hole in the multilayer structure

Selective thermal removal of polynorbornene-based sacrificial polymers has been successfully demonstrated [2]. However, according to the thermal gravimetric analysis (TGA) profiles of Avatrel and POSS, they have relatively close degradation temperatures both of which are well above 300 °C [3, 4]. Because of this, thermal degradation was considered as an impractical tool for the removal of the sacrificial polymer in this particular multilayer system. Nonetheless, some attempts were made by placing the sample in the oven and increasing the temperature slowly to 405 °C at a ramp-up rate of 1 °C min^{-1}. After allowing the sample to rest at 405 °C for 2 hours, it was again cooled down to room temperature at the same rate. The SEM image showing the results of the selective thermal etching attempts can be seen in Figure 2.10. Avatrel layers were able to

be removed successfully without leaving any residues behind; yet, the remaining POSS layers were severely damaged and shattered into pieces due to the thermal expansion effects.

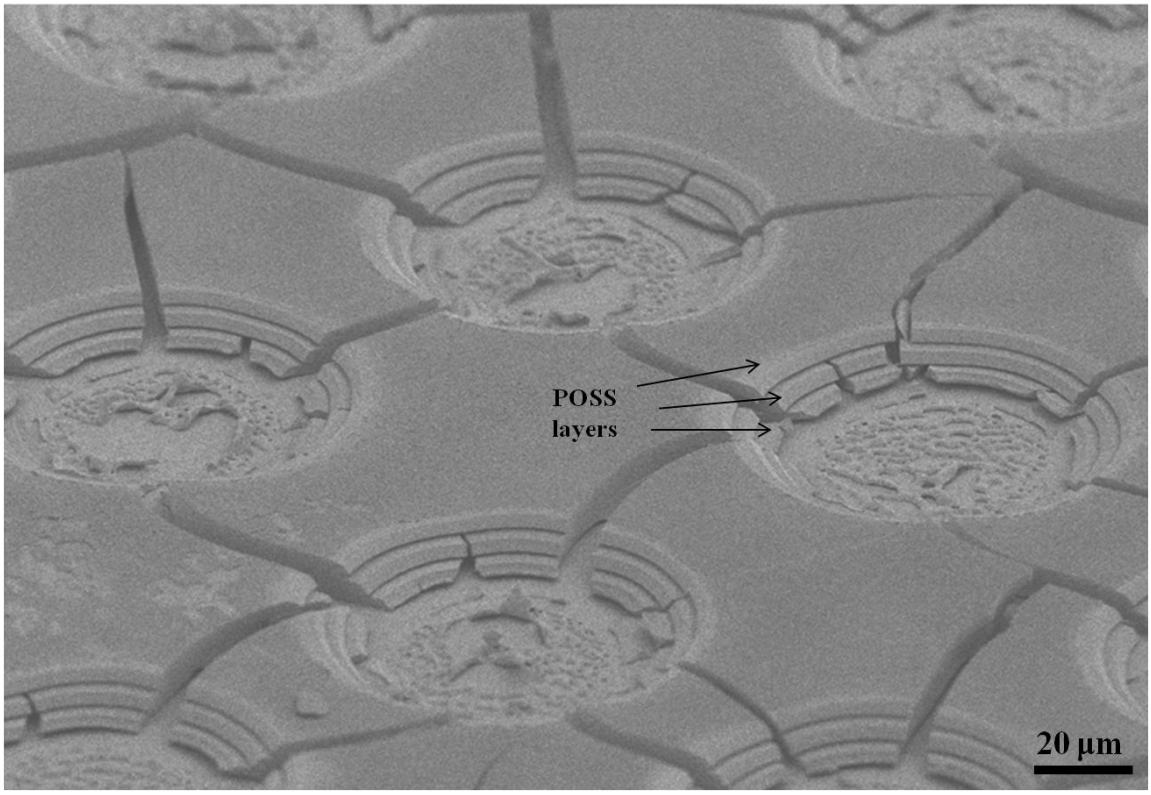

Figure 2.10: POSS layers following the thermal removal of Avatrel at 405 ^{o}C

Therefore, plasma treatment remained as the only option to selectively remove the sacrificial layers. Oxygen plasma containing small amounts of sulfur hexafluoride (SF_6) has been demonstrated to be successful in selective removal of the Avatrel over POSS [4]. However, certain problems exist regarding the use of plasma for this kind of applications. First, plasma etching is a rather complicated process since there are many parameters (e.g., choice of gas, power, gas flow rate, and pressure) that must be fine-tuned to optimize the etching rate, so that a highly selective and relatively fast etching can be enabled. Second, unless a barrel asher plasma is utilized, the plasma process itself

is highly anisotropic and therefore, etching of the sacrificial layers in the lateral dimension becomes quite complicated. Lastly, even if the isotropy is improved, the complete removal of the sacrificial layers is quite challenging, as the plasma will only be able to attack from the outer perimeter of the multilayer structure. Because of this, an alternative fabrication process had to be developed which involves partial removal of the sacrificial layers, as demonstrated in Figure 2.7. In this approach, the laser-ablated holes are not filled with the structural polymer. Instead, similar to the case of partially-etched metallic multilayer structures, they serve as etching holes which improve the access of the plasma to the sacrificial layers.

In order for this method to be efficient, the number of holes needs to be increased, which provides a faster etching rate for plasma. Figure 2.11 shows the optical images of the multilayer structure with a denser array (20x20) of holes. To improve the isotropy of the plasma process, the chamber pressure was increased while the power was being reduced. Details of the plasma specifications can be found in Table 2.4.

Table 2.4: Plasma specifications for the removal of the sacrificial polymer layers

Plasma type	**Reactive Ion Etcher (Plasma-Therm)**
Pressure	500 mTorr
Power	75 W
O_2 Flow Rate	90 sccm
SF_6 Flow Rate	1 sccm
Duration	1 hour

An array of 20x20 holes shown in Figure 2.11.A was fabricated on a footprint area of 3.24 mm^2. For single layer thin-film structures, the etching rate of the plasma can simply be determined experimentally by periodically measuring the thickness of the film throughout the plasma etching process. However, in this case, where the etching occurs in the lateral direction, assuming a constant etching rate over the course of the entire plasma etching process is not realistic. Yet, a method had to be found to determine the surface

area obtained after the etching process. SEM images showing the tilted view of the holes in Figure 2.12 confirm that no matter how much tilted, visually it is not possible to measure the depth of etching by means of SEM. However, it was found that the undercut resulting from the partial removal of the sacrificial polymers can be visible due to the change in transparency of the multilayer polymer structure. By making use of an optical microscope, the boundaries of the undercut regions in the form of light yellow rings around the holes can clearly be seen, as demonstrated in Figure 2.11.C.

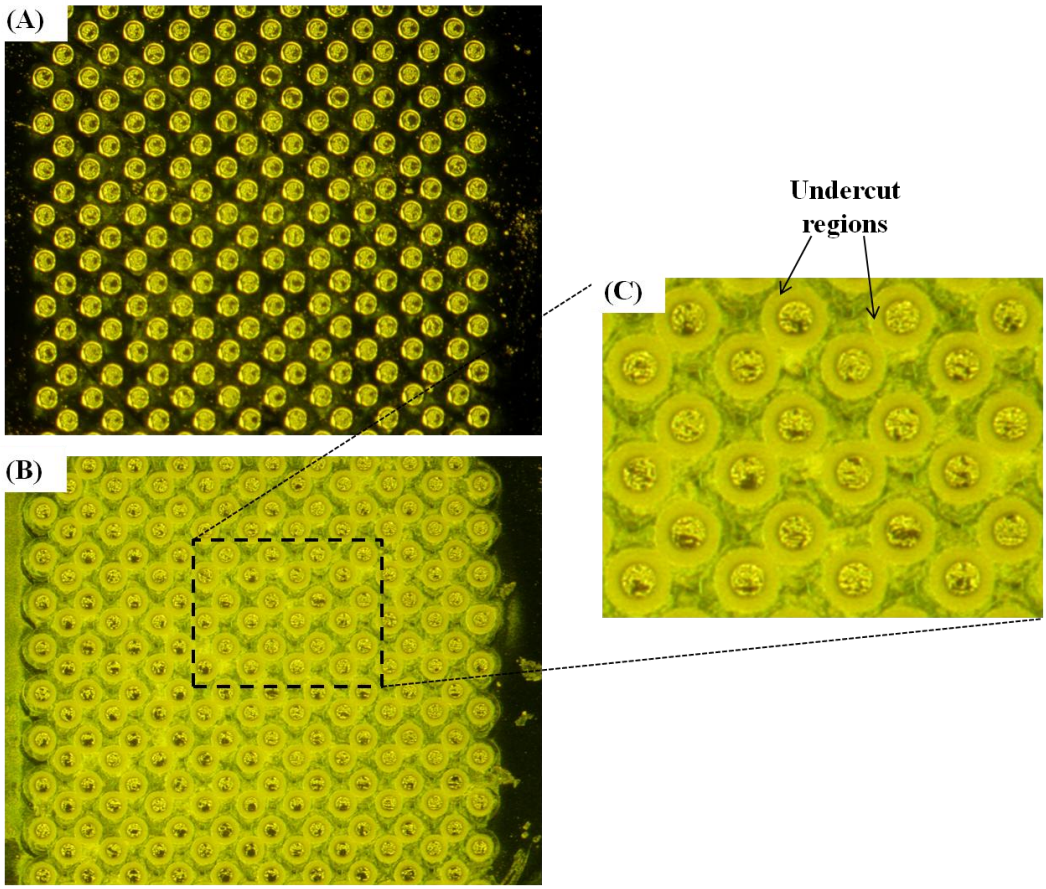

Figure 2.11: Optical images showing the top view of the high-density array of holes enabled by laser ablation: (A) holes before plasma etching, (B) holes after 1-hour-long plasma etching, and (C) closed-up view of the holes after the plasma etching

The closed-up view of the holes given in Figure 2.11.C clearly shows a quite uniform etching profile enabled by the plasma process. To estimate the maximum

achievable depth in the lateral direction, plasma process whose recipe is given in Table 2.4 was applied for various lengths of durations. It was found that after approximately one hour, no significant advancement of etching was observed, and the process reached saturation. Therefore, this etching depth of approximately 40 μm should be taken into account when designing functional, polymer-based structures with maximum surface area.

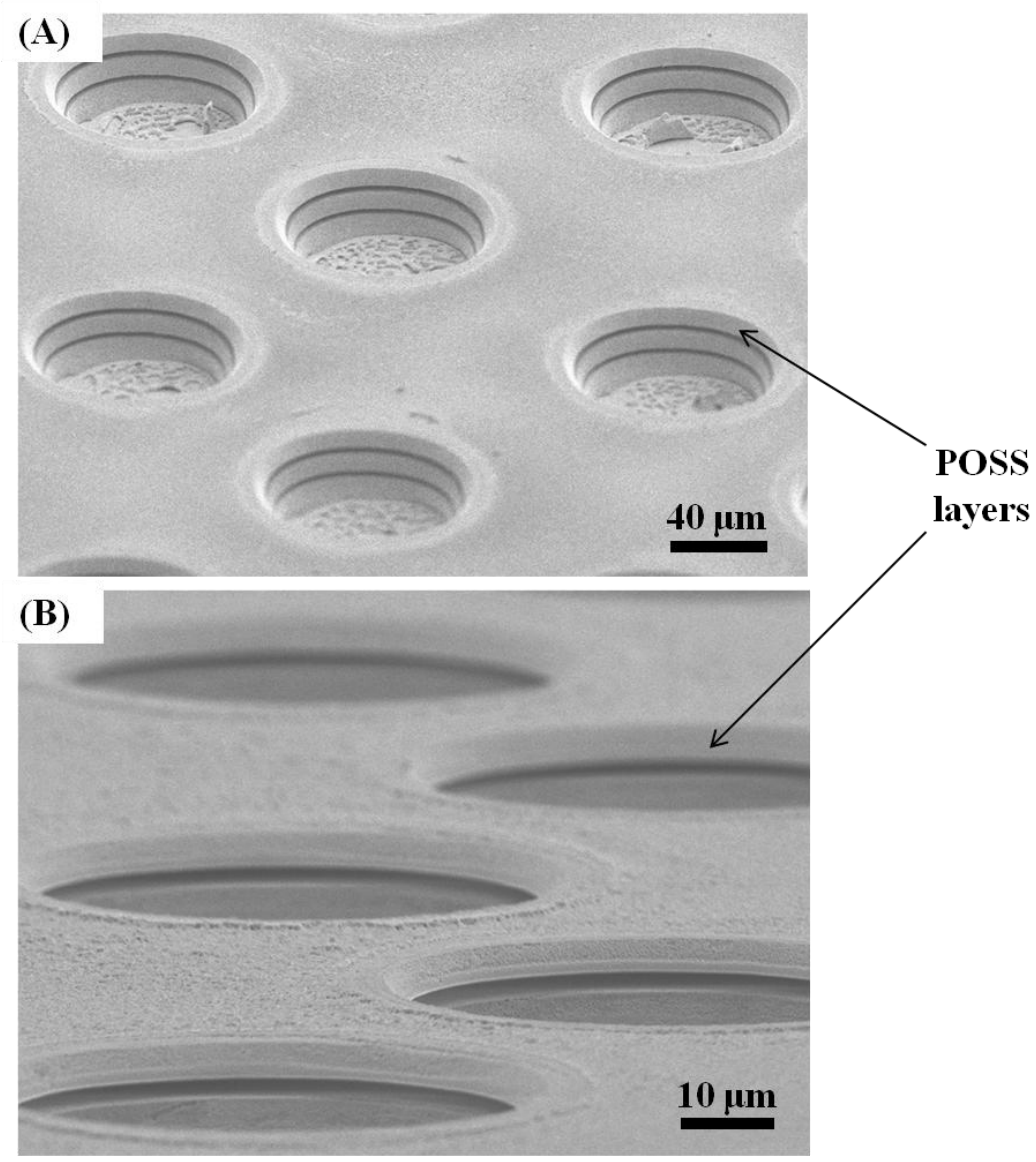

Figure 2.12: SEM images of the multilayer POSS/Avatrel structures following partial plasma etching of Avatrel layers

Despite the aforementioned advantages of the polymer-based approach and promising progress in the realization of these multilayer structures, certain difficulties have been encountered during the fabrication process. First, the processing times for the polymer-based structures are substantially longer than for their metallic counterparts. For example, deposition of a single layer of polymer includes soft-bake, exposure, and hard-bake steps whose total durations add up to nearly 10 minutes, while the electrodeposition of a single layer of metal, depending on the current density, can take only half as much time. In addition, the long processing time of the photoresist mold for the metal structures is easily compensated by the long duration of the laser ablation step for polymers which, even for a multilayer structure composed of 3 pairs of layers, takes several hours to prepare the same amount of samples as with metals.

Second, the processing of polymer-based structures involves expensive equipment such as photolithography tool for the exposure of individual layers; UV laser to perform the ablation; and plasma tool to carry out the etching. Although the photolithography and plasma processes are used in the fabrication of metallic structures too, they are only required for the preparation of the mold and for much shorter durations.

Lastly, the lack of a similar, robotically-assisted experimental setup for the lab-scale fabrication of the multilayer structures prohibits the realization of highly laminated structures. While a simple robotic arm suffices to perform the sequential electrodeposition of metallic layers, a similarly simple approach is not possible with polymers since a wide variety of processes, including spinning, soft- and hard baking, and lithography, is required to deposit each polymer layer. Hence, a more complicated automation needs to be implemented to achieve multilayer polymer structures comprising comparable amount of laminations with the metal-based approach, which is not available in our lab.

Taking all of these facts into account, polymer-based approach was not pursued further to fabricate electrodes for energy storage applications. Nonetheless, the

demonstration of the applicability of the multilayer fabrication to the polymer-based structures was quite remarkable in several ways. In the diverse world of polymers, there may be other pairs of coherent polymers which involve much simpler deposition processes, such as those relying solely on immersion or single-step spin-coating. Using this kind of polymers would significantly shorten the processing time and simplify the fabrication process. Also, by rendering them photodefinable through introducing photoactive materials, it is possible to pattern polymers without utilizing any laser for ablation. Moreover, some polymers are known to be readily electrochemically active. By implementing these polymers in the fabrication process, the possibility exists to fabricate electrodes for energy storage applications through a simple and environmentally friendly process.

2.1.2 Vertical High-Aspect-Ratio Structures

The fabrication process of the vertical high-aspect-ratio structures starts with the deposition of high-aspect-ratio photoresist pillars onto the glass substrate. For this application, transparent substrates are required since the fabrication process involves backside exposure of the photoresist film, as will be explained in detail in Chapter 6.3.1. Hence, Si wafers are not suitable for this application. Unlike the previous approaches in this study, where the photoresist films were utilized as temporarily formed molds, in this particular approach, they constitute an essential and permanent component of the final structures. Therefore, in addition to its capability to form high-aspect-ratio pillars, the chemical and mechanical stability of the photoresist is also an important criterion when selecting the appropriate material. Both SU-8 and AZ 125 nXT have been reported to possess these features. However, once cross-linked, SU-8 proved to be more stable and resistive than AZ. Also, higher aspect ratio structures were obtained with SU-8.

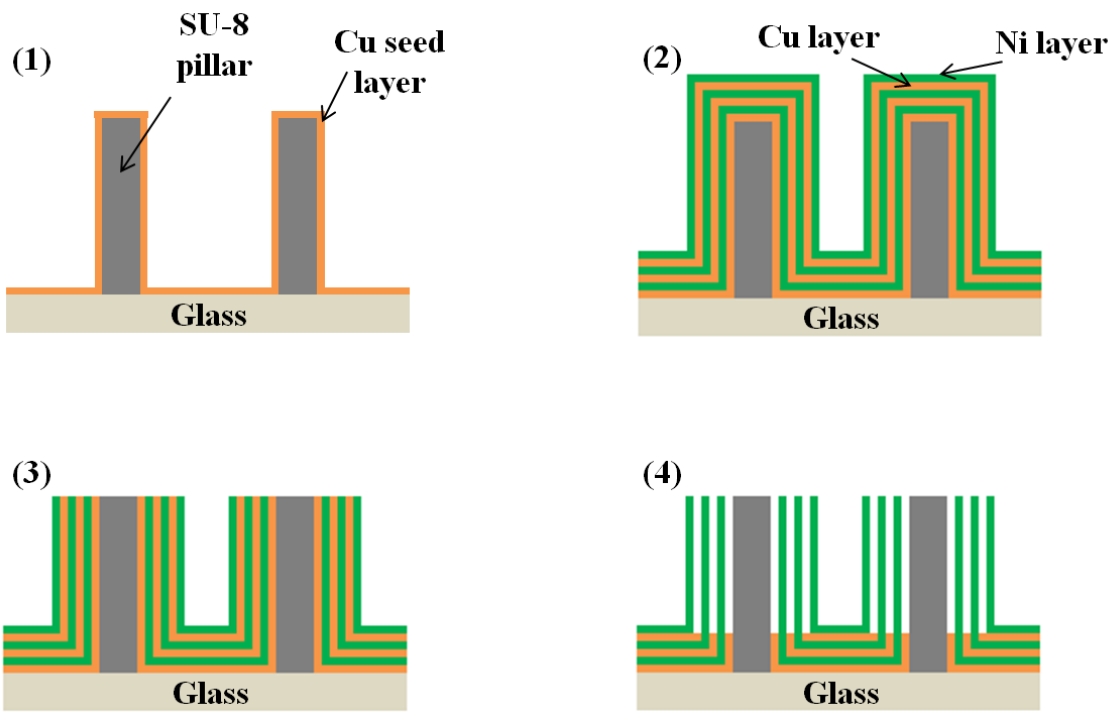

Figure 2.13: Fabrication scheme for the vertical high-aspect-ratio structures: (1) deposition and metallization of high-aspect-ratio SU-8 pillars, (2) sequential electroplating of Ni and Cu layers, (3) mechanical lapping of the top side, and (4) selective etching of Cu layers

Following the deposition and patterning of the high-aspect-ratio SU-8 pillars onto the substrate, metallization is performed by sputtering Ti and Cu layers. In this application, the deposition of an additional Ti layer onto the Cu layer is not required, since the sputter process is immediately followed by the electrodeposition of Cu and Ni layers without the sample undergoing any pretreatment or further processing.

Upon completion of the sequential electrodeposition process, the pillars are mechanically polished from the top side using emery papers of various grades. This polishing process is carried out until all of the electroplated Ni and Cu layers accumulated on top of the SU-8 pillars are removed. In this way, the interleaved Cu layers are exposed, as shown in the third step of the fabrication sequence in Figure 2.13. In the last step, the substrate is immersed in the selective Cu etchant for the removal of

the Cu layers. More details about the individual steps of the fabrication process will be described in Chapter 6.3.1.

2.2 Mold Preparation

Preparation of the mold is one of the most crucial steps in the fabrication process of the metal-based, lateral high-aspect-ratio electrodes described herein, as the mold will determine the final geometry of the multilayer structures that are to be electroplated in the subsequent step. Hence, adequate structures that can serve as mold are required. These molds are required to possess the following properties: (1) nonconductive, easily patternable, high aspect ratio structures with feature sizes on the order of microns; (2) good adhesion to the substrates (e.g., glass or silicon); (3) high chemical and physical resistance when exposed to highly corrosive electroplating solutions for extended periods of time, and (4) relatively easy removability upon completion of the electrodeposition process. Taking these requirements into account, the options are narrowed down to a few photoresist candidates.

2.2.1 NR-21

NR-21 (Futurrex) is a negative-tone photoresist that was utilized as a mold for the electroplating of structures with thicknesses of up to approximately 125 μm. In addition to its relatively short and simple photolithography process, it is able to be removed easily via acetone following the electroplating process, rendering it an appealing choice. Although acetone was found to not dissolve the photoresist completely, it was shown to be very effective at removing the photoresist by weakening the adhesion between the photoresist and the substrate. More information about the fabrication process using NR-21 is available in the subsequent chapters of this study.

However, for higher capacity applications which require structures with a greater number of laminations (i.e., a total thickness of significantly higher than 125 μm), the use

of NR-21 was found to be problematic. Complications arose during the pre-exposure bake and the photolithography steps of the fabrication process, which prohibited the realization of thicker molds using NR-21.

The photoresist was also found to be not suitable for electroplating processes that comprise long durations of exposure to electroplating baths, particularly in the case of high corrosive baths with low pH (e.g., Cu bath). After long electroplating processes exceeding 12 hours, color changes and wrinkles were observed on the surface of the photoresist mold, which most likely is an indication of chemical interactions between the chemicals in the bath and NR-21. Although the photoresist remained intact throughout the electroplating process, these interactions could easily contaminate the electroplating bath and hence, have an adverse effect on the quality of the deposition. Also, on some occasions, photoresist delaminations were observed in certain regions, principally at the edges of the substrate. Therefore, photoresist chemistries for mold formation were sought for applications requiring higher thicknesses and long electroplating durations.

2.2.2 SU-8

SU-8 is an epoxy-based negative photoresist that has been known to be a good candidate for the fabrication of high-aspect-ratio structures [5]. Some of the applications involving high-aspect-ratio SU-8 structures serving as templates for the multilayer structures were demonstrated in the section 2.1.2. Fabrication process of these SU-8 pillars is covered in more detail in Chapter 6.3.1.

Processing parameters pertaining to the fabrication of SU-8 structures, with dimensions ranging from submicron up to millimeter thicknesses, have been well established. However, their fabrication process becomes problematic when they are utilized as temporary structures. For example, the molds used for multilayer structures demonstrated in this study need to be removed upon deposition of the multilayer structures.

Once cross-linked, SU-8 exhibits a high chemical resistance, and its removal by means of chemical etching without damaging other structures on the same substrate can be quite challenging. Other methods such as burning the SU-8 or immersing it in molten-salt baths have also been suggested; however, none of these fabrication steps are compatible with the metallic structures existing on the same substrate as the SU-8 [6].

Plasma-assisted processes, such as reactive-ion etching (RIE) proved to be successful in the removal of a variety of polymers. Several recipes have also been developed for the etching of SU-8 [7]. However, in order to remove large quantities of SU-8 (e.g., molds with thicknesses up to 1 mm), high-power plasma with prolonged etch times are required. Such processes were found to cause delamination of the seed layers from the substrate along with the multilayer structures fabricated on them. The use of plasma for the removal of large quantities of SU-8 is also not favorable for the long-term maintenance of the plasma tool.

An interesting phenomenon shown in Figure 2.14 was observed when the RIE was applied for relatively short durations: Portions of the SU-8 mold located in the proximity of the metallic multilayer structure were able to be removed, suggesting an improved etching rate nearby the metal surface. This phenomenon was postulated to be stemming from the catalytic effects of the metals. However, the mechanism behind this process was not clearly understood.

To determine if the spacing between the pillars and the multilayer structure would suffice to provide the required opening for the diffusion of ions during both the etching and electrochemical operation processes, electrodes with partially etched SU-8 mold were fabricated. It can be seen from Figure 2.14 that the presence of the partially etched SU-8 mold does not inhibit the etching of Cu layers.

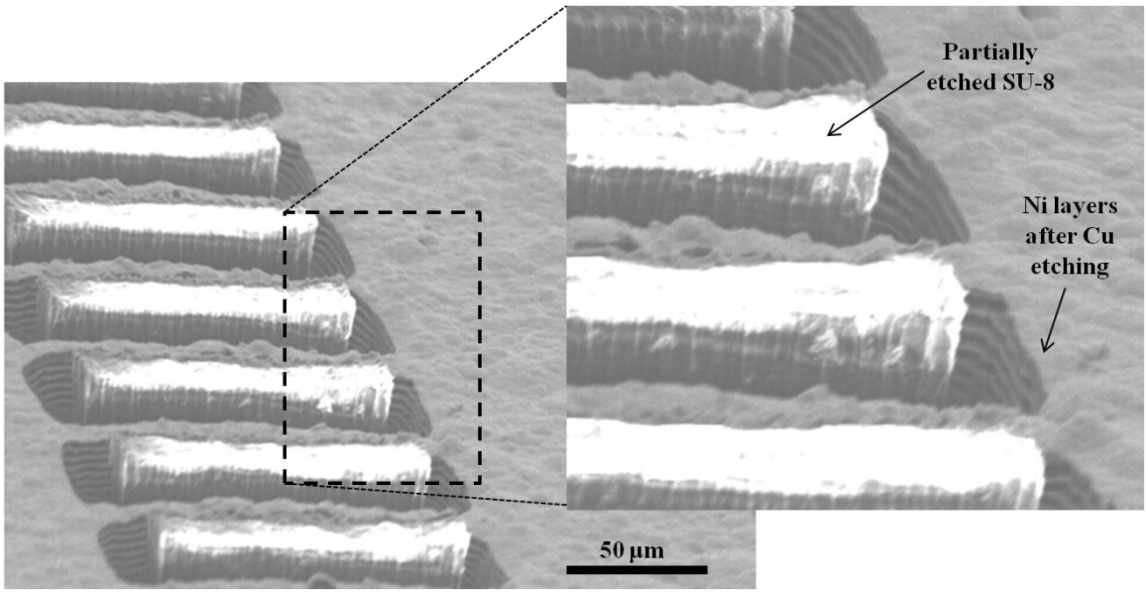

Figure 2.14: SEM images of the partially etched SU-8 mold and multilayer Ni/Cu structure following partial etching of the Cu layers

For the complete removal of the SU-8 molds, removal techniques relying on physical interactions were found to be more promising than the approaches comprising chemical reactions. One of these techniques involves the utilization of strong adhesive tapes. In this technique, the tape is carefully stuck to the top surface of the multilayer structure, ensuring a decent contact between the tip of the SU-8 pillars and the adhesive, as illustrated in Figure 2.15. Then, by carefully peeling off the tape from the substrate, SU-8 pillars are able to be removed. However, in order for this method to work, the fabrication must be performed so that the total thickness of the multilayer structure is always significantly less than the thickness of the SU-8 mold. If the thickness difference is not quite significant, the tape may stick to the topmost layer of the multilayer structure and promote a severe distortion of the structure.

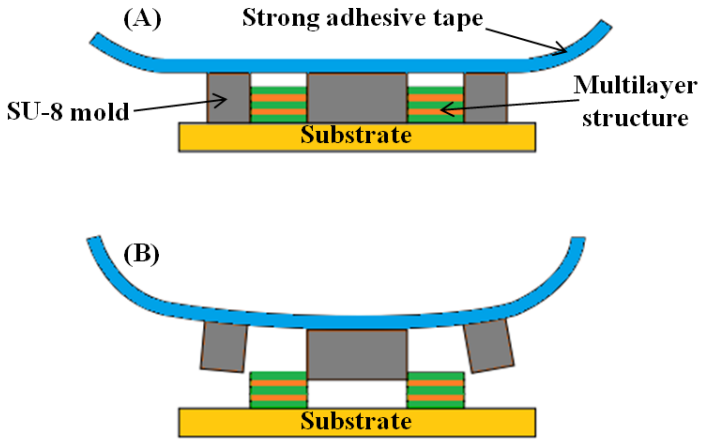

Figure 2.15: Schematic illustration of removal of SU-8 molds with the help of a strong adhesive tape: (A) the tape stuck to the top of the SU-8 mold, (B) peeling off the tape from the substrate

Another physical removal technique involves immersion of the substrates with SU-8 mold in boiling water for many hours. This process relies on the mismatch of the thermal expansion coefficients between the polymer and metallic structures, as well as the bubbles applying force on the SU-8 mold, as illustrated in Figure 2.16. Introducing sonication to the boiling water was found to enhance the removal rate. However, most of the time, a number of multilayer structures were also found to be released from the substrate during the boiling water treatment.

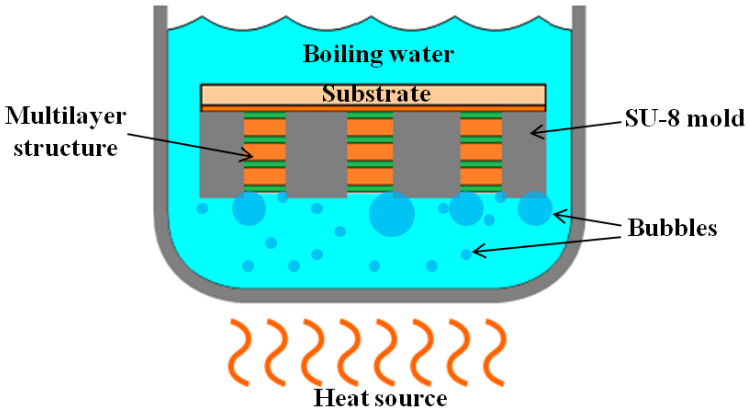

Figure 2.16: Conceptual rendering of the SU-8 removal process via boiling water

Among all these techniques aiming to remove SU-8 mold, none of them was able to provide a complete removal of the mold in a consistent way without causing any damage to the multilayer structures. The most consistent technique with satisfactory end results was found to be the partial plasma removal of the mold near the sidewalls of the multilayer structures; yet, still a significant amount of SU-8 remains on the substrate. Even if the presence of the remaining SU-8 would not constitute a problem for the diffusion of ions during both the etching and operation of the electrodes, it would cause an increase in the total mass of the electrode resulting in reduced power and energy densities. In addition, some fabrication processes, such as the anchor-supported multilayer structures, require a second lithography step to form another photoresist mold for the electrodeposition of the anchors. The presence of the partially etched SU-8 molds could severely alter the deposit quality of the second photoresist mold. Moreover, plasma-assisted removal is a relatively expensive process, which reduces the cost-effectiveness of the whole fabrication process of the electrodes. Therefore, the utilization of the SU-8 molds for the lateral high-aspect-ratio metallic structures has not been pursued any further. It was concluded that the only use of SU-8 in this study is to provide a template for the vertical high-aspect-ratio multilayer structures, which will be covered in more detail in Chapter 6.

2.2.3 AZ 125 nXT

Recently, a new type acrylic photoresist (AZ 125 nXT) has been shown to enable structures with thicknesses exceeding 1 mm, which also possess aspect ratios as high as 20:1 and above [8]. Its ability to be removed through wet stripping without the need for a plasma-assisted process has made the photoresist an attractive choice for our studies.

Figure 2.17 and 2.18 demonstrate some of the high-aspect-ratio molds in the form of cylindrical and rectangular pillars, respectively. As can be seen from these figures, a

large number of pillars (>1000) can be fit on a footprint of 1 cm^2, indicating that structures with more than 1000 etching holes can be fabricated if necessary.

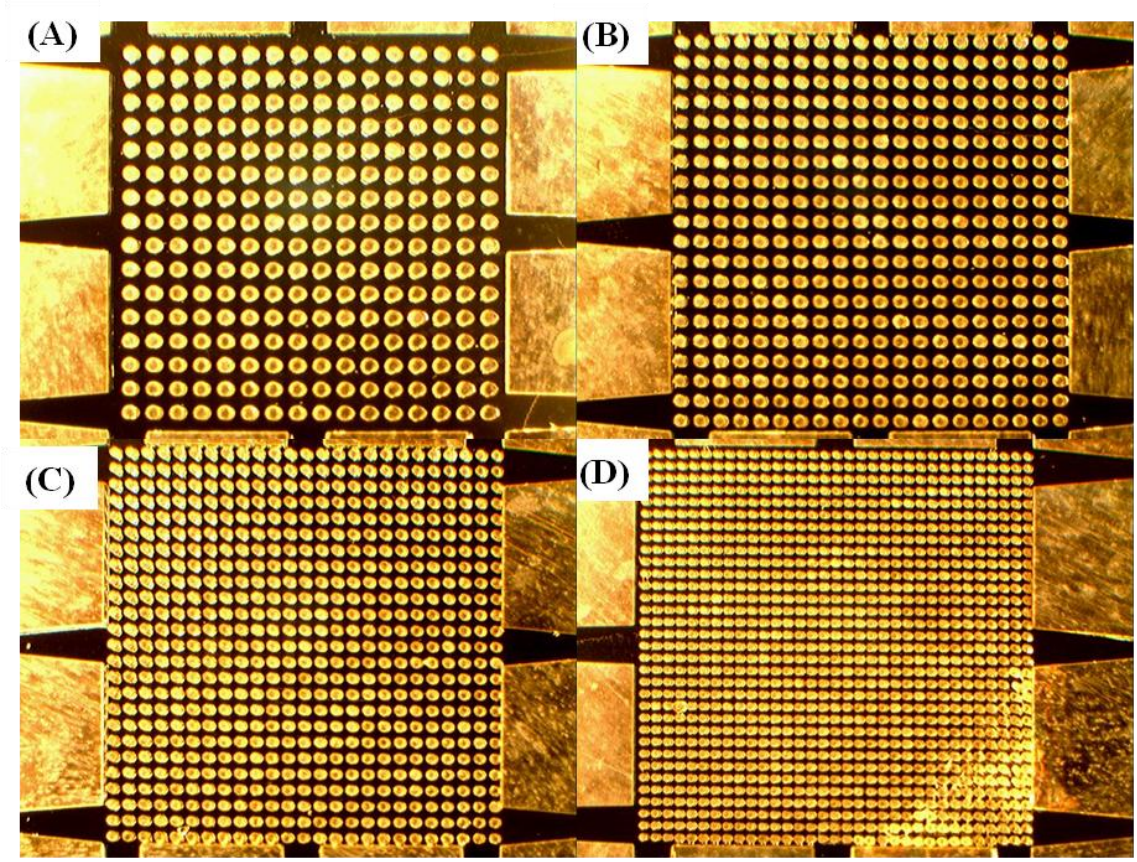

Figure 2.17: Optical images showing the top view of the AZ molds in the form of varying number of cylindrical pillars all built on a footprint of 1 cm^2: (A) 16x16, (B) 20x20, (C) 25x25, and (D) 33x33

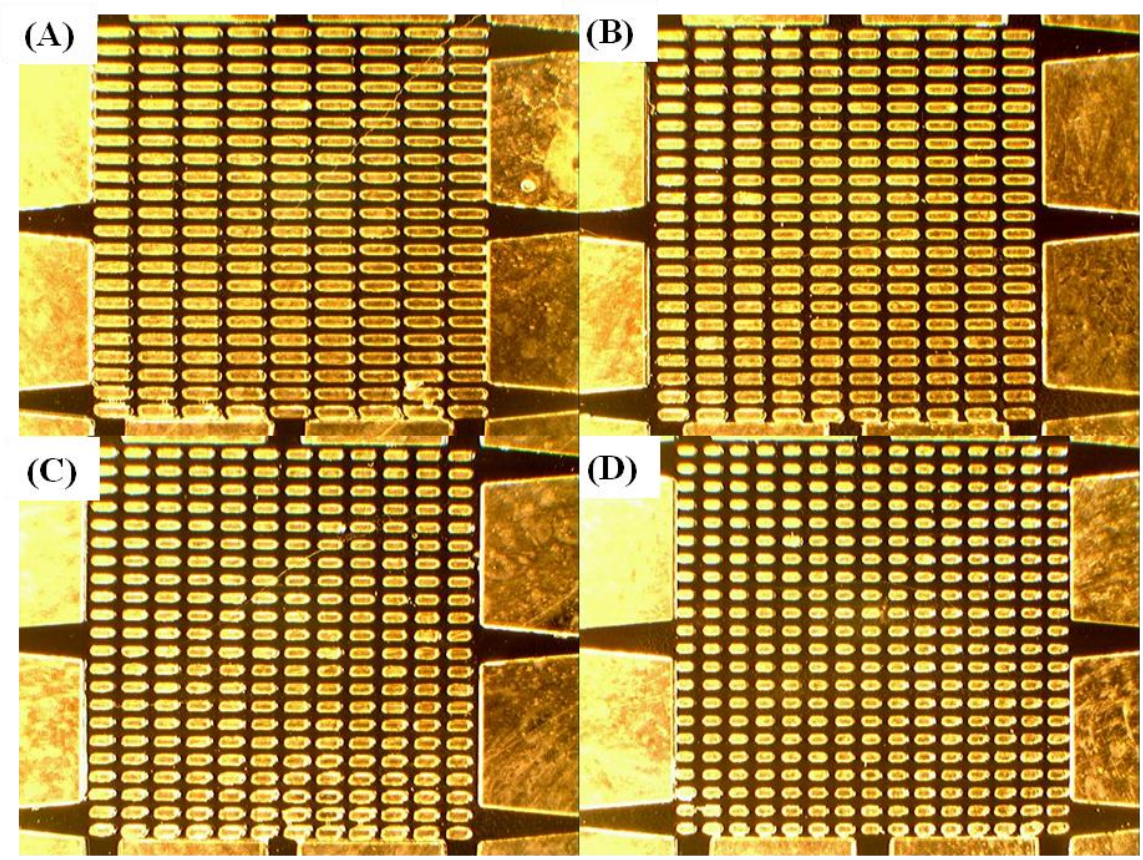

Figure 2.18: Optical images showing the top view of the AZ molds in the form of varying number of rectangular pillars all built on a footprint of 1 cm^2: (A) 22x9, (B) 22x10, (C) 25x12, and (D) 22x15

However, there are some problems associated with this photoresist as well. First, the pre-exposure bake conditions for this photoresist needs to be optimized, especially for thick structures since the solvent content must be maintained within a specific range (12.5% to 25%) during the baking process [8]. If the amount of solvent drops below that critical range, the photoresist becomes impossible to develop. If the baking time is too short, such that the amount of the solvent remains above the given range, the photoresist is too soft to be processed further.

Since this particular photoresist is used for the fabrication of ultra-thick molds, relatively high resolution, hard-contact exposure is performed which may last as long as a couple of hours, depending on the intensity of the UV source. After such long exposure times under hard-contact with chrome-mask and while being relatively soft due to the presence of the solvent within, the photoresist tends to stick to the chrome mask. To avoid this, a non-adhesive, transparent thin-film material (e.g., 12.5 μm low-density polyethylene (LDPE)) must be inserted. These films, however, would reduce the resolution and absorb some of the UV light during the exposure, which needs to be taken into account when setting the exposure time.

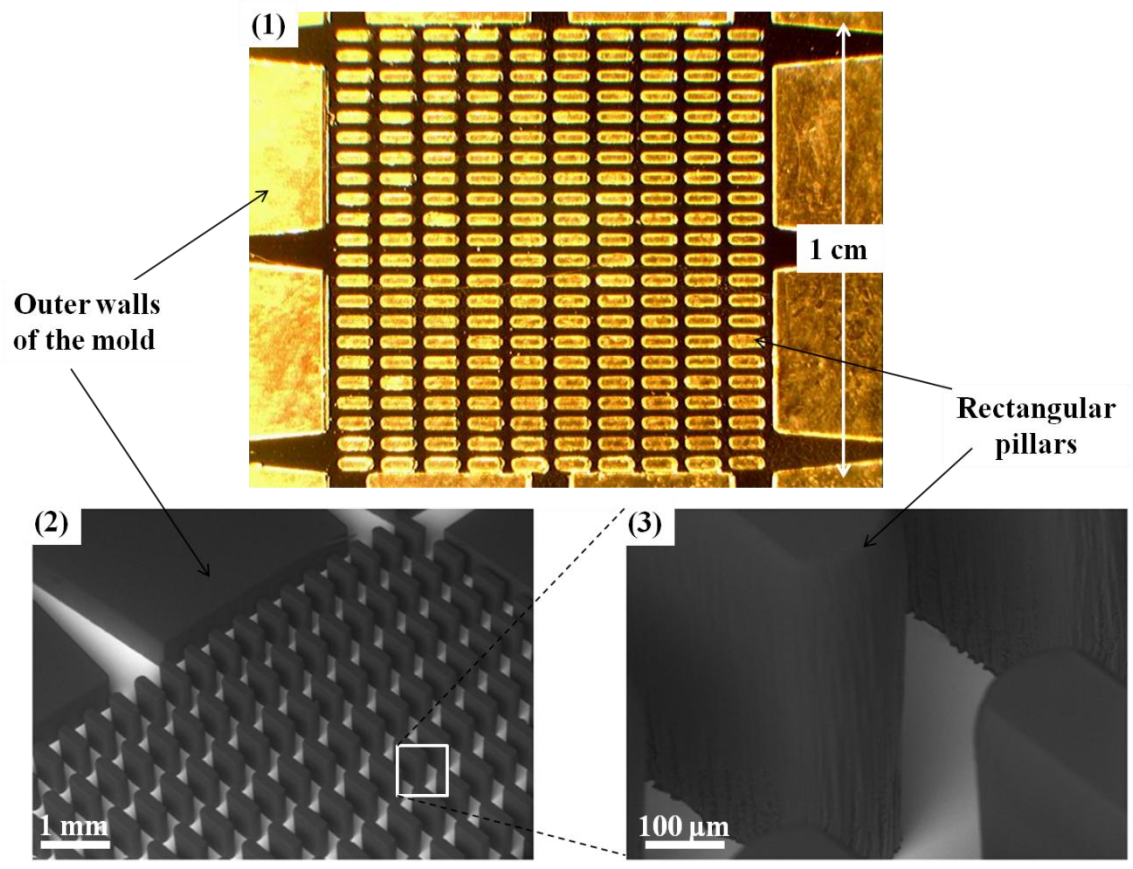

Figure 2.19: Thick AZ mold with rectangular pillar array: (1) optical image showing the top view of the mold developed for a single electrode with a footprint of 1 cm^2, (2) VP-SEM image of the pillar array and outer walls, and (3) closed-up view of the individual pillars

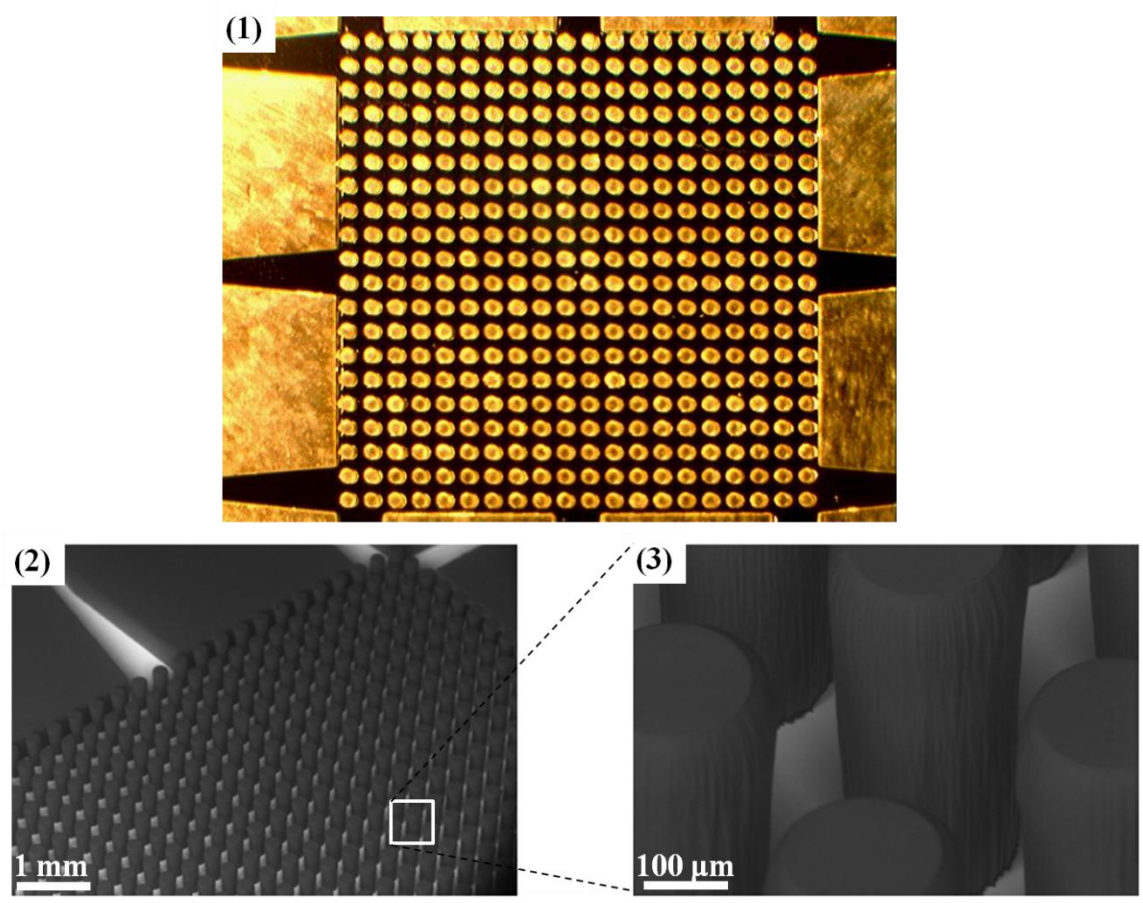

Figure 2.20: Thick AZ mold with cylindrical pillar array: (1) optical image of the top view for one electrode, (2) VP-SEM image showing the pillar array and outer walls, and (3) closed-up image of the individual pillars

One last processing complication concerns the removal of the photoresist. Although it was mentioned earlier in this section that the removal is possible via wet stripping, it is not as simple a process as in the case of NR-21. Acetone works well with the removal of the bulk pieces of the photoresist that surround the multilayer structures; yet, it is unable to remove the photoresist pillars positioned inside the etching holes of the structures. To achieve a complete removal, dimethyl sulfoxide (DMSO) at 80 °C with the assistance of ultrasound sonication was used. Even under these conditions, 100% removal of the photoresist was not always achieved.

Nonetheless, ultra-thick molds made of AZ 125 nXT with high aspect ratios and various geometries have been successfully demonstrated. More information pertaining to the fabrication details can be found in Chapter 4.3.2. Optical and SEM images of some of the fabricated structures are shown in Figures 2.19 and 2.20.

2.3 Etching of the Sacrificial Layers

Etching is one of the most crucial steps in the fabrication of these multilayer electrodes. High-surface-area structures can only be achieved if the etching is performed adequately. The multilayer structures reported herein highly rely on a robust sacrificial etching process, where the sacrificial material is removed without damaging the structural layers.

For the metallic multilayer structures, two types of etching have been utilized: chemical etching which was used to selectively remove the Cu layers (section 2.3.1), and electrochemical etching performed for the selective removal of Ni layers (section 2.3.2). Etching methods pertaining to sacrificial polymers were discussed in section 2.1.1.3.

2.3.1 Cu-etchant (Blue Etch)

Following the sequential electroplating of the Ni and Cu layers, Cu layers were subjected to etching process. The etchant that was used for this purpose was named after its color, hence the name “blue etch”. It was prepared by slowly adding copper sulfate ($CuSO_4$) to the ammonium hydroxide (NH_4OH) solution (30% NH_3 basis) while performing a gentle stirring. In terms of the consistency of the etching rate over the course of the etching process, the best results were empirically determined by mixing 50 g of $CuSO_4$ with 500 ml of NH_4OH.

Mass transport is a quite critical phenomenon in the etching process. For processes which involve high-aspect-ratio structure, such as the structures proposed herein, providing a uniform etching over the course of the whole etching process may be

quite challenging, since the ions are expected to diffuse hundreds of microns deep into the structures.

A consistently encountered symptom pertaining to mass transfer limitations across a number of multilayer samples is shown in Figure 2.21. The apparent etch rate of the Cu layers located at the bottom portion of the multilayer structures was found to be significantly less than for the layers located at the upper portion of the structures. This was the case when the substrate was placed on the bottom of the blue etch container.

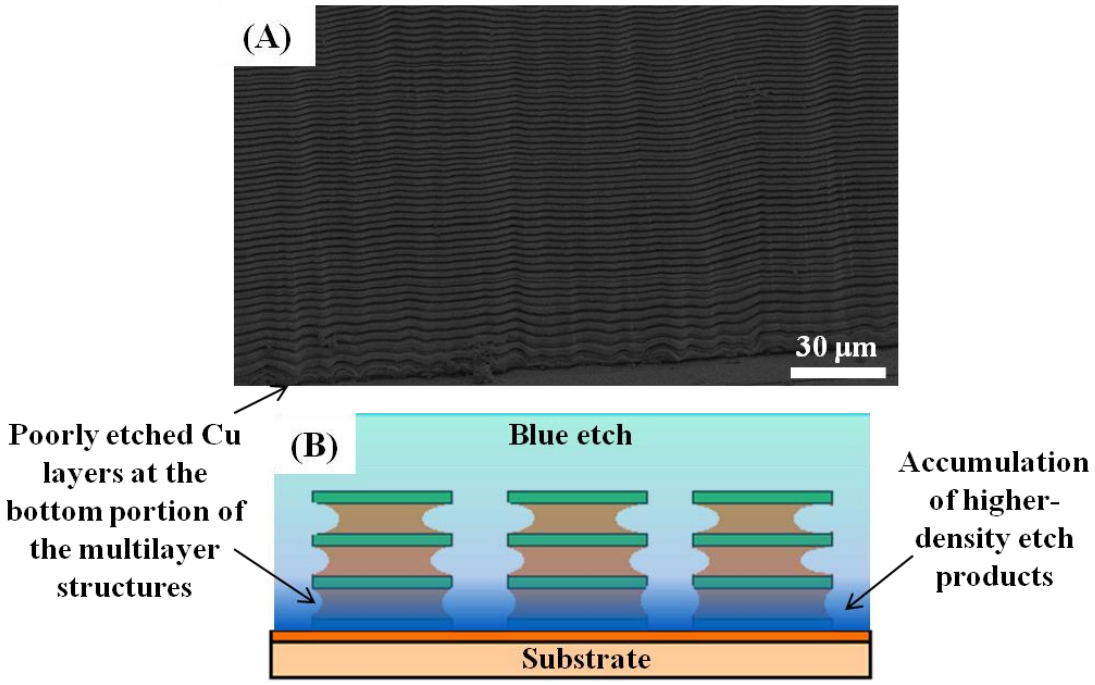

Figure 2.21: Uneven etching distribution across the multilayer structures due to the accumulation of the higher-density etch products on the bottom: (A) SEM image showing poorly etched Cu layers, (B) schematic illustration of the phenomenon

The uneven rate distribution within the structure was postulated to be originating from the accumulation of relatively denser etch products in the partially etched sidewalls of the multilayer structure. As mentioned earlier, blue etch was prepared by saturating the NH_4OH solution with $CuSO_4$. Hence, it is plausible to hypothesize that increased concentration of dissolved Cu ions and the consumption of ammonium ions in the

complexing of newly-dissolved Cu ions would lead to the precipitation of the solution. These precipitates were usually found on the surface of the substrate following a relatively long etching process that was performed without any stirring.

To alleviate this issue, the orientation of the substrate during the etching process was altered. With the help of laser-processed plastic platforms made up of mesh layers of poly(methyl methacrylate) (PMMA) which are resistive to the etchant, the structures were placed in an upside down orientation while a stir-bar was rotating underneath. In this way, heavier etch products were carried away from the sample, particularly in vertical high-aspect-ratio structures with concentric cylinders, enabling more uniform and faster etching. The platforms prepared for this purpose can be seen in Figure 2.22.

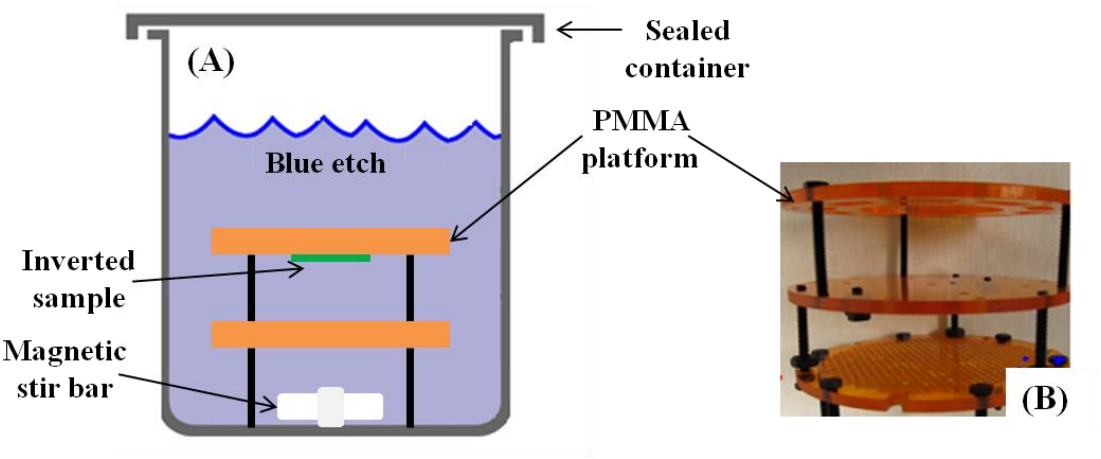

Figure 2.22: Illustration of the PMMA platforms used for the Cu etching: (A) schematic view during the operation, (B) optical image of the actual platform

The Cu etchant can be reused if the etchant container is sealed well during the etching process and storage to avoid evaporation of NH_3, which is critical for the etching process. In addition, care must be taken to prevent the contamination of the solution through avoiding the presence of materials, other than Cu, which can also be attacked by the etchant (e.g., Zn).

Another problem associated with the blue etch is the non-uniformity of the etching rate and non-conformal etching of the Cu layers over the course of the etching process with durations exceeding several hours. This issue is illustrated in Figure 2.23.

To analyze the etching characteristics over a long period of time, one surface of a glass substrate was first coated with a ~2-μm-thick Cu film formed via DC sputtering. Next, the Cu surface was patterned with rectangular pillars of NR-21 photoresist. Following the photoresist development, a 2-μm-thick Ni film was deposited via electroplating. Upon completion of the Ni plating process, the photoresist was removed with acetone. Hence, a two-layer sample consisting of a Cu layer and Ni layer was formed. This sample was then immersed in blue etch. Periodically, the sample was taken out from the Cu etchant, rinsed thoroughly, and imaged from the back-side with a high-resolution optical microscope.

During the first 2 hours, it was observed that the etching had advanced quite uniformly, as shown in the first two optical images in Figure 2.23. However, after four hours, deviations from the uniformity of the etching profile started to appear which can be clearly seen around the etching holes located in the center of the 3rd image in Figure 2.23. After 7 hours, most of the Cu layer except in the center regions was found to be etched in a non-uniform fashion, as demonstrated in the 4th image.

Hence, the Cu etching rate is not uniform over the entire course of the etching processes with long durations. This is most likely because of the increased diffusion lengths of the larger scale structures. To alleviate this issue, the number of etching holes could be increased such that the distance between two adjacent etching holes is kept minimal. However, this would happen at the expense of the capacity of the final electrode, since higher number of etching holes results in reduced surface area per layer. Therefore, in applications with large footprint area, where relatively long diffusion path lengths exist, structures with partially etched Cu layers as described in section 2.1.1.1

were avoided. Instead, processes involving complete removal of the sacrificial layers were preferred.

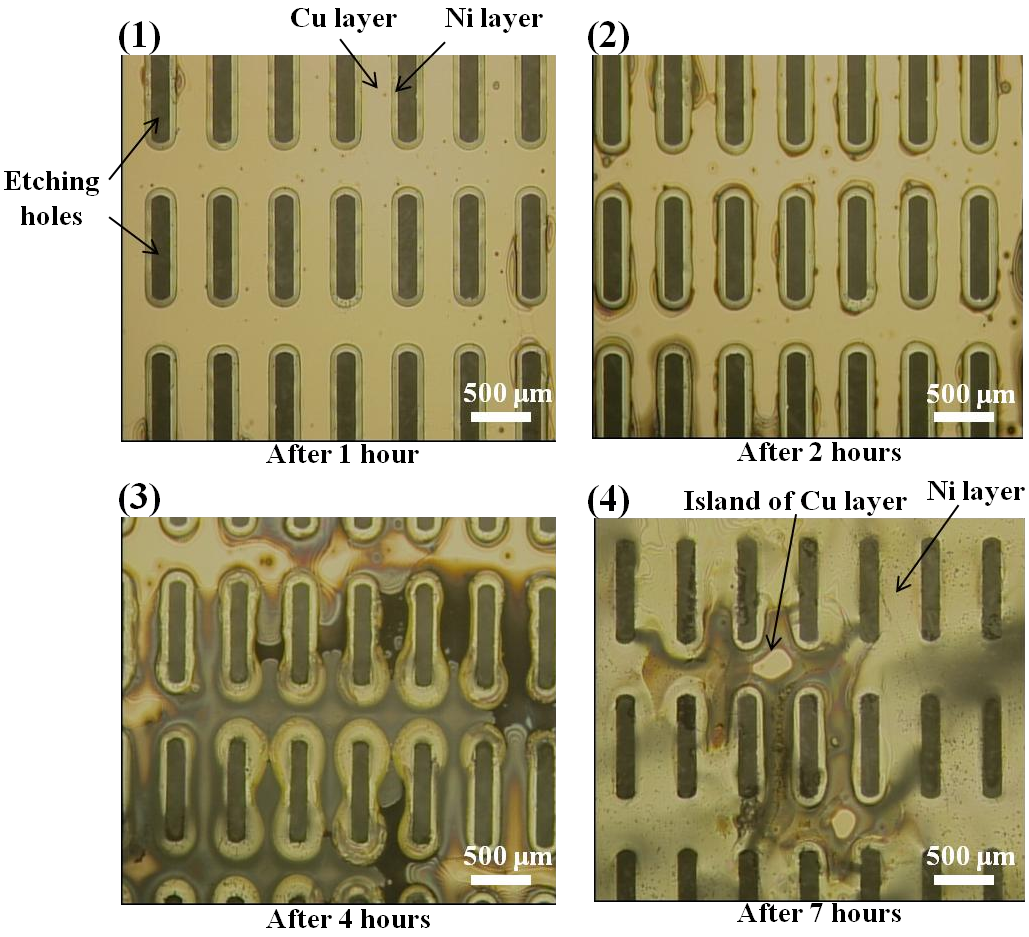

Figure 2.23: Optical images showing the backside of the Cu/Ni-coated glass substrate following various durations of Cu etching

2.3.2 Selective Electrochemical Etching

For the multilayer structures described thus far, Cu layers have been used as the sacrificial layers in Ni/Cu multilayer structures. However, for certain applications, having a Cu backbone instead of Ni might also be beneficial. For example, in terms of electrical and thermal conductivities, Cu is approximately 4 times as conductive as Ni. Hence, a Cu

structure may be more appealing than a Ni structure for certain applications, such as heat sinks and current collectors for some electrodes.

Although Cu is more noble (i.e., less reactive) than Ni, it is hard to find a chemical etchant that only attacks Ni but not Cu [9]. To the best of our knowledge, no chemical etchant has been reported for the selective removal of Ni over Cu that works as effectively as the previously described blue etch works for the removal of Cu. However, the removal of Ni over Cu has been demonstrated by means of electrochemical etching, where a potential was applied that lies between the corrosion potential of Ni and Cu in a sulfuric acid (H_2SO_4) solution [9].

Selective electrochemical dissolution of metals has been widely studied for various mixtures of metals [10-13]. Most of these studies comprise dealloying where the least noble element in a homogeneous solid-phase solution consisting of two or more metals is selectively dissolved in an electrolyte, enabling porous structures. These structures usually have high surface-to-volume ratio. In our case, however, it would not be considered as dealloying, since no homogeneous solution is formed by Ni and Cu.

As mentioned before, Cu is thermodynamically more stable than Ni. The standard electrode potential (SEP) for the Ni^{2+}/Ni couple relative to the standard hydrogen electrode (SHE) is reported as -0.25 V, whereas the SEP of Cu^{2+}/Cu couple is 0.34 V. Hence, Ni layers are expected to be selectively dissolved in acidic solutions when a potential is applied that lies between the redox potentials of $Ni^{2+/}$Ni and $Cu^{2+/}$Cu. However, this is usually not the case since Ni undergoes passivation in acidic solutions which complicates the selective dissolution process. The passivation has been shown to be less effective in the presence of sulfur [9, 14]. For this reason, H_2SO_4 was preferred as the etching solution.

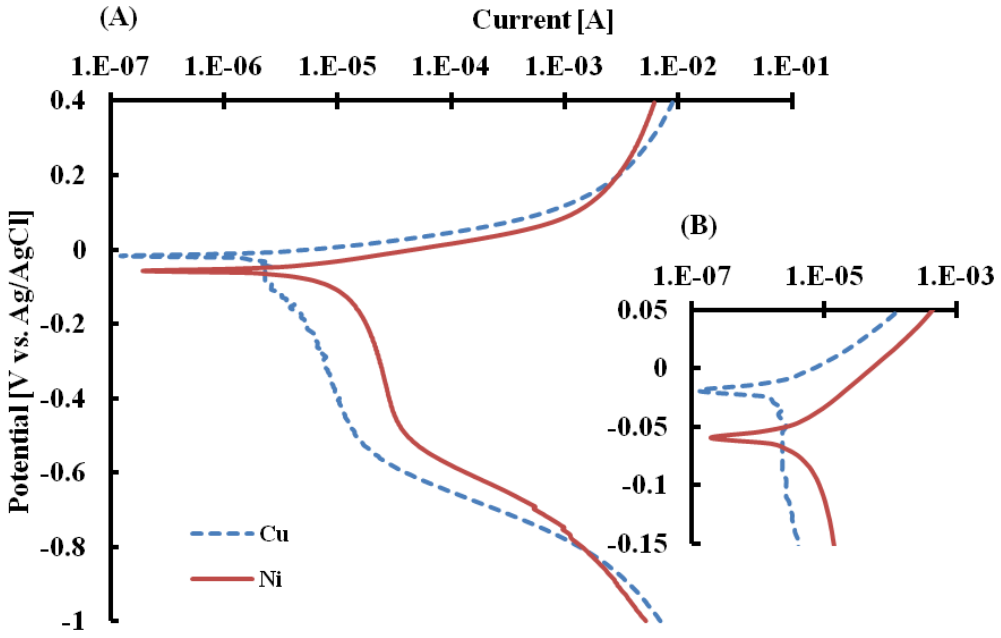

Figure 2.24: Potentiodynamic curves for Cu and Ni in 0.1 M H_2SO_4 solution: (A) current profiles of the Cu and Ni electrodes as a function of potential swept from -1 to 0.4 V (vs. Ag/AgCl) at a scan rate of 5 mV s^{-1}, (B) closed-up view of showing the difference between the corrosion potentials of Cu and Ni

Figure 2.24 illustrates the potentiodynamic curves generated to find the optimal potential for the selective removal of the Ni layers in 0.1 M H_2SO_4. These curves were obtained through linear voltammetry by sweeping the potential from the cathodic potential of -1.0 V up to anodic potential of 0.4 V at a scan rate of 5 mV s^{-1}. A clear difference was observed between the corrosion potentials of Cu and Ni, which were determined to be -18 and -58 mV, respectively. In order to enable Ni dissolution with nearly infinite selectivity, the applied potential should be located between the corrosion potentials of Cu and Ni. In addition, in order to maximize the selective dissolution rate of Ni layers without sacrificing any Cu, the applied potential has to be adjusted to a value slightly below the corrosion potential of Cu. Hence, the optimum potential based on the values obtained from Figure 2.24 was found to be -20 mV.

Multilayer Cu structures, fabricated by using this selective electrochemical etching technique, were utilized as current collectors in electrochemical capacitors.

Further details regarding the use and fabrication, as well as the SEM images of these structures can be found in Chapter 6.3.1.

2.4 Surface Area Characterization

As mentioned in the first chapter, the surface area is one of the most crucial parameters affecting the performance of the electrode and needs to be maximized in order to enable high-power capabilities. In the case of well-ordered structures composed of multiple layers of well-defined geometries, such as rectangular planes and concentric cylinders as described in this work, the theoretical surface area can easily be calculated. Yet, it is also well known that the real surface area of the electrode (i.e., electrochemically active surface area accessible to the electrolyte) may significantly differ from its physically apparent geometrical surface area due to the surface roughness and the morphology of the deposits, particularly if the fabrication process involves electrodeposition. It has been demonstrated that factors such as the composition and aging of the electroplating bath, the temperature of the bath, plating current density, and the choice of the substrate to be electroplated can have a substantial effect on the porosity and grain size of the deposited films [15-19]. The surface roughness can easily be determined for simple geometries, such as single layer thin films, by making use of scanned probe techniques. However, these scanned probe techniques would only work for the topmost layer of the structures comprising relatively complex geometries, as described in this study.

Also, to have a precise control over the thickness of the active material that is to be deposited onto the high-surface-area 3D backbone structure in a conformal way, an accurate measure of the surface area is required to adjust the current density prior to the electrodeposition of the active material. Moreover, in certain processes, as described earlier in this chapter, where Ni serves as the sacrificial layer and selectively etched by electrochemical means, the surface area analysis needs to be performed to determine the

extent of etching. This is achieved by simply measuring the change in the surface area with etching time. For these reasons, surface area analysis is an important step in both the fabrication and characterization steps.

Brunauer-Emmett-Teller (BET) technique is a powerful analysis technique, which is widely used for determining the porosity and surface area of various materials, including catalysts and active materials utilized in energy storage applications [20]. The working principle of this technique is based on the physical adsorption of gas molecules on a solid surface.

However, this technique has limited utility when it comes to complex structures consisting of electrodes, connection pads, packaging material, and substrate. In addition, several shortcomings have been reported regarding its operating conditions including the need for large amounts of sample due to lack of sensitivity and treatments involving relatively high temperatures that exceed 100 °C, for contaminant removal, which may cause unexpected physical, and in some circumstances chemical, deformations in the electrode material [21].

Also, the surface area of an electrode determined by the BET technique may not necessarily be equal to the electrochemically accessible surface to the electrolyte, where the former one is generally significantly higher than the latter one, because of the gas-phase nature of the process [22]. The difference between the two areas may be even more severe if solid electrolytes are utilized in the system.

Lastly, depending on the sample size and geometry, it may take several hours to characterize a single sample due to the long durations of the outgassing step during the BET analysis, rendering it unsuitable for some of the aforementioned fabrication processes requiring frequent analyses of the changes in surface area. For these reasons, BET was omitted, and underpotential deposition (UPD) was preferred as an inexpensive and relatively fast electrochemical tool for determining the surface area of the fabricated structures.

2.4.1 Underpotential Deposition (UPD)

UPD refers to a phenomenon where the electrodeposition of a species, typically a metal cation, to a solid substrate takes place at a more positive potential than the equilibrium, i.e. Nernst potential, for the reduction of this metal. It is a cost-effective and relatively fast technique enabling a precise and reproducible surface modification through formation of up to a monolayer thickness on the electrode surface [23]. This phenomenon originates from the fact that the metal-substrate interaction is energetically more favorable than the metal-metal interaction at that given potential.

UPD has been utilized for various applications including the detection of heavy metal ions in solutions, synthesis of catalytic surfaces with enhanced activity, formation of multilayered structures by electrochemical atomic layer epitaxy [24-34]. The utility of UPD for determining the active surface has also been well established for certain metals including platinum (Pt), gold (Au), silver (Ag), and Cu [21, 35-41]. Unfortunately, there is not a single electrolyte that can be used to determine the surface area of a variety of metals. Each metal has its own potential range that can be applied in only certain electrolytes containing specific cations. To the best of our knowledge, no electrolyte has been reported utilizing UPD to determine the surface area of Ni structures. For Cu, on the other hand, a few studies exist, which involve the UPD of thallium (Tl) to find the active surface area of Cu deposits [42-44]. Therefore, UPD could only be performed for determining the active surface area of the 3D Cu electrodes where Tl-based electrolyte is selected as a probe of the surface area. These Cu electrodes are fabricated by selective electrochemical removal of the Ni layers, as described earlier in this chapter. Details pertaining to surface area characterization of the Cu electrodes via UPD of Tl can be found in Chapter 6.3.1.1.

2.5 References

[1] M. Schlesinger and M. Paunovic, *Modern Electroplating* vol. 55: John Wiley & Sons, 2011.

[2] P. A. Kohl, Q. Zhao, K. Patel, D. Schmidt, S. A. Bidstrup-Allen, R. Shick, *et al.*, "Air-Gaps for Electrical Interconnections," *Electrochemical and Solid-State Letters,* vol. 1, pp. 49-51, 1998.

[3] C. M. Bertelsen, C. A. Craft, B. T. Fannin, D. C. Graham, K. A. Killeen, B. A. Mansdorf, *et al.*, "Hydrophobic nozzle plate structures for micro-fluid ejection heads," ed: Google Patents, 2011.

[4] N. Fritz, R. Saha, S. A. B. Allen, and P. A. Kohl, "Photodefinable Epoxycyclohexyl Polyhedral Oligomeric Silsesquioxane," *Journal of Electronic Materials,* vol. 39, pp. 149-156, 2010.

[5] J. Kim, M. G. Allen, and Y.-K. Yoon, "Computer-controlled dynamic mode multidirectional UV lithography for 3D microfabrication," *Journal of Micromechanics and Microengineering,* vol. 21, p. 035003, 2011.

[6] P. M. Dentinger, W. M. Clift, and S. H. Goods, "Removal of SU-8 photoresist for thick film applications," *Microelectronic Engineering,* vol. 61, pp. 993-1000, 2002.

[7] G. Hong, A. S. Holmes, and M. E. Heaton, "SU8 resist plasma etching and its optimisation," *Microsystem Technologies,* vol. 10, pp. 357-359, 2004.

[8] M. Staab, F. Greiner, M. Schlosser, and H. F. Schlaak, "Applications of novel high-aspect-ratio ultrathick UV photoresist for microelectroplating," *Microelectromechanical Systems, Journal of,* vol. 20, pp. 794-796, 2011.

[9] S. Arai, T. Hasegawa, and N. Kaneko, "Fabrication of 3-D Ni/Cu multilayered microstructure by selective etching of Ni," *Journal of the Electrochemical Society,* vol. 150, pp. C798-C801, 2003.

[10] Y. Yu, C. Yan, L. Gu, X. Lang, K. Tang, L. Zhang, *et al.*, "Three-Dimensional (3D) Bicontinuous Au/Amorphous-Ge Thin Films as Fast and High-Capacity Anodes for Lithium-Ion Batteries," *Advanced Energy Materials,* vol. 3, pp. 281-285, 2013.

[11] Q. Zhang and Z. Zhang, "On the electrochemical dealloying of Al-based alloys in a NaCl aqueous solution," *Physical Chemistry Chemical Physics,* vol. 12, pp. 1453-1472, 2010.

[12] J. F. Huang and I. W. Sun, "Fabrication and Surface Functionalization of Nanoporous Gold by Electrochemical Alloying/Dealloying of Au–Zn in an Ionic

Liquid, and the Self-Assembly of L-Cysteine Monolayers," *Advanced Functional Materials,* vol. 15, pp. 989-994, 2005.

[13] K. Liang, X. Tang, B. Wei, and W. Hu, "Fabrication and characterization of a nanoporous NiO film with high specific energy and power via an electrochemical dealloying approach," *Materials Research Bulletin,* vol. 48, pp. 3829-3833, 2013.

[14] N. Sato and G. Okamoto, "Kinetics of the anodic dissolution of nickel in sulfuric acid solutions," *Journal of The Electrochemical Society,* vol. 111, pp. 897-903, 1964.

[15] V. Vas' ko, I. Tabakovic, S. Riemer, and M. Kief, "Effect of organic additives on structure, resistivity, and room-temperature recrystallization of electrodeposited copper," *Microelectronic Engineering,* vol. 75, pp. 71-77, 2004.

[16] M. Stangl, J. Acker, S. Oswald, M. Uhlemann, T. Gemming, S. Baunack, *et al.*, "Incorporation of sulfur, chlorine, and carbon into electroplated Cu thin films," *Microelectronic Engineering,* vol. 84, pp. 54-59, 2007.

[17] S. A. El Rehim, S. A. El Wahaab, E. Fouad, and H. Hassan, "Effect of some variables on the electroplating of zinc from acidic acetate baths," *Journal of Applied Electrochemistry,* vol. 24, pp. 350-354, 1994.

[18] U. Sahaym, S. L. Miller, and M. G. Norton, "Effect of plating temperature on Sn surface morphology," *Materials Letters,* vol. 64, pp. 1547-1550, 2010.

[19] S. Mathew, M. Osterman, M. Pecht, and F. Dunlevey, "Evaluation of pure tin plated copper alloy substrates for tin whiskers," *Circuit World,* vol. 35, pp. 3-8, 2009.

[20] S. Brunauer, P. H. Emmett, and E. Teller, "Adsorption of gases in multimolecular layers," *Journal of the American Chemical Society,* vol. 60, pp. 309-319, 1938.

[21] Y. Liu, S. Bliznakov, and N. Dimitrov, "Comprehensive study of the application of a Pb underpotential deposition-assisted method for surface area measurement of metallic nanoporous materials," *The Journal of Physical Chemistry C,* vol. 113, pp. 12362-12372, 2009.

[22] D. Qu, "Studies of the activated carbons used in double-layer supercapacitors," *Journal of Power Sources,* vol. 109, pp. 403-411, 2002.

[23] E. Herrero, L. J. Buller, and H. D. Abruna, "Underpotential deposition at single crystal surfaces of Au, Pt, Ag and other materials," *Chemical Reviews,* vol. 101, pp. 1897-1930, 2001.

[24] G. Herzog and D. W. Arrigan, "Determination of trace metals by underpotential deposition–stripping voltammetry at solid electrodes," *TrAC Trends in Analytical Chemistry,* vol. 24, pp. 208-217, 2005.

[25] P. L. Sanchez and J. M. Elliott, "Underpotential deposition and anodic stripping voltammetry at mesoporous microelectrodes," *Analyst,* vol. 130, pp. 715-720, 2005.

[26] K. C. Honeychurch, J. P. Hart, and D. C. Cowell, "Voltammetric Behavior and Trace Determination of Lead at a Mercury-Free Screen-Printed Carbon Electrode," *Electroanalysis,* vol. 12, pp. 171-177, 2000.

[27] V. Beni, H. V. Newton, D. W. Arrigan, M. Hill, W. A. Lane, and A. Mathewson, "Voltammetric behaviour at gold electrodes immersed in the BCR sequential extraction scheme media: Application of underpotential deposition–stripping voltammetry to determination of copper in soil extracts," *Analytica Chimica Acta,* vol. 502, pp. 195-206, 2004.

[28] S. Uhm, S. T. Chung, and J. Lee, "Activity of Pt anode catalyst modified by underpotential deposited Pb in a direct formic acid fuel cell," *Electrochemistry Communications,* vol. 9, pp. 2027-2031, 2007.

[29] Y. Du, B. Su, N. Zhang, and C. Wang, "A novel preparation method of Sn-modified Pt nanoparticles and application for methanol oxidation," *Applied Surface Science,* vol. 255, pp. 2641-2645, 2008.

[30] G. Zhang, Y. Kuang, J. Liu, Y. Cui, J. Chen, and H. Zhou, "Fabrication of Ag/Au bimetallic nanoparticles by UPD-redox replacement: Application in the electrochemical reduction of benzyl chloride," *Electrochemistry Communications,* vol. 12, pp. 1233-1236, 2010.

[31] C. Jin and I. Taniguchi, "Electrocatalytic activity of silver modified gold film for glucose oxidation and its potential application to fuel cells," *Materials Letters,* vol. 61, pp. 2365-2367, 2007.

[32] S. Ben Aoun, Z. Dursun, T. Sotomura, and I. Taniguchi, "Effect of metal ad-layers on Au (111) electrodes on electrocatalytic reduction of oxygen in an alkaline solution," *Electrochemistry Communications,* vol. 6, pp. 747-752, 2004.

[33] Q. Tang, L. Jiang, Q. Jiang, S. Wang, and G. Sun, "Enhanced activity and stability of a Au decorated Pt/PdCo/C electrocatalyst toward oxygen reduction reaction," *Electrochimica Acta,* vol. 77, pp. 104-110, 2012.

[34] B. W. Gregory and J. L. Stickney, "Electrochemical atomic layer epitaxy (ECALE)," *Journal of Electroanalytical Chemistry and Interfacial Electrochemistry,* vol. 300, pp. 543-561, 1991.

[35] S. Trasatti and O. Petrii, "Real surface area measurements in electrochemistry," *Pure and Applied Chemistry,* vol. 63, pp. 711-734, 1991.

[36] N. Bogolowski, T. Nagel, B. Lanova, S. Ernst, H. Baltruschat, K. S. Nagabhushana, *et al.*, "Activity of selenium modified ruthenium-electrodes and

determination of the real surface area," *Journal of Applied Electrochemistry,* vol. 37, pp. 1485-1494, 2007.

[37] C. L. Green and A. Kucernak, "Determination of the platinum and ruthenium surface areas in platinum-ruthenium alloy electrocatalysts by underpotential deposition of copper. I. Unsupported catalysts," *The Journal of Physical Chemistry B,* vol. 106, pp. 1036-1047, 2002.

[38] D. Chen, Q. Tao, L. W. Liao, S. X. Liu, Y. X. Chen, and S. Ye, "Determining the active surface area for various platinum electrodes," *Electrocatalysis,* vol. 2, pp. 207-219, 2011.

[39] T. Nagel, N. Bogolowski, and H. Baltruschat, "Towards a determination of the active surface area of polycrystalline and nanoparticle electrodes by Cu upd and CO oxidation," *Journal of Applied Electrochemistry,* vol. 36, pp. 1297-1306, 2006.

[40] J. M. Elliott, P. R. Birkin, P. N. Bartlett, and G. S. Attard, "Platinum microelectrodes with unique high surface areas," *Langmuir,* vol. 15, pp. 7411-7415, 1999.

[41] E. Rouya, S. Cattarin, M. Reed, R. Kelly, and G. Zangari, "Electrochemical characterization of the surface area of nanoporous gold films," *Journal of the Electrochemical Society,* vol. 159, pp. K97-K102, 2012.

[42] A. Vaškelis, E. Norkus, and G. Stalnionis, "Effect of the Cu electrode formation conditions and surface nano-scale roughness on formaldehyde anodic oxidation," *Electrochimica Acta,* vol. 49, pp. 1613-1621, 2004.

[43] E. Norkus, A. Vaškelis, J. Jačiauskienė, I. Stalnionienė, and G. Stalnionis, "Obtaining of high surface roughness copper deposits by electroless plating technique," *Electrochimica Acta,* vol. 51, pp. 3495-3499, 2006.

[44] E. Norkus, A. Vaškelis, and I. Stalnioniene, "Changes of the Cu electrode real surface area during the process of electroless copper plating," *Journal of Solid State Electrochemistry,* vol. 4, pp. 337-341, 2000.

CHAPTER 3

ZINC-AIR MICROBATTERIES

3.1 Background and Motivation

Zn-air batteries have gained a substantial interest in recent years, primarily because they offer the highest energy density on a volumetric basis among commercially available electrochemical systems [1]. This high volumetric energy density originates from the use of atmospheric oxygen as one of their electrodes which therefore does not occupy space within the battery system. In addition to the high energy density, other unique attributes of Zn including its low equilibrium potential, stability in aqueous electrolytes, abundance, low toxicity, low cost, and ease of handling, result in it being an attractive choice for primary (i.e., non-rechargeable) energy storage applications [1].

During the discharge of the Zn-air battery, oxygen from the atmosphere diffuses into the carbon-based air cathode where the catalyst facilitates the conversion of the oxygen molecules to hydroxide ions (OH^-) using the electrons generated from the oxidation of Zn in the counter electrode. As more oxygen is reduced to OH^- ions, the pressure inside the cell drops, resulting a pressure gradient between the air and the cell. This pressure gradient triggers the diffusion of more oxygen into the cell.

There are three main electrochemical components in commercial Zn-air batteries: (1) Zn in a fine powder form, (2) catalytic cathode reducing atmospheric oxygen to OH^- ions, and (3) aqueous alkaline electrolyte, all of which can be seen in the simplified schematic of the system in Figure 3.1. Utilizing Zn in powder form is a good way of achieving high surface area, as well as high energy density. During the discharge of the battery, this Zn powder undergoes a series of anodic reactions which are given in Equations 3.1 to 3.3:

$$Zn \rightarrow Zn^{2+} + 2e^{-} \quad (3.1)$$

$$Zn^{2+} + 4OH^{-} \rightarrow Zn(OH)_4^{2-} \quad (3.2)$$

$$Zn(OH)_4^{2-} \rightarrow ZnO + H_2O + 2OH^{-} \quad (3.3)$$

These reactions generate a potential of -1.25 V vs. standard hydrogen electrode (SHE) [2]. The electrons generated as a result of these reactions are transferred to the cathode where the oxygen is reduced to OH^- ions as follows:

$$O_2 + 2H_2O + 4e^{-} \rightarrow 4OH^{-} \quad (3.4)$$

providing a potential of 0.4 V. The overall reaction summarizing the discharge chemistry in the Zn-air battery can then be given as:

$$2Zn + O_2 \rightarrow 2ZnO \quad (3.5)$$

yielding a total theoretical cell potential of 1.65 V.

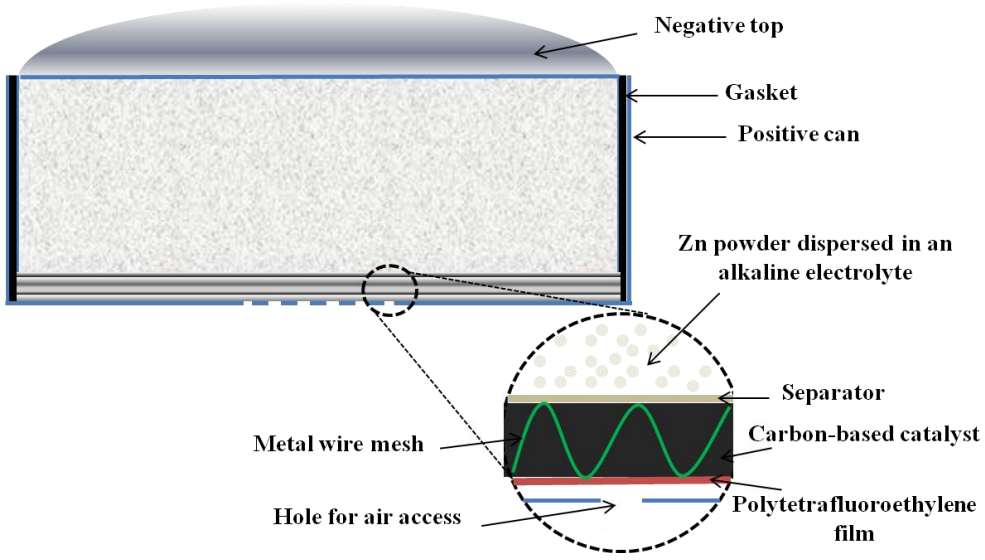

Figure 3.1: A simplified schematic demonstrating the key features of a Zn-air cell [1]

Despite the widespread use of Zn-air batteries, their performance has been reported to be inadequate for a range of applications demanding high power, due to the limiting current property of the Zn-air system [1, 3, 4]. This limiting current phenomenon takes place when the power demand is increased to a point where the cell cannot provide a corresponding current for the required power. At the beginning of the discharge process, the rate-limiting step is usually attributed to the transport of oxygen which is determined by the cell components such as vent hole configuration, PTFE, or the air cathode [1]. However, as the discharge proceeds, the anode becomes the rate limiting element due to the zinc oxide (ZnO) formation on the Zn powder surface, resulting in a decrease in the active surface area of the metallic Zn and hence, in an increase in the internal resistance of the electrode [1, 5].

To mitigate the issues pertaining to high-power applications, various approaches have been utilized which maintain the high surface area while enhancing the power capability. Some of these approaches include: utilization of different forms of particulates such as ribbons, flakes, needles, or fibrous materials; non-conventional designs which improve the interface area; and fabrication of microposts that rely on Kirkendall effect [5-9]. Although these high-surface-area structures enabled an improved electrode performance, they involve relatively low utilization of the active material, particularly in the case of powder-based electrodes which was reported to be as low as 60 wt% [3]. In the case of fibrous Zn anodes, the utilization was shown to increase up to 86 wt% [3]. The low utilization of the active material mainly stems from the lack of a current collector to support the active material and to provide uniformly distributed diffusion and conduction path lengths across the electrode.

Herein, the first demonstration of the contribution of the multilayer structures to the improved power capabilities of the energy storage systems is demonstrated by utilizing Zn-air battery chemistry [10, 11]. As in the case of the aforementioned attempts

aiming to enhance the performance of the electrode, the multilayer backbone structure serving as the current collector provides an increased surface area for the electrode. Additionally, this mechanically strong and chemically inert backbone structure reinforces the anode and enables very high utilization of the active material, i.e. Zn, even at high discharge rates. The trade-off, however, is the reduced energy density due to the presence of the electrochemically inactive metallic backbone. To compensate for the loss in the energy density, the total thickness of the electrode (i.e., the number of layers in the metallic backbone) needs to be increased.

3.2 Fabrication Process

The electrodes fabricated for the Zn-air systems are based on the partially etched lateral high-aspect-ratio structures that were described in Chapter 2.1.1.1. In this chapter, a more thorough description will be provided.

3.2.1 Alternative Fabrication: Zn/Cu Multilayer Structure

The initial approach focused on the fabrication of multilayer electrodes composed of sequential layers of Zn with sacrificial Cu layers, as illustrated in Figure 3.2. However, certain complications arose when attempting to build the structures in the proposed fashion as shown in Figure 3.2. The first complication pertained to finding a suitable Cu bath which would not attack Zn layers in the sequential deposition process. The Cu baths used in our conventional processes are highly acidic and thus, electrodeposition of Cu onto Zn layers is not possible. Some cyanide-based Cu plating baths have been reported to be compatible with Zn. However, the use of a cyanide-based bath in the robotic plating setup is not desirable due to the size constraints which prohibits the use of a standard fume hood [12].

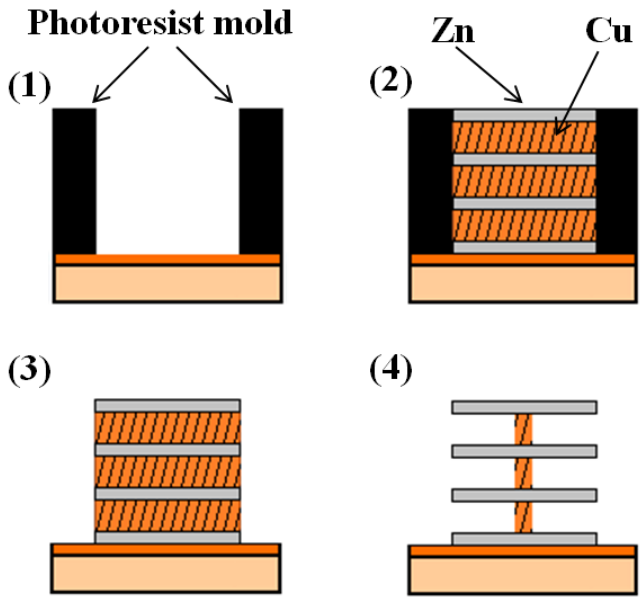

Figure 3.2: Alternative fabrication process for Zn/Cu pairs: (1) deposition of the photoresist mold on the metalized substrate, (2) sequential deposition of Zn and Cu layers, (3) removal of the mold, and (4) partial etching of the sacrificial Cu layers

To overcome this compatibility issue between Zn and Cu, an immersion plating bath was utilized for the deposition of Cu which consists of an aqueous solution containing copper sulfate (Cu_2SO_4), tartaric acid ($C_4H_6O_6$), ammonium hydroxide (NH_4OH), and high-purity DI water [13]. The detailed composition of the solution can be found in Table 3.1.

The deposition mechanism of the Cu plating is based on the displacement reaction between the Zn and Cu layers. It differs from the electroless plating process since no reducing agents are required to reduce the Cu ions to the Zn surface. Instead, Zn itself acts as a reducing agent following the simple reaction mechanism:

$$Zn_s + Cu_{aq}^{2+} \rightarrow Zn_{aq}^{2+} + Cu_s \tag{3.6}$$

Using immersion baths can be beneficial in the sense that no power source is required. Hence, isolated areas on the substrate can be coated without worrying about

establishing an electrical connection. Also, it provides an excellent coverage on the surface of the base metal. However, the thickness of the deposited layers through immersion plating is limited and cannot be adequately controlled, which is against the premise of this study.

Table 3.1: The composition of Cu immersion and Zn electroplating baths

Compounds	**Cu Immersion Plating Bath**	**Zn Electroplating Bath**
$CuSO_4$	30 g	
$C_4H_6O_6$	52.5	
NH_4OH (33% NH_3)	55 ml	
$ZnSO_4$		240 g
NH_4Cl		15 g
$(NH_4)_2SO_4$		30 g
Saccharin		1 g
DI water	1 L	1 L

For demonstration purposes, a structure with three pairs of Zn/Cu layers was fabricated. An acid chloride Zn electroplating bath was chosen to electroplate a Zn layer, which is composed of zinc sulfate ($ZnSO_4$), ammonium chloride (NH_4Cl), ammonium sulfate ($(NH_4)_2SO_4$), saccharin and high-purity DI water [12]. The detailed composition of this electroplating bath is given in Table 3.1. A two-electrode-cell configuration was adapted where a high-purity Zn sheet was utilized as the anode. Prior to electroplating process, the Zn anode was polished with high-grade (>600) sandpaper, degreased with acetone-methanol-isopropyl alcohol (IPA) treatment, and rinsed thoroughly with DI water.

Figure 3.3 shows the SEM images of the multilayer structures composed of Zn and Cu layers. In order to create contrast between the layers and improve the visibility, Zn layers were slightly etched with diluted hydrochloric acid solution for 10 seconds. The protruding brighter layers in Figure 3.3 are Cu, whereas the receding darker layers are Zn.

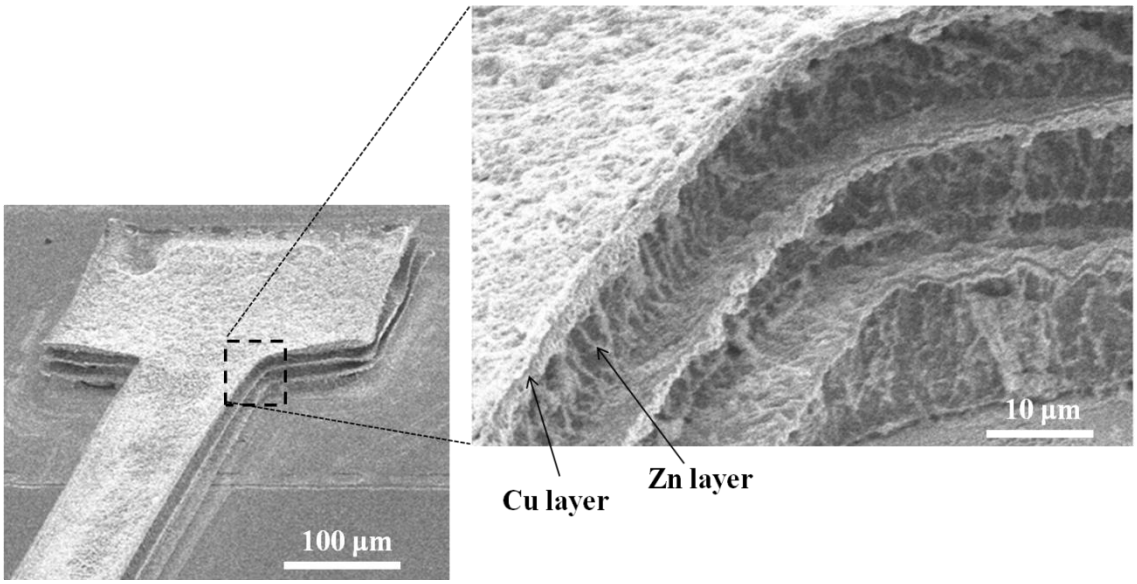

Figure 3.3: Multilayer structure fabricated by sequential deposition of electroplated Zn and electrolessly plated Cu layers

The main problem that needed to be overcome concerns the selective etching of the sacrificial Cu layers. As in the case of electroplating baths, the conventional Cu etchant that was used to selectively remove Cu layers from the Ni/Cu-based multilayer structures is not suitable for use with structures containing Zn layers, because the rate of Zn dissolution is much faster than that of Cu. None of the other recommended Cu etchants (e.g., $FeCl_3$ and thiourea-based solutions) were found to have the selectivity to realize the desired structures. Yet, an empirically-found electrochemical etching method proved to possess relatively high etching selectivity of Cu over Zn. This method involves high potential anodization of the sample in an aqueous solution composed of 1 M potassium hydroxide (KOH) and 0.5 M sodium chloride (NaCl).

The SEM images of the structures made up of three Cu/Zn pairs following 10-minute-long anodization in the KOH solution can be seen in Figure 3.4. Although a higher etching rate for Cu was able to be achieved than for Zn, it can be noticed that a significant amount of Zn was etched as well. Because of the difficulty in finding an etchant with desired selectivity, this approach was ultimately not pursued any further.

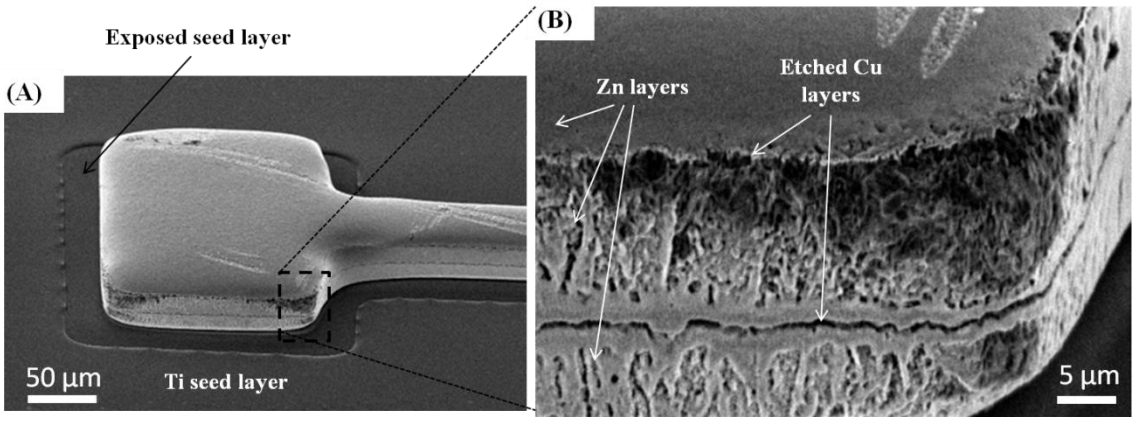

Figure 3.4: Multilayer Zn/Cu structures following the anodization process

3.2.2 Conventional Fabrication: Zn-Coated Ni/Cu Multilayer Structures

A slightly extended version of the conventional fabrication scheme discussed in Chapter 2.1.1.1, which includes the active material deposition and battery assembly can be seen in Figure 3.5. As the initial step, seed layers of Ti/Cu/Ti (500 nm/ 2000 nm/500 nm) were sputtered onto a thermally oxidized silicon wafer. Next, the mold preparation was carried out by spin-coating a negative tone photoresist (NR-21) at 2500 rpm for 10 seconds on the top Ti seed layer, resulting in an approximate thickness of 50 µm. A pre-exposure bake step was performed at 80 and 150 °C for 5 and 1.5 minutes, respectively. After cooling for 10 minutes, the final shape of the NR-21 film was obtained via hard-contact UV exposure through a glass mask with Cr patterns. A total energy of 3000 mJ was provided by the UV light with a wavelength of 365 nm. After performing the post-exposure bake on a hotplate at 80 °C for 5 minutes, the sample was allowed to cool to room temperature, which took approximately 20 minutes. The development of the photoresist was carried out in an aqueous tetramethylammonium hydroxide (TMAH) solution (RD6, Futurrex). Before moving to the electroplating step, a brief descumming step was performed for 1 minute to remove the remaining photoresist residues via reactive-ion etching O_2 plasma (Plasma-Therm).

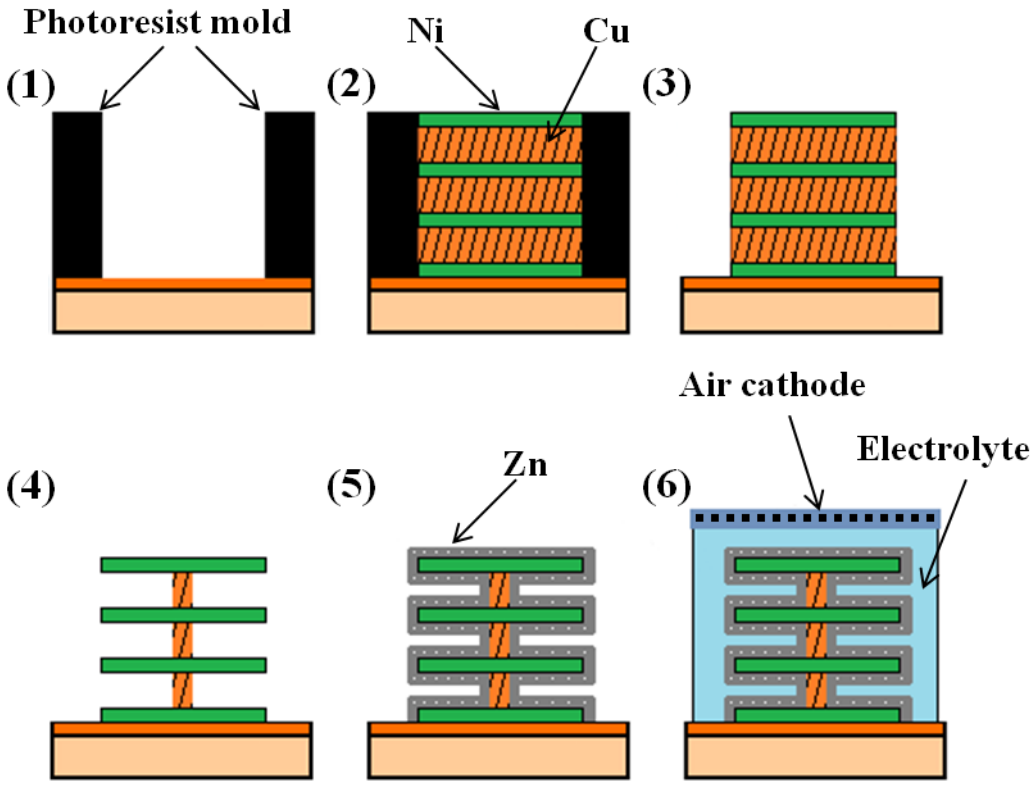

Figure 3.5: Fabrication sequence for the Zn-air batteries: (1) deposition of the photoresist mold on the metalized substrate, (2) sequential electrodeposition of alternating Ni and Cu layers, (3) removal of the mold, (4) partial etching of the sacrificial Cu layers, (5) electrodeposition of Zn on the multilayer current collector, and (6) sealing the top with the commercial air cathode and injection of the electrolyte into the case surrounding the electrode

Upon preparation of the mold, the exposed top Ti seed layer was removed using diluted hydrofluoric acid (HF) solution (HF:DI water, 1:50). The underlying Cu layer was utilized as a seed layer for the robotically assisted sequential electroplating process. In this process, 10 pairs of Ni/Cu layers were alternately electroplated at a constant current density of 10 mA cm^{-2}. An all-sulfate Ni electroplating bath and a commercial Cu electroplating bath (details can be found in Chapter 2.1.1) were utilized for the repetitive alternating deposition of structural Ni and sacrificial Cu layers. Following the electroplating process, the photoresist mold was removed by acetone.

Figure 3.6 shows the SEM images of the fabricated multilayer structures immediately after the removal of the mold. The etching holes labeled in Figure 3.6.D refer to the areas that were initially occupied by the photoresist pillars during the sequential electroplating process. These holes are vertically separated from each other by the air bridges which have a width of 15 μm.

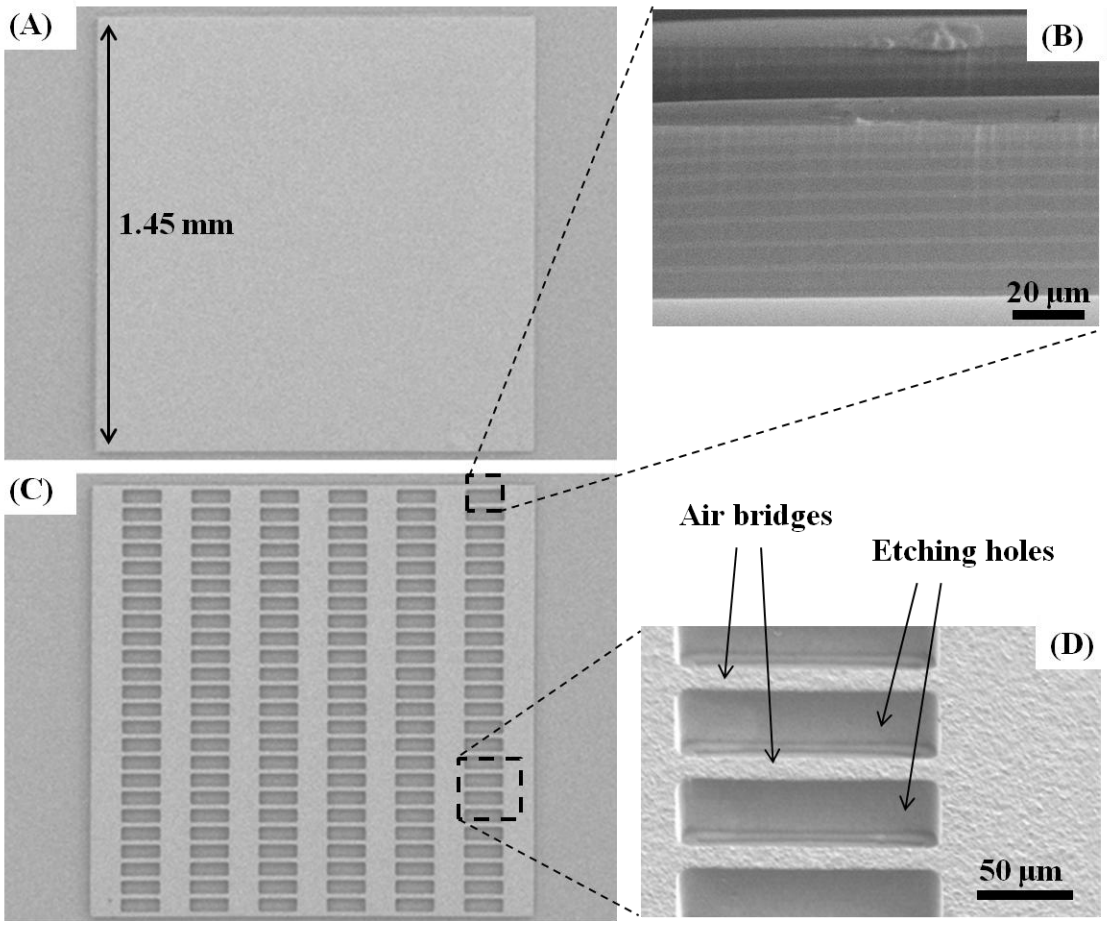

Figure 3.6: SEM images showing the multilayer structure after photoresist removal: (A) unpatterned structure, (B) side view of the air bridges showing the Ni and Cu layers, (C) patterned structure with etching holes and air bridges, and (D) closed-up view of the etching holes and air bridges

The sacrificial Cu layers were partially and selectively etched through a timed wet etching process by using the aforementioned Cu etchant. The etching process was performed for 30 minutes, which was sufficient to remove all the Cu between vertically

adjacent air bridges and to form a controlled amount of undercut in the vicinity of the etching holes. Figure 3.7 illustrates the advancement of the etching process.

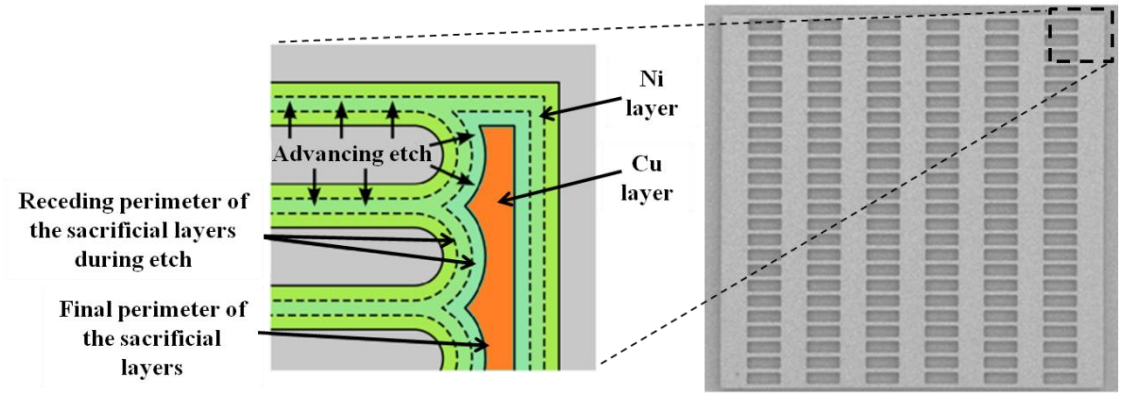

Figure 3.7: Schematic description of the release process of the air bridges during the sacrificial etching of Cu layers

The mechanical support between the Ni layers, as well as the interlayer electrical connection, was provided by the remaining Cu located between the horizontally adjacent etching holes shown in Figure 3.6. The air bridges, on the other hand, are suspended and have no Cu in between to mechanically support them. Therefore, they are susceptible to collapsing if not handled properly. To prevent these bridges from collapsing following the completion of the etching process, the structures are immersed in a series of liquids: DI water, IPA, and methanol, where each following liquid has lower capillary forces than its predecessor.

Proof-of-concept structures with 10 pairs of Ni/Cu layer were prepared. Individual thickness values for Ni and Cu layers were measured to be approximately 1.5 and 4 μm, respectively. The theoretical surface area of the metallic backbone following the partial removal of the Cu was estimated by making use of the following formula:

$$A_{tot} = A_{Ni} + 2 \cdot N_{Cu} \cdot (A_{Ni} - A_{Cu}) + N_{Ni} \cdot P_{Ni} \cdot h_{Ni} + N_{Cu} \cdot P_{Cu} \cdot h_{Cu} \qquad (3.7)$$

where A_{Ni} and A_{Cu} are the respective net top surface area of the Ni and Cu layers, N_{Ni} and N_{Cu} are the respective number of Ni and Cu layers, h_{Ni} and h_{Cu} refers to the respective thicknesses of Ni and Cu layers, and P_{Ni} and P_{Cu} represent the net perimeter of the Ni and Cu layers, respectively [14]. Under the reported conditions, the surface area was calculated to be approximately 11 mm^2 for a 10-layer structure, which indicates more than 5 times increase in comparison to the footprint area.

Accurate knowledge of the surface area of the multilayer structure is critical, since the current density plays a vital role on the morphology of the electroplated Zn. Also, in order for the gap between two adjacent Ni layers to be maintained and thus, to preserve the high surface area of the multilayer structure, it is important to control the thickness of the electroplated Zn deposit. The control over the Zn thickness is only possible with the precise knowledge of the surface area, since both the current density and the plating duration will be determined according to the surface area.

Based on Equation 3.7, it is possible to achieve significant improvements in the surface area by increasing the number of layers, as well as by increasing the amount of the Cu etched. In addition, higher surface areas can also be obtained by modifying the size, geometry, and the number of the etching holes.

3.2.3 Fabrication of the Anode Electrode

The fabrication of the anode is achieved by electrodepositing Zn onto the multilayer backbone. Zn electroplating was carried out at a constant current density of approximately 10 A dm^{-2} utilizing the same acid-chloride electroplating bath and cell configuration as the one mentioned earlier in this chapter [12].

Electroplating current density is one of the primary determinants of the surface roughness of the deposits. Figure 3.8 illustrates the surface profile of two different Zn films electroplated at two different current densities, 10 and 20 A dm^{-2}. The profiles were obtained by a noncontact, optical surface profiler (Wyko Profilometer NT3300, Veeco).

The parameters R_a, R_q, and R_t in Figure 3.8 represent arithmetic average, root mean squared, and the maximum height of the profile, respectively. According to the profiles, as well as the parameters, it can be seen that increasing the current density from 10 to 20 A dm^{-2} nearly doubles the surface roughness of the Zn deposits. Although the surface roughness is usually considered as a desired feature in energy storage applications due to the increased surface area, it would render the process more complicated for applications involving well ordered structures as presented herein.

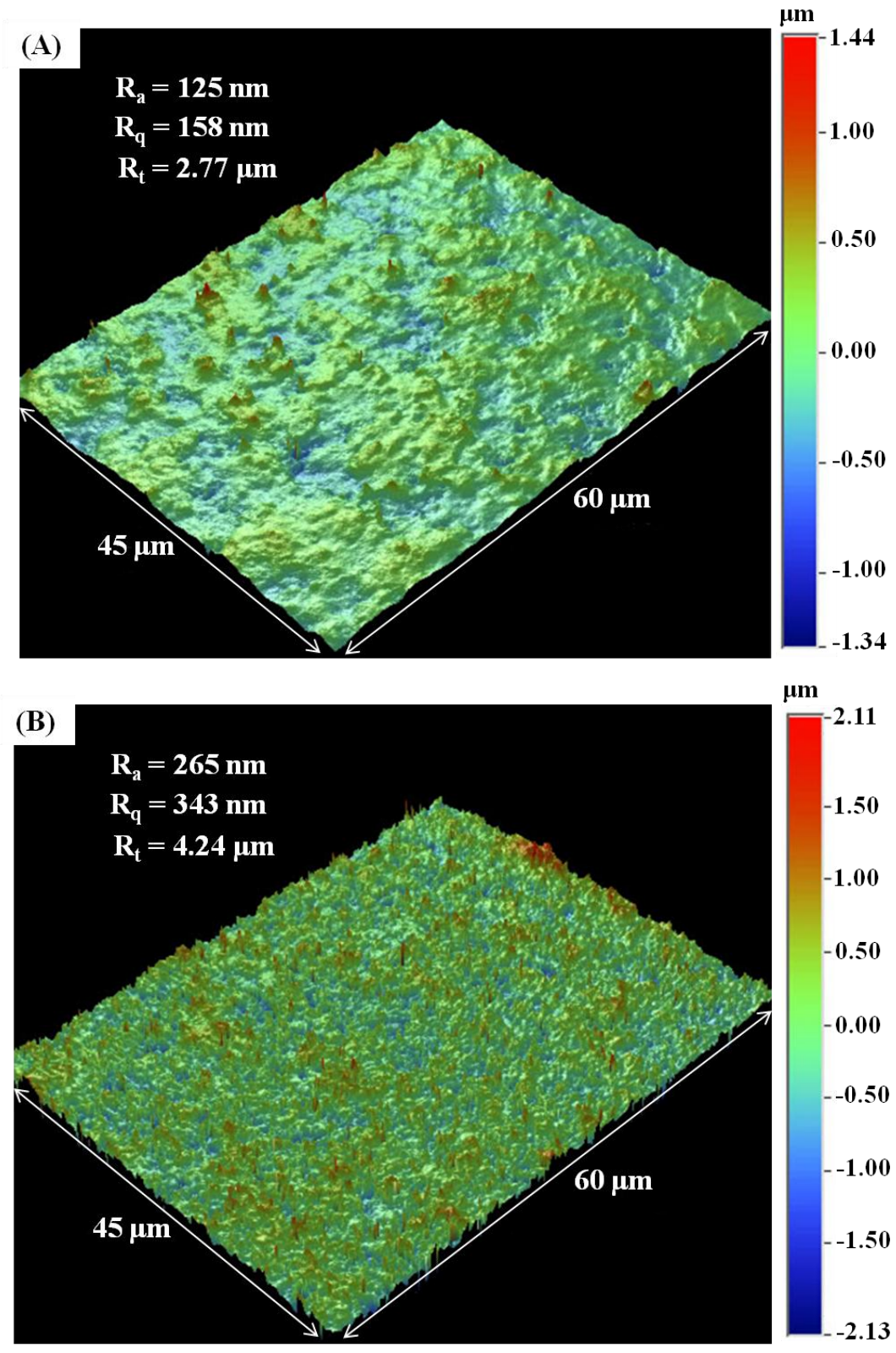

Figure 3.8: Surface profiles of Zn films deposited at two different current densities: (A) 10 A dm^{-2}, (B) 20 A dm^{-2}

Prior to the electroplating process, a vacuum treatment was applied with the sample immersed in the plating solution for 10 minutes. This ensured the removal of the trapped air in the etching holes, as well as in between the Ni layers, thus establishing a better exposure of the electrode to the plating solution.

SEM images showing the multilayer structures before and after Zn electroplating process are given in Figure 3.9. As can be seen from the figure, a conformal Zn coating was achieved with DC plating. It is also shown that the clearance between two adjacent Ni layers around the etching holes (i.e., air bridges) persists after the plating process.

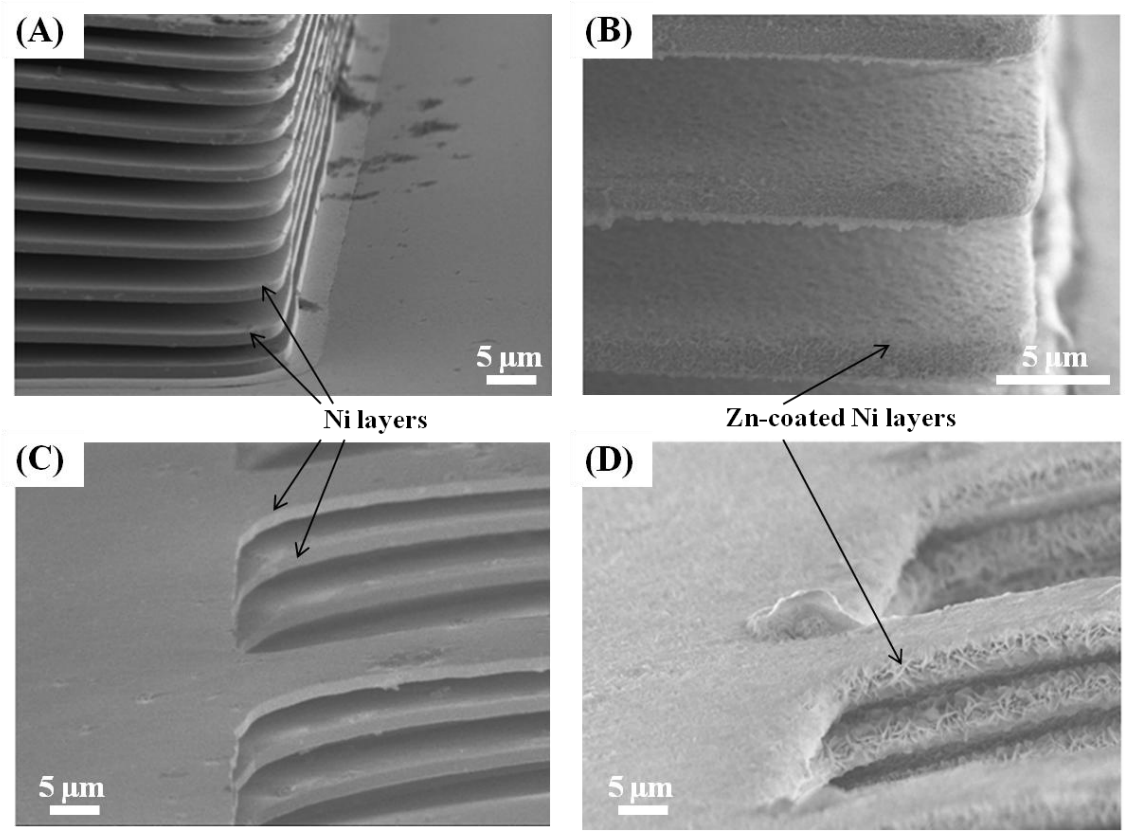

Figure 3.9: Multilayer Ni backbone before and after Zn electroplating: (A) the corner of the multilayer electrode, (B) closed-up view of the corner after Zn electroplating, (C) etching holes after Cu etch, and (D) etching holes after Zn electroplating

To demonstrate the contribution of the partially etched metallic backbone structure to the performance of the electrode, the same amount of Zn was electroplated

under the same conditions as before onto an unpatterned and unetched Ni/Cu multilayer structure with the same total thickness and the same footprint area as the partially etched structures which can be seen in Figure 3.6.A. The reason behind electroplating Zn film onto the unetched multilayer structure, instead of directly onto the Cu seed layer with the same footprint area is to eliminate any performance discrepancies that may originate from the use of different material as a current collector, as well as from the difference in the total height of the structures which determines the inter-electrode distance once the battery assembly is finalized.

For further performance comparison, another thin-film anode electrode was formed by electroplating the same amount of Zn directly onto the seed layer without utilizing any backbone structure. An SEM image showing the enlarged view of the Zn deposit is given in Figure 3.10. It can be seen that the film is in the form of Zn nanosheets.

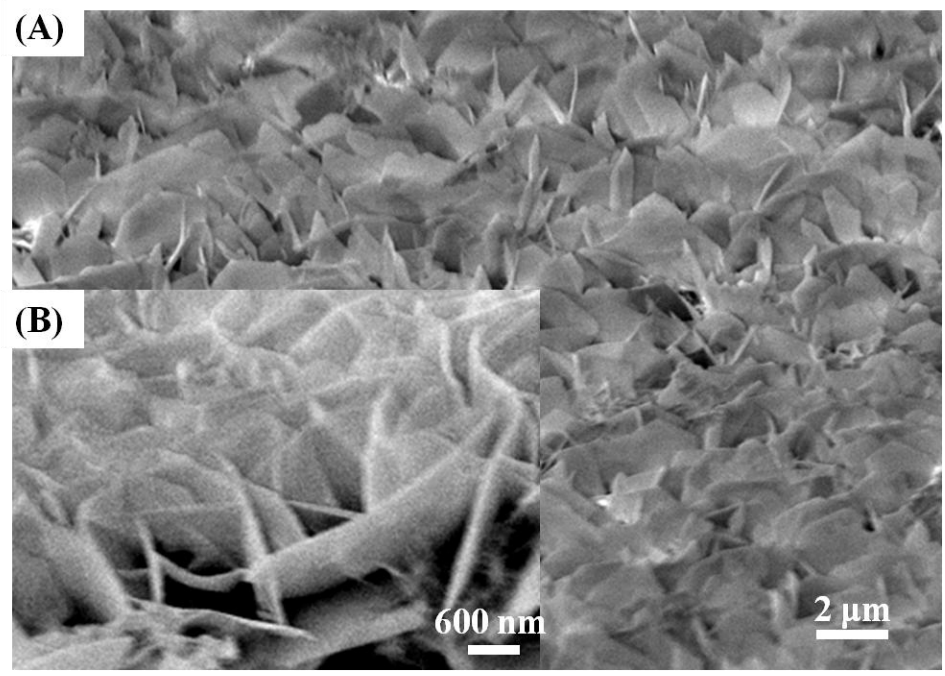

Figure 3.10: Enlarged view of the Zn film electroplated at 10 A dm^{-2}

3.2.4 Assembly of the Zn-air Battery

The conceptual rendering of the final form of the Zn-air battery can be seen in Figure 3.11. The Zn anode, surrounded by an epoxy case containing the electrolyte, was assembled with a commercial air cathode (E4A, Electric Fuel). The oxygen entering the air cathode is reduced by the catalyzed carbon resulting in the formation of OH^- ions. These OH^- ions diffuse to the Zn anode and react with Zn forming soluble zincate ions most of which eventually precipitate to form ZnO as the discharge proceeds.

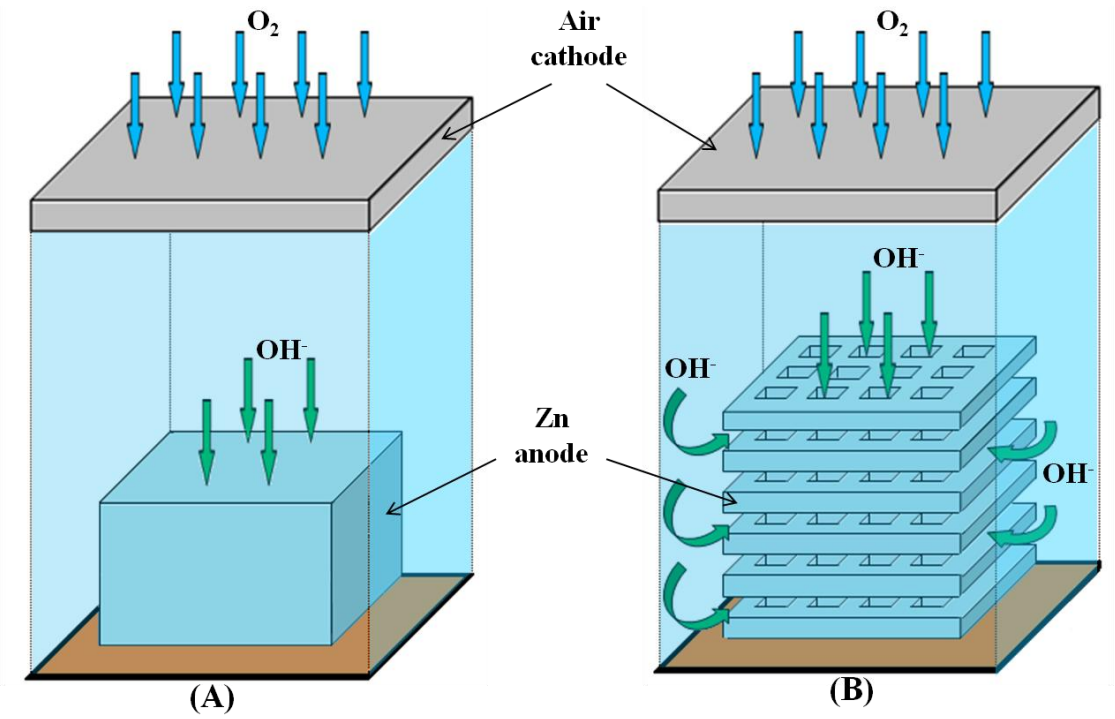

Figure 3.11: Conceptual rendering of the battery assembly: (A) Zn deposited on the seed layer, (B) Zn deposited on the multilayer backbone

The air cathode is composed of three major layers as illustrated in Figure 3.1. The outermost layer comprises a laminated porous Teflon film allowing oxygen to diffuse in and serving as a blocking layer by preventing the battery from leaking the electrolyte. The median layer consists of an active cathode material which is manganese-based catalyzed carbon supported by a woven Ni mesh. In addition to providing mechanical

stability, the Ni mesh serves as a current collector. To enable an electrical connection to the cathode, a thin Cu wire was soldered to the edge of this Ni mesh after removing the carbon. The innermost layer in contact with the electrolyte serves as a separator layer consisting of a laminate of a polypropylene microporous film with a thin polypropylene non-woven film that was rendered hydrophilic with a surfactant. This innermost layer also serves as an insulator between the Zn anode and the air cathode to prevent shorting, while allowing transport of ions to and from the electrolyte.

As mentioned earlier in this chapter, a large majority of the Zn-air batteries utilize alkaline electrolytes including KOH, sodium hydroxide (NaOH), and lithium hydroxide (LiOH) [2]. Among these solutions, KOH has been the most widely used one due to its superior ionic conductivity. For the batteries reported herein, a 7 M aqueous KOH solution was used as the battery electrolyte. It was injected into the epoxy case surrounding the anode. KOH solution at such a high concentration possesses relatively high viscosity which was observed to inhibit a decent contact between the Zn anode and the electrolyte. To mitigate this issue, a vacuum treatment was carried out immediately after the injection of the electrolyte for 10 minutes, as in the case of the Zn electroplating process. The optical image showing the battery assembly can be seen in Figure 3.12.

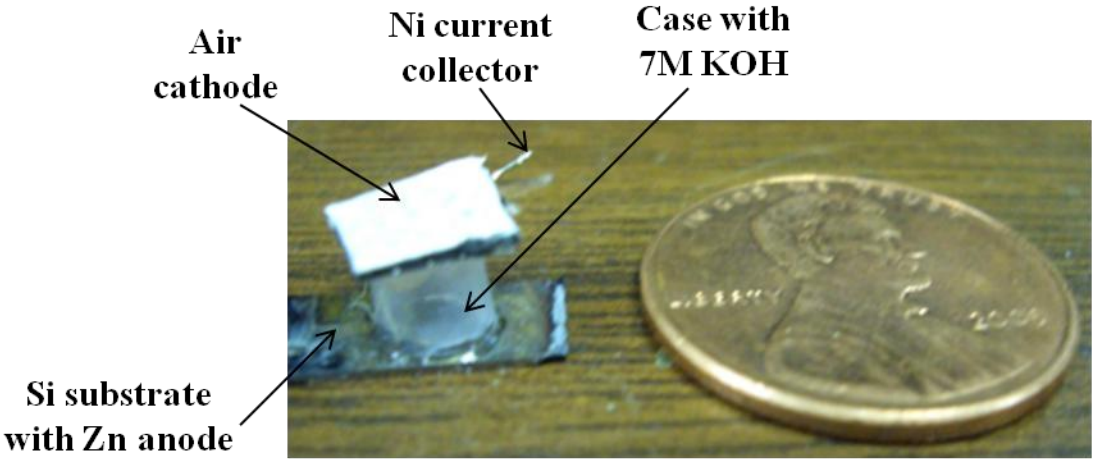

Figure 3.12: Zn-air battery prior to performance characterization

3.3 Performance Characterization of the Microbatteries

To evaluate the performance of the multilayer electrodes, proof-of-concept Zn-air batteries based on a multilayer backbone composed of 10 layers were prepared. These batteries were characterized by discharging under five different electrical loads with resistances of 100, 250, 500, 1000, and 3000 Ω. The main reason behind performing the discharge tests under constant loads rather than galvanostatically (i.e., constant current) was to be able to compare the discharge profile to the commercial batteries (DA10, Duracell) which were also tested under the same conditions [15]. Similarly, thin-film Zn-air electrodes fabricated on unpatterned and unetched multilayer backbone, as well as, directly on the seed layer were also discharged under the same electrical loads. During the discharge tests, voltage values were simultaneously measured and recorded with respect to time using LabVIEW software (SignalExpress, National Instruments).

The experimental setup used to characterize the fabricated Zn electrodes is shown in Figure 3.13. As can be seen from the figure, the battery is connected in series with a resistor while a data acquisition device connected in parallel to the battery measures the potential of the cell over the entire course of the discharge process. The potential was monitored on the computer display via LabVIEW software. The discharge process continued until the cut-off potential of 1.0 V.

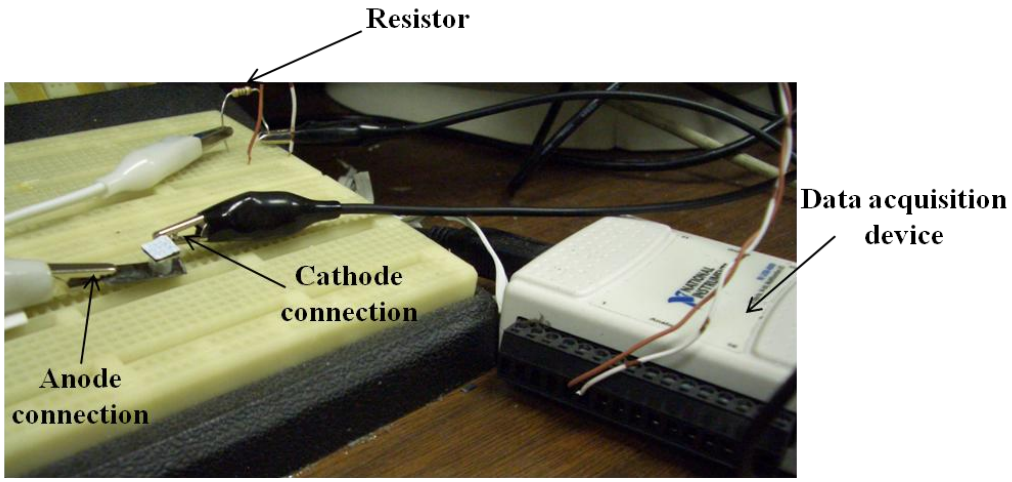

Figure 3.13: Experimental setup for the characterization of the discharge performance of the multilayer Zn electrodes

The discharge profiles of the batteries based on multilayer electrode under various electrical loads can be seen in Figure 3.14. According to Ohm's law, a higher load indicates a lower discharge rate. As can be seen from Figure 3.14, the discharge curves of the batteries with the 10-layer electrode maintain a relatively flat voltage profile both at high and low discharge rates. A small voltage decrease is observed immediately after start-up, and a sharp voltage drop occurs near the total discharge. These discharge characteristics are in good agreement with previously reported Zn-air batteries [1, 5].

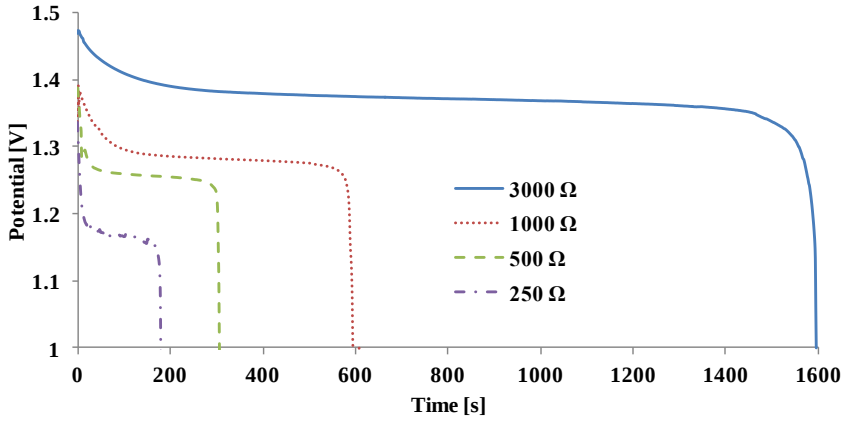

Figure 3.14: Discharge profiles of the Zn-air microbattery based on multilayer Zn anode under various electrical loads

These discharge data were used to calculate the areal capacity, C_A, and the areal energy density, E_A, of the Zn-air batteries. The former one was obtained by integrating the discharge current, I, over time, t, and dividing by the footprint area, A, as given in Equation 3.8. The latter one was then simply calculated by multiplying the average discharge potential, V_{av}, by the areal capacity:

$$C_A = \int \frac{I}{A} dt \tag{3.8}$$

$$E_A = C_A \cdot V_{av} \tag{3.9}$$

The same parameters were also calculated for the aforementioned thin-film electrodes. The comparison of the areal energy densities of the fabricated microbatteries with different electrode structures is shown in Figure 3.15. The Zn-air battery based on the 10-layer Zn electrode demonstrated higher areal energy densities than its thin-film counterparts at higher discharge rates, indicating better high-power capability. The difference between the energy density of these batteries increases further as the discharge rate is increased.

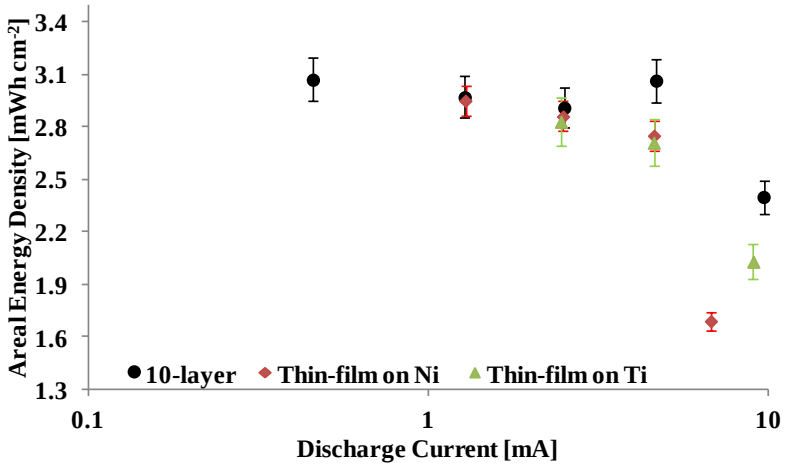

Figure 3.15: Areal energy densities of various microbatteries as a function of discharge current

In addition, it can be seen that the battery with 10-layer electrode is able to maintain a high areal energy density of ~3 mWh cm^{-2} until a discharge current of approximately 5 mA, whereas a clear decreasing trend is observed in the energy density of the thin-film microbatteries as the discharge rate is increased and then a drastic drop is observed around 10 mA of discharge current. A similar decreasing trend in the energy density has also been reported for the batteries utilizing Zn powder as the anode, as in the case of commercial Zn-air batteries [5].

Although it was technically possible to increase the discharge rates even further by simply reducing the electrical load and measure the response in the energy density, it was not performed since the air cathode starts to become the limiting factor in the performance of the microbattery, primarily because of the insufficient oxygen diffusion from the air, as well as slow kinetics of oxygen reduction inside the cathode.

The nominal current density for the commercial air cathode was reported to be ~300 mA cm^{-2}. The approximate area of the air cathode utilized in the fabricated Zn-air battery was 4 mm^2, corresponding to a nominal current of 12 mA. This means that the use of any load below 100 Ω during the discharge test may be problematic.

To determine the percentage of the electroplated Zn that was able to be utilized during the discharge experiments, first, the amount of electroplated Zn was calculated using Equation 3.10.

$$m = \frac{i \cdot t \cdot A \cdot M}{n \cdot F} \tag{3.10}$$

where m is the weight of the electroplated metal (g), i is the plating current density (A cm^{-2}), t is the plating duration (s), A is the surface area of the working electrode (cm^2), M is the molecular weight of the deposited metal (g mol^{-1}), n is the valence of the dissolved metal in the plating solution in equivalents per mole (2 for Zn), and F is the Faraday's

constant (96485 C mol^{-1}). As mentioned earlier, the anodes of the microbatteries were formed by electroplating Zn at a current density of 10 A dm^{-2} for 1 minute. This corresponds to an approximate Zn mass of 0.3 mg per structure. Using the same correlation, the mass of the discharged Zn was also calculated with the data shown in Figure 3.14. Based on these results, on average, 88% of the electroplated Zn onto the multilayer backbone was able to be utilized. This percentage drops to 85% in the case of microbatteries with thin-film Zn electrodes. Commercial batteries utilizing Zn powder as the anode, on the other hand, reportedly have significantly lower Zn utilization, which is in the range of 25-35% [16].

Following the discharge tests, SEM images of the multilayer electrodes were acquired, as shown in Figure 3.16. It can be seen that the electrodeposited Zn film onto the backbone was completely dissolved. It is also apparent that the metallic multilayer backbone was able to maintain its integrity and remain intact throughout the discharge process.

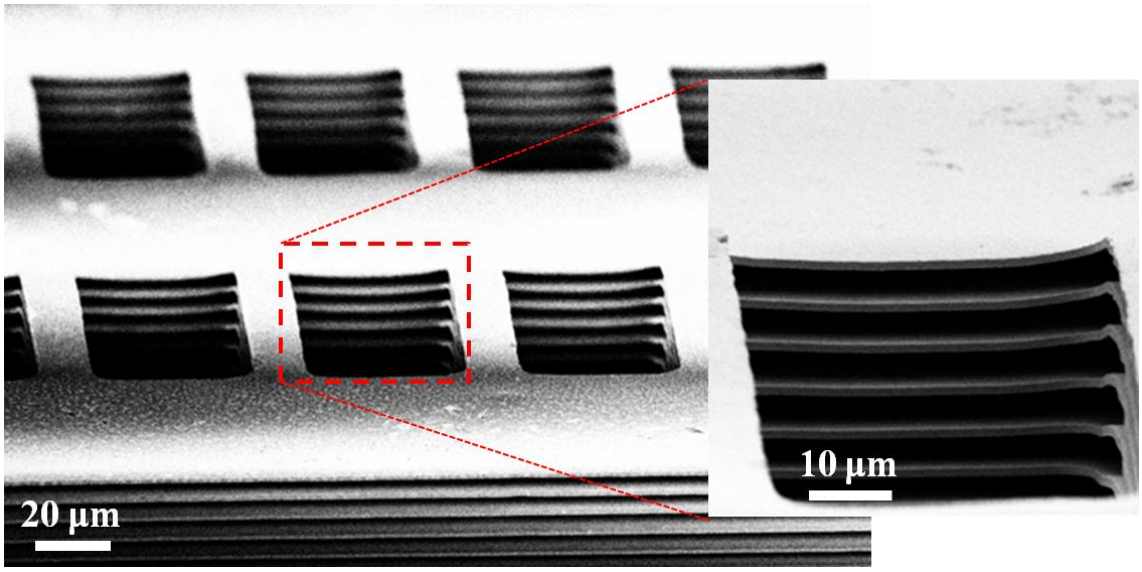

Figure 3.16: Multilayer Ni backbone following the discharge of the microbattery at high rates

3.4 Conclusions

This chapter presents the first utilization of the MEMS-enabled, metallic multilayer structures for electrochemical energy storage applications. The multilayer structures demonstrated herein are based on sequential deposition of alternating Ni and Cu layers, followed by partial and selective removal of the Cu layers. Zn-air battery chemistry was selected as one of the most popular primary battery system and the anode electrode of that chemistry was prepared by electroplating a conformal Zn layer onto the multilayer metallic backbone.

A proof-of-concept 3D Zn-air microbattery composed of a microfabricated metallic scaffold supporting electrodeposited Zn as the anode and a commercial air cathode has been successfully developed, fabricated, and tested. To demonstrate the improvement in the performance enabled by the use of multilayer metallic backbone, thin-film microbatteries of the same footprint area with and without any backbone structures were also prepared and characterized. Despite the fact that each one of the fabricated microbatteries had the same amount of Zn in their anode electrodes, the microbatteries with the electrodes based on the multilayer backbone was shown to be superior to their thin-film counterparts in terms of areal energy density, particularly at high discharge rates, which is due to the enhanced power capability. The areal energy density of the microbattery with the multilayer electrode was measured as 3 mWh cm^{-2}.

One of the underlying reasons for the enhanced power performance is the high surface area provided by the multilayer metallic scaffold, allowing more contact points between the Zn and the electrolyte. In addition to the improved surface area, the metallic current collector maintains a consistent and continuous electrical access to the Zn film with a minimum ohmic loss. Also, the presence of the etching holes enabled a shorter path for the inter-electrode transport of the liquid-state ions in the electrolyte.

An important feature of the multilayer electrode approach reported herein is the ability to increase the energy density further by simply increasing the number of layers in

the skeleton without compromising the footprint area. Also, this mechanically stable and chemically inert skeleton can be easily incorporated into other battery chemistries, as long as it is possible to coat the metallic backbone with the electrochemically active material. A more advanced version of this multilayer fabrication approach will be discussed in the following chapters, where secondary battery chemistries are implemented.

3.5 References

[1] T. B. Reddy, *Linden's Handbook of Batteries* vol. 4: McGraw-Hill New York, 2011.

[2] J. S. Lee, S. Tai Kim, R. Cao, N. S. Choi, M. Liu, K. T. Lee, *et al.*, "Metal–air batteries with high energy density: Li–air versus Zn–air," *Advanced Energy Materials,* vol. 1, pp. 34-50, 2011.

[3] X. G. Zhang, "Fibrous zinc anodes for high power batteries," *Journal of power sources,* vol. 163, pp. 591-597, 2006.

[4] C.-C. Yang and S.-J. Lin, "Improvement of high-rate capability of alkaline Zn–MnO2 battery," *Journal of power sources,* vol. 112, pp. 174-183, 2002.

[5] F. Chamran, H.-S. Min, B. Dunn, and C.-J. Kim, "Zinc-air microbattery with electrode array of zinc microposts," in *Micro Electro Mechanical Systems, 2007. MEMS. IEEE 20th International Conference on*, 2007, pp. 871-874.

[6] L. F. Urry, "Zinc anode for an electochemical cell," ed: Google Patents, 2000.

[7] N. C. Tang, "Electrode for an electrochemical cell including ribbons," ed: Google Patents, 2001.

[8] M. Malservisi and J.-y. Huot, "Zinc powders for use in electrochemical cells," ed: US Patent 20,040,115,532, 2004.

[9] B. Coffey, Q. G. Holloter, R. C. Kainthla, D. J. Manko, and C. E. Sesock, "Cylindrical battery cell having improved power characteristics and methods of manufacturing same," ed: Google Patents, 2007.

[10] A. Armutlulu, Y. Fang, S. Kim, C. Ji, S. Allen, and M. Allen, "High-current zinc-air microbattery based on a micromachined multilayer lateral metallic scaffold," *Proc. of PowerMEMS,* pp. 107-110, 2010.

[11] A. Armutlulu, Y. Fang, S. Kim, C. Ji, S. B. Allen, and M. Allen, "A MEMS-enabled 3D zinc–air microbattery with improved discharge characteristics based on a multilayer metallic substructure," *Journal of Micromechanics and Microengineering,* vol. 21, p. 104011, 2011.

[12] M. Schlesinger and M. Paunovic, *Modern electroplating* vol. 55: John Wiley & Sons, 2011.

[13] S. Hirsch and C. Rosenstein, "Immersion plating," *Metal Finishing,* vol. 93, pp. 415-419, 1995.

[14] P. Galle, S.-H. Kim, U. Shah, and M. G. Allen, "Micromachined capacitors based on automated multilayer electroplating," in *Micro Electro Mechanical Systems (MEMS), 2010 IEEE 23rd International Conference on*, 2010, pp. 332-335.

[15] Online. (2010, June). *http://media.ww2.duracell.com/en-US/Global-Technical-Content-Library/Product-Data-Sheets.jspx*.

[16] E. Malone, M. Berry, and H. Lipson, "Freeform fabrication and characterization of Zn-air batteries," *Rapid Prototyping Journal*, vol. 14, pp. 128-140, 2008.

CHAPTER 4

NICKEL HYDROXIDE-BASED ELECTRODES

4.1 Background and Motivation

In this chapter, the use of previously developed multilayer structures for secondary (i.e., rechargeable) battery chemistries is examined. Rechargeable systems allow the characterization of various features of the multilayer structures, including their capacity delivery following ultra-fast charging rates, as well as their cycling stability after numerous charge and discharge cycles. Such characterizations are not possible with the primary battery chemistries.

For the demonstration of the improved power capability due to the deterministically engineered multilayer electrodes, nickel hydroxide ($Ni(OH)_2$) was selected as the active material prototype for deposition onto the multilayer structures [1, 2]. Although Li-ion batteries compose the vast majority of today's battery market for portable electronic devices, a number of reasons lie behind the choice of the $Ni(OH)_2$-based batteries as a starting point.

Unlike the Li-ion batteries which are relatively difficult to handle and require a complicated experimental set-up (see Chapter 5), the $Ni(OH)_2$ chemistry is much easier to incorporate for testing the performance of the 3D electrodes proposed in this study. It is also one of the most well-studied active material in secondary battery systems after Li-ion batteries. The systems involving $Ni(OH)_2$ chemistry include nickel-iron, nickel-cadmium, nickel-zinc, and nickel-metal hydride batteries. Among these battery chemistries, the latter two reportedly exhibit better power characteristics, rendering the systems more appealing for our work [3]. Finally, in addition to the easy synthesis of $Ni(OH)_2$, factors such as its environmentally benign nature and cost effectiveness have also played an important role in selecting this chemistry.

$Ni(OH)_2$ exhibits a reversible charge storage redox mechanism in which it converts to nickel oxyhydroxide (NiOOH) via the diffusion of protons through its solid state lattices as given in Equations 4.1 and 4.2 [3]:

$$Ni(OH)_2 + OH^- \rightarrow NiOOH + H_2O + e^- \quad (4.1)$$

$$NiOOH + H_2O + e^- \rightarrow Ni(OH)_2 + OH^- \quad (4.2)$$

The former and latter reactions are associated with the charging and discharging of the electrode, respectively. Proton (i.e., H^+) diffusion into the bulk of the active material enables these reactions to continue at the interface. Apart from batteries, this reversible chemistry is also an attractive choice for supercapacitor applications, and it will be discussed in Chapter 6.2 in more detail.

In this chapter, the design and modeling of the multilayer electrodes will be presented for $Ni(OH)_2$-based rechargeable batteries. Next, the fabrication details of the multilayer backbones to be coated with $Ni(OH)_2$ will be covered. Thereafter, the methodologies pertaining to the synthesis of the active material and the selection of the deposition techniques will be discussed. The following section will cover the characterization and performance testing of the fabricated electrodes. In the last section, a comparison of the experimental results with the model predictions, as well as the model projections of the optimum design and performance will be provided.

4.2 Design and Modeling of the Electrodes

One of the premises of this study is the ability to control the characteristic dimensions (e.g., surface area, active material thickness, etc.) of the fabricated electrodes. As discussed in Chapter 1, to realize electrodes with enhanced power performance, their surface area needs to be maximized while the diffusion and conduction path lengths are minimized. In the multilayer fabrication approach, the former can be achieved by

increasing the number of layers; however, this can be limited by fabrication constraints, including the total height of the electrode (i.e., achievable mold thickness), as well as by the minimum allowed thickness for individual layers to remain mechanically intact. In terms of active material thickness, a thinner material layer improves the power performance but at the cost of decreasing the storable energy. Therefore, the optimum active material thickness value should be determined for a given charge and/or discharge rate.

In this portion of the study, our goal is to develop models using fundamental mass transport principles that could be used to optimize the characteristic dimensions in the multilayer electrodes to enable a high performance rechargeable battery. The first model involves determining the optimum thickness for the deposited active material film on each layer of the metallic backbone, taking into account the tradeoffs between the energy storage and diffusion. The second model is developed for the estimation of the optimum spacing between the layers and the distance between the etching holes, based on the optimum active material thickness obtained from the first model.

4.2.1 Diffusion-Limited Model to Determine the Optimum Active Material Thickness

First, a one-dimensional (1D) spatial model for the H^+ diffusion in the active material is developed, considering an infinite plane sheet of thickness L with one side exposed to the electrolyte, while the other one is in contact with the current collector (see Figure 4.1). This simple diffusion-limited model has proven quite useful in predicting the performance of Li-ion batteries [4, 5].

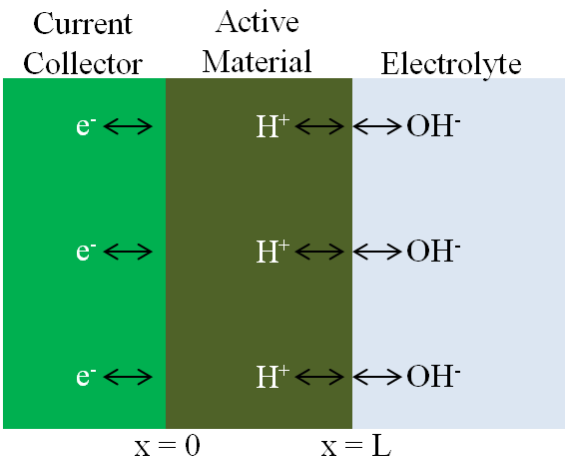

Figure 4.1: Electrode model assuming an infinitely wide plane sheet of thickness L

The model is based on the assumption that among the three forms of mass transport (i.e., diffusion, convection, and migration), diffusion is the dominating mechanism for the transportation of the H^+ ions. Hence, the constant-current charge and discharge times are solely limited by the utilization of the active material; losses originating from the electrolyte and reaction kinetics are neglected. It was also assumed that the ion and electron fluxes are uniformly distributed over the entire surface. Following the aforementioned assumptions, the equation of continuity in one spatial dimension can be written as:

$$\frac{\partial C_{H^+}}{\partial t} = D \cdot \frac{\partial^2 C_{H^+}}{\partial x^2} \tag{4.3}$$

where C_{H^+} and D are the concentration (mol cm^{-3}) and the diffusion coefficient (cm^2 s^{-1}) of the H^+ ions in the active material, respectively. It is known from the Arrhenius equation that D is a function of the temperature. However, for the purposes of this model, the charging and discharging were assumed to take place under isothermal (i.e. constant temperature) conditions at room temperature. Diffusivity is also known to depend on the state of charge (SOC) of the active material. In its fully charged form (i.e., NiOOH), the

diffusivity of the active material has been reported to be in the order of 10^{-8} cm^2 s^{-1}, whereas the fully discharged form (i.e., $Ni(OH)_2$) features a diffusivity which is in the order of 10^{-11} cm^2 s^{-1} [6-8]. Therefore, assuming a constant diffusivity despite such a substantial difference throughout the whole charging/discharging process would not be realistic. Motupally et al. developed a formula that takes SOC into account and successfully predicts the diffusivity of H^+ as shown in Equation 4.4 [7, 9, 10]:

$$D = D_1 \cdot \left[\theta + (1-\theta) \cdot \left(\frac{D_2}{D_1}\right)^{0.5}\right]^2 \tag{4.4}$$

where D_1 is the diffusion coefficient of pure NiOOH (10^{-8} cm^2 s^{-1}), D_2 is the diffusion coefficient of pure $Ni(OH)_2$ (10^{-11} cm^2 s^{-1}), and θ is the SOC ($0 \leq \theta \leq 1$), where 0 and 1 refer to the complete discharge and complete charge, respectively. This equation is based on a mixing rule in terms of the root mean square displacement of the diffusing species in a solid solution involving a homogeneous mixture of two phases [7, 9].

The initial and boundary conditions for this model are given as:

at t = 0: $$C_{H^+} = C_0 \tag{4.5}$$

at x = 0: $$\frac{\partial C_{H^+}}{\partial x} = 0 \tag{4.6}$$

at x = L: $$D \cdot \frac{\partial C_{H^+}}{\partial x} = \frac{i}{n \cdot F} \tag{4.7}$$

where C_0 is the initial H^+ concentration in the active material (mol cm^{-3}), i is the charge or discharge current density (A cm^{-2}), n is the valence number (1 for H^+), and F is Faraday's constant (96485 C mol^{-1}).

Since the charge and discharge experiments were performed galvanostatically, (i.e., at constant current), the flux at the electrode-electrolyte interface was assumed to be

uniform and constant, as indicated in Equation 4.7. At the interface of the current collector and the active material, no mass transfer is taking place and hence, the flux equals zero.

During the charging process, H^+ ions diffuse from the active material (i.e., $Ni(OH)_2$) to the electrolyte, resulting in a concentration gradient that forms within the active material film. This concentration gradient becomes more severe as the charge rate (i.e., current density) increases. If the rate is too high, it may not be possible for the H^+ ions to diffuse away from the active material in a desired duration of time. As an example, a charging duration of one minute (i.e., 60 C) was selected. The goal of the simulations was then to find the maximum thickness for the active material that allows the diffusion of all H^+ ions into the electrolyte in one minute.

In a fully discharged state, the concentration of hydrogen can be estimated by dividing the density of $Ni(OH)_2$ (3.55 g cm^{-3}) by its molecular weight (92.71 g mol^{-1}), yielding 0.0383 mol cm^{-3}. The change in the volume of the active material during the charging process is neglected. From that concentration value, the capacity of the electrode can be calculated for a given thickness of the active material, which also determines the required current density enabling charging of the electrode in one minute.

The partial differential equation (PDE) given in Equation 4.3 was solved by finite element method (FEM). For this type of 1D parabolic PDE, Matlab's pdepe function was utilized whose detailed code can be found in the Appendix. Starting with an active material thickness of 0.05 μm, the capacity of the active material was calculated along with the current density required to discharge the electrode in 60 seconds. Then, the simulation was performed, and the concentration profiles across the thickness of the active material were plotted as a function of time. Thereafter, the thickness was increased and the same procedure was repeated for the increased thickness value. The resultant profiles at three different thicknesses are provided in Table 4.1.A.

Table 4.1: Concentration profiles of H^+ within the $Ni(OH)_2$ active material as a function of time at various thicknesses: (A) 3D profiles, (B) 2D profiles at the 60th second

	Active Material Thickness	Concentration Profile
(A)	**0.05 µm**	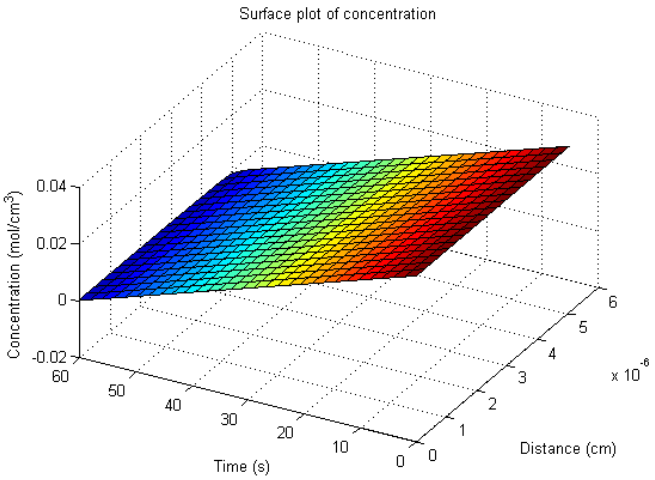
	0.1 µm	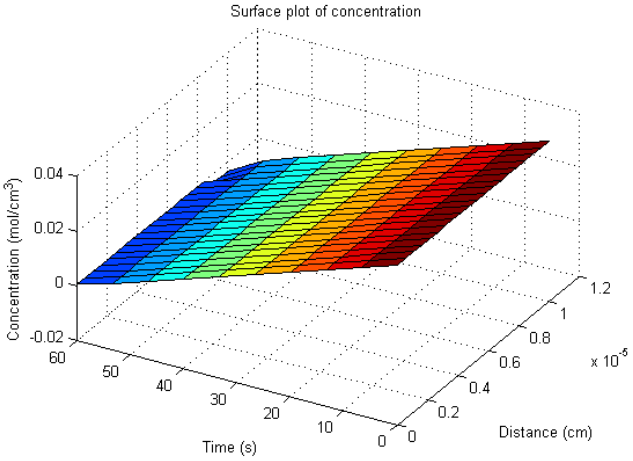
	0.15 µm	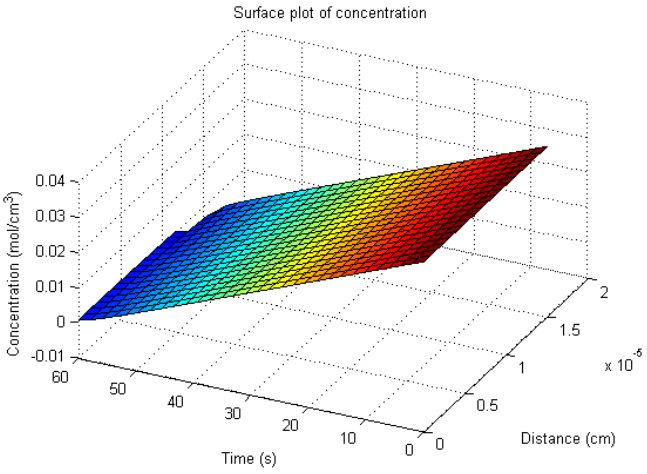

Table 4.1: *Continued*

(B)	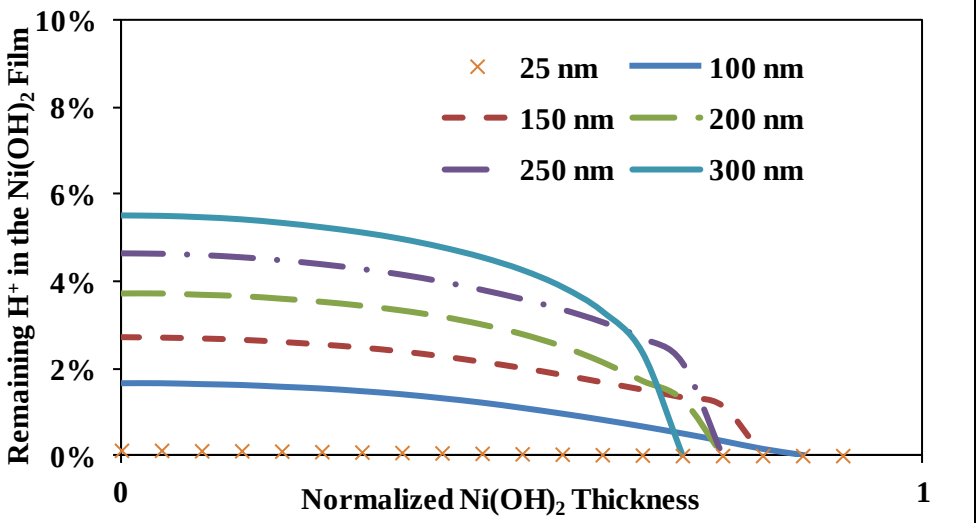

The x, y, and z axes in the figures given in Table 4.1.A refer to the distance, time, and H^+ concentration, respectively. The profile at the zero distance indicates the concentration of H^+ at the current collector-active material interface, where, at any given time after the start-up of the charging process, the highest H^+ concentration is observed. In the ideal case, a uniform H^+ distribution would be expected across the thickness of the active material, similar to the profile that is observed at the time zero (dark red line).

For an active material thickness of 0.15 µm, a significant gradient was observed at the 60th second (blue line) where the concentration of the H^+ drops slightly below zero at the electrode-electrolyte interface, and remains slightly above zero at the electrode-current collector interface, indicating that some of the H^+ ions were not able to be transported to the electrolyte. Hence, the thickness of the active material must be below 0.15 µm in order to completely charge the electrode in 60 seconds. When the thickness was set to 0.1 µm, a very small gradient can be observed in a small portion of the electrode located in the close proximity of the electrolyte. At a thickness of 0.05 µm, a completely flat line with zero concentration of H^+ ions is observed at the 60th second of the charging time, suggesting that the maximum active material thickness to enable

complete charging in 60 seconds should lie between 0.05 and 0.1 μm. For purposes of the diffusion-limited model study described in the next section, the ideal thickness of the active material was rounded to 0.1 μm.

To help visualize the gradient formation at the end of the charging process (i.e., 60^{th} second), concentration gradients formed across the $Ni(OH)_2$ films with various thicknesses ranging from 0.1 to 0.3 μm are drawn as shown in the figure in Table 4.1.B. It can be seen that as the thickness of the $Ni(OH)_2$ film increases, fewer H^+ ions are able to be transferred to the electrolyte, resulting in the formation of significant concentration gradients.

4.2.2 Diffusion-Limited Model to Determine the Optimum Inter-Layer Spacing

A second model was developed to determine the optimum inter-layer spacing between the layers. The model involves a two-dimensional (2D) analysis of the OH^- ion distribution across the electrolyte located between two adjacent layers of the multilayer electrode (Schematically illustrated in Figure 4.2, showing both top view and side view of the electrode). The distance between the etching holes in the top view corresponds to the width L of the channel in the side view. This width is determined by the mask design used during the lithography process, and its flexibility is rather limited due to fabrication-related constraints of the photoresist mold. Having etching holes too close to each other (i.e., a small L), for example, requires a dense packing of the photoresist pillars, which renders the fabrication process more difficult, as discussed in Chapter 2.2.3. Therefore, a width of 300 μm was selected for the initial modeling of optimum spacing between the layers, as this was the smallest dimension achievable using the current fabrication technology developed in this project.

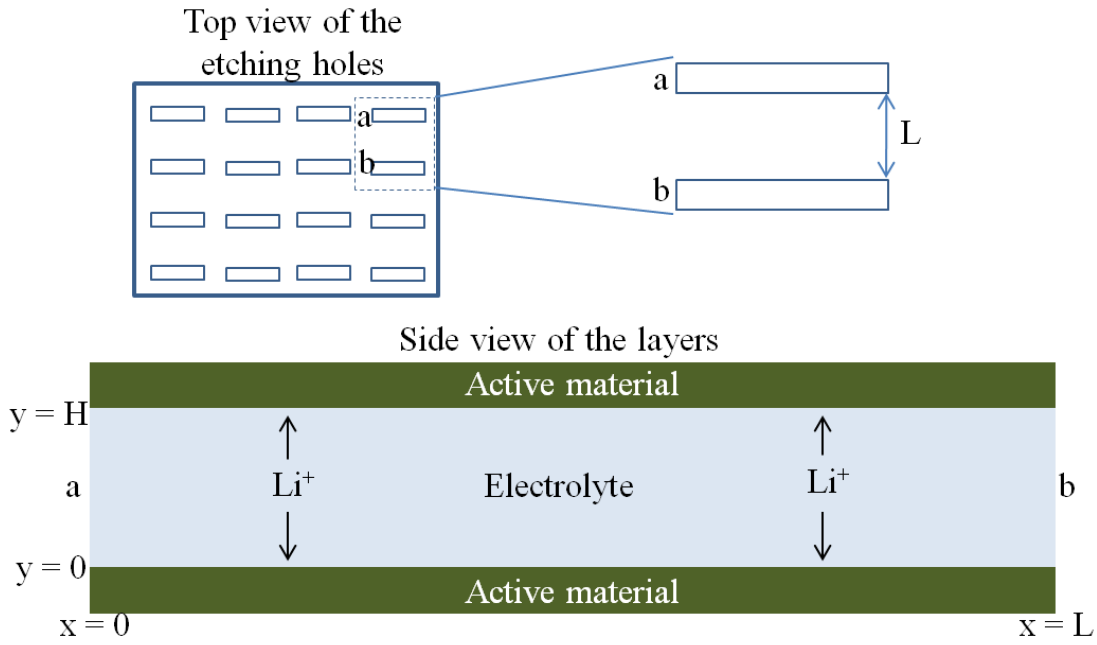

Figure 4.2: Model of the KOH electrolyte between two adjacent layers of the multilayer electrode

For a given size (150 μm x 600 μm) of the etching holes (i.e., the photoresist pillar size), as the width L becomes smaller, the number of the etching holes on each layer increases, which increases the speed required for etching the sacrificial Cu layers. The downside, however, is that the surface area of each layer is also reduced with increased number of etching holes, which adversely affects the capacity of the electrode. Increasing L, on the other hand, reduces the number of etching holes, and yields layers with higher surface area; yet, it results in longer diffusion path lengths for the liquid-state ions (i.e. OH^-), which is detrimental to the power density. To compensate for the power loss, a larger spacing (H) is required between the Ni layers. The height H of the channel between the Ni layers is solely determined by the electroplating conditions and thus, has much greater flexibility. By adjusting the thickness of the sacrificial Cu layers, the H dimension can be easily tailored. The focus of the model will be on determining the optimum height of these channels for a given width.

The assumptions made for the previous 1D model, including diffusion-limited transport and uniform distribution of ion fluxes at the electrode surface, also hold for this 2D model of the channel. Additionally, it was also assumed that the OH^- ion concentration within the etching holes is the same as the bulk electrolyte outside the electrode during the operation of the electrode. Also, the diffusion coefficient is assumed to be constant throughout the charge and discharge processes.

The equation of continuity for two spatial dimensions can be written as:

$$\frac{C_{OH^-}}{\partial t} = D \cdot \left(\frac{\partial^2 C_{OH^-}}{\partial x^2} + \frac{\partial^2 C_{OH^-}}{\partial y^2}\right) \tag{4.8}$$

An aqueous electrolyte of potassium hydroxide (KOH) with a concentration of 6 M was chosen for the characterization of the $Ni(OH)_2$ electrode. The diffusion coefficient for that given concentration at 25 °C has been reported to be in the order of 10^{-5} cm^2 s^{-1}[11]. This value is several orders of magnitude higher than the diffusion coefficient reported for the $Ni(OH)_2$ in the previous section, suggesting a faster mass transfer in the liquid phase. The boundary conditions for the 2D model of the channel are given as:

at t = 0: $$C_{OH^-} = C_{OH^-,b} \tag{4.9}$$

at x = 0: $$C_{OH^-} = C_{OH^-,b} \tag{4.10}$$

at x = L: $$C_{OH^-} = C_{OH^-,b} \tag{4.11}$$

at y = 0: $$D \cdot \frac{\partial C_{OH^-}}{\partial y} = \frac{i}{n \cdot F} \tag{4.12}$$

at y = H: $$D \cdot \frac{\partial C_{OH^-}}{\partial y} = \frac{i}{n \cdot F} \tag{4.13}$$

where $C_{OH^-,b}$ is the concentration of the bulk electrolyte (6 M). During the charging process, the OH^- ions inside the channel diffuse towards the active material in y direction as shown in Figure 4.2, and react with $Ni(OH)_2$ to form H_2O molecules as given in Equation 4.1. The depleted OH^- ions are replenished by the OH^- ions diffusing into channel from the bulk electrolyte in x direction. The goal of this model was to find the minimum height of the channel that allows the replenishment of the OH^- ions consumed during the lithiation process of the active material at high rates (e.g., 60 C). Minimizing the channel height is important as this will reduce the overall thickness of the structure, and enable deposition of more layers, yielding electrodes with higher capacities for a given volume.

Equation 4.8 was solved by utilizing Matlab's PDE toolbox. The resultant concentration profiles of the OH^- ions within the channel, both in 3D and 2D, are plotted as shown in Table 4.2. In the 3D profiles, the x, y, and z axes refer to the width of the channel, height of the channel, and concentration of the OH^- ions within the channel, respectively.

To help visualize the concentration distribution across the width of the channel more easily, 2D profiles are also provided in Table 4.2.B. The plotted profiles were obtained at the end of the charging process (i.e., at the 60^{th} second). When performing the simulations, the same strategy used in the 1D modeling of the active material was followed, where the channel height was first set to 0.1 μm, and then systematically increased by 0.05 μm. As expected, the lowest concentration was observed in the center region of the channel (i.e., x = L/2). For channel heights smaller than 0.25 μm, the concentration of the OH^- ions in the center region was found to be below zero, indicating that the ions were not able to be replenished by the lateral diffusion from the bulk electrolyte.

Table 4.2: Concentration profiles of the OH^- ions in the electrolyte located inside the channels with a width of 300 µm: (A) 3D profiles, (B) 2D profiles at the 60th second

	Channel Height	Concentration Profile (3D)
(A)	**0.20 µm**	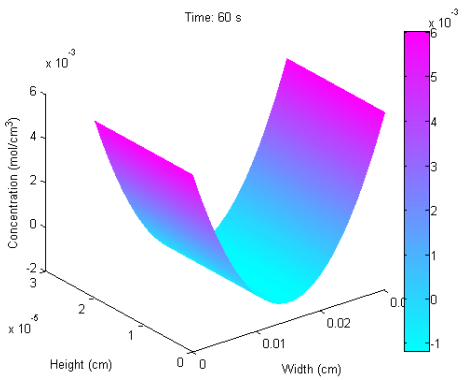
	0.25 µm	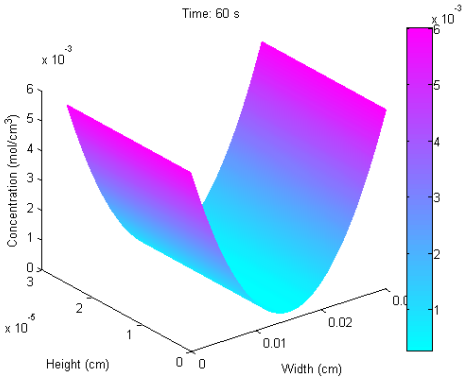
(B)		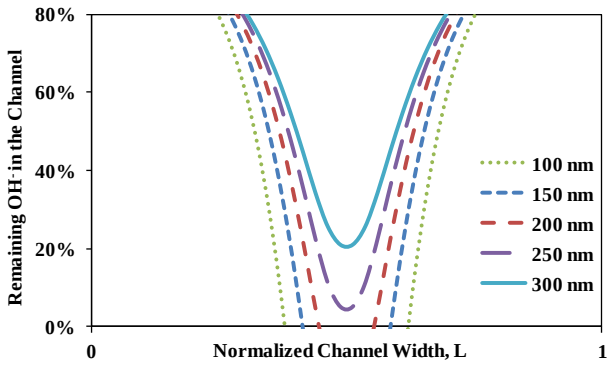

To determine the impact of the channel width on the optimum spacing, the modeling was repeated for widths ranging from 300 µm to 1 mm. The results are shown

in Table 4.3. The second column in Table 4.3 shows the corresponding inter-layer spacing obtained from the models for a given width. In the third column, the total number of the etching holes on a single layer with a footprint of 1 cm^2 was calculated using the aforementioned dimensions (i.e., 150 µm x 600 µm) of the etching holes and the distance (i.e., the width L) between the etching holes. This number was then used to estimate the available surface area on each layer, as listed in the fourth column. In the extreme case of zero etching holes, the area per layer would be 2 cm^2. As expected, increasing the width between the etching holes results in a reduced number of holes, and thus, in a larger surface area per layer. The number of layers given in the fifth column was calculated by using the information from the second column, the minimum individual Ni layer thickness (i.e., 1.5 µm), the maximum active material thickness found in the previous section (i.e., 0.1 µm), and the total thickness of the electrode (i.e., 300 µm). The last column shows the theoretical capacity of the electrodes estimated by using the information in the previous columns.

Table 4.3: Modeling results for various channel dimensions

Width, L (µm)	**Height, H (µm)**	**Number of etching holes per layer**	**Net area per layer (cm^2)**	**Number of layers**	**Areal capacity ($mAh\ cm^{-2}$)**
200	0.11	280	1.50	165	2.54
300	0.25	220	1.60	153	2.53
400	0.41	180	1.68	142	2.45
500	0.60	150	1.73	130	2.32
600	0.80	130	1.77	120	2.18
700	0.90	110	1.80	115	2.13
1000	1.13	80	1.86	106	2.03

It can be seen from Table 4.3 that although increasing the width L of the channels results in layers with higher surface area, and hence, higher capacities per layer, the total capacity of the electrode decreases. This is because the spacing between the layers needs to be increased to compensate for the increased diffusion path lengths for the OH^- ions in

the channels, which eventually leads to reduced number of depositable layers for a given total thickness (i.e., 300 μm). Increasing the width is also not favorable from the fabrication point of view, as it will prolong the fabrication duration due to the significantly increased etching times. Reducing the width from 300 μm to 200 μm, on the other hand, does not cause any significant improvement in the areal capacity of the electrode. This is also graphically shown in Figure 4.3, where the capacity is plotted as a function of the distance between the etching holes. As a result of these calculations and processing constraints, widths less than 300 μm were not fabricated in this study.

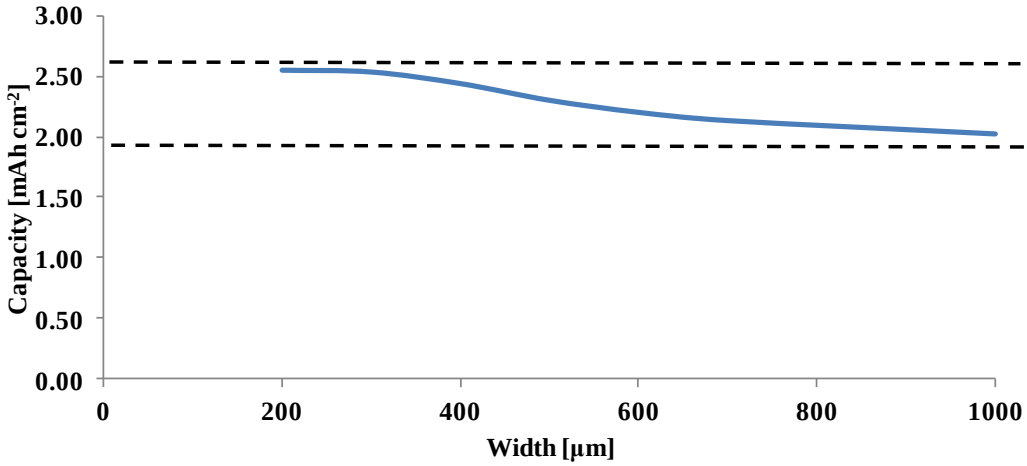

Figure 4.3: Capacity as a function of the distance between the etching holes (L) for a multilayer electrode with a total thickness of 300 μm, Ni layer thickness of 1.5 μm, and active material film thickness of 0.1 μm

In summary, according to the simulation results of the H^+ diffusion within the active material and the OH^- diffusion inside the inter-layer channels given in their respective Tables 4.1 and 4.2., the optimum multilayer electrode that can be completely charged in 1 minute should possess a maximum active material thickness of 0.1 μm on each layer, and the spacing between two adjacent active material films should be set to at least 0.25 μm, for a channel width of 300 μm. This also necessitates that the minimum thickness of the sacrificial Cu layers during the multilayer electroplating step should be

set to 0.45 μm (0.25 μm + (2 x 0.1 μm)). Although multilayer Ni backbones with even less than 0.45 μm inter-layer spacing can easily be fabricated by controlling the thickness of the Cu deposits, such small spacing values would render the conformal deposition of the active material much more complicated, as will be discussed in section 4.4. Therefore, to ensure the conformal deposition of the active material on each layer, electrodes with larger inter-layer spacing had to be fabricated.

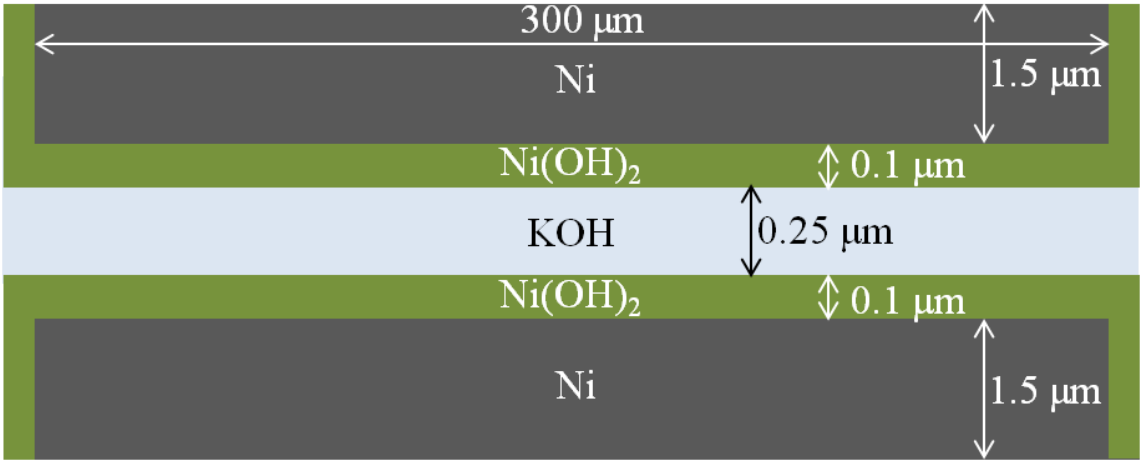

Figure 4.4: Optimum dimensions for the $Ni(OH)_2$ film thickness and the inter-layer spacing for a channel with a width of 300 μm

In addition, the thickness of the Ni layers serving as the current collector was set as 1.5 μm because of the fabrication constraints. Although much thinner Ni layers are theoretically able to deliver required amounts of currents to the active material, it was found that handling Ni layers with thicknesses less than 1 μm was quite problematic due to the deformations taking place during the fabrication process, in particular during the removal of the Cu layers. Based on the modeling results, a multilayer electrode fabricated under the conditions shown in Figure 4.4 has a theoretical capacity of 2.53 mAh which can be charged in 1 minute with a negligible forfeit in its capacity.

4.3 Fabrication of the Multilayer Current Collector

As described in Chapter 2.1, the electrodes fabricated for the $Ni(OH)_2$ electrodes are based on the anchor-supported lateral high-aspect-ratio structures. Depending on the number of layers which is, based on the data provided in Table 4.3, the main determinant of the capacity, the fabricated structures can be grouped into two categories: low-capacity applications and high-capacity applications. Electrodes which belong to the group of low-capacity applications are defined as having a total thickness of less than or equal to ~100 μm, which corresponds to multilayer structures with no more than 50 layers. Two different photoresists are used to produce molds with the appropriate thicknesses: NR21 for low-capacity applications and AZ 125 nXT for high-capacity applications.

In theory, the latter photoresist can be used for the low-capacity applications as well. However, as mentioned briefly in Chapter 2.2 and will be covered more thoroughly in this chapter, the fabrication process for AZ 125 nXT is complicated and requires extensive optimization studies for different thickness values. In contrast, NR21 has a well established recipe for a wide range of thickness values and its processing duration is much shorter than that of the AZ photoresist.

The multilayer electrodes to be utilized in secondary battery systems are based on anchor supported structures (see Chapter 2.1). Hence, the sacrificial Cu layers are completely etched following the deposition of the Ni anchors. This fabrication process differs from what was reported for Zn-air batteries in Chapter 3, where only partial removal of the sacrificial layers were performed and thus, no anchors were required. The partial etching process is not suitable for these larger scale structures, since the etching advancement occurs in a non-uniform fashion as the etching depth increases. Therefore, the use of the partial etching approach was limited to structures with relatively small footprints (e.g., 2-3 mm^2). Using the anchored structures, the footprint could be increased to 1 cm^2 and therefore, the number of laminations required to reach the higher energy capacities could be reduced significantly.

4.3.1 Fabrication of the Low-Capacity Current Collectors

In addition to the mask patterns used for the Zn electrodes in Chapter 3.2.2, alternative geometries were also adapted by incorporating different mask patterns for the lithography step, as shown in Figure 4.5. The primary reason for switching to alternative architectures was to reduce the total duration of the fabrication process by minimizing the etching duration which can take up to more than 10 hours with the conventional geometries shown in Figure 4.5.C. Structures with the patterns shown in Figure 4.5.A and Figure 4.5.B, however, are much easier to etch due to the ease of access of the etchant.

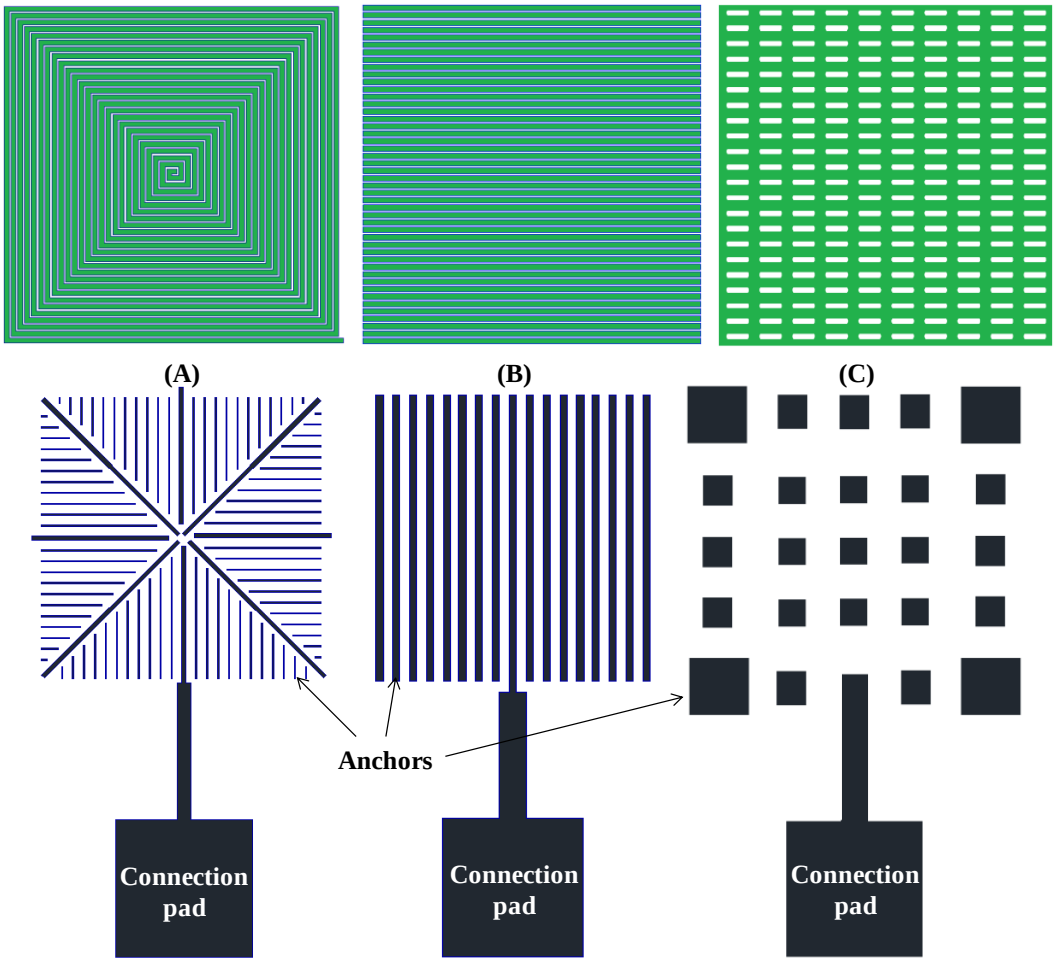

Figure 4.5: Patterns of the multilayer structures (top row) and their corresponding anchors (bottom row): (A) rectangular spiral, (B) parallel lines, and (C) conventional mesh

The fabrication process for a 50-μm-thick NR-21 mold was described in detail in Chapter 3.2.2. For this application, the recipe was slightly modified to achieve a thickness of 100 μm. Ti/Cu/Ti seed layers (500 nm/2000 nm/500 nm) were sputter deposited onto a glass or Si substrate. Next, the substrate was spin-coated with NR-21 at 1200 rpm for 10 seconds, resulting in an approximate thickness of 100 μm. A pre-exposure bake was performed on a hotplate at 80 and 150 °C for 10 and 5 minutes, respectively. Following the 20-minute-long cool-down process, hard-contact UV exposure was performed through a glass mask with Cr patterns. A total energy of 5000 mJ was applied by UV with a wavelength of 365 nm. Upon completion of the UV lithography, the post-exposure bake on a hotplate at 80 °C was carried out for 10 minutes. The sample was allowed to cool down to room temperature, which took approximately 20 minutes. Then, the same procedure was followed as described in Chapter 3.2.2 until the aftermath of the photoresist removal step.

Following the preparation of the multilayer electrodes and the removal of the first photoresist mold, the sample underwent another photoresist development process for the electroplating of the Ni anchors. Immediately before the photoresist deposition step, the sample was immersed in the selective Cu etchant for 2 minutes to enable a slight etching of Cu layers to a depth of approximately 2 μm. In this way, the anchor, which is electroplated in the subsequent step, provides better mechanical support by buttressing the Ni layers both vertically and laterally.

The same photoresist (i.e., NR-21) was utilized to build the mold for the anchors. NR-21 was deposited onto the substrate to completely coat all of the multilayer structures on the substrate. The sample was then placed on a flat surface and allowed to rest for 10 minutes to ensure that the photoresist dispersed evenly into the empty spaces within the multilayer structure. The air bubbles trapped inside the photoresist were collected with a plastic pipette. Next, a spin-coating process was carried out at a speed of 1200 rpm for 10 seconds. Following the spinning step, the sample was again allowed to rest for another 10

minutes to minimize the edge effects both on the outer perimeter of the substrate and on the edges of the multilayer structures. After the resting was completed, the photoresist underwent the same soft-bake, lithography, hard-bake, development, and descumming steps as in the case of first mold.

Upon completion of the deposition of the second mold, the sample was immersed in diluted hydrofluoric acid solution (H_2O:HF = 50:1) to remove the topmost Ti layer in the exposed regions of the substrate. Following the removal of the Ti layer, the sample was thoroughly rinsed in DI water. The sample was quickly immersed in the Ni plating bath to perform the electrodeposition of the anchors. The current density was set to 10 mA cm^{-2}, and the solution was gently stirred throughout the electrodeposition process. Anchors (approximately 20 μm thick) were electroplated onto specific regions of the sidewalls of the multilayer structures. These anchors not only maintained an electrical connection between individual Ni layers, but also provided a mechanical support to prevent the Ni layers from collapsing following the complete etching of the sacrificial Cu layers. Upon completion of the anchor electrodeposition, the second mold was removed by acetone. After the entire mold was stripped, the sample was rinsed with methanol, isopropyl alcohol (IPA), and finally with DI water.

Before proceeding with the etching of the sacrificial Cu layers, the substrate was diced, and the samples were separated. Then, the samples were immersed in the selective Cu etchant, and a slow agitation was applied. The structures based on the conventional mesh pattern shown in Figure 4.5.C were allowed to etch for nearly 12 hours, whereas for the structures with rectangular-coil and parallel-line patterns, the etching time was reduced by half. Since the etchant had an infinite selectivity over Ni layers, keeping the structure in the etchant for prolonged durations did not harm the resulting multilayer Ni backbone. After 12 hours, the samples were taken out carefully and placed quickly in large amount of DI water to ensure the dissolution of the copper sulfate ($CuSO_4$) residues from the etchant which otherwise may clog the gaps between the Ni layers. In order to

minimize the effect of the capillary forces on the individual Ni layers which may cause the layers to deform, the samples were immersed in a series of liquids in the following order: DI water – IPA – methanol where each following liquid has lower capillary forces than its predecessor. As the last step, the samples were placed in the oven at 65 °C for 15 minutes. The SEM images of the resulting multilayer structures based on rectangular coil and parallel line after the drying step can be seen in Figure 4.6 and 4.7, respectively.

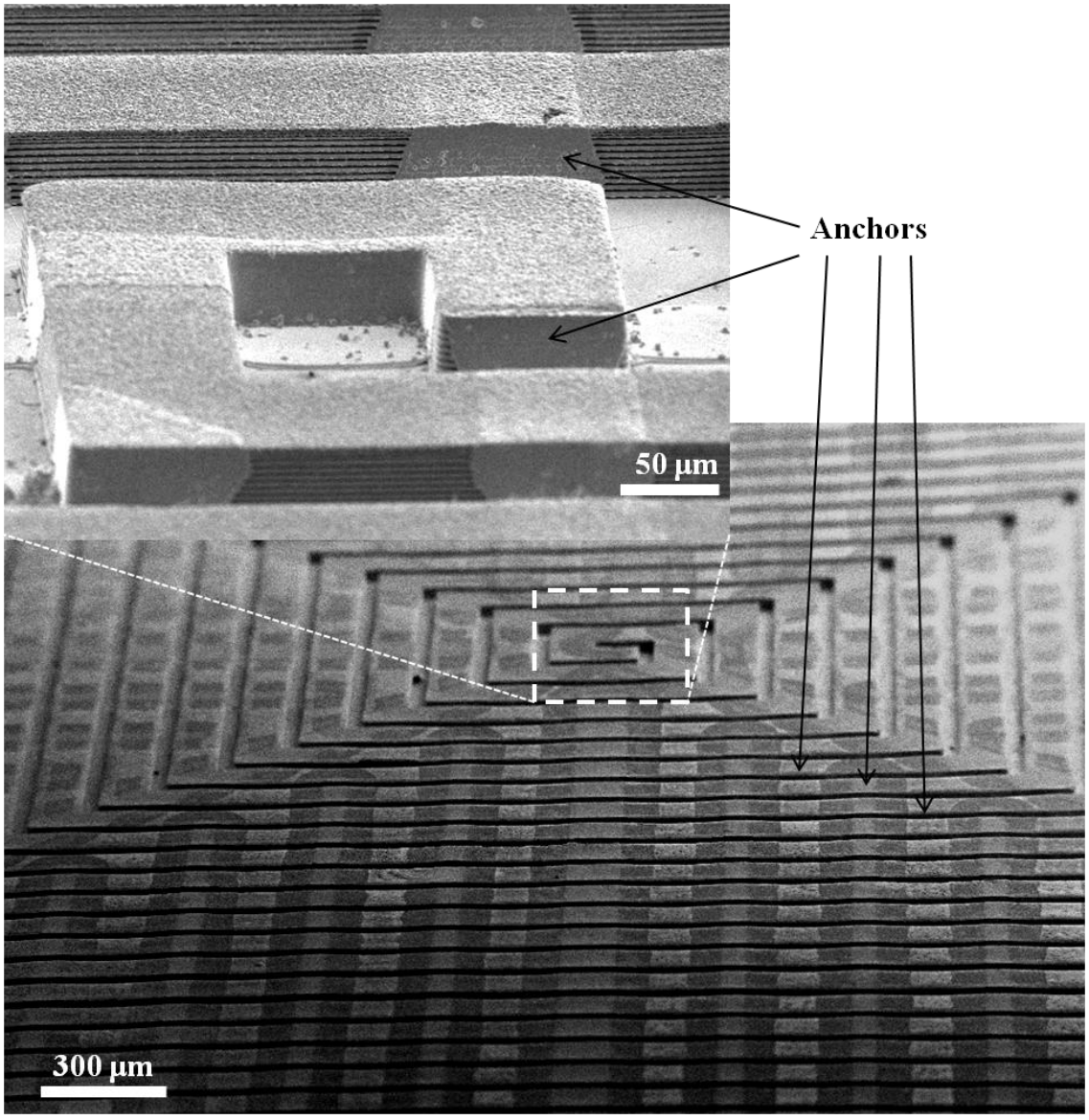

Figure 4.6: Anchor-supported multilayer Ni structure based on rectangular-spiral pattern following the selective etching of the Cu layers

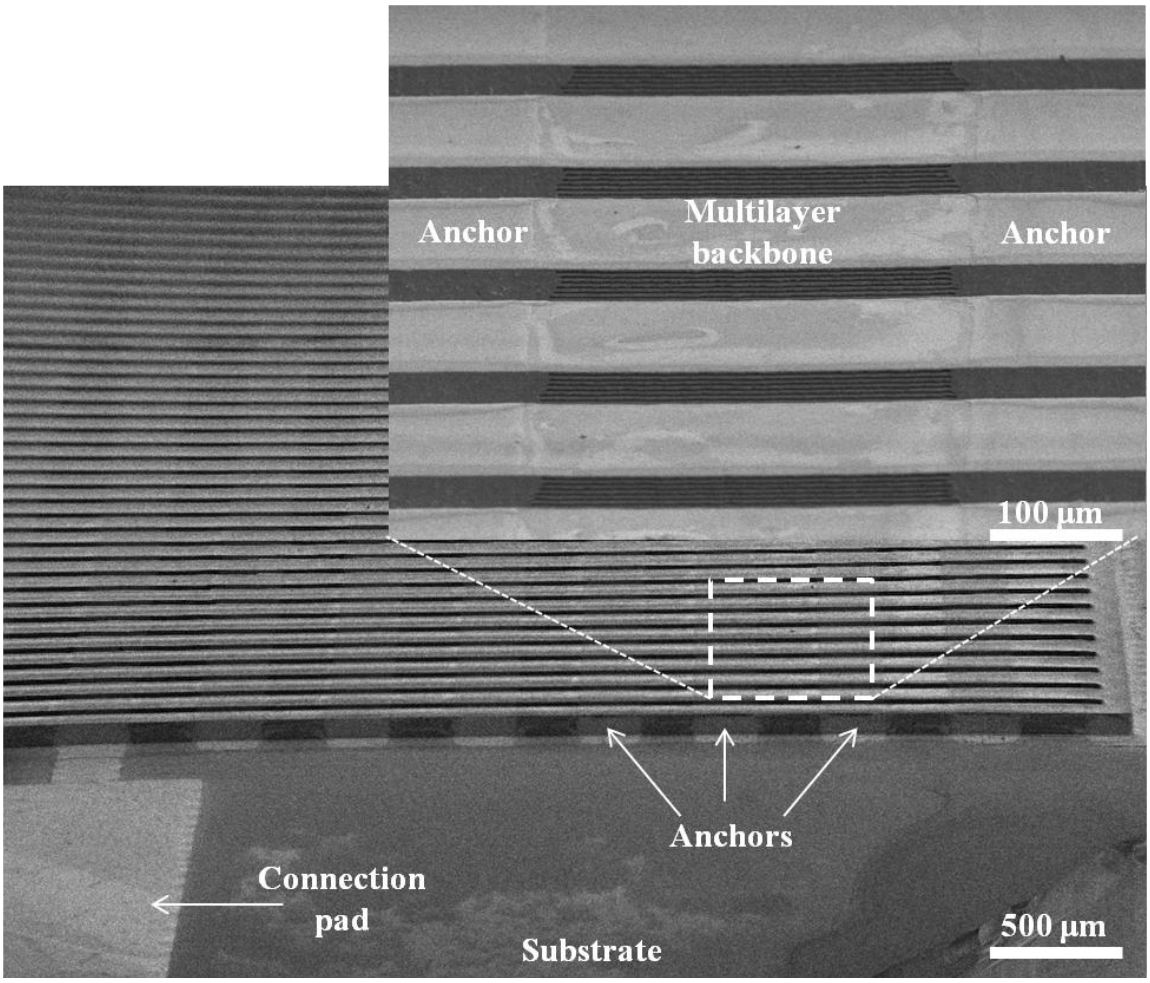

Figure 4.7: Anchor-supported multilayer Ni structure based on parallel-line pattern following the selective etching of the Cu layers

4.3.2 Fabrication of the High-Capacity Current Collectors

This section describes the development of processing conditions to use AZ 125 nXT photoresist as a mold for the fabrication of high-aspect-ratio multilayer structures. The same photoresist was also used for the fabrication of the electrodes to be utilized in Li-ion systems as will be covered in the next chapter.

There were a series of problems and limitations associated with the use of AZ 125 nXT as a mold, which were mentioned in Chapter 2.2.3. In addition, it was found to be quite problematic to build AZ molds using the mask patterns given in Figure 4.5.A and 4.5.B. As can be seen from the Figures 4.6 and 4.7, these specific patterns involve high

length-to-width ratios. These ratios were able to be sustained with relatively thin molds prepared by NR-21. However, when the mold thickness was substantially increased with the use of AZ, severe deformations in the form of bending and cracks were observed in the patterns following the photoresist development step. This was speculated to be originating from the internal stress that builds up in the thick molds during the development process.

Initially, AZ photoresist with an approximate thickness of 0.5 mm was carefully and uniformly poured onto the Ti/Cu/Ti (500 nm/2000 nm/ 00 nm) coated glass or Si substrate with the help of a plastic measuring syringe. This thickness was calculated by measuring the mass of the deposit and dividing it by the product of its density and the surface area of the substrate. Any air bubbles trapped within the photoresist were carefully removed with a pipette. After the removal of the relatively large bubbles, a very low spinning rate of 100 rpm was applied for 60 seconds to ensure uniformity of the photoresist on the substrate.

Following the spinning process, the substrate was allowed to rest on a flat surface for 15 minutes to minimize the edge effects. Next, the pre-exposure bake was performed. For this type of thickness, a long baking time is required. Also, for this specific photoresist, care should be taken when performing soft baking because the amount of the solvent in the resist plays a vital role. As described in Chapter 2.2.3, the weight percentage of the solvent should remain within a given range (12.5% - 25%), so that the photoresist will not be too soft to handle or impossible to develop properly. The amount of the remaining solvent was estimated by rapid measurements of the weight of the sample periodically during the soft-bake process. To minimize the temperature gradient within the photoresist, the sample was carefully covered with an aluminum dish. For a photoresist film with a final total thickness of 0.5 mm, the optimum baking time at 105 °C was found to be 12-13 hours. Prior to soft-baking, it is very important to make sure that the hot plate is level. Otherwise, even a slight incline causes the thick photoresist

layer to flow towards one of the edges of the substrate, causing non-uniform molds to form.

Once the soft baking was completed, the sample was allowed to cool down for 2 hours at room temperature. Then the film was UV exposed at 365 nm through a hard-contact mask. For these thick photoresist films, prolonged exposure times were required, which depend both on the feature size of the patterns and the thickness of the film. To ensure sufficient exposure, the total energy dose was set to 60 J cm^{-2}. Since the solvent is not completely evaporated during the pre-exposure bake process, the photoresist film remains relatively soft over the course of the UV exposure, which leads to the stiction of the film to the chrome mask.

To overcome this stiction issue, a protective, transparent thin-film (low-density polyethylene (LDPE)) was placed between the photoresist and the chrome mask. Although an ultra-thin (12.5 μm) LDPE film with a high transparency was utilized, the plastic film was determined to absorb significant amount of UV light. A 10% decrease in power resulting from this absorption was measured, which is approximately the same loss caused by the glass mask that is nearly 100 times thicker than the plastic film. The power losses originating from both the mask and the plastic film were taken into account when calculating the required time to deliver the necessary amount of energy to the photoresist.

Upon completion of the exposure, the plastic film was carefully removed from the substrate and the sample was allowed to cool down for approximately 30 minutes at room temperature. Thereafter, the photoresist was developed in a tetramethylammonium hydroxide (TMAH)-based developer (AZ 300 MIF, AZ Electronic Materials) for 45 minutes. During the development process, the sample was placed upside down so that the unexposed part could sink to the bottom of the container after dissolution, since the products of the development reaction have a higher density than the developer. For structures that did not possess delicate features, the development time reduced in half via introducing ultrasonic agitation. However, this sonication process was found to be quite

destructive for both high-aspect-ratio rectangular and cylindrical pillars of AZ. Following the development process, the sample was thoroughly rinsed in DI water and then dried. Care should be taken when performing the drying process as the structure exhibits high-aspect-ratio features that can easily be destroyed.

The photoresist mold was then treated with reactive-ion etching (RIE) O_2 plasma (Plasma-Therm). This step increases the hydrophilicity of the photoresist and thus, enables an enhanced wettability of the surface, which has been observed to significantly improve the electroplating quality. In particular for applications that involve ultra-thick photoresist molds, the diffusion of the aqueous electroplating solution may be a limiting factor for the deposit quality. The O_2 flow rate in the plasma tool was set to 60 sccm under a chamber pressure of 200 mTorr. The plasma was applied for 1 minute at a power of 200 W. Following the plasma, the sample was allowed to rest in the chamber for 15 minutes in order to cool down to room temperature. When exposed to air immediately after the plasma, cracks were observed to form within the photoresist film which would eventually lead to delamination of the mold during the electroplating process.

The electroplating process was performed to deposit desired number of layers. An all-sulfate plating bath and a commercial plating bath were utilized for the electroplating of Ni and Cu layers, respectively. The details pertaining to the operation of the robot, as well as the electroplating setup and composition of the baths and can be found in Chapter 2.1.

Upon completion of the robotically-assisted electroplating process, the photoresist mold was stripped from the substrate. By suspending the sample in acetone with top side facing down and slightly elevated from the bottom, the bulk photoresist surrounding the multilayer structures could easily detach from the substrate and sink to the bottom of the container. The pillars, however, which served as the mold for the formation of the etching holes, could not be removed as easily. The photoresist pillars were observed to swell in

the acetone. Therefore, it is speculated that the compressive force applied by the surrounding metal structures prevented the removal of the pillars.

According to the method suggested in Chapter 2.2.3 to alleviate this issue, the sample was immersed in a dimethyl sulfoxide (DMSO) solution at 80 °C for 30 minutes. This process enabled the partial dissolution of the photoresist film, softening the pillars. This was followed by a sequence of ultrasonication processes of the sample in acetone for 10 minutes, in methanol-IPA mixture for 5 minutes, and finally in DI water for another 5 minutes. As in the case of the initial acetone treatment for the bulk film, the sample was suspended in these solutions with its top surface facing down. At the end of this treatment, the vast majority of the photoresist pillars on the substrate were removed.

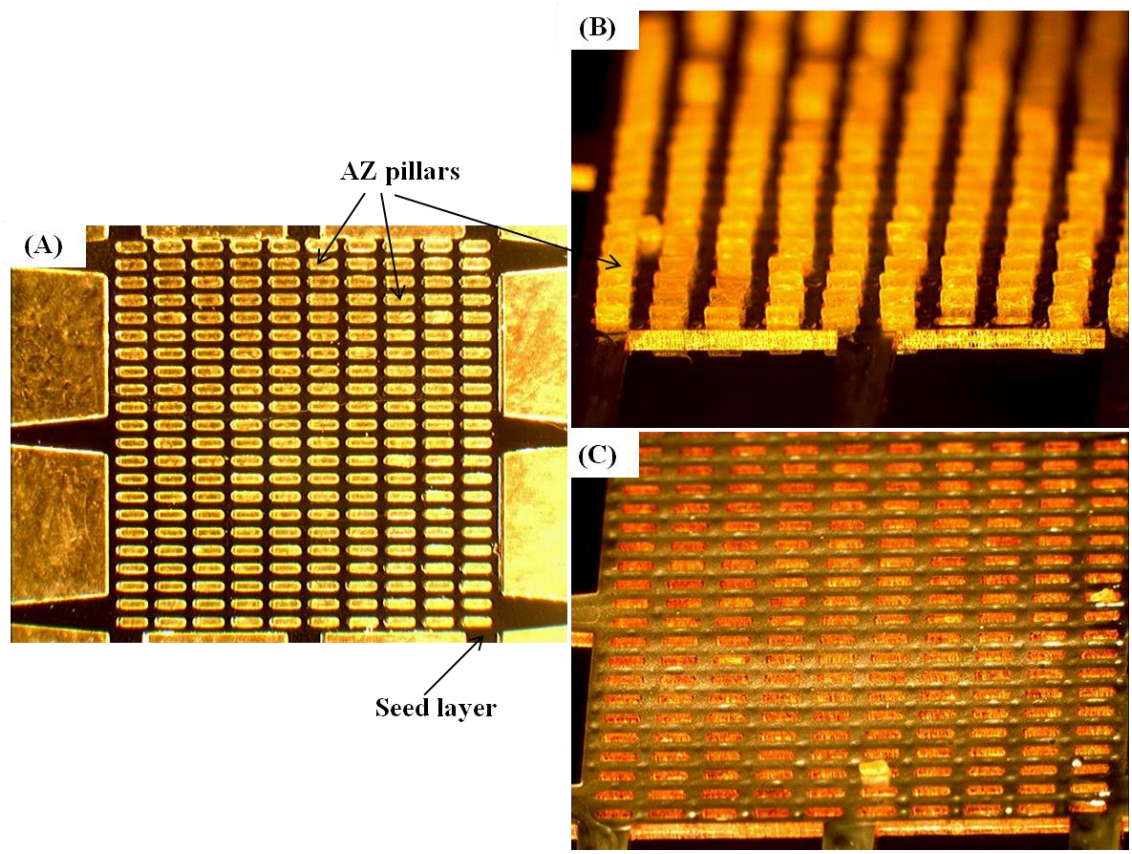

Figure 4.8: AZ 125 nXT mold for thick multilayer structures: (A) top view of the mold before the sequential electrodeposition, (B) after the formation of the multilayer structure, and (C) following the removal of the photoresist

Figure 4.8 shows the optical images of the AZ, as well as the multilayer structure before and after the removal of the pillars. As can be seen in Figure 4.8.C, only a few pillars remained within the substrate which could either be removed manually by adhering a tape and then gently peeling it off or by performing the ultrasonic removal routine for a longer time period.

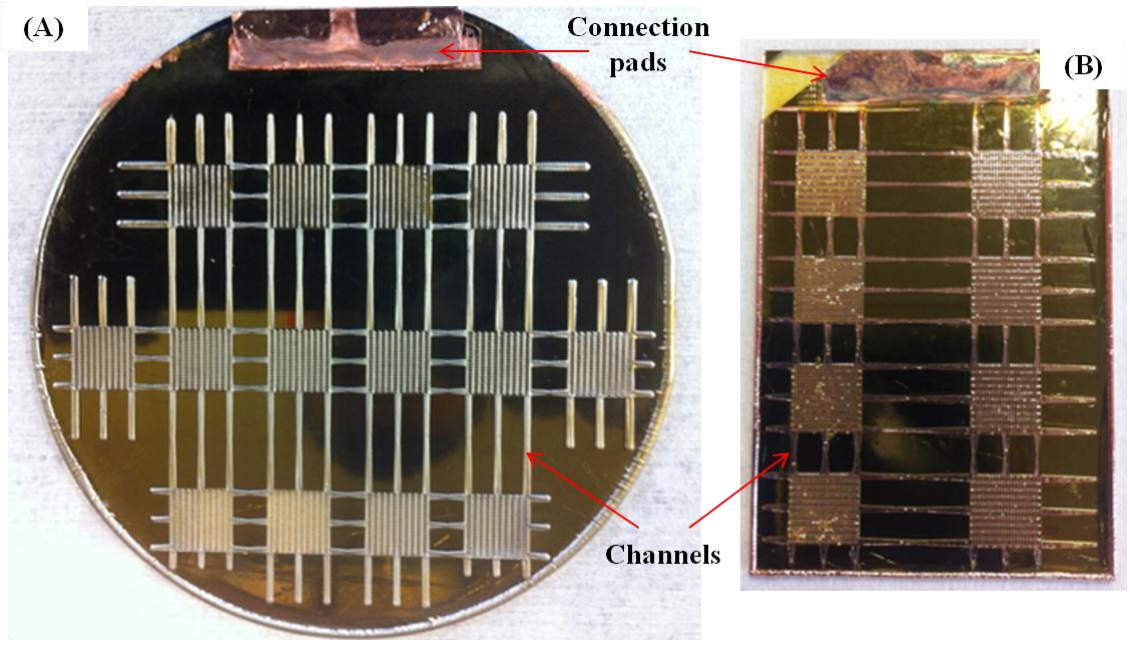

Figure 4.9: Substrates following the electrodeposition of the multilayer structures: (A) 4-inch wafer with 14 samples on it, and (B) 2x3 inch glass slides with 8 samples

The fabricated structures along with their substrates are shown in Figure 4.9. As mentioned in Chapter 2.1, the robotic plating setup is able to handle substrates as large as 4-inch wafers. The connection pads labeled in Figure 4.9 are the regions that stay outside the solution during the plating process, and provide electrical connection between the robotic arm and the substrate.

The lines connecting the samples to each other are called channels and their surface area was also taken into account when calculating the current density for plating. In earlier attempts, the samples were spread on the substrate in an isolated fashion where

they were surrounded by the photoresist mold only. It was observed that this kind of configuration results in poor wetting of some of the samples and thus, a non-uniform electroplating across the substrate. Having the channels formed between the samples, however, was found to enable a better fluid access to each sample. The length of the channels in these structures were not optimized. The optimization of the channel length would enable an increased packing density of the structures fabricated on the surface of the substrate.

Following the fabrication of the samples shown in Figure 4.9, the electrodeposition of the Ni anchors was performed. The same procedure as in the case of low-capacity current collectors (see section 4.3.1) was carried out for the deposition of the anchors. The only modification was the duration of the UV exposure which was doubled for the high-capacity current collectors. Since these structures were much thicker (>300 μm) than the maximum achievable thickness of the photoresist mold (~100 μm), a vertical photoresist accumulation on the edges of these multilayer structures was observed which was at least two to three times thicker than the photoresist film dispensed on the lateral surface. Hence, longer exposure times were required for the sections of the photoresist located in the proximity of the edges. These edge effects can be clearly seen in Figure 4.10 showing the optical images of the mold prior to the electrodeposition of the anchors.

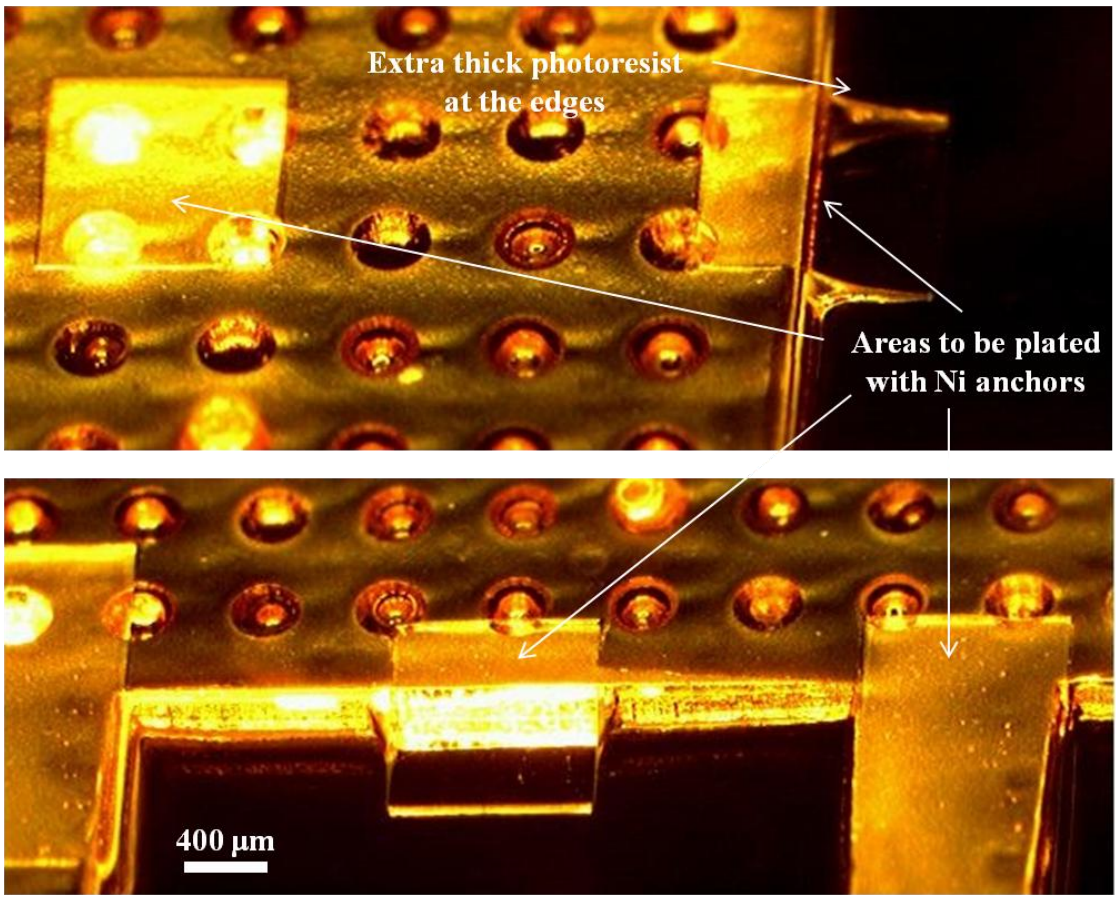

Figure 4.10: Optical images showing the thick multilayer structure with the NR-21 film deposited and patterned on it prior to the electrodeposition of the Ni anchors

After the electrodeposition of the anchors, the same procedure was followed as used in the case of low-capacity structures described in section 4.3.1. The anchor mold was removed, and the Cu layers were etched completely. It was noted that the sidewall profiles within the etching holes and on the outer perimeter of the multilayer structures electroplated through the AZ mold were not as clean as those obtained by plating through the NR-21 mold. It is postulated that this is due to the AZ mold being relatively softer than NR-21 because of its higher solvent content and because it undergoes much longer electroplating processes (>36 hours). Thus, it is possible that the plating solution seeps between the mold and the plated structure, forming microscale metal residues on the sidewalls. As it is shown in Figure 4.11.A, some of the gap openings between the layers

on the sidewalls of the etching holes are partially clogged following the complete removal of the Cu layers. To overcome this issue and render cleaner sidewall profiles, an additional electropolishing step was performed by applying anodic pulse currents (t_{on} = 1 s, t_{off} = 9 s, 10% duty cycle, 10 mA cm^{-2} current density) to the substrate in the Ni electroplating solution for approximately 30 minutes. As a result, the layers became smoother as shown in Figure 4.11.B.

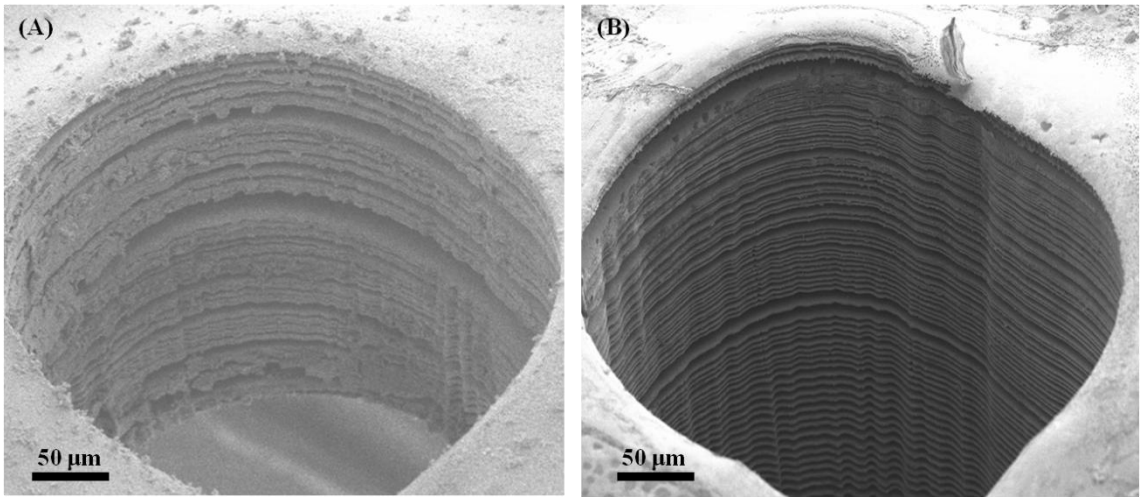

Figure 4.11: Etching holes of a multilayer structure electroplated through AZ mold: (A) immediately after Cu etching process and (B) after the anodization process

4.4 Synthesis of $Ni(OH)_2$

Following the fabrication process of the multilayer Ni structures that serve as current collectors for the battery electrodes, $Ni(OH)_2$ was deposited onto the multilayer structures. Several methods can be found in the literature for the deposition of $Ni(OH)_2$. These methods each have their own advantages and disadvantages. The primary selection criteria for this application were the ability to form a conformal film of the active material on the multilayer backbone structure and the capability to deliver as much capacity as possible at high charge and discharge rates.

The resistance that the protons encounter during the solid-state diffusion within the lattices has been reported to have a significant influence on the capacity of the $Ni(OH)_2$ electrode, especially at high charge and discharge rates [12]. This resistance is associated with the conductivity and the morphology, as well as the grain size of the $Ni(OH)_2$ films. Therefore, several studies have focused on altering these aspects in order to minimize the resistance and thus, increase the performance of the electrode [13-17].

To further address the issues pertaining to the delivery of the capacity at higher rate, nanoscale $Ni(OH)_2$ structures possessing various morphologies in the form of nanosheets, nanoribbons, nanotubes, and nanowires have been synthesized [18-25]. Although these structures have been demonstrated to retain improved specific capacitance, they are mainly in powder form, which renders their deposition onto the current collectors with relatively complex 3D architectures rather difficult.

To enhance the adhesion of the active material particles to the current collectors, materials with adhesive properties, such as conductive organic binders, need to be utilized. However, the inclusion of the organic binder compounds could result in poorer contact between the particles of the active material and the current collector, which negatively contributes to the internal resistance of the electrode, and thus, leads to a reduced performance. In addition, the presence of these organic additives adds to the total mass and the volume of the electrode yielding a decrease in its specific capacity and power. Moreover, when the current collector comprises meso- or even microporous materials, such as Ni nanofoams, it is possible for the applied active material particles to disseminate unevenly in the highly porous structure, clogging the outer pores and generating dead spaces within the structure resulting in inefficient utilization of the electrode surface area during the charge and discharge processes. In some cases, where the current collector lacks sufficient mechanical robustness, the application process of the active material particles might even cause irreversible damages to the structure.

Taking all of these aspects into account, the most suitable approach to combining the current collector with the active material is either through the electrodeposition of the active material onto the current collector or through the growth of the active material directly on the current collector. The latter approach can be investigated by using either electrochemical growth or the spontaneous growth of the active material. Gas-phase deposition, such as atomic layer deposition (ALD) and chemical vapor deposition (CVD), would also be a rather attractive approach for high-power applications, as they have proven quite successful in conformal deposition. However, this would require extra studies to develop the appropriate precursors, as well as the optimization of the deposition conditions. Also, utilization of techniques such as ALD and CVD substantially reduces the cost-effectiveness of the whole fabrication process.

4.4.1 Methods for Growing $Ni(OH)_2$ on the Backbone Structure

Electrochemical growth of the $Ni(OH)_2$ film involves direct anodic oxidation of Ni in alkaline solutions. This method, however, yields relatively thin $Ni(OH)_2$ films consisting of no more than two to three monolayers due to the self-limiting nature of the hydroxide layer growth [26-28]. This amount of active material is not sufficient for high-capacity energy storage applications.

To mitigate this limited-thickness issue, a method has been proposed that involves anodic galvanostatic charging of Ni in a pH 7.65 borate buffer solution producing a highly porous oxide film [29]. This relatively thick oxide layer was speculated to be composed of NiOOH film, and it was shown to be distinctly different from the NiO film that serves as a passivation layer. The thickness of this active material exceeded 100 nm, and when performance at room temperature was assessed, the amount of charge converted was 6 mC cm^{-2} after 14 hours of anodic charging at a current density of 80 μA cm^{-2}. For our multilayer Ni structure of 90 layers with a surface area of approximately 150 cm^2, the total amount of charge stored would be 900 mC, which corresponds to an

electrode capacity of 0.25 mAh. Although this approach provides a significant improvement in the amount of charge when compared to previous studies involving only several monolayers of $Ni(OH)_2$, the total capacity is obviously not attractive, considering the capacity goals in this study.

One other technique to grow relatively thick layers of $Ni(OH)_2$ involved high-frequency potential cycling conditions [30]. This was achieved by the application of periodic square-wave potentials at high frequencies exceeding 1 kHz. Nonetheless, the amount of the active material formed through this technique is still much less than can be obtained via electrodeposition. Hence, this technique was also omitted in this study.

More recently, another mechanism for $Ni(OH)_2$ growth, that comprises a template-free growth of $Ni(OH)_2$ nanosheets on Ni substrates in the absence of potentiometric conditions, has been proposed [12]. According to this method, a pretreated Ni sample is placed in an aqueous solution consisting of nickel nitrate $(Ni(NO)_3)_2$, ammonium nitrate (NH_4NO_3), and ammonium hydroxide (NH_4OH) at 90 °C for several hours, which yields a time-dependent growth of significant amounts of $Ni(OH)_2$ on the Ni sample. For example, for a 12-hour-long period, the amount of $Ni(OH)_2$ grown has been reported to be as high as 7 mg cm^{-2} [12].

A disadvantage associated with this method, however, is that the reaction rates are not well-defined, and therefore, having an exact control over the amount of the active material is not possible. Nonetheless, this technique was utilized in this study to fabricate electrodes with high energy densities, and the performance of the electrodes was compared to those obtained via electrodeposition.

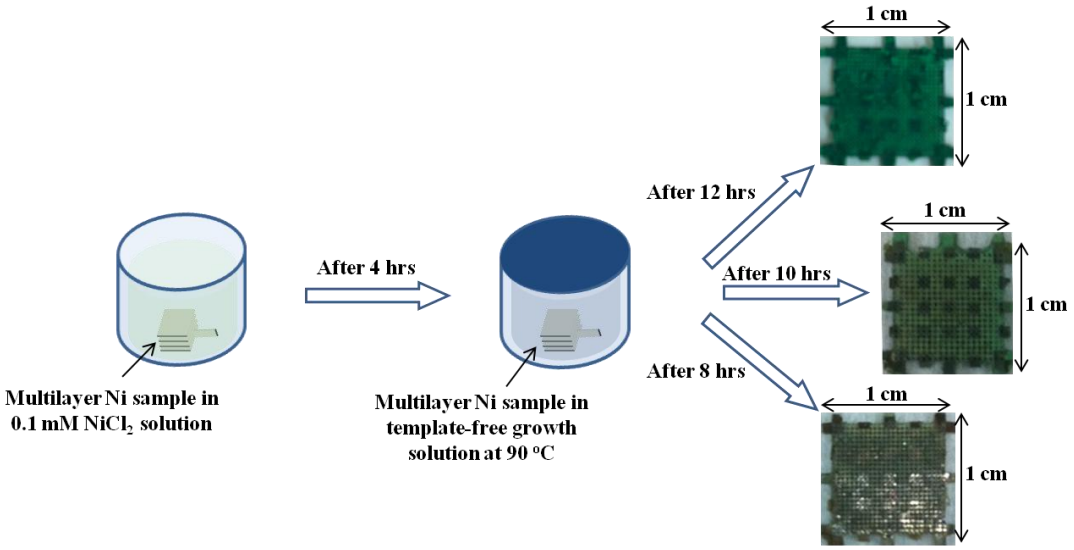

Figure 4.12: Process flow for the template-free growth of the $Ni(OH)_2$ nanosheets on the multilayer Ni structures and the optical images of the resulting electrodes following varying durations of growth

A schematic describing the fabrication sequence of the $Ni(OH)_2$ electrode through template-free growth technique is given in Figure 4.12. First, multilayer Ni samples, prepared by following the procedures described in section 4.2, were thoroughly cleaned with acetone, methanol, and IPA. After the cleaning step, the samples were pretreated by soaking them in 0.1 mM nickel chloride ($NiCl_2$) solution for 4 hours. Upon completion of the pretreatment step, the samples were rinsed in high-purity DI water and then immersed in the template-free growth solution at 90 °C which was prepared by dissolving 10 mmol $Ni(NO)_3$ and 6 mmol NH_4NO_3 in a mixture of DI water and ammonium hydroxide (30 wt%) with the respective volumes of 35 and 15 cm^3. Following various durations of immersions, the samples were removed, carefully rinsed in DI water, soaked briefly in IPA, and placed in the oven at 90 °C for another 2 hours. As shown in Figure 4.12, a clear difference can be seen in the color of the deposits where the intensity of the green color increases with increased duration of soaking, indicating an increasing amount of $Ni(OH)_2$.

For the characterization purposes, samples with a soaking duration of 10 hours were utilized. Eight hours of exposure to the template-free growth solution was insufficient to produce a conformal coating of the active material, according to the SEM images. However, under a 12-hour-long exposure, excess amounts of $Ni(OH)_2$ nanosheets were synthesized which caused some of the etching holes of the multilayer backbone to get partially or fully clogged. Also, the handling of these electrodes was quite problematic, as the excess active material was susceptible to flaking off the electrode when transferring from one solution to another. For these reasons, the focus of this study has been on electrodes featuring the $Ni(OH)_2$ nanosheets that were grown for 10 hours.

SEM images showing the Ni multilayer structures before and after the growth of $Ni(OH)_2$ nanosheets can be seen in Figure 4.13. In the first image of Figure 4.13, the etching hole of a 75-layer structure can be seen where the individual layers are clearly visible. Upon the growth of the nanosheets, however, the individual layers essentially disappeared due to the coverage of the active material. As shown in the second image of Figure 4.13, the 75-layer structure clustered into 5 to 6 layers after the growth of the nanosheets. This, obviously, means a significant decrease in the previously calculated surface area of the structure, which adversely affects the power performance of the electrode. For these reasons, electrodeposition techniques for the active material deposition were explored.

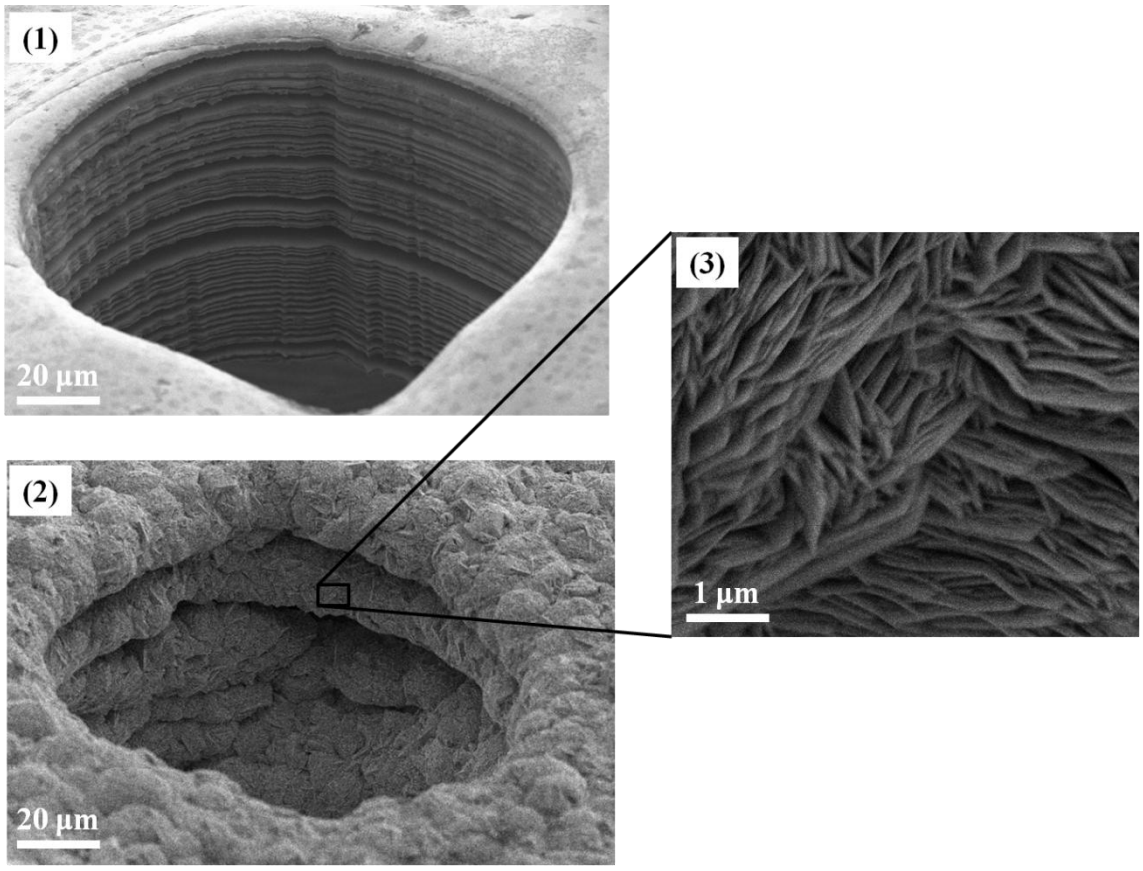

Figure 4.13: SEM images showing the multilayer Ni structure before and after the template-free growth of the $Ni(OH)_2$ for 10 hours: (1) Ni layers inside the etching hole, (2) Ni layers inside the etching hole covered with $Ni(OH)_2$ nanosheets, and (3) enlarged view of the grown nanosheets

4.4.2 Methods for Electrodepositing $Ni(OH)_2$ onto the Backbone Structure

Electrodeposition of the $Ni(OH)_2$ film can be investigated under two main categories: anodic and cathodic electrodeposition. Numerous studies have been reported on the use of both methods, most of which, along with the substrates and electrolytes used, are summarized in Table 4.4. While all of them proved to be successful in depositing a $Ni(OH)_2$ film that is substantially thicker than the electrochemically grown films, our focus has been on a particular cathodic deposition method studied by Streinz et al. [31, 32].

Table 4.4: Comparison of the electrodeposition methods for $Ni(OH)_2$/NiOOH

Working Electrode	Deposition Method	Electrolyte	Reference
Polycrystalline Pt sheet	Cathodic deposition, galvanostatically at 100 μA cm^{-2}, 23 ^oC	0.1 M $Ni(NO_3)_2$	[33]
Pt disk	Anodic deposition, CV between 0.3 and 1.1 V (vs. SCE) at 50 mv s^{-1}	0.13 M $NiSO_4.6H_2O$ 0.13 M NaOAc 0.1 M Na_2SO_4	[34]
Pt and graphite disk	Anodic deposition, CV between 0.3 and 1.1 V (vs. SCE) at 50 mv s^{-1}	0.5 M NaOAc 0.05 M $NiSO_4$	[35]
Fluorine-doped tin oxide (FTO)	Cathodic deposition, galvanostatically at 0.04 mA cm^{-2}	0.01 M $Ni(NO_3)_2$	[36]
Indium tin oxide (ITO)	Anodic deposition, galvanostatically at 300 μA cm^{-2}, 25 ^oC	0.005 M $NiSO_4$ 0.015 M $(NH_4)_2SO_4$	[37]
Ni and Au-plated foil	Cathodic deposition, galvanostatically at 8 mA cm^{-2}	0.1 M $Ni(NO_3)_2$	[38]
Au-sputtered quartz crystal	Cathodic deposition, galvanostatically at 0.01 to 1 mA cm^{-2}, 25 ^oC	0.2 M $Ni(NO_3)_2$ in 50/50 vol.% EtOH and H_2O	[31, 32]
Ni sinter plaques	Multiple current steps at 70 ^oC	1.8 M $Ni(NO_3)_2$ 0.18 M $Co(NO_3)_2$ in 50/50 vol.% EtOH and H_2O	[39]
Au foil	Cathodic deposition, galvanostatically at 5 mA cm^{-2}, 25 ^oC	1.8 M $Ni(NO_3)_2$ 0.075 M $NaNO_3$ in 50/50 vol.% EtOH and H_2O	[40]
Au and Pt plates	Cathodic deposition, potentiostatically at -0.5 to -0.8 V (vs. Ag/AgCl), 70 ^oC	0.02 M $Ni(NO_3)_2$ with surfactants	[24]
Pt foil and carbon paper	Cathodic deposition, galvanostatically at 4 mA cm^{-2}	0.1 M $Ni(NO_3)_2$	[41]
Stainless steel foils	Anodic deposition, galvanostatically at 0.05 mA cm^{-2}, 25 ^oC	0.13 M $NiSO_4$ 0.13 M NaOAc 0.1 M Na_2SO_4	[42]
Stainless steel foils	Anodic deposition, potentiostatically at 1.05 V (vs. Ag/AgCl), 25 ^oC	0.13 M $NiSO_4$ 0.13 M NaOAc 0.1 M Na_2SO_4	[43]

Two main reasons lie behind our choice of this particular method: (1) This method was shown to have a high Faradaic efficiency even at room temperature deposition, which is quite critical for the applications in this study as will be discussed in the following paragraphs; (2) the chemistry behind the electrodeposition process, as well as the kinetics as a function of temperature, $Ni(NO_3)_2$ concentration, ethanol (EtOH) content, and current density, are well-understood, and a formula has been developed that can accurately predict the mass of the electrodeposited $Ni(OH)_2$ film under certain conditions [31, 32].

Depending on the concentration of $Ni(NO_3)_2$, two different reaction mechanisms have been proposed for the electrodeposition of $Ni(OH)_2$ [31]. For low concentrations of nitrate ions (e.g., 0.1 M), the mechanism includes a reduction reaction, followed by the precipitation of $Ni(OH)_2$:

$$NO_3^- + 6H_2O + 8e^- \rightarrow NH_3 + 9OH^- \quad (4.14)$$

$$Ni^{2+} + 2OH^- \rightarrow Ni(OH)_2 \downarrow \quad (4.15)$$

In the case of high concentrations of nitrate ions (e.g., 2 M), a substantial decrease has been observed in the efficiency, which was attributed to the diffusion of the Ni complex away from the substrate before the deposition takes place [32]. In this case of high concentration, the active material has been reported to undergo a two-step reaction mechanism as follows:

$$4Ni^{2+} + 4OH^- \leftrightarrow Ni_4(OH)_4^{4+} \quad (4.16)$$

$$Ni_4(OH)_4^{4+} + 4OH^- \rightarrow 4Ni(OH)_2 \downarrow \quad (4.17)$$

Streinz et al. developed a formula to predict the mass of the electrodeposited active material as a function of current density and concentration:

$$\frac{dm}{dt} = \frac{9 \cdot i \cdot A \cdot M \cdot \varepsilon}{16 \cdot F} \quad (4.18)$$

where m is the mass of the deposit (g), i is the applied current density (A cm^{-2}), A is the surface area (cm^2), M is the molecular weight of $Ni(OH)_2$ (g mol^{-1}), F is the Faraday's constant (96485 C mol^{-1}), and ε is the efficiency of utilization of the electrochemically generated OH^- ions. The efficiency can be calculated by:

$$\varepsilon = \left[\left(\frac{0.321 - 0.015 \cdot (5 - i)}{C} - 0.065\right)^{-3.5} + 1\right]^{-\frac{1}{3.5}} \quad (4.19)$$

where C is the concentration of the $Ni(NO_3)_2$ solution (mol L^{-1}). Limitations have been reported regarding the use of Equations 4.18 and 4.19. For example, in order for these equations to predict the mass of the deposits accurately, the electrodeposition process should be carried out at room temperature and the solution needs to be composed of 50 v% EtOH [32].

It is important to be able to carry out the electrodeposition at room temperature since the $Ni(NO_3)_2$ solution contains significant amounts of EtOH which results in increased vapor pressure and thus, higher volatility of the solution. Depending on the structure to be coated with $Ni(OH)_2$, the electrodeposition process can take up to many hours to complete. If the process was carried out at elevated temperatures, which is the case for some of the processes listed in Table 4.4, a significant amount of solvent would easily evaporate and hence, the concentration would drastically change, which would eventually and substantially affect the deposition conditions.

Although the presence of EtOH adds complications to the processes involving long durations of operation by increasing the volatility of the solvent, it is beneficial as it increases the wettability of the solution. Increasing the wettability can be quite crucial, particularly for structures with relatively complex 3D architectures that require conformal

deposition, since it enables an improved contact between the solid electrode and liquid solution. Combined with the pulsed deposition, it supports the development of a conformal layer of active material on the 3D scaffold structure.

The experimental setup used for the cathodic electrodeposition of the $Ni(OH)_2$ is schematically illustrated in Figure 4.14. A two-electrode cell configuration was prepared where the multilayer Ni electrode and a platinum (Pt) sheet were utilized as working and counter electrodes, respectively. To introduce convective effects to the transport of the ions, the electrolyte solution was also gently stirred with the help of a magnetic stir bar.

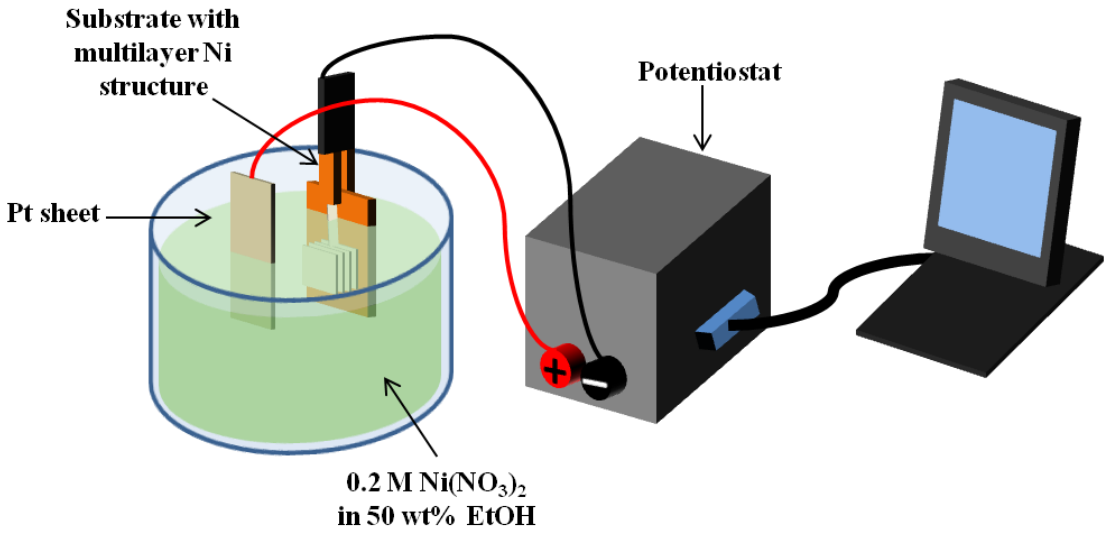

Figure 4.14: Schematic of the experimental setup illustrating the cathodic electrodeposition of $Ni(OH)_2$

As can be seen from Equation 4.19, the efficiency of the electrodeposition process is a function of the concentration of $Ni(NO_3)_2$. When the working electrode involves structures with relatively complicated 3D architectures as the ones reported herein, ion concentrations in the proximity of the electrode surface, particularly nearby the substrate, can be substantially reduced or even depleted when a current pulse is applied. Due to the long diffusion path lengths between the electrode surface and the bulk of the solution, the

local replenishment of the electrolyte in the proximity of the surface may not take place instantaneously. Hence, in these circumstances, pulse plating may be preferred over DC plating in order to allow the ions sufficient time to diffuse from the bulk of the solution after each pulse. To ensure conformal coating of the electrodes, $Ni(OH)_2$ was electrodeposited under pulse current conditions (t_{on} = 1 s, t_{off} = 9 s, 10% duty cycle) with the help of a potentiostat (PowerLab 2/20, ADInstruments). SEM images of the resultant structures with conformal coating of $Ni(OH)_2$ can be seen in Figure 4.15.

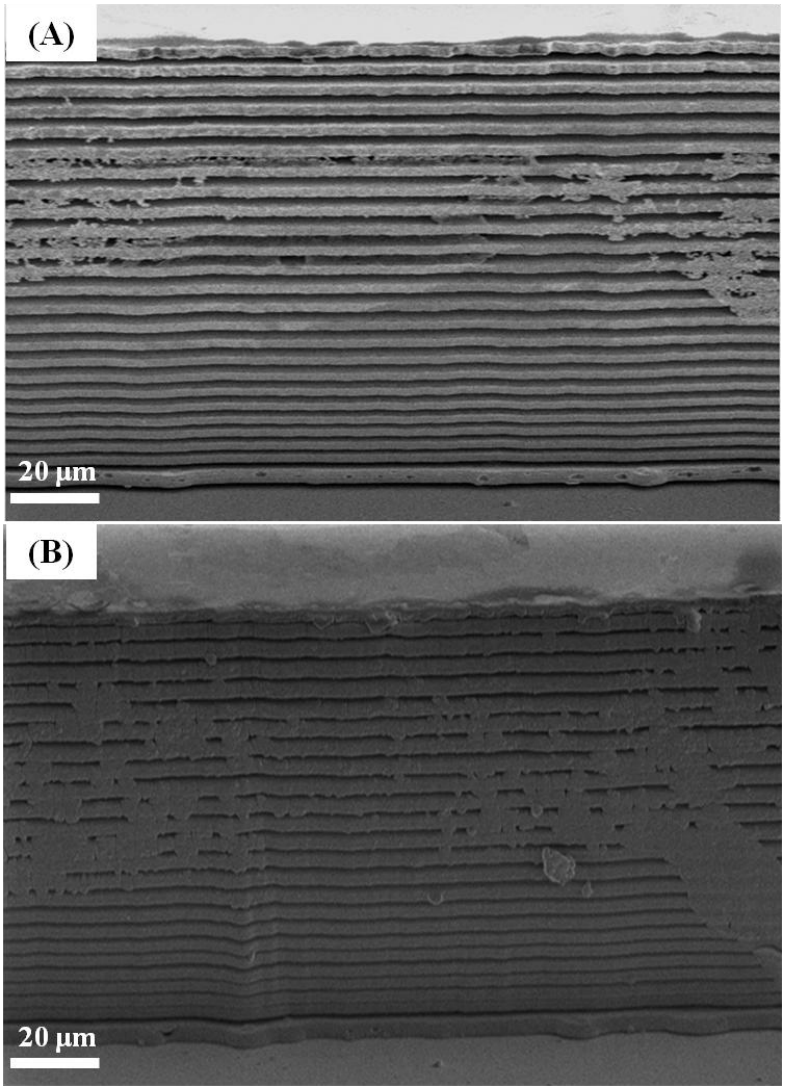

Figure 4.15: Multilayer Ni backbone: (A) prior to the electrodeposition of $Ni(OH)_2$ and (B) after the conformal electrodeposition of $Ni(OH)_2$

4.5 Performance Characterization of the Electrodes

The performance of the fabricated electrodes were evaluated by galvanostatically charging and discharging at various currents. To examine the charge and discharge characteristics of these electrodes, a two-electrode-cell configuration similar to the one shown in Figure 4.11 was prepared where a 6 M KOH solution and a large Zn sheet were utilized as the electrolyte and the counter electrode, respectively. The distance between the two electrodes was set to approximately 1 cm. In this way, a secondary Ni/Zn battery chemistry was achieved. It should be noted that there is a series of $Ni(OH)_2$-based battery chemistries, mentioned in section 4.1, all of which can be potentially used to characterize the performance of the $Ni(OH)_2$ electrode. Among alternative anodes such as Fe and Cd, Zn was chosen due to its ease of handling and environmentally benign nature.

Using a large sheet as the counter electrode minimizes the limiting effects of the Zn anode on the overall performance of the system. Some of these anode effects include the lack of sufficient surface area to sustain high currents and the dissolution of Zn in the electrolyte after long charge and discharge cycles.

4.5.1 Discharge Profile and Capacitance

Electrodes with a varying number of laminations (15, 25, 75, 90, and 100) were prepared and tested at room temperature. Charging and discharging rates ranging from 1 to 120 C were applied. As a reminder, x-C rate indicates the rate at which the electrode is completely charged or discharged in x^{-1} hours. According to this definition, for example, 1 C refers to a rate at which the battery is completely charged in 1 hour, whereas 120 C corresponds to a charging time of 30 seconds. During these charge and discharge cycles, the potential between the multilayer electrode and the Zn sheet was continuously monitored and recorded with the help of a potentiostat (PowerLab 2/20, ADInstruments). A cut-off potential of 1.3 V was determined at which the discharge process was

terminated. The electrochemical performance of the electrodes prepared by electrodeposition and template-free growth of $Ni(OH)_2$ will be discussed separately.

4.5.1.1 Electrodeposited $Ni(OH)_2$

Figure 4.16 illustrates the discharge profiles of four electrodes with different numbers of laminations, and thus, different capacities. In terms of both the shape and the operating potential, the profiles are in good agreement with the previously reported Ni/Zn batteries [44-46]. A relatively flat voltage profile at around 1.7 V was maintained both at high and low discharge rates, with a small voltage decrease immediately after start-up, and a sharp potential drop near the total discharge.

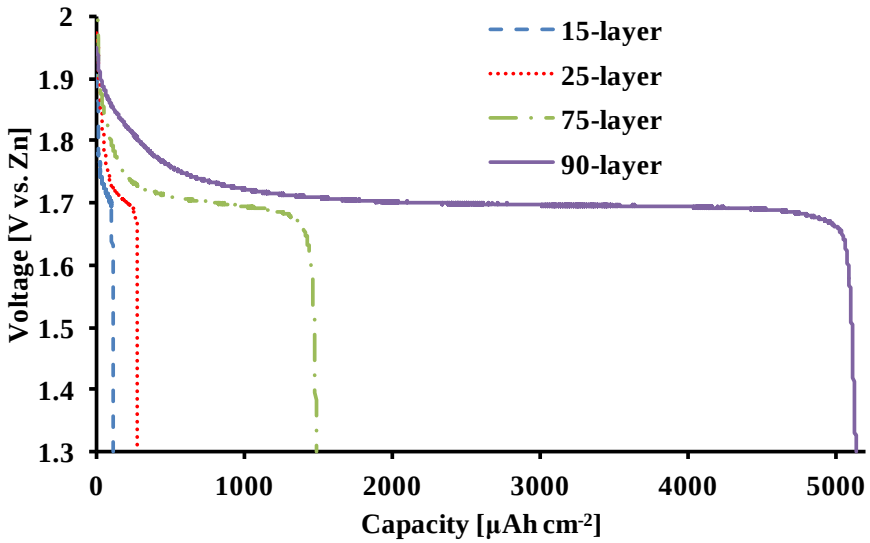

Figure 4.16: Capacity and discharge profiles of the electrodes with varying number of layers

An interesting point to note in Figure 4.16 is that the 15-layer electrode was able to exhibit an areal capacity of 0.1 mAh cm^{-2}, whereas the measured areal capacity for the 90-layer electrode was 5.1 mAh cm^{-2}. Hence, a 6-fold increase in the number of laminations resulted in more than 50-fold increase in the areal capacity. The underlying reason for the deviation from a linear increase in the capacity is a result of the distance

between the individual layers of the multilayer electrode and the thickness of the active material deposit on each layer.

Figure 4.17.A and 4.17.B demonstrate the side wall inside the etching hole of the 75-layer and 90-layer electrodes, respectively, prior to the electrodeposition of $Ni(OH)_2$. The latter electrode has an interlayer spacing that is nearly twice as wide as the former one allowing more volume to be occupied by $Ni(OH)_2$. Although having a wider interlayer spacing to be able to deposit more active material is beneficial in terms of improved capacity, it can have a negative impact on the power density, as indicated in the modeling results in section 4.2.1.

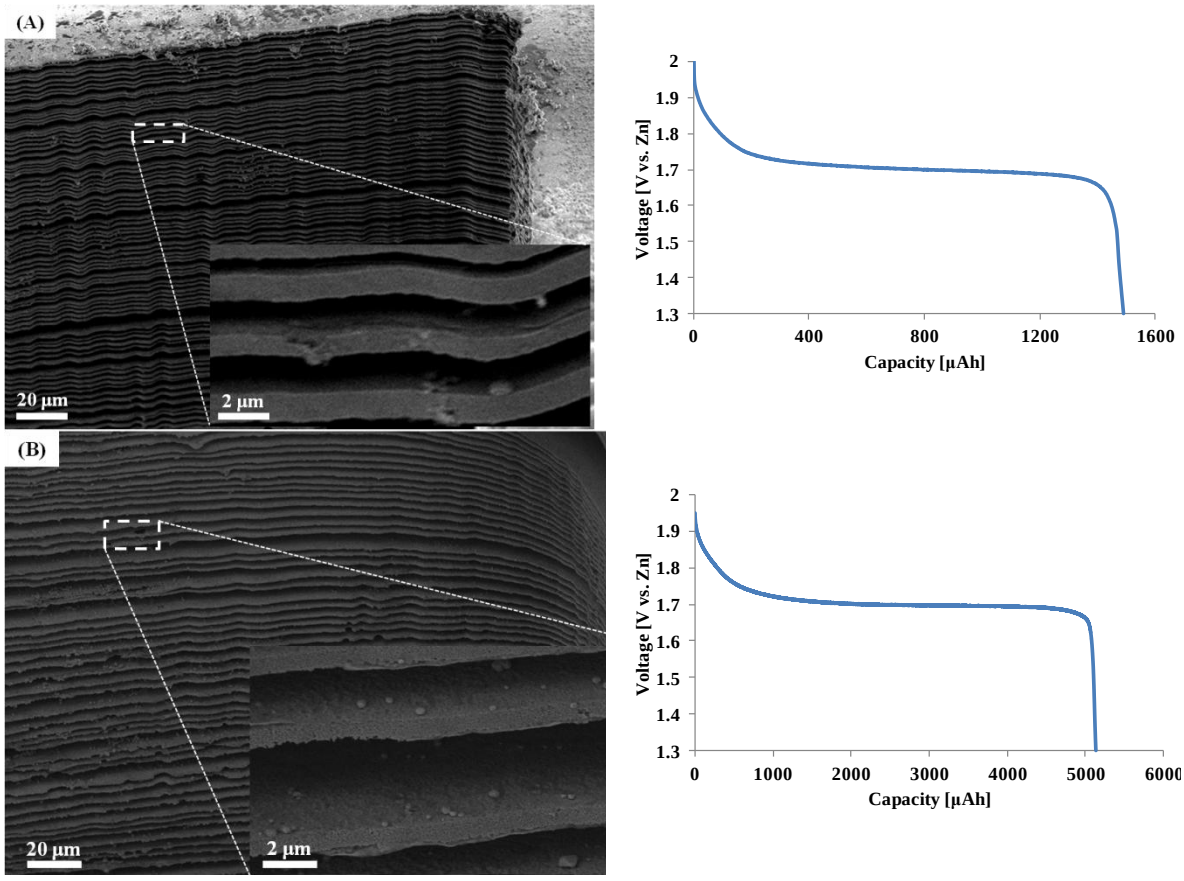

Figure 4.17: Areal capacities of two multilayer electrodes with different number of laminations and interlayer distance: (A) 75-layer electrode with an areal capacity of ~1.5 mAh cm^{-2}, and (B) 90-layer electrode with an areal capacity of ~5.1 mAh cm^{-2}

4.5.1.2 Template-free grown $Ni(OH)_2$

The discharge profile of a 90-layer electrode fabricated through template-free growth of $Ni(OH)_2$ can be seen in Figure 4.18. This electrode is based on the same multilayer Ni backbone (i.e., same batch) as the one shown in Figure 4.17.B. It can be noticed that the utilization of the template-free growth for the same number of laminations caused a significant increase in the capacity of the electrode. When discharged at 0.5 C, the electrode with electrodeposited $Ni(OH)_2$ shown in Figure 4.17.B exhibited an areal capacity of 5.1 mAh cm^{-2} while the measured capacity for the electrode involving template-free grown $Ni(OH)_2$ was 7.1 mAh cm^{-2}. This 40% increase in the capacity mainly stems from the fact that a larger amount of active material deposition is enabled through template-free growth. These results indicate that the template-free growth method is more effective for applications requiring high energy densities at low discharge rates.

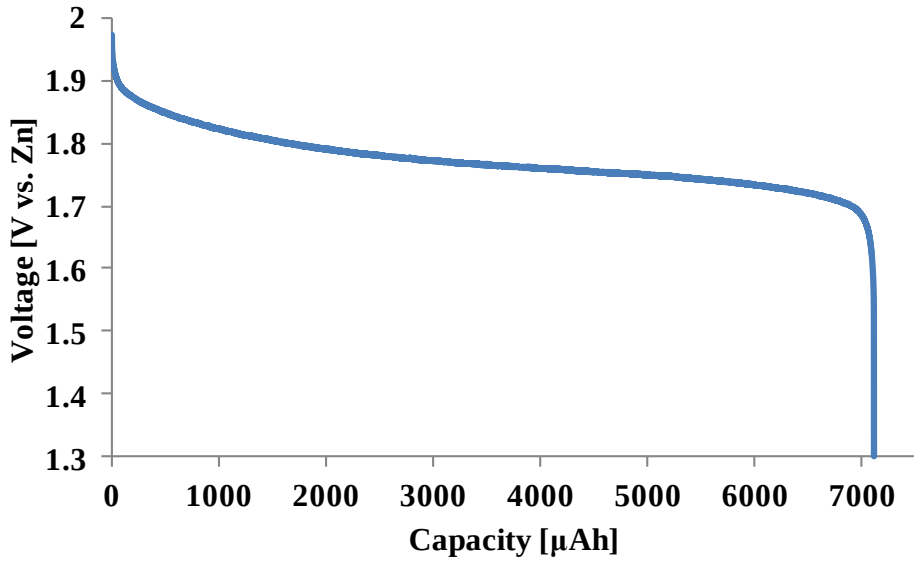

Figure 4.18: Discharge profile of a 90-layer electrode based on template-free grown $Ni(OH)_2$

4.5.2 Power Capability and Capacity Retention

The power capability of the $Ni(OH)_2$ electrodes was evaluated by applying various charge and discharge rates. The capacities obtained were recorded and the capacity retention was calculated.

4.5.2.1 Electrodeposited $Ni(OH)_2$

The relation between the areal capacity of a 25-layer electrode and the discharge rate is illustrated in Figure 4.19. The electrode was charged at a constant rate of 10 C and then discharged at seven different rates ranging from 2 to 90 C. As expected, a decay in the areal capacity was observed as the discharge rate was increased. However, compared to its previously reported counterparts in the literature, the capacity degradation of this multilayer electrode was substantially reduced [39, 47].

The amount of the active material on the Ni backbone was first determined theoretically by utilizing Equations 4.18 and 4.19. According to these equations, it was found that 0.37 mg $Ni(OH)_2$ was electrodeposited. This was validated with a high-precision microscale by measuring the weight of the Ni multilayer structure before and after the active material deposition. The mass difference between the coated and uncoated electrode was measured to be 0.4 mg, which turned out to be in good agreement with the theoretically calculated value.

Prior to the electrodeposition of the active material, the mass of the 25-layer Ni structure was measured as 31 mg. Theoretically, the mass of a single layer can be approximately found by multiplying the density of Ni (8.9 g cm^{-3}) by the product of surface area (0.8 cm^2) and the thickness of the layer (1 μm), giving 0.7 mg. For a 25 layer structure, the total mass should be 17.5 mg, excluding the mass of the connection pad and the anchors, which is assumed to account for the difference between the measured and theoretically estimated mass.

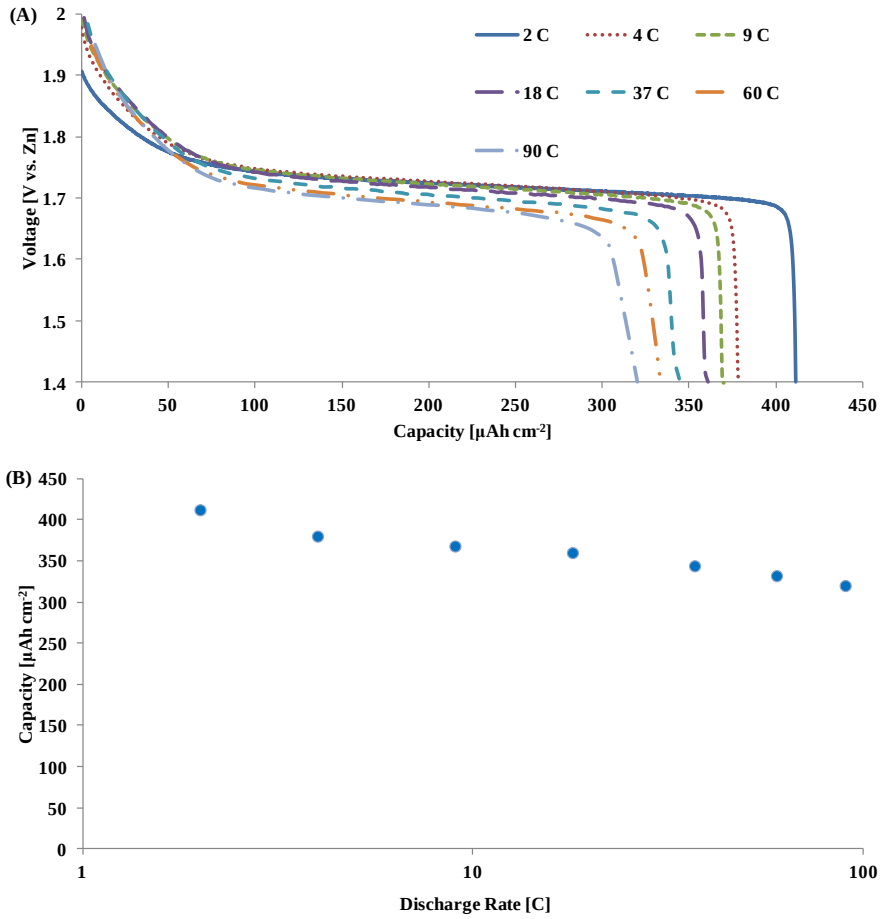

Figure 4.19: Power performance of a 25-layer electrode charged at 10 C and discharged at various rates ranging from 2 to 90 C: (A) discharge profile, and (B) capacity at various discharge rates

The areal capacity obtained by discharging at 2 C (i.e., in 30 minutes) following a charge rate of 10 C was measured to be 0.41 mAh cm^{-2}. When the mass of the active material is taken into account, the specific capacity at 2 C discharge rate was found to be 278 mAh g^{-1} which is very close to the theoretical value for a single electron transfer process, indicating that having the active material electrodeposited on a multilayer Ni backbone does not have a negative impact on its properties [38, 48].

When the electrode was discharged at 90 C (i.e., in 40 seconds) following a charge rate of 10 C, the areal capacity was determined as 0.32 mAh cm^{-2} referring to a

capacity retention of ~78%. This indicates a supercapacitor-like behavior for the battery, which is a desired feature considering the premise of this study.

4.5.2.2 Template-free grown $Ni(OH)_2$

The electrodes prepared through template-free growth of $Ni(OH)_2$ were evaluated in a similar fashion by applying different discharge rates. However, their power capability was inferior in comparison with electrodes containing electrodeposited $Ni(OH)_2$. Figure 4.20.A and 4.20.B show the discharge profiles of a 90-layer electrode discharged at 0.3 and 7 C, respectively. The areal capacity of the electrode at 0.3 C (7.1 mAh cm^{-2}) was observed to drop to 2.3 mAh cm^{-2} when the discharge rate was increased to 7 C. It was postulated that the main reason behind this significant capacity drop at high rates was due to the uncontrolled and nonconformal growth of the active material on the current collector as observed in Figure 4.13. Although higher capacities are more easily obtained via this template-free growth method, the high-power performance of the electrode was not as strong as the performance of the electrodes with the electrodeposited active material.

These electrodes were also evaluated by performing more than 250 charge and discharge cycles at relatively high rates of 14 and 7 C, respectively. The discharge profile at every 50^{th} cycle was recorded and shown in Figure 4.20.C. It can be seen that the change in the capacity of the electrode did not exceed more than 10% even after 250 cycles. This is an indication of the stability of the active material on the Ni backbone.

However, unlike the conventional electrodes whose capacity would be expected to decline over time, the capacity of the tested electrode was observed to fluctuate. For example, the capacity was found to drop to 1.80 mAh cm^{-2} after the 150^{th} cycle; yet, then increased to 1.93 mAh cm^{-2} after the 200^{th} cycle. These fluctuations in the capacity may have originated from the nonconformal nature of the active material as well. It is possible that some of the $Ni(OH)_2$ grown on the Ni backbone, particularly in the central regions between the layers further away from the sidewalls of the multilayer structures, may not

have been exposed to the electrolyte initially due to the excess amount of $Ni(OH)_2$ formed on the sidewalls as shown in Figure 4.13. As the charge and discharge cycles proceed at relatively high rates, some of the excess active material on the sidewalls may have deformed or even detached from the current collector, allowing the electrolyte to reach previously inaccessible regions of the active material and hence, resulting in an increase in the capacity.

Better high-power performance may be obtained from the electrodes prepared through template-free growth method by controlling and limiting the growth of the $Ni(OH)_2$ nanosheets and thus, enabling a conformal coating on the multilayer Ni backbone with sufficient inter-layer gap allowing electrolyte access to every region. However, this would require a thorough study of the growth kinetics and fine-tuning of the growth conditions, such as temperature, process duration, and solution concentrations, which was beyond the scope of this study. Therefore template-free growth method was not pursued any further.

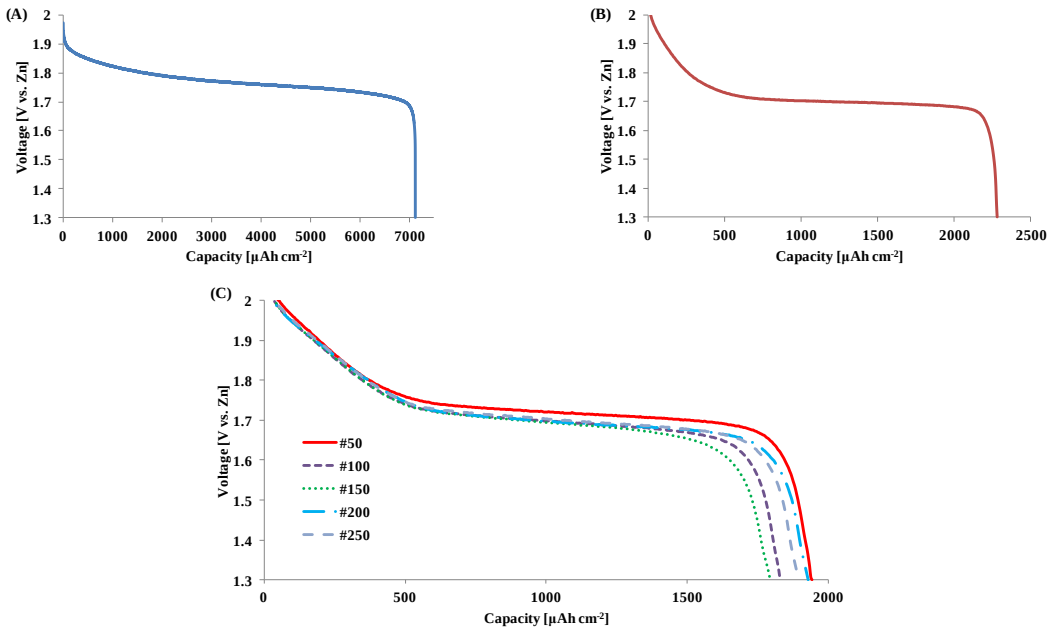

Figure 4.20: Discharge profiles of a 90-layer electrode: (A) discharged at 0.3 C, (B) discharged at 7 C, (C) 250 charge (14 C) and discharge (7 C) cycles

4.5.3 Cycling Stability

The electrodes with electrodeposited active material were shown to be capable of retaining a large portion of their capacities at both high charge and discharge rates. However, their high-power capabilities would only be meaningful for practical applications if they can demonstrate a long-term sustainability. Therefore, the cycle life of the $Ni(OH)_2$ electrodes was also evaluated at high charge and discharge rates.

When performing the experiments pertaining to the cycling stability of the $Ni(OH)_2$ electrodes, the Zn electrode was observed to severely degrade following the long charge and discharge cycles, particularly at high rates, as shown in Figure 4.21. In addition to the dendrites forming on the surface of the Zn electrode, which may potentially cause shorting of the cell due to the relatively small distance between the electrodes, precipitates were observed on the bottom of the electrolyte container located right underneath the Zn sheet. Large amounts of dissolved Zn can also contaminate the electrolyte, which could eventually affect the performance of the electrode.

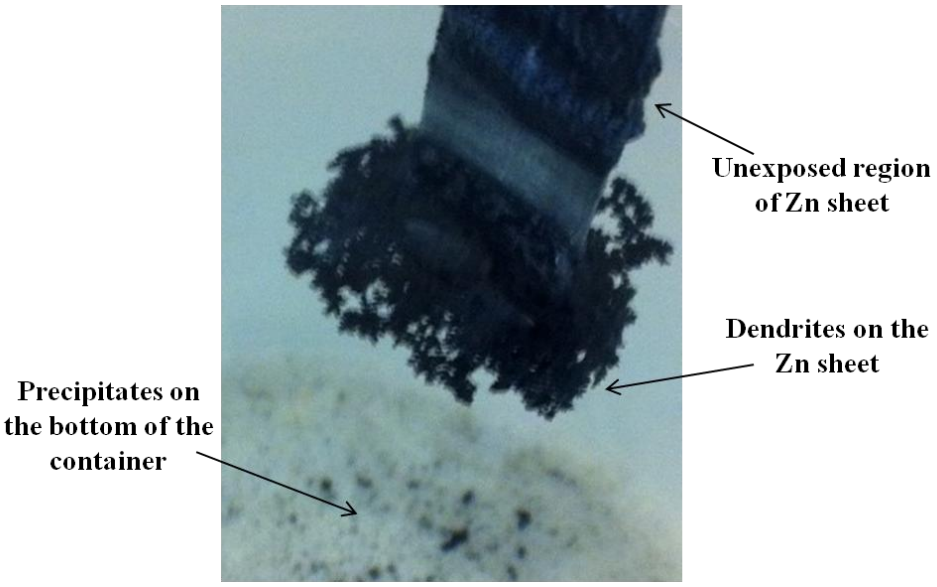

Figure 4.21: Zn anode after 200 cycles at high charge and discharge rates

To avoid the potential problems associated with Zn degradation, a three-electrode-cell configuration was utilized for the cycle life characterization of the electrodes. A platinum mesh and an Ag/AgCl electrode were utilized as the counter and reference electrodes, respectively. As can be seen from Figure 4.22, the change of the electrode-cell configuration did not affect the overall discharge profile of the cell. The only difference is the potential range (i.e., 0.5 to -0.2 V).

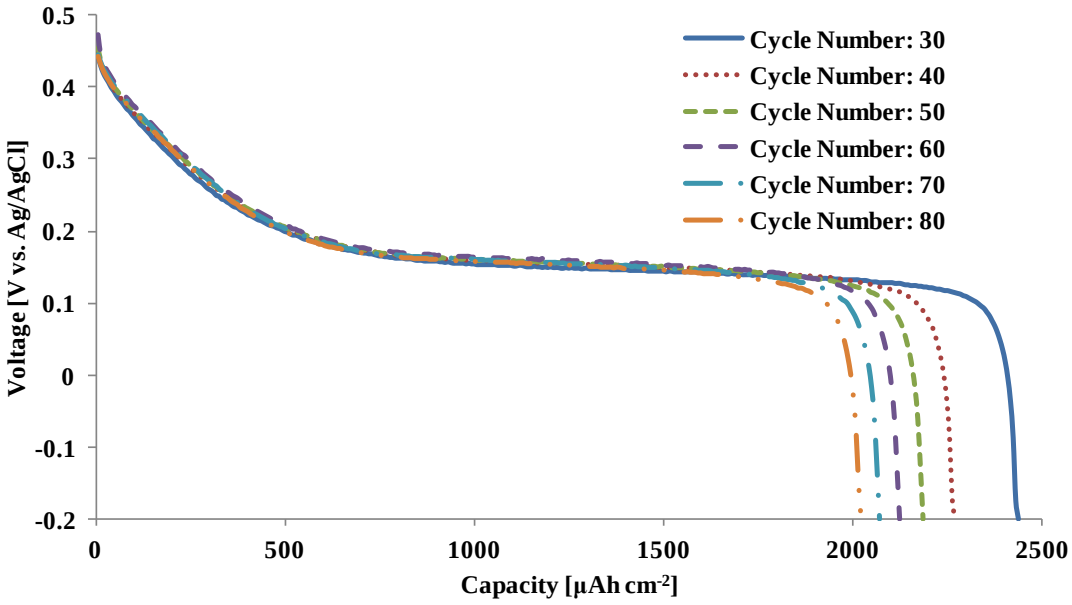

Figure 4.22: Discharge profile of a 100-layer electrode at various charge and discharge cycles tested in a three-electrode-cell configuration by charging and discharging at 20 C and 10 C, respectively

As shown in Figure 4.22, a 100-layer electrode was tested at high charge and discharge rates of 20 and 10 C, respectively. The measured capacity of 2.43 mAh cm^{-2} after the 30^{th} cycle was found to drop to 2.02 mAh cm^{-2} after the 80^{th} cycle, corresponding to a remarkable capacity retention of 83% even at high rates. This high cycling stability also indicates that the electrodeposited $Ni(OH)_2$ was able to maintain its mechanical stability and integrity on the multilayer Ni backbone.

When charging the electrodes galvanostatically at high rates (e.g., >10 C), the potential was observed to reach values exceeding 2 V and as a result, large amounts of bubbles form on the Ni electrode, potentially distorting the $Ni(OH)_2$ film on the multilayer structure. To mitigate this bubble formation, a 3-step charging process was utilized where the current is gradually reduced when the threshold potential is reached. The currents during this process were adjusted in such a way that the total amount of charge transferred was equal to the capacity of the electrode.

The normalized capacity of a 100-layer electrode at various charging rates using the 3-step charging method can be seen in Figure 4.23. In excess of 80 charge and discharge cycles were performed and outstanding capacity retention was reported even at extremely high charging rates. For example, at a charging rate of 150 C which corresponds to a charging time of 24 seconds, the electrode was able to deliver approximately 50% of its 4 C capacity, confirming the supercapacitor-like behavior of the $Ni(OH)_2$ electrode.

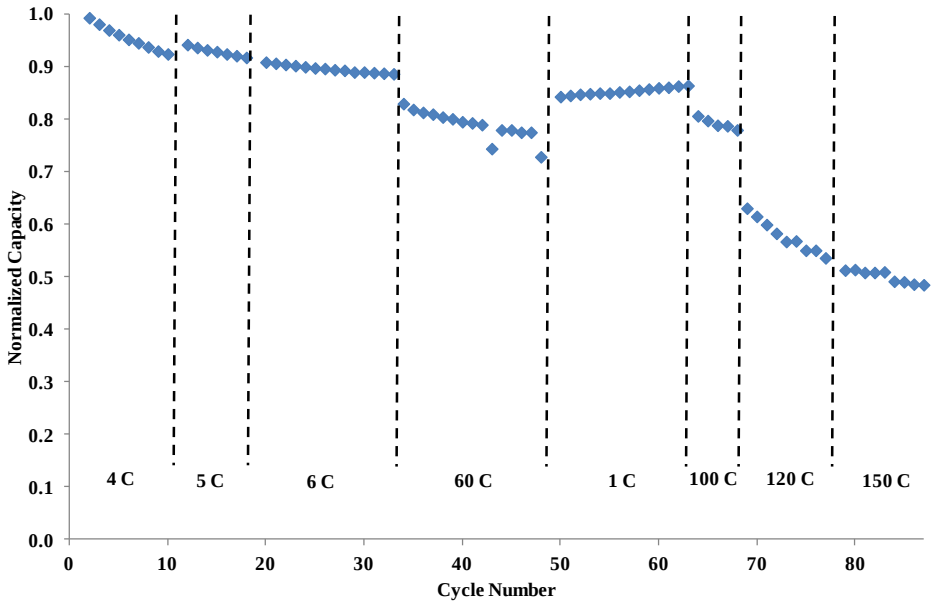

Figure 4.23: Normalized capacity of a 100-layer electrode charged in three steps at various rates and discharged at 4 C for over 80 cycles

To confirm the mechanical stability and integrity of the $Ni(OH)_2$ film on the multilayer backbone at high rates visually, high-resolution SEM images were taken following the charge and discharge cycles. As shown in Figues 4.23, some cracks were observed in the active material film but overall, the film remained mainly intact, indicating a good adhesion between the current collector and the active material even at large currets.

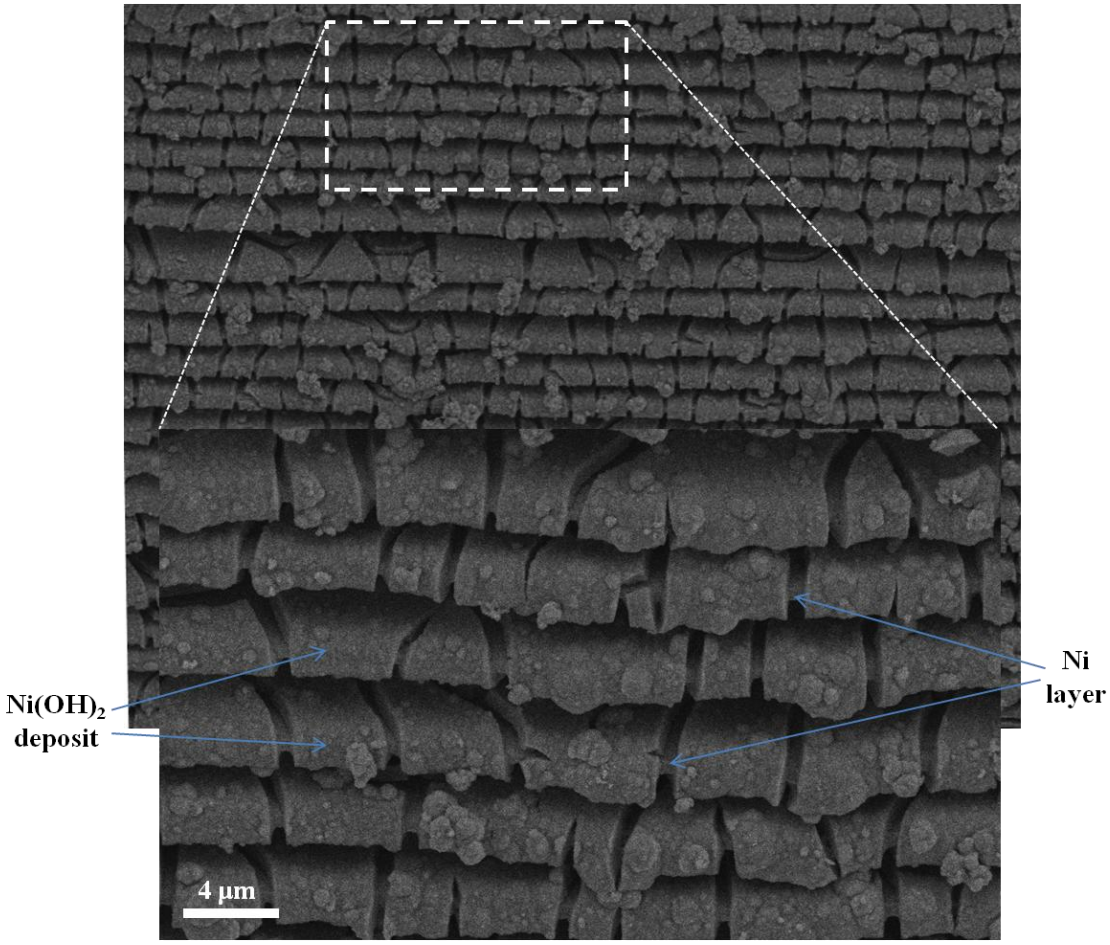

Figure 4.24: Sidewall of a multilayer structure following more than 100 charge and discharge cycles

In order to assess the integrity of the active material located in the center parts of the layers further away from the sidewalls, tape was adhered to the bottommost layer of the multilayer electrode and carefully pulled away. The separated layer was then imaged

as shown in Figure 4.25. It can be seen that the active material was able to preserve its conformality not only on the sidewalls, but also on the inner regions of the layers. This also confirms the capability of conformal active material deposition onto relatively complex 3D architectures, which is an essential part of this study where a precise control over the dimensions of the active material is claimed.

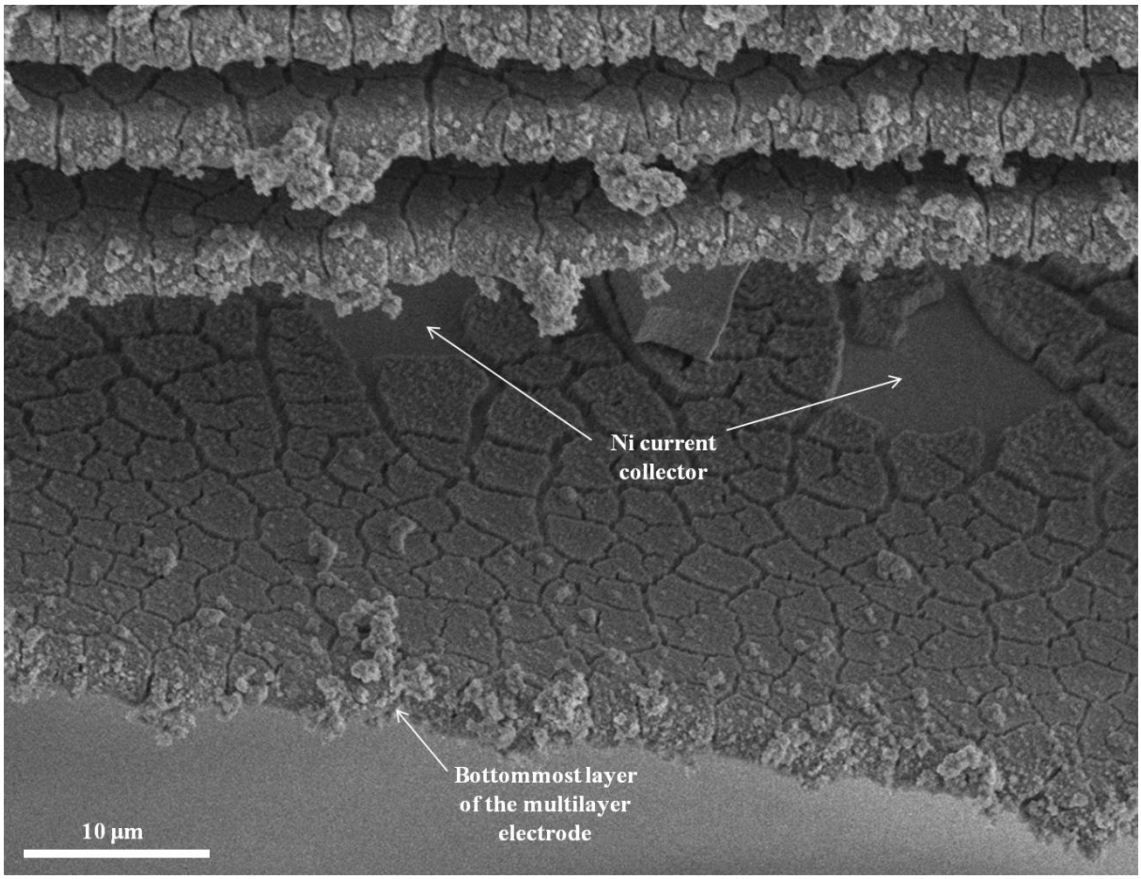

Figure 4.25: Bottommost layer separated from the rest of the multilayer electrode to confirm conformal coating of the active material

It can be seen in Figure 4.25 that some portions of the Ni backbone were exposed due to the cracks that formed in the active material following the charge and discharge cycles at high rates. One concern was whether the exposed regions of the Ni backbone contributed to the performance of the electrode because of the $Ni(OH)_2$ formation during the charging (i.e., anodizing) steps, especially at high rates. It was mentioned earlier in

this chapter that anodization of Ni is a method to build $Ni(OH)_2$ electrodes. However, due to the self-limiting nature of the $Ni(OH)_2$ growth, the resulting film would be expected to be of insignificant thickness (~1-2 nm) unless specific techniques, such as periodic square-wave potentials at high frequencies, are applied. Therefore, the contribution originating from anodically grown $Ni(OH)_2$ film was expected to be negligible. To further confirm this experimentally, a blank electrode composed of 90 Ni layers was prepared. This electrode underwent the same charge and discharge tests. It was found that the capacity of this electrode was less than 1% of what was obtained from the $Ni(OH)_2$-coated electrode.

4.5.4 Electrodes with Higher Capacities

When applications requiring larger quantities of energy (>50 mWh) are considered, higher capacities than the ones reported thus far are required. According to Equation 4.20, the energy stored in an electrode (E) in terms of Wh can be found by multiplying capacity (C) by the average discharge potential which is 1.7 V for the current chemistry.

$$E = C \cdot V \tag{4.20}$$

The highest capacity obtained from the fabricated electrodes with electrodeposited $Ni(OH)_2$ onto a 90-layer structure was measured to be 5.1 mAh, referring to an energy of 8.6 mWh which is nearly one order of magnitude less than what is generally expected for macroscale devices. Therefore, a significant increase in the capacity is required in order to make the electrodes more appealing for macroscale applications.

One of the obvious methods to enable higher capacities is by increasing the lateral aspect ratio of the structures, which would result in electrodes with higher footprint areas.

However, it would not be desirable due to the limited available space to place the power source, particularly in portable electronic devices. Another obvious way of achieving such a high capacity is by fabricating electrodes with higher number of laminations; yet, fabrication-related constraints originating from the lack of an appropriate mold do not allow the realization of such structures. In fact, Ni structures with 250 layers were able to be demonstrated while the total thickness was kept constant (~0.5 mm). However, the individual Ni layer thickness and inter-layer distance (i.e., thickness of Cu layers) were substantially smaller than for the 90-layer structures due to the limitation on the mold thickness. Therefore, no significant increase in the amount of active material and thus, in the capacity of the electrode was able to be achieved.

To overcome the fabrication limitations pertaining to the photoresist mold, stack of simultaneously fabricated structures was prepared. For the demonstration purposes, three 90-layer electrodes were combined by soldering at their connection pads. The discharge profile of the resultant structure can be seen in Figure 4.26. This stack of electrodes was able to exhibit a capacity of 17 mAh (29 mWh) when discharged at 2.4 C.

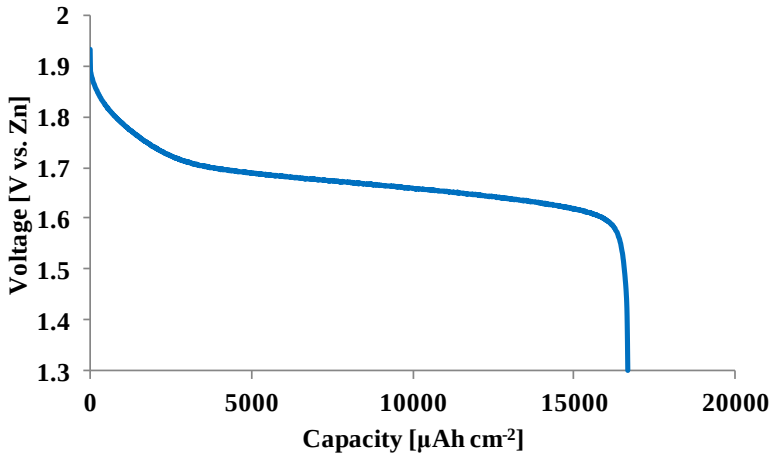

Figure 4.26: Discharge profile of a $Ni(OH)_2$ electrode at 2.4 C composed of a stack of 3 90-layer electrodes

Hence, higher capacities can be achieved by forming stacks with higher number of electrodes. However, higher capacities require similarly high discharge currents in order to be able to characterize the power capability of the electrodes. For example, a stack of 6 90-layer electrodes is expected to deliver an approximate capacity of 35 mAh. When the high-power performance of this electrode is desired to be evaluated at 60 C, a current of 2.1 A needs to be drawn which cannot be characterized in our lab due to the equipment-related (e.g., potentiostat) limitations.

One way of overcoming these high levels of currents is through changing the electrode configuration. By connecting these six electrodes in parallel, the current can be reduced to its one-sixth (350 mA) while maintaining the total capacity. Another way of reducing the current is by switching to other secondary battery chemistries. Li-ion batteries, for example, are known to exhibit discharge potentials of more than 3.5 V. Based on Equation 4.20, this corresponds to at least double the energy of the $Ni(OH)_2$ electrodes with the same capacities. Electrodes based on Li-ion chemistries will be discussed in detail in the next chapter.

4.6 Modeling of the Fabricated Electrodes

As described in section 4.2, the electrode design is limited by fabrication-related constraints, including the individual Ni layer thickness, the total thickness of the structure, and the spacing between the Ni layers. The underlying reasons (i.e., mechanical integrity of the layers and maximum height of the photoresist mold) for the limitations pertaining to the former two characteristic dimensions were discussed in section 4.2. The limitation concerning the inter-layer spacing, however, was briefly mentioned, but not discussed thoroughly.

Following the removal of the sacrificial Cu layers, the electrodeposition of the $Ni(OH)_2$ film was performed under pulse current conditions, as described in detail in section 4.4.2. This process ensures a conformal coating of the $Ni(OH)_2$ film on the

multilayer Ni current collector. According to the modeling results, for a distance of 300 μm between the adjacent etching holes, the minimum theoretical Cu layer thickness should be 0.45 μm, in order to realize electrodes that can be charged in 1 minute (i.e., at 60 C charge rate). However, when attempts were made to fabricate electrodes with inter-layer spacing (i.e., Cu layer thickness) of less than 1 μm, a conformal coating of the $Ni(OH)_2$ was not able to be achieved as easily. Even after increasing the t_{off}/t_{on} ratio from 9 to 20 during the pulse deposition process, the channels were observed to be clogged due to the excess and uneven deposition of the active material onto the sidewalls of the multilayer backbone. Therefore, the spacing was increased to a minimum value of 2 μm, although it is much higher than the minimum required spacing. In this way, the problems pertaining to the deposition of a conformal active material film is alleviated at the expense of reduced capacity, since the increase in inter-layer spacing results in deposition of fewer number of layers for a given total thickness.

The increase in the inter-layer spacing also allowed electrodeposition of thicker $Ni(OH)_2$ films, and thus, realization of electrodes with higher energy densities at the expense of power density. The multilayer electrodes given in Figure 4.24, for example, have an active material film thickness of approximately 1 μm which is ten times the maximum allowed thickness calculated from the modeling to be able to charge the electrode in 1 minute with a negligible forfeit in the capacity. It can be seen in Figure 4.23 that the electrode was able to deliver 80% of its 1 C capacity when charged at 60 C. When the charge rate was increased to 120 C (i.e., charging time of 30 seconds), the capacity delivery was reduced further to the range of 50-60% which is still quite impressive for a battery electrode.

To determine if the model can predict a similar power delivery, the simulations were performed based on the dimensions of the fabricated electrodes. Figure 4.27 shows the theoretical capacity retention of the fabricated electrodes with an active material thickness of 1 μm as a function of the charge rate and compares the modeling results to

the experimental data. The inter-layer spacing for these electrodes is well above the minimum thickness of 0.45 µm. Therefore, it does not affect the modeling results. When charged at a low rate of 4 C, the modeling results showed that the concentration of the H^+ ions within the active material was reduced to 5% of its initial value of 0.0383 mol cm^{-3}, indicating a capacity delivery of 95% which is in good agreement with the experimental data shown in Figure 4.23. When the charge rate was increased to 60 C, the theoretical capacity delivery dropped to approximately 85% which is still quite close to the experimental value of ~80%. However, when the charging rate in the model was increased to 120 C, a significant deviation was observed from the experimental data. The model predicts a capacity retention of approximately 80%, whereas, in reality, the capacity retention was in the range of 50-60%.

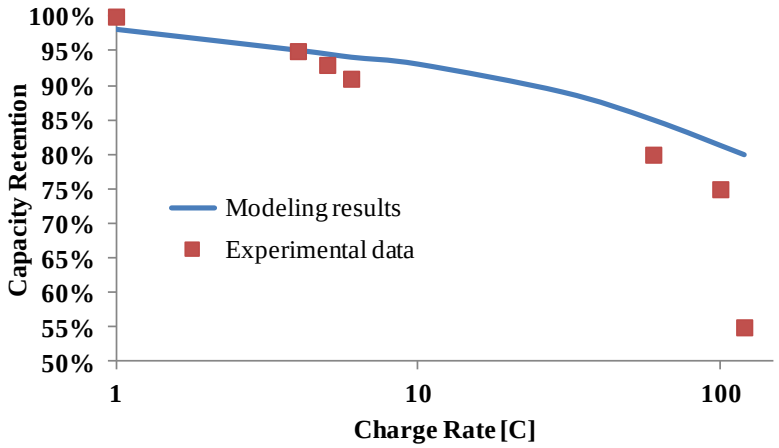

Figure 4.27: Theoretical capacity retention vs. experimental data of a 100-layer electrode with a 1-µm-thick active material at various charge rates

The discrepancies between the modeling and experimental results at high rates may stem from several factors. One cause may be the assumption that a uniform film of $Ni(OH)_2$ is present on each Ni layer. Yet, as indicated in Figures 4.24 and 4.25, cracks are observed in the active material, which may originate from the expansion and contraction of the $Ni(OH)_2$ film during the charge and discharge processes, and therefore

are accentuated at high rates. The SEM images also show dendrite-like structures formed on the surface of the active material, which, in some regions, are more than twice as much than the original thickness of the as-deposited active material itself. This would result in much longer diffusion path lengths for the ions, which would have an adverse effect on the power performance. Other factors, such as the negligence of the polarization effects and assumption of a constant electrolyte concentration within the etching holes might have also contributed to these discrepancies.

4.7 Performance Projections Using the Models

Using the diffusion-limited models introduced in section 4.2, projections regarding the performance of the multilayer $Ni(OH)_2$ electrodes were made. This was achieved by fine-tuning the aforementioned characteristic dimensions, including the individual Ni layer thickness of the multilayer backbone and the active material thickness on each layer.

The impact of the individual Ni layer thickness on the performance of the multilayer electrode can be seen in Figure 4.28, where the areal capacity of the electrode is shown as a function of the thickness of the individual Ni layers. This projection is based on the width, active material thickness, and inter-layer spacing of 300 μm, 0.1 μm, and 0.25 μm, respectively. Reducing the thickness of the Ni layer further below the experimentally determined value of 1.5 μm results in an increase in the areal capacity, since this would allow deposition of higher number of layers, and thus, more active material within a given volume of the electrode. An approximately three-fold improvement in the areal capacity can be realized, if the thickness of the individual Ni layers can be reduced to 0.3 μm. This would obviously result in an improved power and energy density of the electrode, as the mass and volume ratios of the electrochemically inactive material (i.e., Ni backbone) to the total mass and volume of the electrode are

reduced as well. Potential methods that can be utilized to achieve structures with thinner backbone layers are discussed in the future work section of this work (see Chapter 7).

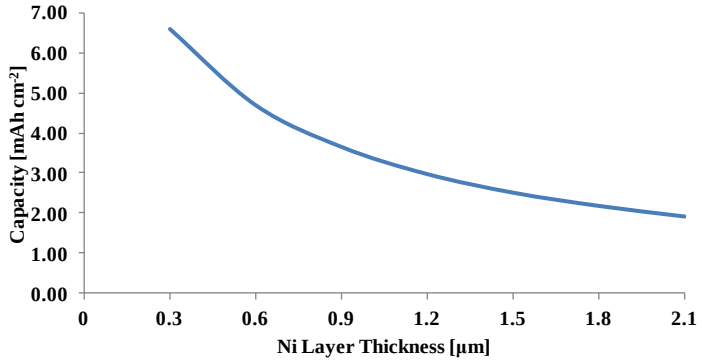

Figure 4.28: Model projections of the areal capacity of a 300-µm-thick $Ni(OH)_2$ electrode as a function of the individual Ni layer thickness

An opposite trend was observed with an increase in the active material thickness. For the same total electrode thickness of 300 µm, Ni layer thickness of 1.5 µm, and the channel width of 300 µm, increasing the thickness of the $Ni(OH)_2$ film was shown to increase the areal capacity, as illustrated in Figure 4.29. Increasing the thickness of the $Ni(OH)_2$ film, however, has a negative impact on the power performance due to increased diffusion and conduction path lengths.

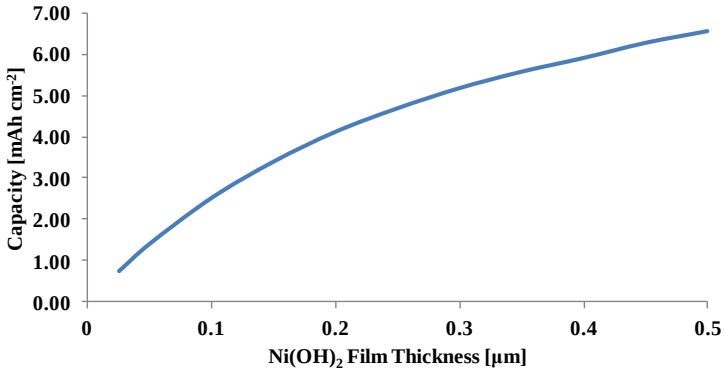

Figure 4.29: Model projections of the areal capacity of a 300-µm-thick $Ni(OH)_2$ electrode as a function of the $Ni(OH)_2$ film thickness

The impact of the active material thickness, as well as the Ni layer thickness, on both the energy and power density of the electrodes is shown in Figure 4.30.A and 4.30.B. The gravimetric density is more important for macroscale applications where the mass of the power source is usually the limiting factor (e.g., cell phones), whereas the volumetric density is generally the main concern for applications with limited space (e.g., microsensors and microactuators). Therefore, the application area should be taken into account when designing the electrodes according to Figures 4.30.A and 4.30.B.

The projections in Figure 4.30 were made by using the aforementioned diffusion-limited models. First, the maximum possible charging rate was calculated for a given thickness of the active material film, which was found by estimating the minimum amount of time at which the concentration of H^+ within the active material film drops to less than 1% of the initial concentration (i.e., 0.0383 mol cm^{-3}). The corresponding current density that enables the charging at the calculated rate was then used in the second model to find the minimum required inter-layer spacing H. From these values, the number of depositable layers within the total thickness of 300 μm was calculated. Finally, based on the number of layers and the amount of the active material, the energy and power densities of the electrode were estimated. For the power and energy density calculations, the discharge potential of the electrode was assumed to be 1.7 V.

It can be seen that increasing the $Ni(OH)_2$ film thickness from 0.1 to 0.2 μm can cause an order of magnitude drop in the volumetric power density of the electrode, while the increase in the volumetric energy density is not as significant. Also, minimizing the mass of the electrochemically inactive material (i.e., Ni backbone) by reducing the thickness of the individual Ni layers is shown to cause substantial improvements in both gravimetric and volumetric power and energy densities.

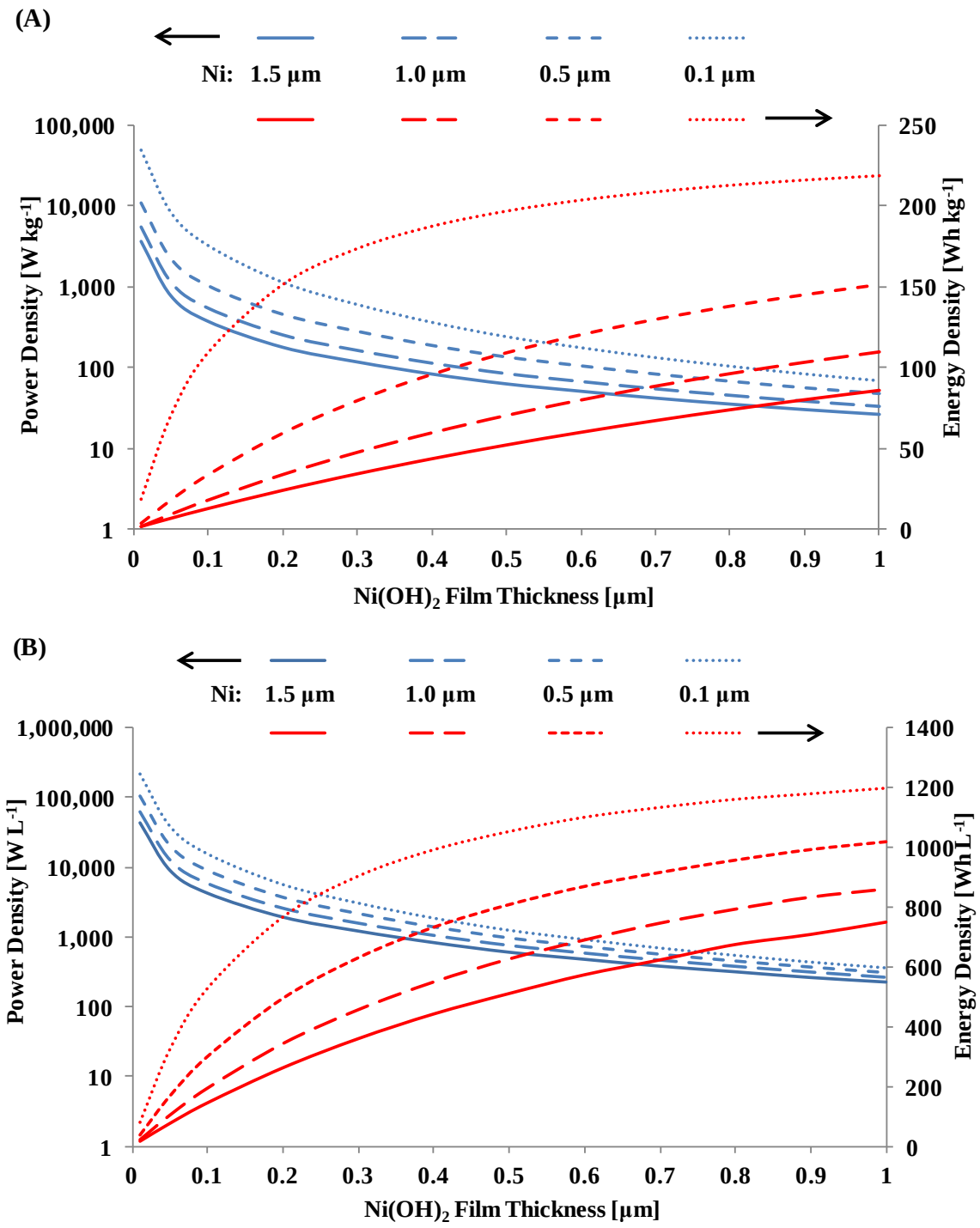

Figure 4.30: Theoretical power and energy density of the electrodes as a function of the $Ni(OH)_2$ film thickness and the Ni layer thickness: (A) gravimetric density, (B) volumetric density

4.8 Conclusions

In this chapter, MEMS-enabled, metallic multilayer structures with precisely controlled dimensions were demonstrated as secondary battery electrodes. $Ni(OH)_2$ was chosen as the active material of secondary battery chemistry deposited onto the multilayer backbone. Two methods have been considered for the formation of the active material film on the current collector. The first method involves the cathodic electrodeposition of $Ni(OH)_2$ under current-controlled conditions. The second method comprises the template-free growth of $Ni(OH)_2$. The latter method was found to yield electrodes with substantially higher capacities than the former one; yet, a conformal coating on the Ni backbone was not able to be achieved, which adversely affected the power performance of the electrode. The former method, on the other hand, enabled a better control over the thickness and the mass of the electrodeposited active material, resulting in a better conformality and hence, a better power performance.

A unique feature of the multilayer scaffold approach reported in this chapter is the ability to remove the sacrificial Cu layers completely due to the presence of the Ni anchors supporting the remaining Ni layers and thus, to achieve structures with significantly higher surface area as compared to the electrodes based on structures with partially etched Cu layers. Another unique feature presented was the ability to fabricate structures with much higher total thicknesses (e.g., >300 μm) as compared to what has been reported in the case of Zn-air batteries in Chapter 3. This was realized by developing a new way to use an existing photoresist (i.e., AZ 125 nXT) to create high-aspect-ratio molds for the electroplating process, leading to the realization of the electrodes with substantially improved capacities.

The concept introduced in this study was able to address several aspects of battery dynamics that are essential for enhanced battery performance. First, the high surface area enabled by the fabrication of relatively higher number of Ni layers and by the complete removal of the Cu layers provides larger contact area between the electrode and

electrolyte, resulting in higher number of active sites to host the redox reactions of the active material. Second, the realization of a thin and conformal active material coating on each layer reduces the diffusion and conduction path lengths for the solid-state ions and electrons, respectively. Hence, the power-limiting effect originating from the low conductivity of the active material ($Ni(OH)_2$) is significantly mitigated. Finally, the mechanically stable and electrochemically inert metallic backbone serving as a current collector with high electronic conductivity, exhibits minimized resistance for the transfer of electrons to and from the active material.

The resultant electrodes with the electrodeposited $Ni(OH)_2$ provided areal capacities as high as 5.1 mAh cm^{-2}. These electrodes demonstrated remarkable power capability by delivering more than 50% of their capacities even after ultra-fast charge rates of 120 C. Diffusion-limited models, that have been developed to design multilayer structures with optimum characteristic dimensions (e.g., active material thickness, inter-layer spacing) were utilized to predict the performance of the fabricated electrodes. The experimental results up to the charging rates of 60 C were found to be in good agreement with the theoretical results obtained from the FEM models. The resultant electrodes also exhibited improved cycling stability when charged and discharged at high rates in excess of 80 times.

For the quantitative realization of the contributions provided by the approaches reported in this chapter, both gravimetric and volumetric power and energy densities of the electrodes were calculated and compared to the existing energy storage systems. This comparison can be seen in Figures 4.31 and 4.32 where the performance of the 25-layer $Ni(OH)_2$ electrode (Point A) that was previously demonstrated in Figure 4.19 is illustrated along with the existing energy storage systems. The performance value labeled as point A is based on the total mass of the electrode (i.e., Ni backbone and the active material). Point B, on the other hand, is the theoretical performance of the electrode with optimized dimensions that were determined by using the aforementioned diffusion-

limited models. This electrode features a Ni layer thickness of 0.1 µm, a $Ni(OH)_2$ film thickness of 0.1 µm, an inter-layer spacing of 0.23 µm, and a total thickness of 300 µm. The location of these points indicates that the contribution of the multilayer electrodes in terms of volumetric energy and power density is much more significant than the contribution pertaining to the gravimetric energy and power density.

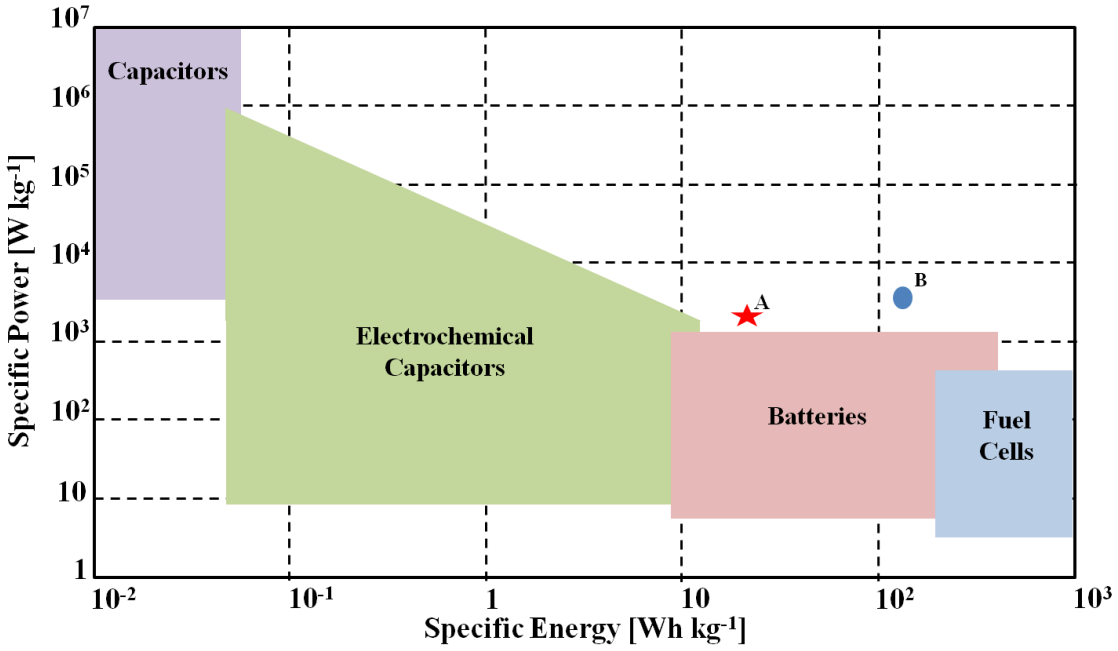

Figure 4.31: Ragone plot comparing the gravimetric power and energy densities of the 25-layer $Ni(OH)_2$ electrode (point A) and the modeled electrode with the optimized dimensions (point B) to the existing energy storage systems

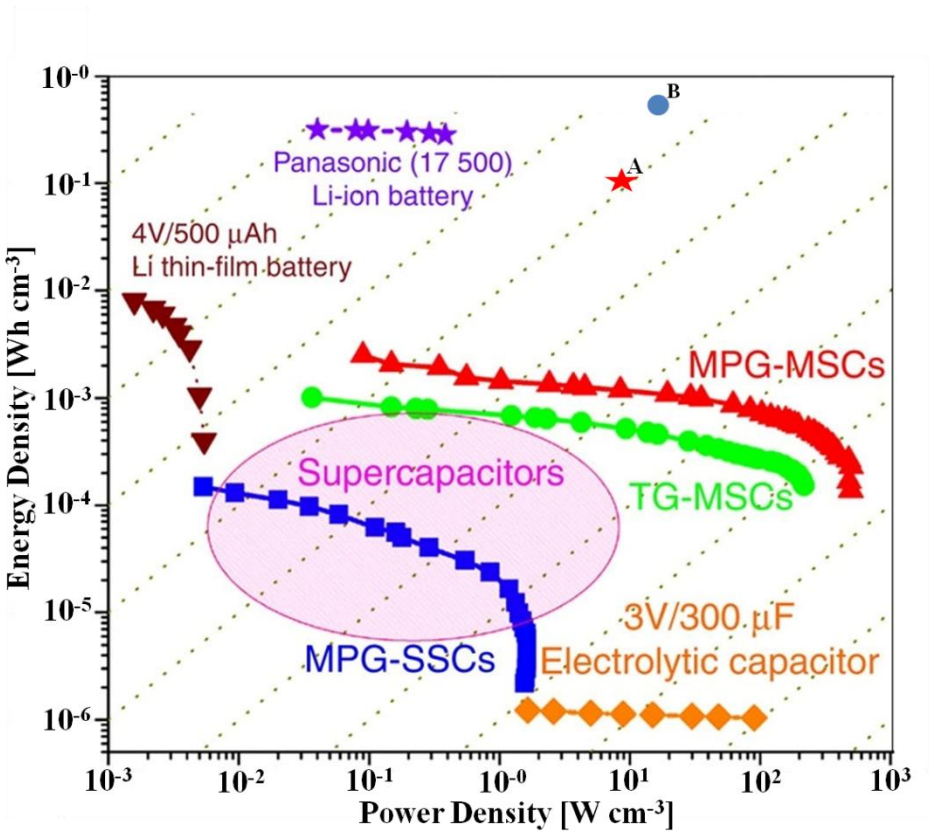

Figure 4.32: Ragone plot comparing the volumetric power and energy densities of the 25-layer $Ni(OH)_2$ electrode (point A) and the modeled electrode with the optimized dimensions (point B) to the existing energy storage systems [49]

4.9 References

[1] A. Armutlulu, S. B. Allen, and M. Allen, "3D microstructures for fast charge and discharge batteries," *PowerMEMS 2012,* 2012.

[2] A. Armutlulu, S. B. Allen, and M. Allen, "Microfabricated nickel-based electrodes for high-power battery applications," *Journal of Micromechanics and Microengineering,* vol. 23, p. 114008, 2013.

[3] T. B. Reddy, *Linden's Handbook of Batteries* vol. 4: McGraw-Hill New York, 2011.

[4] S. Atlung, K. West, and T. Jacobsen, "Dynamic aspects of solid solution cathodes for electrochemical power sources," *Journal of The Electrochemical Society,* vol. 126, pp. 1311-1321, 1979.

[5] J. P. Fellner and S. S. Sandhu, "Diffusion-limited model for a lithium/polymer battery," *Electrochimica Acta,* vol. 43, pp. 1607-1613, 1998.

[6] B. Paxton and J. Newman, "Modeling of nickel/metal hydride batteries," *Journal of the Electrochemical Society,* vol. 144, pp. 3818-3831, 1997.

[7] V. Srinivasan, J. W. Weidner, and R. E. White, "Mathematical models of the nickel hydroxide active material," *Journal of Solid State Electrochemistry,* vol. 4, pp. 367-382, 2000.

[8] P. M. Gomadam, J. W. Weidner, R. A. Dougal, and R. E. White, "Mathematical modeling of lithium-ion and nickel battery systems," *Journal of Power Sources,* vol. 110, pp. 267-284, 2002.

[9] S. Motupally, C. C. Streinz, and J. W. Weidner, "Proton diffusion in nickel hydroxide films: measurement of the diffusion coefficient as a function of state of charge," *Journal of The Electrochemical Society,* vol. 142, pp. 1401-1408, 1995.

[10] S. Motupally, C. C. Streinz, and J. W. Weidner, "Proton diffusion in nickel hydroxide: prediction of active material utilization," Journal of The Electrochemical Society, vol. 145, pp. 29-34, 1998.

[11] R. A. Noulty and D. G. Leaist, "Activity coefficients and diffusion coefficients of dilute aqueous solutions of lithium, sodium, and potassium hydroxides," Journal of Solution Chemistry, vol. 13, pp. 767-778, 1984.

[12] Y. Wang, D. X. Cao, G. L. Wang, S. S. Wang, J. Y. Wen, and J. L. Yin, "Spherical clusters of beta-Ni(OH)(2) nanosheets supported on nickel foam for nickel metal hydride battery," *Electrochimica Acta,* vol. 56, pp. 8285-8290, Oct 2011.

[13] D. E. Reisner, A. J. Salkind, P. R. Strutt, and T. D. Xiao, "Nickel hydroxide and other nanophase cathode materials for rechargeable batteries," *Journal of Power Sources,* vol. 65, pp. 231-233, Mar-Apr 1997.

[14] H. S. Kim, T. Itoh, M. Nishizawa, M. Mohamedi, M. Umeda, and I. Uchida, "Microvoltammetric study of electrochemical properties of a single spherical nickel hydroxide particle," *International Journal of Hydrogen Energy,* vol. 27, pp. 295-300, Mar 2002.

[15] X. Y. Wang, H. Luo, P. V. Parkhutik, A. C. Millan, and E. Matveeva, "Studies of the performance of nanostructural multiphase nickel hydroxide," *Journal of Power Sources,* vol. 115, pp. 153-160, Mar 2003.

[16] W. G. Zhang, W. Q. Jiang, L. M. Yu, Z. Z. Fu, W. Xia, and M. L. Yang, "Effect of nickel hydroxide composition on the electrochemical performance of spherical Ni(OH)(2) positive materials for Ni-MH batteries," *International Journal of Hydrogen Energy,* vol. 34, pp. 473-480, Jan 2009.

[17] E. Shangguan, Z. R. Chang, H. W. Tang, X. Z. Yuan, and H. J. Wang, "Synthesis and characterization of high-density non-spherical Ni(OH)(2) cathode material for Ni-MH batteries," *International Journal of Hydrogen Energy,* vol. 35, pp. 9716-9724, Sep 2010.

[18] K. Matsui, T. Kyotani, and A. Tomita, "Hydrothermal synthesis of single-crystal Ni(OH)(2) nanorods in a carbon-coated anodic alumina film," *Advanced Materials,* vol. 14, pp. 1216-+, Sep 2002.

[19] Z. H. Liang, Y. J. Zhu, and X. L. Hu, "beta-nickel hydroxide nanosheets and their thermal decomposition to nickel oxide nanosheets," *Journal of Physical Chemistry B,* vol. 108, pp. 3488-3491, Mar 2004.

[20] F. S. Cai, G. Y. Zhang, J. Chen, X. L. Gou, H. K. Liu, and S. X. Dou, "Ni(OH)(2) tubes with mesoscale dimensions as positive-electrode materials of alkaline rechargeable batteries," *Angewandte Chemie-International Edition,* vol. 43, pp. 4212-4216, 2004.

[21] D. Yang, R. Wang, J. Zhang, and Z. Liu, "Synthesis of nickel hydroxide nanoribbons with a new phase: A solution chemistry approach," *The Journal of Physical Chemistry B,* vol. 108, pp. 7531-7533, 2004.

[22] C. Coudun and J. F. Hochepied, "Nickel hydroxide "stacks of pancakes" obtained by the coupled effect of ammonia and template agent," *Journal of Physical Chemistry B,* vol. 109, pp. 6069-6074, Apr 2005.

[23] D. N. Yang, R. M. Wang, M. S. He, J. Zhang, and Z. F. Liu, "Ribbon- and boardlike nanostructures of nickel hydroxide: Synthesis, characterization, and electrochemical properties," *Journal of Physical Chemistry B,* vol. 109, pp. 7654-7658, Apr 2005.

[24] Y. W. Tan, S. Srinivasan, and K. S. Choi, "Electrochemical deposition of mesoporous nickel hydroxide films from dilute surfactant solutions," *Journal of the American Chemical Society,* vol. 127, pp. 3596-3604, Mar 2005.

[25] M. H. Cao, X. Y. He, J. Chen, and C. W. Hu, "Self-assembled nickel hydroxide three-dimensional nanostructures: A nanomaterial for alkaline rechargeable batteries," *Crystal Growth & Design,* vol. 7, pp. 170-174, Jan 2007.

[26] J. F. Wolf, L. S. R. Yeh, and A. Damjanovic, "Anodic oxide-films at nickel electrodes in alkaline-solutions .1. kinetics of growth of the beta-Ni(OH)2 phase," *Electrochimica Acta,* vol. 26, pp. 409-416, 1981.

[27] A. Seghiouer, J. Chevalet, A. Barhoun, and F. Lantelme, "Electrochemical oxidation of nickel in alkaline solutions: a voltammetric study and modelling," *Journal of Electroanalytical Chemistry,* vol. 442, pp. 113-123, Jan 1998.

[28] M. Alsabet, M. Grden, and G. Jerkiewicz, "Electrochemical Growth of Surface Oxides on Nickel. Part 1: Formation of alpha-Ni(OH)(2) in Relation to the Polarization Potential, Polarization Time, and Temperature," *Electrocatalysis,* vol. 2, pp. 317-330, Dec 2011.

[29] B. Macdougall and M. J. Graham, "Growth of thick anodic oxide-films on nickel in borate buffer solution," *Journal of the Electrochemical Society,* vol. 128, pp. 2321-2325, 1981.

[30] A. Visintin, A. C. Chialvo, W. E. Triaca, and A. J. Arvia, "The electroformation of thick hydrous nickel-hydroxide films through the appllcation of periodic potential signals," *Journal of Electroanalytical Chemistry,* vol. 225, pp. 227-239, Jun 1987.

[31] C. C. Streinz, A. P. Hartman, S. Motupally, and J. W. Weidner, "The effect of current and nickel nitrate concentration on the deposition of nickel hydroxide films," *Journal of the Electrochemical Society,* vol. 142, pp. 1084-1089, 1995.

[32] C. C. Streinz, S. Motupally, and J. W. Weidner, "The effect of temperature and ethanol on the deposition of nickel hydroxide films," *Journal of the Electrochemical Society,* vol. 142, pp. 4051-4056, 1995.

[33] J. L. Ord, "An optical study of the deposition and conversion of nickel hydroxide films," *Surface Science,* vol. 56, pp. 413-424, 1976.

[34] D. Tench and L. F. Warren, "Electrodeposition of conducting transition metal oxide/hydroxide films from aqueous solution," *Journal of The Electrochemical Society,* vol. 130, pp. 869-872, 1983.

[35] Y. W. D. Chen and R. N. Noufi, "Electrodeposition of nickel and cobalt oxides onto platinum and graphite electrodes for alkaline water electrolysis," *Journal of the Electrochemical Society,* vol. 131, pp. 731-735, 1984.

[36] M. K. Carpenter, R. S. Conell, and D. A. Corrigan, "The electrochromic properties of hydrous nickel oxide," *Solar Energy Materials,* vol. 16, pp. 333-346, 1987.

[37] S. Morisaki, K. Kawakami, and N. Baba, "Formation of nickel oxyhydroxide thin films by electrodeposition and their electrochromic characteristics," *Japanese journal of Applied Physics,* vol. 27, pp. 314-318, 1988.

[38] D. A. Corrigan and S. L. Knight, "Electrochemical and spectroscopic evidence on the participation of quadrivalent nickel in the nickel hydroxide redox reaction," *Journal of The Electrochemical Society,* vol. 136, pp. 613-619, 1989.

[39] H. Lim and S. Verzwyvelt, "Effects of electrode thickness on power capability of a sintered-type nickel electrode," *Journal of Power Sources,* vol. 62, pp. 41-44, 1996.

[40] E. Kalu, T. Nwoga, V. Srinivasan, and J. Weidner, "Cyclic voltammetric studies of the effects of time and temperature on the capacitance of electrochemically deposited nickel hydroxide," *Journal of Power Sources,* vol. 92, pp. 163-167, 2001.

[41] K.-W. Nam, E.-S. Lee, J.-H. Kim, Y.-H. Lee, and K.-B. Kim, "Synthesis and Electrochemical Investigations of Ni1− x O Thin Films and Ni1− x O on Three-Dimensional Carbon Substrates for Electrochemical Capacitors," *Journal of The Electrochemical Society,* vol. 152, pp. A2123-A2129, 2005.

[42] M.-S. Wu, Y.-A. Huang, and C.-H. Yang, "Capacitive behavior of porous nickel oxide/hydroxide electrodes with interconnected nanoflakes synthesized by anodic electrodeposition," *Journal of The Electrochemical Society,* vol. 155, pp. A798-A805, 2008.

[43] M.-S. Wu, Y.-A. Huang, J.-J. Jow, W.-D. Yang, C.-Y. Hsieh, and H.-M. Tsai, "Anodically potentiostatic deposition of flaky nickel oxide nanostructures and their electrochemical performances," *International Journal of Hydrogen Energy,* vol. 33, pp. 2921-2926, 2008.

[44] P. H. Humble, J. N. Harb, and R. LaFollette, "Microscopic nickel-zinc batteries for use in autonomous microsystems," *Journal of the Electrochemical Society,* vol. 148, pp. A1357-A1361, 2001.

[45] C. Iwakura, H. Murakami, S. Nohara, N. Furukawa, and H. Inoue, "Charge–discharge characteristics of nickel/zinc battery with polymer hydrogel electrolyte," *Journal of Power Sources,* vol. 152, pp. 291-294, 2005.

[46] K. Gerasopoulos, M. McCarthy, E. Royston, J. N. Culver, and R. Ghodssi, "Nanostructured nickel electrodes using the Tobacco mosaic virus for microbattery applications," *Journal of Micromechanics and Microengineering,* vol. 18, p. 104003, 2008.

[47] M. Yao, K. Okuno, T. Iwaki, M. Kato, K. Harada, J.-J. Park, *et al.*, "Nickel substrate having three-dimensional micronetwork structure for high-power nickel/metal-hydride battery," *Electrochemical and Solid-State Letters,* vol. 10, pp. A56-A59, 2007.

[48] H. Zhang, X. Yu, and P. V. Braun, "Three-dimensional bicontinuous ultrafast-charge and-discharge bulk battery electrodes," *Nature Nanotechnology,* vol. 6, pp. 277-281, 2011.

[49] Z. S. Wu, K. Parvez, X. Feng, and K. Müllen, "Graphene-based in-plane micro-supercapacitors with high power and energy densities," *Nature Communications,* vol. 4, 2013.

CHAPTER 5

ELECTRODES FOR LITHIUM-ION BATTERIES

5.1 Background and Motivation

Li-ion batteries are one of the most widely studied battery chemistries and make up the vast majority of the commercial battery market. Ever since the introduction of the first commercial Li-ion battery by Sony in 1991, its market share has grown rapidly, and Li-ion technology has become the standard power source for an increasingly diverse range of products including cell phones, computers, cameras, and more recently, electric vehicles [1]. These batteries possess higher energy density and longer cycle life than the $Ni(OH)_2$-based batteries discussed in the previous chapter and hence, enable the realization of electrodes with higher energy storage capabilities for a given size, rendering them commercially more appealing. In addition, there are a wide variety of possible Li-ion chemistries, offering flexibility in terms of the design and fabrication of the electrodes. Hence, one of the focuses of this study is on the application of the multilayer electrode approach using Li-ion battery chemistries.

The operation principle of the Li-ion batteries relies on the transport of Li ions (Li^+) between the positive and negative electrodes of the battery as the battery is charged and discharged. Therefore, these batteries have often been referred to as rocking chair batteries [1]. The conceptual rendering summarizing the electrochemical processes inside a Li-ion battery during the charge and discharge processes is illustrated in Figure 5.1.

Although metallic Li has an extremely high energy density of 3860 mAh g^{-1}, it is generally not preferred as an anode material in rechargeable batteries. One of the reasons for avoiding the use of metallic Li as the electrode is related to its relatively low melting point (~180 ºC). Also, large dendrites tend to form on the Li surface during the charging process, particularly at high rates, which may penetrate through the separator and lead to

shorting of the cell. Moreover, Li has been reported to exhibit high reactivity toward electrolytes [2]. For these reasons, instead of pure metallic Li, various materials that can host the Li ions have been utilized as the positive and negative electrodes of the Li-ion batteries.

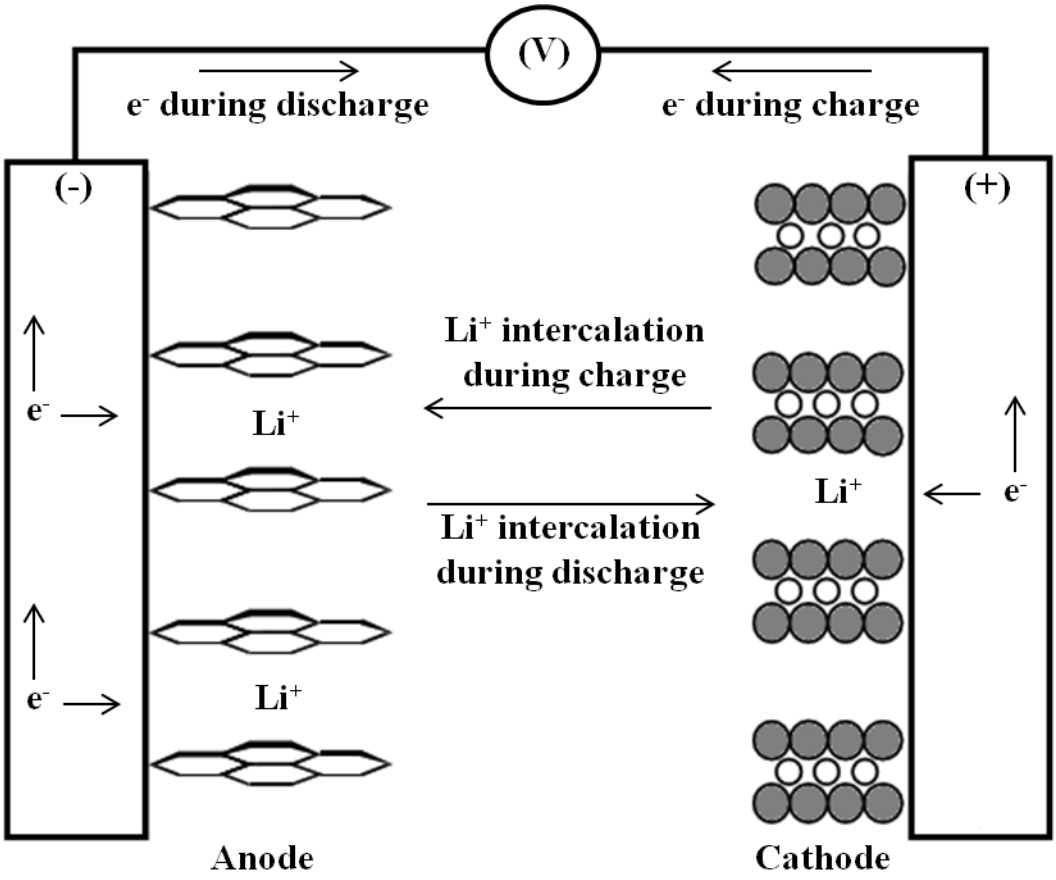

Figure 5.1: Illustration of the electrochemical processes inside a Li-ion battery cell composed of a carbonaceous negative material (anode) and a metal oxide positive material (cathode) [1]

The amount of energy stored in a cell is determined by the ability of the electrode materials to host high content of Li ions. Unlike the other battery chemistries, a wide variety of materials exist for the three main components (i.e., anode, cathode, and electrolyte) of Li-ion batteries and all of these components play a vital role on the overall

performance of the battery. The most popular materials utilized for each component are summarized in Figure 5.2. Depending on the application, certain combinations of materials for the battery components may be preferred over the others. Since the focus of this study is on the high-power electrodes, the emphasis will be on the materials with rapid charge and discharge capabilities.

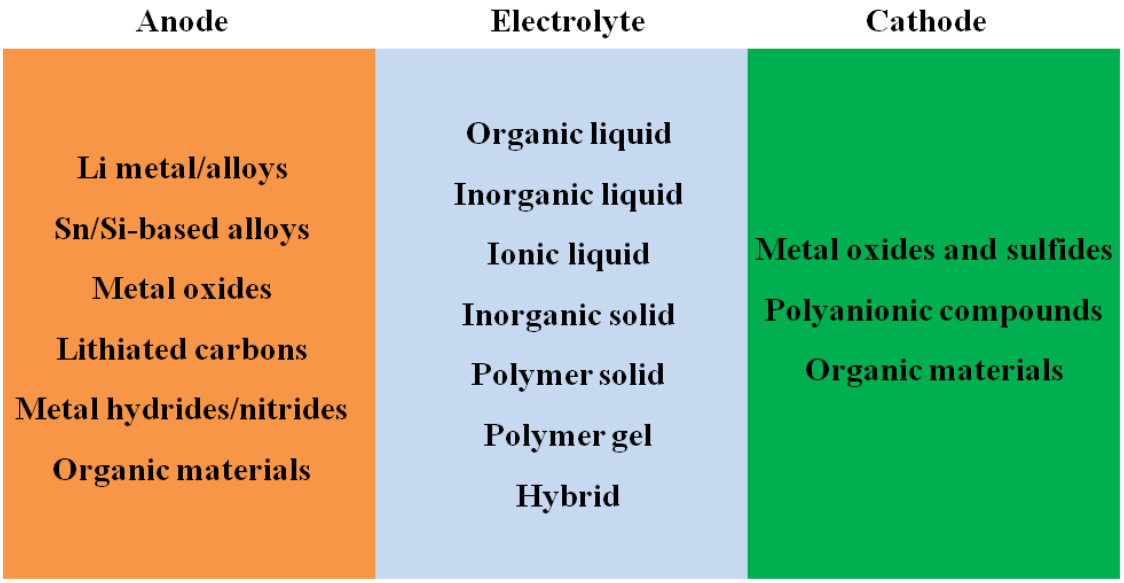

Figure 5.2: Electrode materials and electrolytes studied for Li-ion batteries [3]

There are several active materials exhibiting outstanding capacity for ion storage and thus, possessing high specific energy. However, these materials suffer from the large volume changes that occur during the insertion (i.e., lithiation) and extraction (i.e., delithiation) of Li ions, which potentially lead to significant deformations in the active material, reducing the amount of Li ions it can host. Another commonly encountered issue is the low ionic and electronic conductivity of some of these active materials, resulting in low power densities. The rationally designed and deterministically engineered architectures offered by this study allow one to overcome these limitations to a great extent while maintaining high energy storage capabilities.

5.2 Choice of Materials

As can be seen in Figure 5.2, there are a large number of potential combinations of materials for Li-ion batteries. The main criteria in choosing the best materials combination are its high-power capabilities (i.e., enhanced intrinsic properties such as high ionic and electronic conductivity) and the ability to incorporate the material of choice into the multilayer structures.

In this section, commonly studied materials for anode and cathode electrodes, as well as electrolytes will be briefly discussed and the choice of specific materials for the fabrication of high-power electrodes in this study will be described.

5.2.1 Anode Materials

Based on their Li storage mechanism, active materials used as anodes can be divided into three categories: (1) alloys, (2) intercalation materials, and (3) transition metal compounds.

5.2.1.1 Alloys

The first group of materials involves alloy systems composed of elements such as Si, Ge, Al, Sb, and Sn. These materials are capable of storing more than one Li atom per host metal atom (e.g., $Li_{4.4}Si$, $Li_{4.4}Ge$, Li_3Sb etc.) and thus, yield high energy density [4]. Pure Si, for example, has the highest known theoretical specific capacity of 4200 mAh g^{-1}, which is even higher than pure metallic Li [5]. However, the main obstacle in the use of these pure metals is the significant volume expansion and contraction during lithiation and delithiation processes, respectively. This may result in poor cycling performance of the battery due to cracking or even pulverization of the electrode materials. In order to alleviate this fracture-induced capacity decay problem during cycling, intermetallic materials (AB) involving Sn and Sb have been utilized as electrodes that undergo the following reaction:

$$AB + x\text{Li} \rightarrow \text{Li}_x\text{AB} \quad (5.1)$$

where A and B are two metals forming the alloy. These materials have been shown to be able to accommodate significant volume changes more easily [3]. Some of these alloys reported as potential anode materials include Cu_6Sn_5, NiSn, InSb, and Cu_2Sb [6-9]. However, these alloys have been shown to possess lower gravimetric energy density compared to their pure counterparts [10].

These metallic materials are highly suitable for high-power applications due to their high electronic conductivity. The processing of these metallic materials is also quite compatible with the fabrication processes reported in this study. Among the aforementioned alloys, NiSn was preferred, since its use as an active material for high-power battery anodes with ultrafast charge and discharge capabilities have been successfully demonstrated by electrodepositing a conformal layer onto an inverse opal 3D Ni electrode [11].

5.2.1.2 Intercalation Materials

This group of anode electrodes undergoes insertion reactions during the lithiation process. They are mainly made of carbonaceous (e.g., graphite) materials that tend to maintain their structural integrity throughout long charge and discharge cycles. Hence, capacity fading after numerous charge/discharge cycles is quite insignificant. They are also suitable for high rate charge and discharge operations as their conductivity, as well as the diffusivity of Li within these materials, is rather high. However, compared to other types of anode materials, the number of Li atoms that can be stored per site is limited (e.g., LiC_6), resulting in a relatively lower energy density (e.g., 372 mAh g^{-1} for commercial graphite-based anode) [10].

Although carbonaceous materials are intrinsically suitable for high-power applications, the formation of conformal layers of these materials on relatively complex

3D architectures is difficult. Hence, they were not considered as a potential active material in this study.

5.2.1.3 Transition Metal Compounds

Transition metal compounds used as anode materials are typically binary transition metal oxides that have rock salt structures (i.e., structures having fcc anions with octahedral sites occupied by cations), which do not possess any sites to host Li atoms. Consequently, the lithiation can only occur through conversion reactions as shown:

$$M_mX_n + 2nLi^+ + 2ne^- \rightarrow nLi_2X + mM \quad (5.2)$$

where M represents a transition metal (e.g., Ni, Cu, Fe, Co) and X is either one of the following: O, N, S, or F. As shown in Equation 5.2, this particular mechanism allows the storage of at least two Li atoms per molecule, yielding higher capacities than the carbonaceous materials. However, materials relying on conversion reactions have been reported to exhibit both slow kinetics and a large hysteresis during charging and discharging of the Li-ion battery [12]. As a result, rapid charging can cause plating of the Li metal on the electrode surface instead of lithiation of the active material, which may have undesired outcomes.

Although these materials have been reported to suffer from slow kinetics, NiO was utilized as an active material because of its ease of fabrication. It was previously demonstrated in Chapter 4.3.2 that it is possible to deposit a conformal layer of $Ni(OH)_2$ onto the relatively complex 3D Ni backbone. NiO electrode can then be obtained by simply calcinating $Ni(OH)_2$-coated structures at relatively high temperatures. The same approach was also utilized for the fabrication of NiO-based supercapacitors as will be discussed in Chapter 6.2.

5.2.2 Cathode Materials

In general, cathode materials possess lower specific capacities than their anode counterparts. These materials can be investigated under two major groups: (1) transition metal oxides and sulfides and (2) polyanion-based materials.

5.2.2.1 Transition Metal Oxides and Sulfides

$LiCoO_2$ is currently the dominant cathode material in the Li-ion battery market [10]. It has a relatively high ion diffusivity and electrical conductivity of 10^{-10} - 10^{-8} cm^2 s^{-1} and 10^{-4} S cm^{-1}, respectively [12]. However, this material reportedly suffers from severe structural stability degradation. Although several methods, including doping with trivalent ions and coating with metal oxides, have been proposed to suppress Co dissolution, other factors, including the high cost and high toxicity of Co, resulted in the search for alternative materials [3].

One of the promising alternatives is $LiMn_2O_4$. It is an environmentally benign and low-cost material. However, it exhibits an intrinsic low rate performance due to its low Li ion diffusivity and electrical conductivity, which have been reported to be in the range of 10^{-11} - 10^{-9} cm^2 s^{-1} and 10^{-6} S cm^{-1}, respectively, which are at least an order of magnitude less than $LiCoO_2$. To overcome these intrinsic power limiting issues, nanostructuring of these materials have been suggested [12]. The other problem associated with this material is the slow dissolution of Mn in the electrolyte during the charge and discharge cycles, which can be partially alleviated by coating and doping techniques [10, 12].

Another cathode material that belongs to this group is $LiNi_{0.5}Mn_{1.5}O_4$, which has also been extensively studied as a strong candidate for Li-ion cells with high energy and power density because of its high operating potential and reversible capacity, as well as significant chemical stability. Yet the low conductivity of this material is considered as an obstacle for high power applications. To alleviate this issue, doping the structure with transition metal ions has been suggested. For example, Ru-doped $LiNi_{0.5}Mn_{1.5}O_4$ has been demonstrated to possess a capacity of 135 mAh/g at a discharge rate of 10 C, and a

capacity retention of 82.6% has been reported for it at the 500th cycle with charge and discharge rates of 10 C [12].

Among the aforementioned cathode materials, MnO_2 was chosen as the active material to be tested for high-power electrodes in this study. The main reasons for selecting this particular material are its relatively simple deposition process as compared to other alternatives and its successful demonstration as a microbattery cathode with ultrafast charge and discharge capabilities [13]. It is also an electrodepositable material, rendering it suitable for conformal deposition in a controlled fashion.

5.2.2.2 Polyanionic Materials

Due to its low cost and high thermal stability, as well as eco-friendliness, $LiFePO_4$ is a desirable polyanionic material for use in cathode applications. However, the drawbacks of this material are its relatively sluggish kinetics and its intrinsically low electronic conductivity of 10^{-11} S cm^{-1}, which is several orders of magnitude lower than metal oxides. Hence, its operation at high rates results in significantly reduced capacities. In order to overcome the conductivity-related limitation, various methods have been proposed, which include doping the structure with metal, reducing the particle size, and coating the structure with conductive materials [12].

Coating or mixing the $LiFePO_4$ structure with a conductive material, such as low concentrations of Cu and Ag metal powders, has been shown to increase the power density without affecting the structural integrity [14]. Coating $LiFePO_4$ with carbon shells of 1-2 nm thickness has also been demonstrated as an effective way of increasing the power density, and a capacity of 90 mAh g^{-1} was obtained at a discharge rate of 60 C [15]. The cycling performance has also been shown to be outstanding where 5% capacity loss has been observed after 1100 charge and discharge cycles with a coulombic efficiency of approximately 100%. In another study, a nanocomposite made up of highly dispersed $LiFePO_4$ nanoparticles in a nanoporous carbon matrix filled with liquid electrolyte yielded a capacity of 45 mAh g^{-1} at a rate of 230 C [16]. A significant increase

in the electrical conductivity has also been obtained through doping $LiFePO_4$ with supervalent cations such as Al^{3+}, Ti^{4+}, and Mg^{2+} resulting in an electronic conductivity of 10^{-2} S cm^{-1} [12, 17].

The procedures (e.g., doping) described in the previous paragraphs, in which the polyanionic materials need to undergo to become suitable for high-power applications, render the overall fabrication process quite complicated. Also, these materials are hard to incorporate into the relatively complex 3D architectures in a conformal fashion. Even if a conformal coating is achieved, these materials possess relatively low specific energy, indicating that larger amounts of these materials and thus, multilayer structures with higher number of laminations would be required to enable high-power electrodes with high capacities (> 10 mAh).

5.2.3 Electrolytes

As shown in Figure 5.2, there are also a wide variety of electrolytes that can be utilized in Li-ion batteries. Recently, several studies have focused on the development of solid-state electrolytes [3]. The primary motivation of these studies is to avoid the use of flammable, non-aqueous liquid electrolytes that pose the risk of potential explosion under certain conditions (e.g., high temperature due to internal and/or external factors) [3]. Solid-state electrolytes, however, are generally not suitable for high power applications due to their low ionic conductivities. As shown in Table 1.2 in Chapter 1, the ionic conductivity of liquid electrolytes is several orders of magnitude higher than that of their solid counterparts. In addition, achieving good contact between the solid-state electrolyte and the rather complex 3D electrode architectures can be quite challenging.

In order to minimize the limiting effects that might originate from the choice of electrolyte materials, liquid-state electrolytes with high ionic conductivities were preferred in this study and were also selected in previous studies involving high-power battery electrodes [11, 13]. The electrolyte used in the electrochemical characterization of

the fabricated Li-ion battery electrodes was prepared by adding 1 M lithium perchlorate ($LiClO_4$) into a 1:1 mass ratio mixture of ethylene carbonate (EC) and dimethylene carbonate (DMC). The reported ionic conductivity ($8.4x10^{-3}$ S cm^{-1}) of this solution is one of the highest among the electrolytes used in Li-ion batteries. Also, $LiClO_4$ reportedly exhibits a high anodic stability and forms relatively lower impedance solid-electrolyte interphase (SEI). Moreover, it is relatively less hygroscopic and more stable to ambient moisture, rendering it easier to handle [18].

5.3 Fabrication of the Electrodes

As mentioned in the previous section, three different active materials were incorporated into the multilayer structures: MnO_2 as the cathode active material, and NiO and NiSn as the anode active materials. Except for the case of NiSn electrodes, the current collector was fabricated the same way as for the $Ni(OH)_2$ electrode that was thoroughly described in Chapter 4. Hence, the fabrication details will not be covered again in this chapter. The novel fabrication method used for the preparation of NiSn electrodes will be discussed here in more detail.

5.3.1 MnO_2 Cathode

After the fabrication of the anchor-supported, multilayer Ni structures, the electrodeposition of MnO_2 layer was performed in an aqueous solution consisting of 0.1 M manganese acetate ($Mn(CH_3COO)_2$) and 0.1 M anhydrous sodium sulfate (Na_2SO_4), using a two-electrode cell configuration similar to the one described in Chapter 4.4.2 where the multilayer structure and a platinum sheet were utilized as the working and the counter electrodes, respectively [19]. Through the use of a potentiostat (WaveDriver 10, Pine Instruments), cathodic potential pulses (t_{on} = 1 s, t_{off} = 9 s, 10% duty cycle) were applied to the electrode while the electrolyte solution was gently stirred.

An SEM image showing the sidewall of the Ni layers following the active material deposition along with the x-ray photoelectron spectroscopy (XPS) spectrum of the active material is shown in Figure 5.3. The XPS spectrum was found to be in good agreement with previously reported spectra in the literature [13].

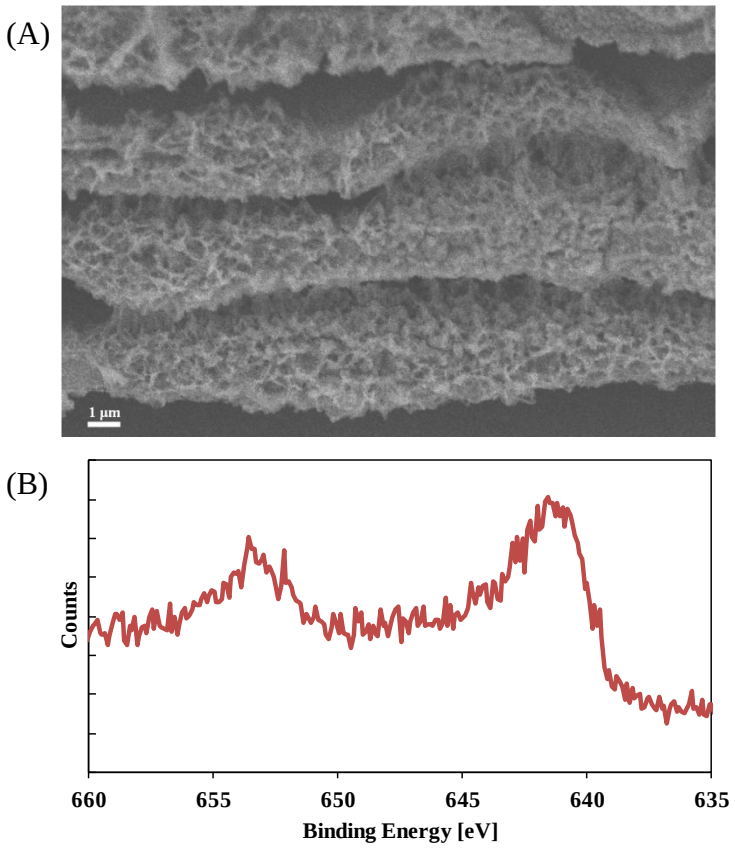

Figure 5.3: (A) SEM image of the sidewall after MnO_2 deposition, (B) XPS spectrum of the electrodeposited MnO_2 film

Following the conformal electrodeposition of the MnO_2 film, the sample was immersed in molten Li salts for the lithiation process. The molten salt was prepared by mixing finely ground 3:2 mole ratio of $LiNO_3$ to LiOH in a glass vial and heating the mixture to 300 °C in an inert atmosphere oven. The sample was held at 300 °C for 1 hour and then cooled down to room temperature. After rinsing with DI water to remove the excess salt residues, the sample was dried at 75 °C for approximately 6 hours.

To prevent MnO_2 from being the rate-limiting electrode, a commercial graphite anode (Sony) with a capacity of at least five times greater than that of the cathode was utilized during the charge and discharge tests.

5.3.2 NiO Anode

The fabrication process of the NiO electrodes is almost identical to the $Ni(OH)_2$ electrodes described in detail in Chapter 4.4.2. The only difference is the very last step where the calcination of $Ni(OH)_2$ is performed.

Upon completion of the electrodeposition of a conformal $Ni(OH)_2$ film onto the multilayer Ni backbone, the electrode was placed in the oven and heated in air from room temperature to 300 °C at a rate of 5 °C min^{-1}. The sample was maintained at 300 °C for two hours, ensuring a complete conversion of $Ni(OH)_2$ to NiO, and subsequently cooled to room temperature. No lithiation process was conducted before the characterization of the electrodes. Instead, a Li foil was utilized as the counter electrode during the performance tests.

5.3.3 NiSn Anode

Initially, NiSn electrodes were fabricated the same way as the previously described electrodes, where the active material was electrodeposited onto the multilayer backbone structure. However, it was later determined that the NiSn deposits are compatible with the other metals, indicating that neither the Ni plating solution nor the Cu plating solution attacks the NiSn films during the sequential electroplating process. This material was also found to be resistant to the selective Cu etchant. Even after being in contact with the etchant for more than 24 hours, no dissolution was observed in the active material.

These findings promoted the development of a novel fabrication approach that involves a triple-bath plating setup as shown in Figure 5.4.A, in which the active material

was electrodeposited concurrently with the structural Ni layers and sacrificial Cu layers. The advantage of this triple-bath approach is that it significantly reduces the total fabrication time by eliminating the pulsed plating steps with long down times where the active material deposition is performed.

(A)

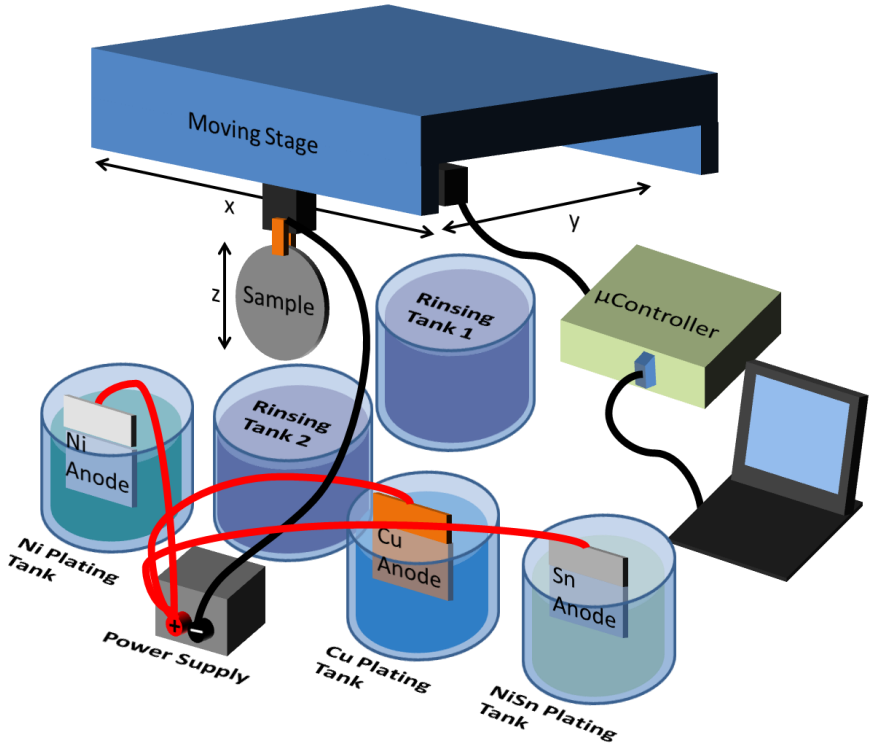

(B)

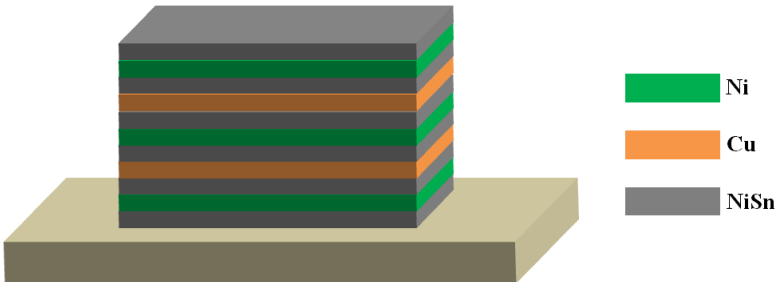

Figure 5.4: (A) Schematic of the triple plating setup utilized for the fabrication of NiSn electrodes, (B) electroplating sequence of the layers using the triple plating setup

The sequence of the layer deposition is schematically illustrated in Figure 5.4.B. First, a NiSn layer was electroplated from a bath whose composition is given in Table

5.1. This was followed by the electroplating of the structural Ni layer. Next, another NiSn layer was electroplated, sandwiching the Ni layer. Thereafter, the sacrificial Cu layer was electroplated and from this point on, the same deposition order was repeated until the multilayer structure with the desired number of layers was obtained. Upon deposition of the Ni anchors, the sacrificial Cu layers were completely removed as described in Chapter 2.3.1.

Table 5.1: The composition of the NiSn electroplating bath [11]

Compounds	**NiSn Electroplating Bath**
$NiCl_2$	8 g
$SnCl_2.2H_2O$	20 g
$K_4P_2O_7$	300 g
$KNaC_4H_4O_6.4H_2O$	8 g
Glycine	8 g
DI water	1 L

A disadvantage of this approach is that smooth layers of NiSn could not be achieved especially if the thickness of the film is close to or exceeds 1 μm. Although a rough surface might be desirable as it increases the surface area, the pattern is transferred to the subsequent layers, and thus, the control over the dimensions of the layers can be lost. As a result, the thickness of the NiSn layers was confined to a maximum of several hundreds of nanometers. The optimum dimensions for the NiSn layers were found by the diffusion-limited models described in the following section.

The x-ray diffraction (XRD) pattern of the NiSn deposit is shown in Figure 5.5. It was found to be in good agreement with the literature [7, 20, 21]. To confirm that the composition of the active material did not change significantly throughout the fabrication process, the XRD patterns of the NiSn layers from the bottom portion of the multilayer electrode were compared to the uppermost layers, and no significant difference was detected.

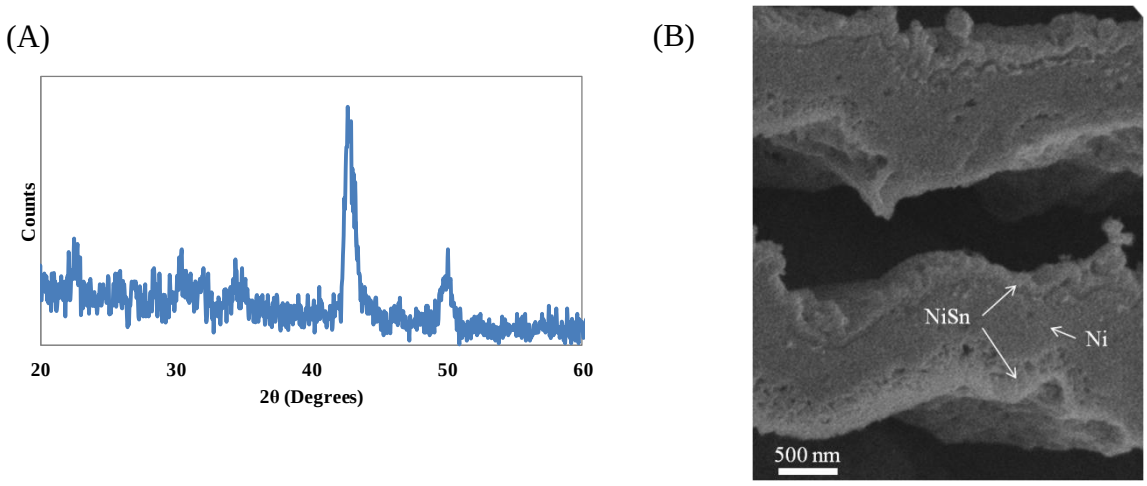

Figure 5.5: (A) XRD pattern of the NiSn film, (B) SEM image showing the cross-sectional view of the Ni layers sandwiched between the NiSn active material films

5.4 Design and Modeling of the Electrodes

A detailed description of the modeling approach and the motivations were discussed in Chapter 4.2. The same principles used for modeling the $Ni(OH)_2$ electrodes were applied to the Li-ion systems. By utilizing diffusion-limited models, the optimum dimensions for the deposited active material film on each layer of the metallic backbone, as well as the inter-layer spacing, were determined.

5.4.1 Diffusion-Limited Model to Determine the Active Material Thickness

A one-dimensional (1D) spatial model for the Li^+ diffusion was developed, considering an infinite plane sheet of thickness L with one side exposed to the electrolyte, while the other one is in contact with the current collector, as shown in Figure 5.6. This simple diffusion-limited model has proven quite useful in predicting the performance of Li-ion batteries [22, 23]. The model is based on the assumption that diffusion is the dominant mechanism for the transportation of the Li^+ ions. Hence, the constant-current charge and discharge times are solely limited by the utilization of the active material;

losses originating from the electrolyte and solid-electrolyte interphase (SEI) are neglected. It was also assumed that the ion and electron fluxes are uniformly distributed over the entire surface.

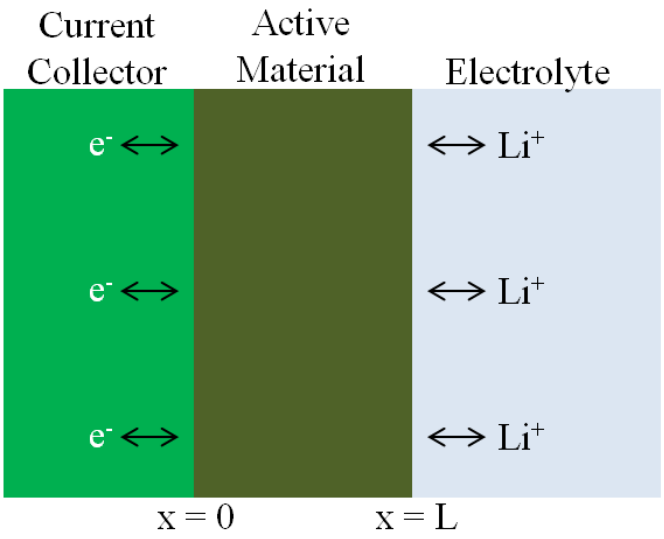

Figure 5.6: Electrode model assuming an infinitely wide plane sheet of thickness L

As will be discussed in section 5.5, the best performance in terms of power delivery was obtained from the NiSn anodes. Therefore, this particular material was taken as a basis when modeling the Li-ion diffusion within the active material. Since NiSn is a metallic alloy and thus, has a relatively high conductivity, the electric field in the anode during current flow is low. Following the aforementioned assumptions, the equation of continuity in one spatial dimension can be written as:

$$\frac{\partial C_{Li}}{\partial t} = D \cdot \frac{\partial^2 C_{Li}}{\partial x^2} \tag{5.3}$$

where C_{Li} and D are the concentration (mol cm^{-3}) and the diffusion coefficient (cm^2 s^{-1}) of the Li ions in the active material, respectively. In general, D is a function of the temperature, the composition of the active material, as well as the concentration of the Li

ions. However, for the purposes of this model, D was assumed to be constant and uniform across the film thickness. Also, isothermal charge and discharge conditions were assumed. The value for D was taken from the literature which has been reported to be in the range of 10^{-9} to 10^{-10} cm^2 s^{-1} [24]. It will be shown later on in this section, the calculation of the optimum active material thickness is strongly dependent on the value selected for the diffusion coefficient. Therefore, the simulations were performed using both of the reported diffusion coefficient values to calculate a range for the optimum active material thickness.

The initial and boundary conditions for this model are given as:

at t = 0: $$C_{Li} = C_0 \tag{5.4}$$

at x = 0: $$\frac{\partial C_{Li}}{\partial x} = 0 \tag{5.5}$$

at x = L: $$D \cdot \frac{\partial C_{Li}}{\partial x} = \frac{i}{n \cdot F} \tag{5.6}$$

where C_0 is the initial Li concentration in the active material (mol cm^{-3}), i is the charge or discharge current density (A cm^{-2}), n is the valence number (1 for Li), and F is Faraday's constant (96485 C mol^{-1}).

Since the charge and discharge experiments were performed galvanostatically, (i.e., at constant current), the flux at the electrode-electrolyte interface was assumed to be uniform and constant, as indicated in Equation 5.6. At the interface of the current collector and the active material, no mass transfer is taking place and hence, the flux equals zero. When modeling the charging process of the electrode (i.e. delithiation process), the Li concentration for the initial condition was determined by the saturation concentration of Li in NiSn active material, which depends on the Li storage capacity of Sn. For an intermetallic compound like NiSn, one of the metals (Ni) reportedly acts as an electrochemically inactive matrix to buffer the variations in the volume of the electrode

during the alloying process of Li with the other metal (Sn) [25]. Several Li:Sn ratios have been reported in the literature [26]. Although it does not affect the simulation results for the optimum active material thickness, for the sake of obtaining quantitative data, the smallest ratio of 0.4 was selected. Based on this ratio, an initial Li concentration of 0.0192 mol cm^{-3} was calculated.

During the delithiation process, Li ions diffuse from the active material to the electrolyte, resulting in a concentration gradient that forms within the active material. This concentration gradient becomes more severe as the charge rate (i.e., current density) increases. If the rate is too high, it may not be possible for the Li ions to diffuse away from the active material in a desired duration of time. As an example, a charging duration of one minute (i.e., 60 C) was selected. The goal of the simulations was then to find the maximum thickness for the active material that allows the diffusion of all Li ions into the electrolyte in one minute.

The partial differential equation (PDE) given in Equation 5.3 was solved by finite element method (FEM). For this type of 1D parabolic PDE, Matlab's pdepe function was utilized (a detailed code can be found in Appendix.A). Starting with an active material thickness of 1 μm, the capacity of the active material was calculated along with the current density required to discharge the electrode in 60 seconds. Then, the simulations were performed using both the upper and lower limits on the diffusion coefficient, and the concentration profiles across the thickness of the active material were plotted as a function of time. Thereafter, the thickness was reduced and the same procedure was repeated for the reduced thickness value. The resultant profiles at each thickness for both diffusion coefficients are summarized in Table 5.2.A. The figure in Table 5.2.B shows the 2D concentration profile for the smaller diffusion coefficient at the 60^{th} second of the charging process for various NiSn film thicknesses.

The x, y, and z axes in the figures given in Table 5.2.A refer to the distance, time, and Li concentration, respectively. The profile at the zero distance indicates the

concentration of Li at the current collector-active material interface, where, at any given time after the start-up of the delithiation process, the highest Li concentration is observed. In the ideal case, a uniform Li distribution would be expected across the thickness of the active material, similar to the profile that is observed at the time zero (dark red line).

In the case of higher diffusion coefficient (i.e., 10^{-9} cm^2 s^{-1}), it can be seen that the concentration gradient across the film thickness does not change significantly throughout the duration of the delithiation process. For an active material thickness of 1 μm, a small gradient can be observed at the 60^{th} second (blue line) where the concentration of the Li drops slightly below zero at the electrode-electrolyte interface, indicating that some of the Li ions were not able to be transported to the electrolyte. Thus, the thickness of the active material must be reduced to be able to charge the electrode in 60 seconds. At thicknesses less than 0.8 μm, the concentration across the active material is zero and no concentration gradients are observed. This suggests that 0.8 μm is the maximum active material thickness for the electrodes that can be charged in 60 seconds, assuming that the diffusion coefficient remains constant and equal to 10^{-9} cm^2 s^{-1} throughout the charging process.

However, in the case of the lower diffusion coefficient (10^{-10} cm^2 s^{-1}), much more severe concentration gradients are observed across the film thickness. These gradients at the electrode-active material interface almost completely disappear when the active material thickness is reduced to 0.2 μm or less. This is also illustrated in the figure shown in Table 5.2.B where the remaining Li^+ concentration is plotted across the NiSn film with various thicknesses. As the active material thickness is increased, fewer Li^+ ions can be transferred into the electrolyte in 60 seconds. The difference between the profiles obtained using the two different diffusion coefficients illustrates the strong impact that the diffusion coefficient has on the optimal thickness of the active material for a high-power electrode.

Table 5.2: Concentration profiles of Li within the NiSn active material as a function of time at various thicknesses: (A) 3D profiles, (B) 2D profiles at the 60th second for D = 10^{-10} cm^2 s^{-1}

(A)		
Diffusion coefficient	**10^{-9} cm^2 s^{-1}**	**10^{-10} cm^2 s^{-1}**
Thickness : 1 µm	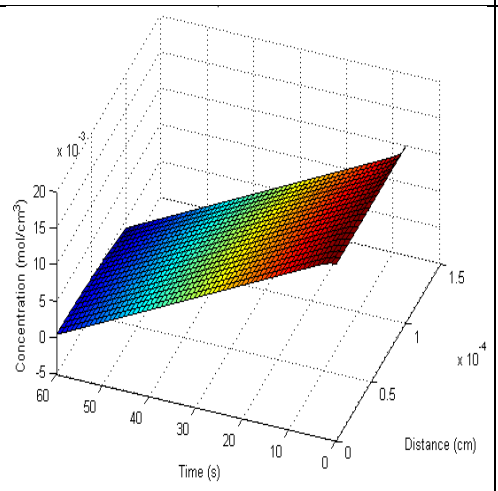	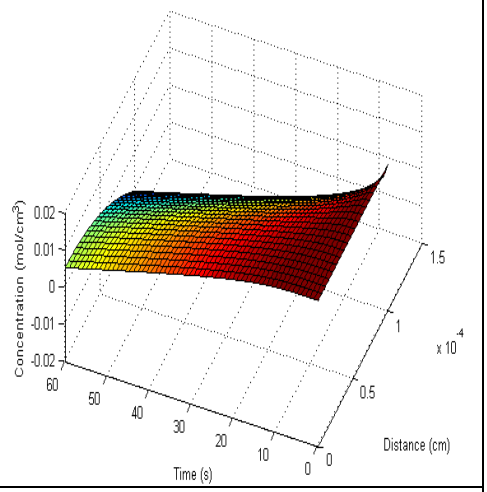
Thickness : 0.8 µm	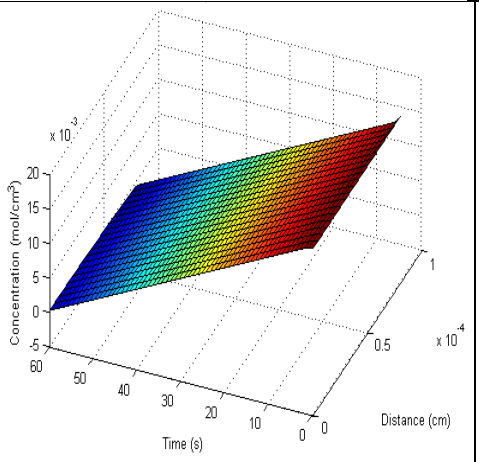	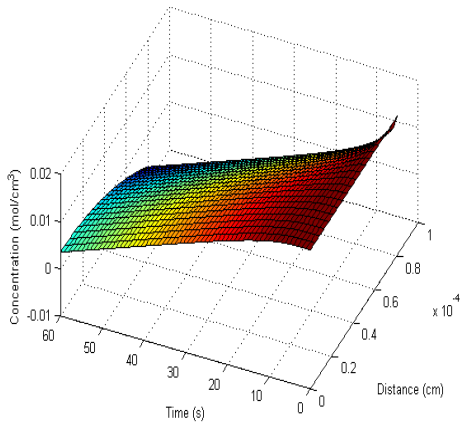
Thickness : 0.6 µm	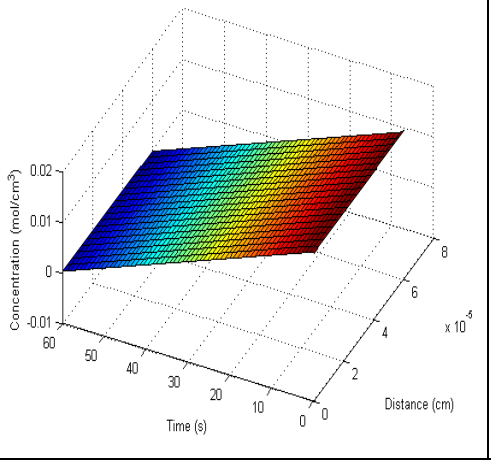	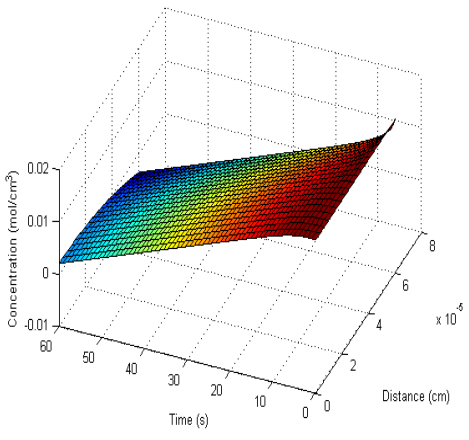

Table 5.2: *Continued*

Thickness: 0.4 µm	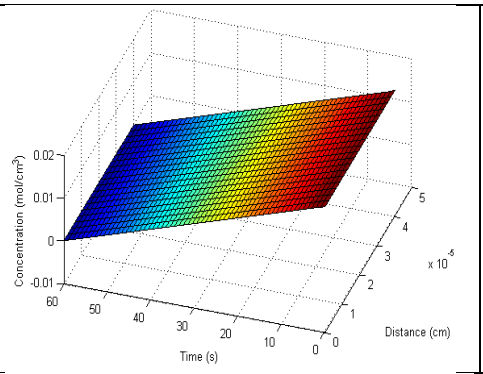	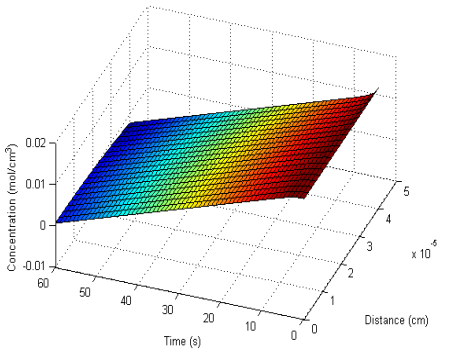
Thickness: 0.2 µm	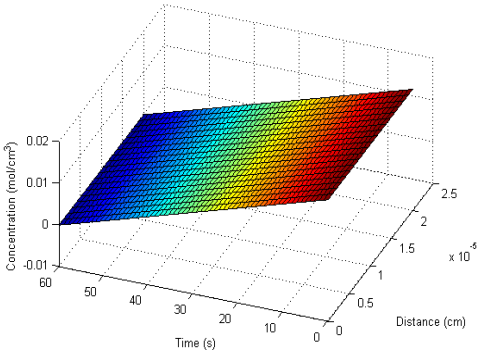	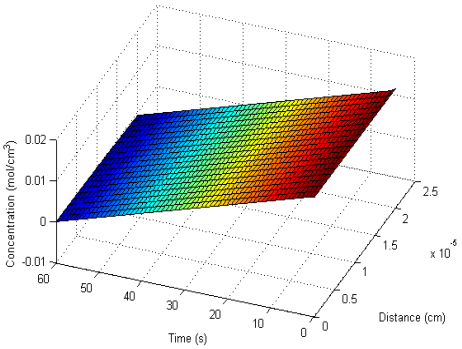
(B)		
	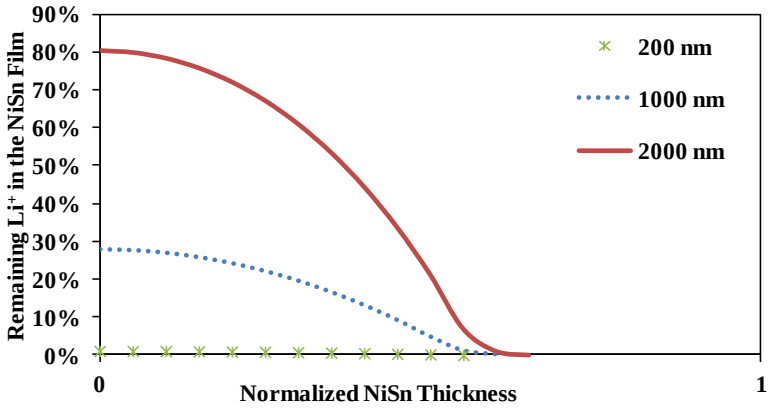	

5.4.2 Diffusion-Limited Model to Determine the Inter-layer Distance

The second model that was developed to determine the optimum inter-layer spacing, Two-dimensional (2D) modeling of the Li ion distribution across the electrolyte located between two adjacent layers of the multilayer electrode was performed. This is illustrated in Figure 5.7, showing both the top view and side view of the electrode. The distance between the etching holes in the top view corresponds to the width L of the

channel in the side view. As mentioned in Chapter 4.2.2, this width is determined by the mask design used during the lithography process and its flexibility is rather limited due to fabrication-related constraints of the photoresist mold.

The height H is the distance between two adjacent layers. This dimension is solely determined by the electroplating conditions and thus, has much greater flexibility. By adjusting the thickness of the sacrificial Cu layers, the H dimension can be easily tailored. The focus of the model will be on determining the optimum height of these channels for a given width L of 300 μm, which is the smallest possible distance due fabrication-related constraints, as discussed in Chapters 2 and 4. In the previous chapter (Table 4.3), it was shown that increasing the width results in the reduced capacity of the electrode due to the decrease in the number of layers that can be deposited for a given total thickness. This same principle applies for the Li-ion batteries. Therefore, the optimum spacing H was first calculated for a width of 300 μm. In addition, the dependency of the optimum spacing H on the channel width L was also explored (see Table 5.4),

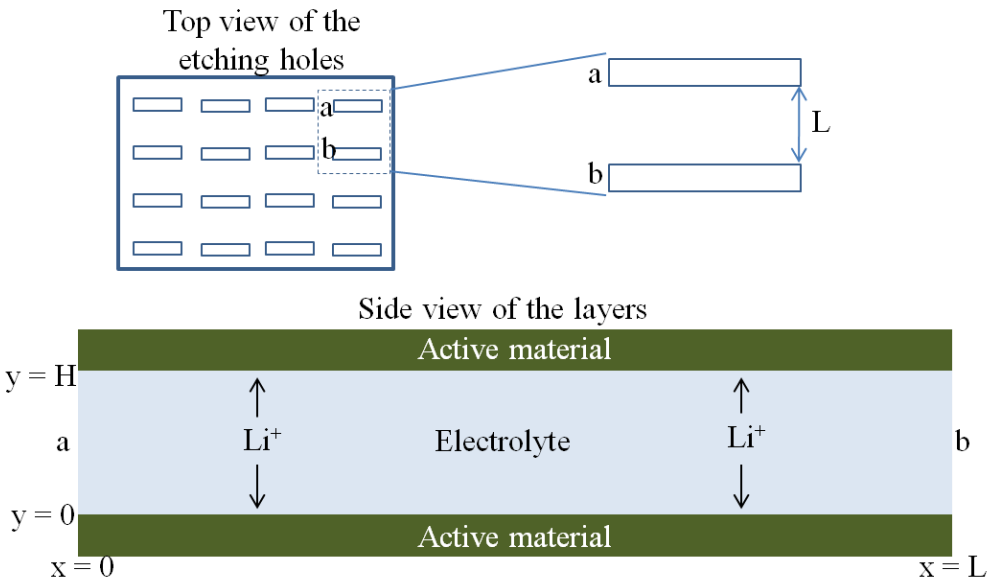

Figure 5.7: Model of the electrolyte between two adjacent layers of the multilayer electrode

The assumptions made for the previous 1D model, including diffusion-limited transport, constant diffusion coefficient, and uniform distribution of ion fluxes at the electrode surface, also hold for this 2D model of the channel. Additionally, it was also assumed that the Li ion concentration within the etching holes is the same as the bulk electrolyte outside the electrode during the operation of the electrode. The equation of continuity for two spatial dimensions can be written as:

$$\frac{\partial C_{Li}}{\partial t} = D \cdot \left(\frac{\partial^2 C_{Li}}{\partial x^2} + \frac{\partial^2 C_{Li}}{\partial y^2} \right) \tag{5.7}$$

As mentioned earlier in this chapter, the electrolyte used in the electrochemical characterization tests was prepared by dissolving 1 M Li salt in an organic solvent consisting of an equal mass mixture of EC and DMC (see section 5.2.3). The reported diffusion coefficient for this particular organic solvent is approximately 10^{-5} cm^2 s^{-1}, which is several orders of magnitude higher than the active material modeled in the previous section [27]. This indicates that the diffusion is not as severe a limiting factor as in the case of the 1D model of the active material.

The initial and boundary conditions for this 2D model are given as:

at t = 0: $$C_{Li} = C_{Li,b} \tag{5.8}$$

at x = 0: $$C_{Li} = C_{Li,b} \tag{5.9}$$

at x = L: $$C_{Li} = C_{Li,b} \tag{5.10}$$

at y = 0: $$D \cdot \frac{\partial C_{Li}}{\partial y} = \frac{i}{n \cdot F} \tag{5.11}$$

at y = H: $$D \cdot \frac{\partial C_{Li}}{\partial y} = \frac{i}{n \cdot F} \tag{5.12}$$

where $C_{Li,b}$ is the concentration of the bulk electrolyte (1 M). During the lithiation process, the Li ions in the electrolyte diffuse into the active material in y direction as shown in Figure 5.7. These depleted ions are replenished by the Li ions diffusing into channel from the bulk electrolyte in x direction. The goal of this model was to find the minimum height of the channel that allows the replenishment of the Li ions consumed during the lithiation process of the active material at high rates (e.g., 60 C). Minimizing the channel height is important as this will reduce the overall thickness of the structure and enable deposition of more layers, yielding electrodes with higher capacities for a given volume.

The necessary current to charge the active material located on the top and bottom portion of the channel (see Figure 5.7) was calculated from the thickness of the active material. As discussed in the previous section, the optimum thickness for the active material was calculated for two different diffusion coefficient values. When modeling the inter-layer spacing, to avoid any overestimation, the diffusion coefficient of the active material thickness was assumed to be the lowest value (i.e., 10^{-10} cm^2 s^{-1}), and hence, the active material thickness was assumed to be 0.2 μm.

Matlab's PDE toolbox was utilized to solve the PDE given in Equation 5.7 and plot the concentration profiles Li ions inside the channel as shown in Table 5.3. The x, y, and z axes in the figures shown in Table 5.3.A refer to the width of the channel, height of the channel, and concentration of the Li ions within the channel, respectively. The plotted profiles were obtained at the end of the charging process (i.e., at 60^{th} second). Both 3D and 2D profiles are provided for various channel heights.

Table 5.3: Concentration profiles of the Li ions in the electrolyte located inside the channels: (A) 3D profiles, (B) 2D profiles at the 60th second

	Channel Height	Concentration Profile (3D)
(A)	**1.30 µm**	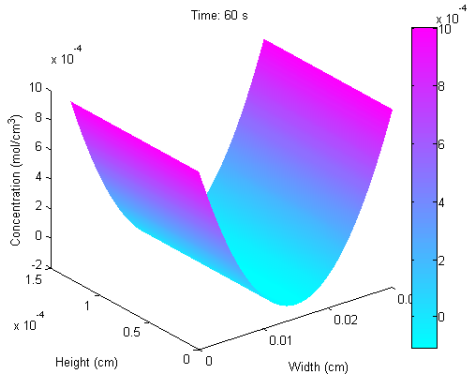
	1.40 µm	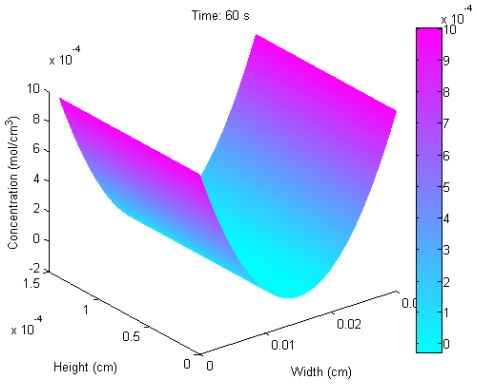
(B)		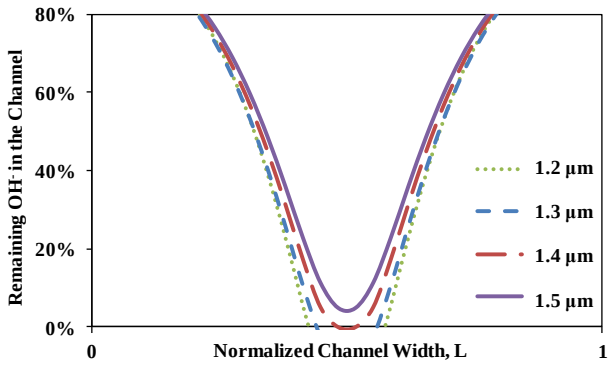

The same strategy as in the case of 1D model of the active material was followed, where the channel height was first set to 0.1 μm and then systematically increased by 0.1 μm. As expected, the lowest concentration was observed in the center region of the channel (i.e., x = L/2). For channel heights smaller than 1.4 μm, the concentration of the Li ions in the center region was found to be below zero, indicating that the ions were not able to be replenished by the lateral diffusion from the bulk electrolyte. This value is significantly larger than what was calculated for the $Ni(OH)_2$-based electrodes in the previous chapter. The primary reason for this difference is that the ion concentration in the KOH electrolyte for the $Ni(OH)_2$-based electrode is six times as high as the Li ion concentration in the EC:DMC electrolyte.

5.4.3 Performance Projections Based on the Diffusion-Limited Models

Based on the modeling results of the Li ions within the active material and the electrolyte provided in Tables 5.2 and 5.3, the optimum multilayer electrode that can be lithiated in 1 minute should feature a maximum NiSn thickness of 0.2 μm on each side of the layer, and the spacing between two adjacent active material films should be set to at least 1.4 μm with a 300 μm spacing between the etching holes. Such design is schematically illustrated in Figure 5.8. Therefore, the thickness of the sacrificial Cu layers should be set to 1.8 μm (1.4 μm + (2 x 0.2 μm)). The reasoning for selecting a thickness of 1.5 μm for the Ni layers was explained in Chapter 4.2.2.

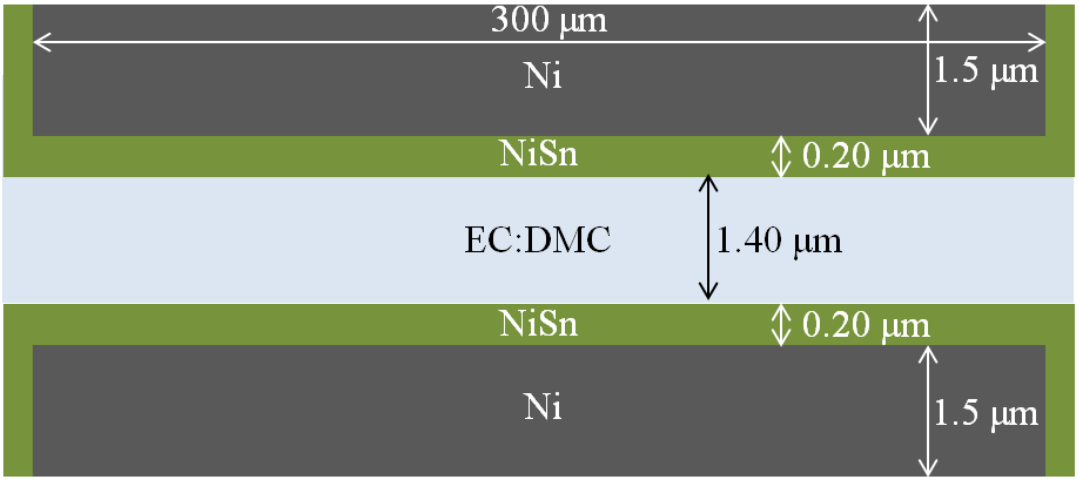

Figure 5.8: Optimum dimensions for the NiSn film thickness and the inter-layer spacing for the multilayer electrode

According to the optimum characteristic dimensions provided in Figure 5.8 and the total thickness constraint of 300 µm, the multilayer electrode fabricated on a footprint of 1 cm^2 should theoretically possess a total of 90 layers, which yields a total capacity of 1.47 mAh. This value is lower than what was obtained for the previous $Ni(OH)_2$-based electrodes under optimum conditions (i.e., 2.53 mAh), as a much higher number of layers (i.e., 153) were able to fit within the same mold volume in the previous case. Although a lower capacity is calculated for the current electrode, it corresponds to a higher energy density, since the operating potentials of the Li-ion electrodes is approximately more than twice as high as for the $Ni(OH)_2$ chemistries. Therefore, for a given volume of the system, NiSn electrodes are theoretically more favorable in terms of the energy and power densities.

Optimum dimensions of the NiSn electrodes were also calculated for different values of L, as shown previously for $Ni(OH)_2$-based electrodes in Chapter 4. Table 5.4 summarizes the modeling results for various width values L from 100 µm to 1 mm. The second column in Table 5.4 shows the corresponding inter-layer spacing for the given widths. Unlike the previous case of the $Ni(OH)_2$-based electrodes, varying width causes a

substantial change in the optimum inter-layer spacing. Increasing the width to 1 mm, for example, results in multilayer structures requiring a minimum inter-layer spacing of nearly 7 μm for complete ion diffusion. Reducing the width from 300 μm to 100 μm, on the other hand, causes the inter-layer spacing to drop from 1.45 μm to 0.18 μm. This also has a significant impact on the capacity, as the number of layers that can fit within a total thickness of 300 μm is profoundly increased from 89 to 144, which enables the capacity to increase from 1.47 to 1.90 mAh.

Table 5.4: Impact of the width between the etching holes (i.e., L) on the other dimensions and capacity of the multilayer electrode with a total thickness of 300 μm

Width, L (μm)	Height, H (μm)	Number of etching holes per layer	Net area per layer (cm^2)	Number of layers	Areal capacity (mAh cm^{-2})
100	0.18	400	1.28	144	1.90
200	0.65	280	1.50	117	1.80
300	1.45	220	1.60	89	1.47
400	2.50	180	1.68	68	1.17
500	3.63	150	1.73	54	0.96
600	4.70	130	1.77	45	0.82
1000	6.82	80	1.86	34	0.65

Figure 5.9 shows the areal capacity of the multilayer NiSn electrodes with a total thickness of 300 μm as a function of the distance (i.e., the width L) between the etching holes. It can be seen that the capacity is confined between two horizontal asymptotes. This figure indicates that the design of the etching holes can be quite critical in the case of NiSn electrodes, since the capacity may vary from approximately 0.6 to 2 mAh. In the case of $Ni(OH)_2$-based electrodes, however, the difference between the maximum and minimum achievable theoretical capacity was around 0.6 μm. This is primarily because the OH^- concentration in the KOH electrolyte for the $Ni(OH)_2$ electrodes is six times as high as the Li^+ concentration in the EC:DMC electrolyte for the NiSn electrodes.

From Table 5.4 and Figure 5.9, it can be concluded that while it is not worth the fabrication effort to reduce the width below 300 μm in the $Ni(OH)_2$-based electrodes due to a negligible increase in the capacity, redesigning the NiSn electrodes by modifying the number of etching holes may have a significant impact on the capacity of these electrodes. However, in this study, the photoresist (AZ 125 nXT) used in the fabrication of the electrodes prohibited the closer spacing of the etching holes (see discussion in Chapter 2.2). Some potential techniques that may be examined to realize a denser array of etching holes will be discussed in the future work section in Chapter 7.

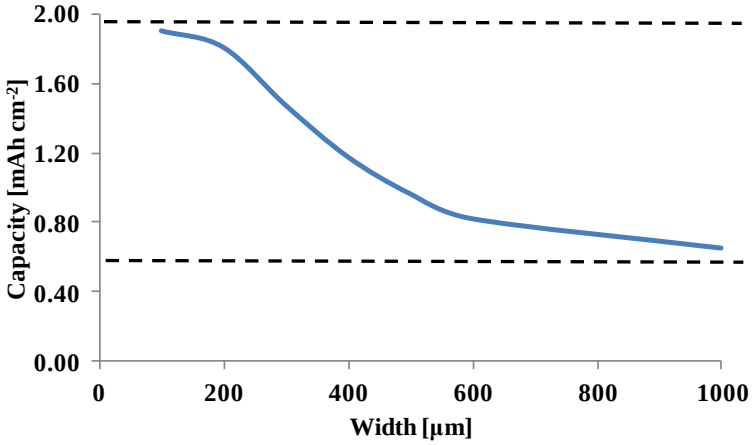

Figure 5.9: Theoretical areal capacity of a 300-μm-thick NiSn electrode as a function of the distance between its etching holes

By fine-tuning the characteristic dimensions of the multilayer electrodes, it is possible to make projections regarding the performance of the electrodes. One of the performance criteria that may be essential for certain applications is the areal energy and power density of the electrodes. Although Ragone plots are commonly used to compare the energy storage systems based on their gravimetric energy and power density, for autonomous applications, as mentioned in Chapter 1.1, that have a limited space onboard for their power source, areal energy and power density may be more critical criteria.

One of the characteristic dimensions that can be fine-tuned is the thickness of the individual Ni layers. For the projections made in Table 5.4, the layer thickness was assumed to be 1.5 μm, which is an experimentally determined dimension, whose justification was made in the previous chapter. By reducing the Ni thickness further, it would be possible to fit more layers within a given total thickness of 300 μm and thus, increase the areal energy and power density. The projection can be seen in Figure 5.10, where the areal capacity is shown as a function of the thickness of the individual Ni layers. This projection is based on the width, active material thickness, and inter-layer spacing of 300 μm, 0.2 μm, and 1.45 μm, respectively. In theory, to maximize the areal energy density, Ni layers should be as thin as possible, so long as they maintain their mechanical integrity and allow the necessary electron transport to and from the active material at high charge rates.

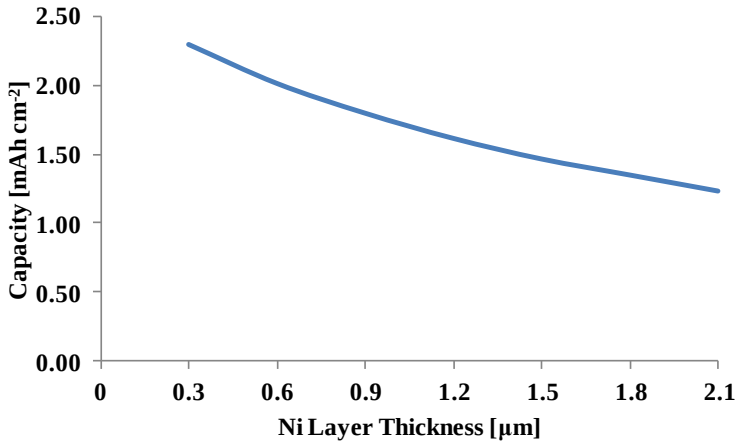

Figure 5.60: Theoretical areal capacity of a 300-μm-thick NiSn electrode as a function of the individual Ni layer thickness

Another critical parameter that can be fine-tuned is the thickness of the active material. For a given total thickness of 300 μm, increasing the thickness of the NiSn film can increase the areal energy density of the electrode because of the higher amount of the active material confined within the volume of the electrode. This trend can be clearly

seen in Figure 5.11, where the areal capacity is shown as a function of the NiSn thickness. For each thickness value of the active material, an optimum inter-layer spacing value was calculated using the aforementioned models. The width L and the individual Ni layer thickness were assumed to be 300 µm and 1.5 µm, respectively.

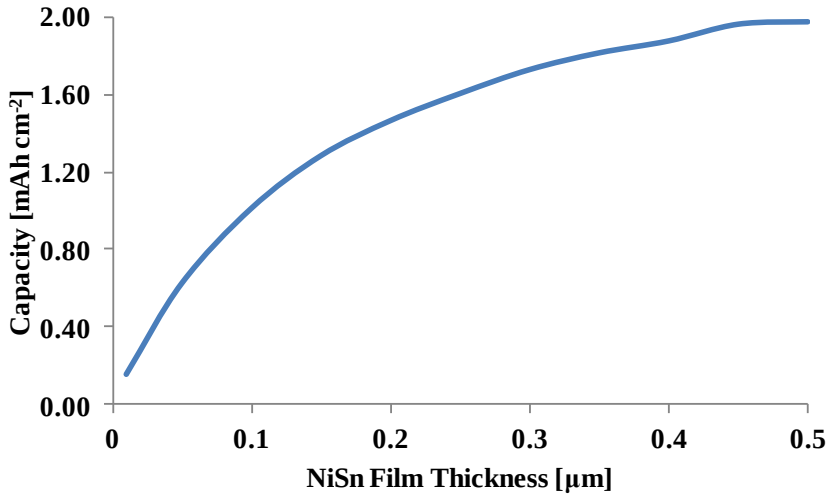

Figure 5.11: Theoretical areal capacity of a 300-µm-thick NiSn electrode as a function of the NiSn layer thickness

The drawback of increased NiSn film thickness, however, is the reduced power density due to longer diffusion and conduction path lengths for the ions and electrons, respectively. The impact of the active material thickness, along with the thickness of the individual Ni layers on the energy and power density of the electrode can be seen in Figures 5.12.A and 5.12.B, where the former is based on the mass of the electrode, whereas the latter is based on the total volume of the electrode. A detailed description concerning the preparation of these figures was provided in Chapter 4.7.

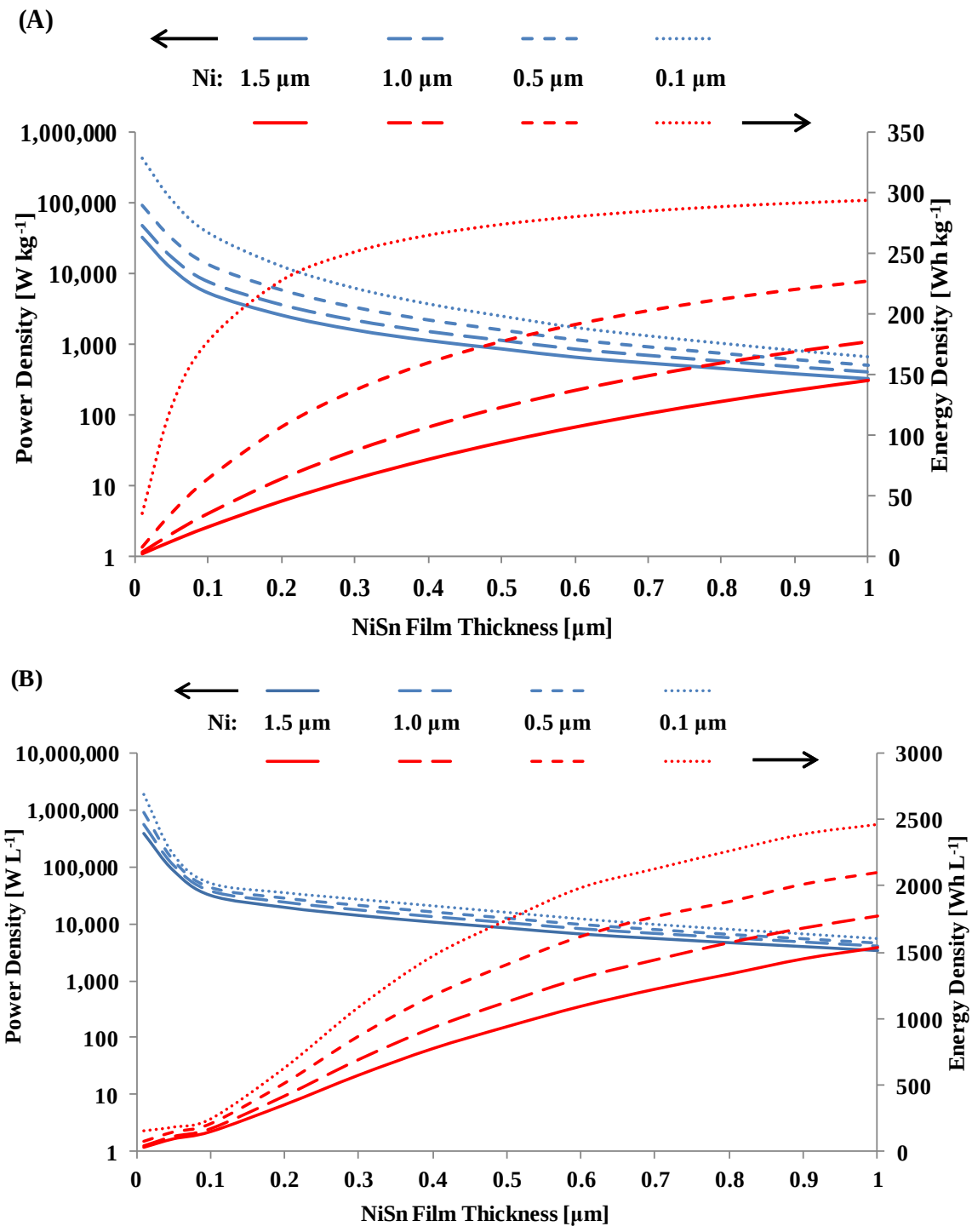

Figure 5.12: Theoretical power and energy density of the electrodes as a function of the NiSn film thickness and the Ni layer thickness: (A) gravimetric density, (B) volumetric density

The operating potential of the electrode was assumed to be 3.5 V for the calculation of the power and energy densities in Figure 5.12, which is more than twice as high as the $Ni(OH)_2$ electrodes discussed in the previous chapter. These figures can prove quite useful when designing electrodes for special application areas.

As in the case of the $Ni(OH)_2$ electrodes, the key to achieving electrodes with profoundly improved power densities is minimized active material film and Ni layer thicknesses. Reducing the thickness of the active material film by half (e.g., from 100 nm to 50 nm) results in nearly an order of magnitude increase in the power density of the electrode, whereas the forfeit in the energy density is not as significant.

5.5 Performance Characterization of the Electrodes

The fabricated electrodes were characterized by charging and discharging under galvanostatic conditions at various rates, using a potentiostat (WaveDriver 10, Pine Instruments). All of the tests were performed in an argon-filled glove box using a two-electrode cell setup. The electrodes were built on a footprint area of 1 cm^2. Hence, the reported capacity values can be considered as areal capacities as well.

5.5.1 MnO_2 Electrodes

MnO_2 electrodes based on a 100-layer Ni backbone were prepared and lithiated as described earlier in this chapter. When characterizing the electrodes, a commercial carbonaceous anode (Sony) was utilized as the counter electrode. A cut-off potential of 1.8 V was selected for the discharge process.

Figure 5.13 shows the discharge profiles of the 100-layer electrode at 5 C following various charge rates. These discharge profiles were found to be in good agreement with the previously reported profiles in the literature [13, 19, 28].

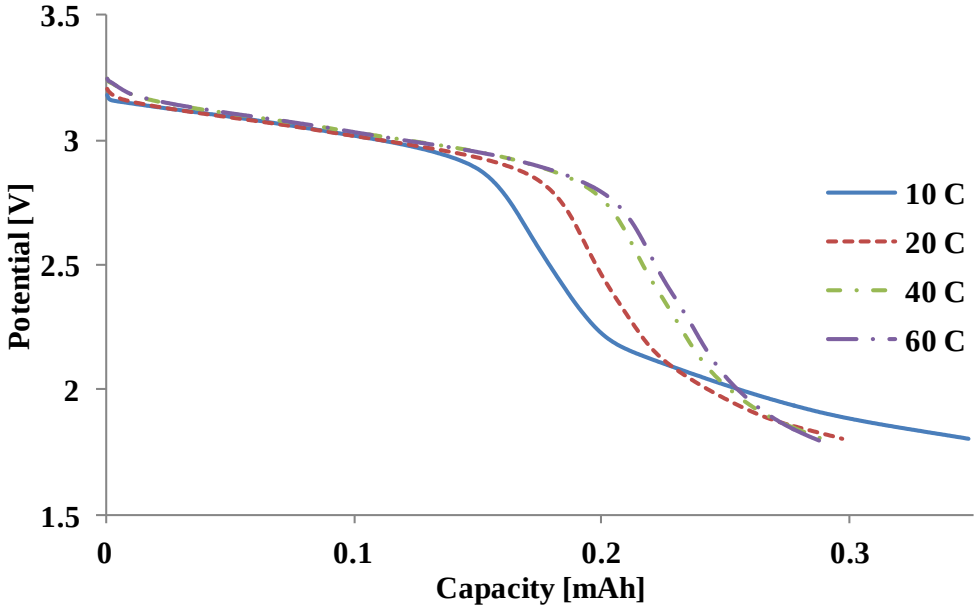

Figure 5.13: Discharge profiles of the MnO_2 electrode charged at various rates and discharged at 5 C

As in the case of $Ni(OH)_2$-based electrodes discussed in Chapter 4, MnO_2-based multilayer electrodes also demonstrated an outstanding performance in terms of capacity delivery at high rates. This particular electrode was able to deliver 83% of its 10 C capacity when charged at 60 C. After running more than 35 cycles at such high charge and discharge rates, no significant capacity degradation was observed in the electrode, indicating good cycling stability.

A drawback of working with cathode materials such as MnO_2, however, is that they intrinsically possess low energy densities as compared to their anode counterparts, some of which reportedly exhibit an order of magnitude higher specific energy. Therefore, the demonstration of high power capabilities with relatively high capacities (>10 mAh) using cathode materials becomes quite challenging. Such capacities can only be achieved through electrodes with much higher number of laminations or stacks consisting of tens of multilayer electrodes.

5.5.2 NiO Electrodes

Unlike the MnO_2 electrodes, which underwent lithiation process prior to the electrochemical characterizations, NiO electrodes were tested against Li foils and thus, no further processing was required after the calcination of $Ni(OH)_2$ electrodes. As shown in Figure 5.14.A, these materials exhibited rather high specific capacities when discharged at relatively low rates (0.1 C). A cut-off potential of 0.01 V was selected for the discharge process. In terms of both the specific capacity and the discharge rate, they were shown to be in good agreement with the previously reported NiO electrodes in the literature [29-31].

Figure 5.14.B shows the cycling performance of a high-capacity NiO electrode based on a stack of three 90-layer structures. This stack of electrodes was charged at alternating rates of 1 C and 30 C, and discharged at a constant rate of 1 C. These electrodes demonstrated a significant high-power capability by delivering more than 50% of their 1 C capacity at rates as high as 30 C. However, large fluctuations were also observed in the capacity of the electrode as the number of charge and discharge cycles increased.

(A)

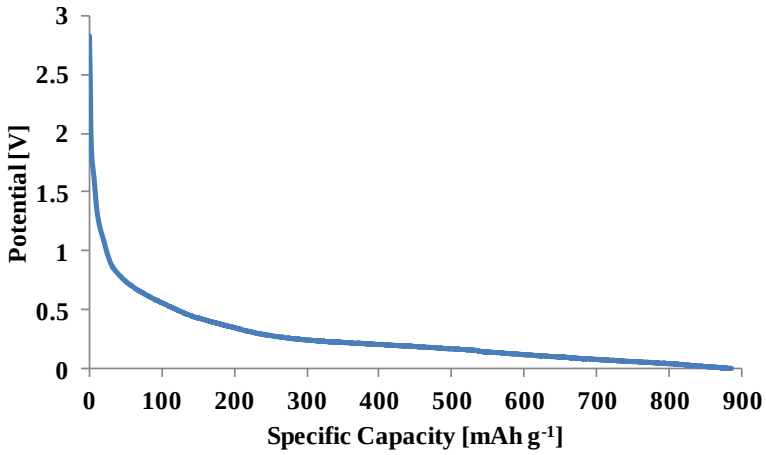

(B)

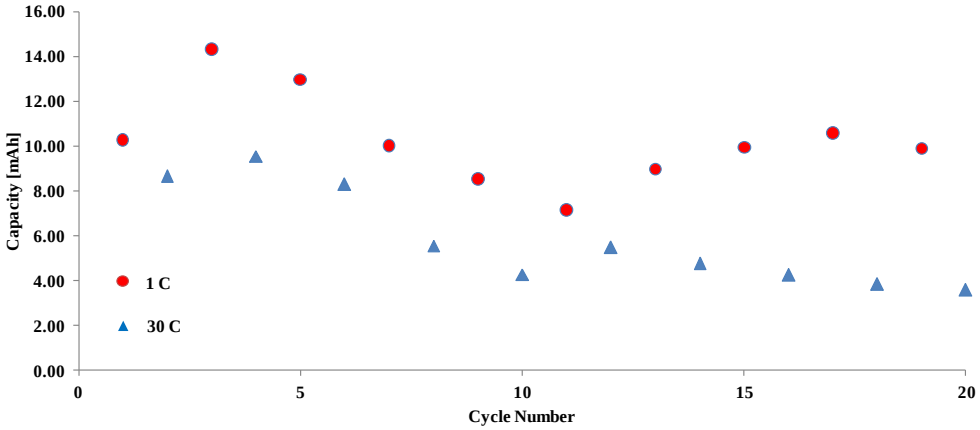

Figure 5.14: (A) Lithiation profile of a NiO electrode at a rate of 0.1 C, (B) cycling performance of a NiO electrode consisting of a stack of three 90-layer structures

It was shown in Chapter 4 that $Ni(OH)_2$ electrodes were able to demonstrate outstanding cycling stabilities even following more than 80 charge and discharge cycles at high rates. However, a similar performance was not observed in the case of NiO electrodes, even though they were fabricated in a similar fashion. This relatively poor cycling stability of NiO electrodes was postulated to originate from the calcination process of the multilayer electrodes coated with $Ni(OH)_2$. As the temperature was increased to 300 ºC, some local deformations due to thermal stress may have taken place in the multilayer structures, limiting the accessible surface area and potentially weakening the adhesion of the active material. This may have also been the cause of the

fluctuations shown in Figure 5.14.B. Also, the conversion of $Ni(OH)_2$ to NiO may adversely affect the adhesion quality of the active material to the Ni backbone, resulting in disintegration of the NiO film during the charge and discharge cycles. This was partially confirmed during the characterization tests, where the NiO particles were observed to flake off the electrode to the bottom of the cell. A similar decay in the capacity following a number of cycles was also reported in the literature [31].

Although higher energy densities can easily be achieved with the NiO-based electrodes due to their high specific capacity, their relatively poor performance in terms of cycling stability at high rates renders them unsuitable for the kind of applications considered herein. Nonetheless, these electrodes could still prove useful in primary battery applications or applications for which only a few charge and discharge cycles are required.

5.5.3 NiSn Electrodes

The final type of electrodes that was characterized was based on NiSn active material. As in the case of the NiO electrodes, NiSn electrodes were characterized by using a Li foil as the counter electrode. The performance of the NiSn electrodes is summarized in Figure 5.15.

Figure 5.15.A demonstrates the lithiation profile of a 90-layer NiSn electrode, discharged galvanostatically at 0.3 C until the cut-off potential of 0.01 V. This profile is consistent with the profiles of the NiSn electrodes reported previously in the literature [21, 32]. It can be noted that the specific capacity of the NiSn electrode is less than half of the NiO shown in Figure 5.15.A.

However, in terms of capacity retention at high power, as well as cycling stability, a much better performance was obtained with the NiSn electrodes than with the NiO electrodes. This high performance is illustrated in Figure 5.15.B, showing the capacity of a 90-layer electrode as a function of cycle number. The electrode was charged at various

rates ranging from 1 C to 60 C, and discharged at a constant rate of 1 C. The sharp decay observed in the capacity immediately after the first cycle was also reported in previous studies [24, 25]. As is shown in Figure 5.15.B, the electrode was able to deliver more than 90% of its capacity even at high charging rates of 60 C.

Higher capacities were achieved by making stack of several simultaneously fabricated multilayer electrodes, as in the case of $Ni(OH)_2$ and NiO electrodes. Figure 5.15.C demonstrates the capacity of the stack of three 90-layer NiSn electrodes as a function of cycle number. These electrodes were charged at alternating rates of 1 C and 30 C, and discharged at a constant rate of 1 C. No significant degradation was observed in the electrode following in excess of 35 charge and discharge cycles at high rates, suggesting a much better cycling performance as compared to the NiO electrodes.

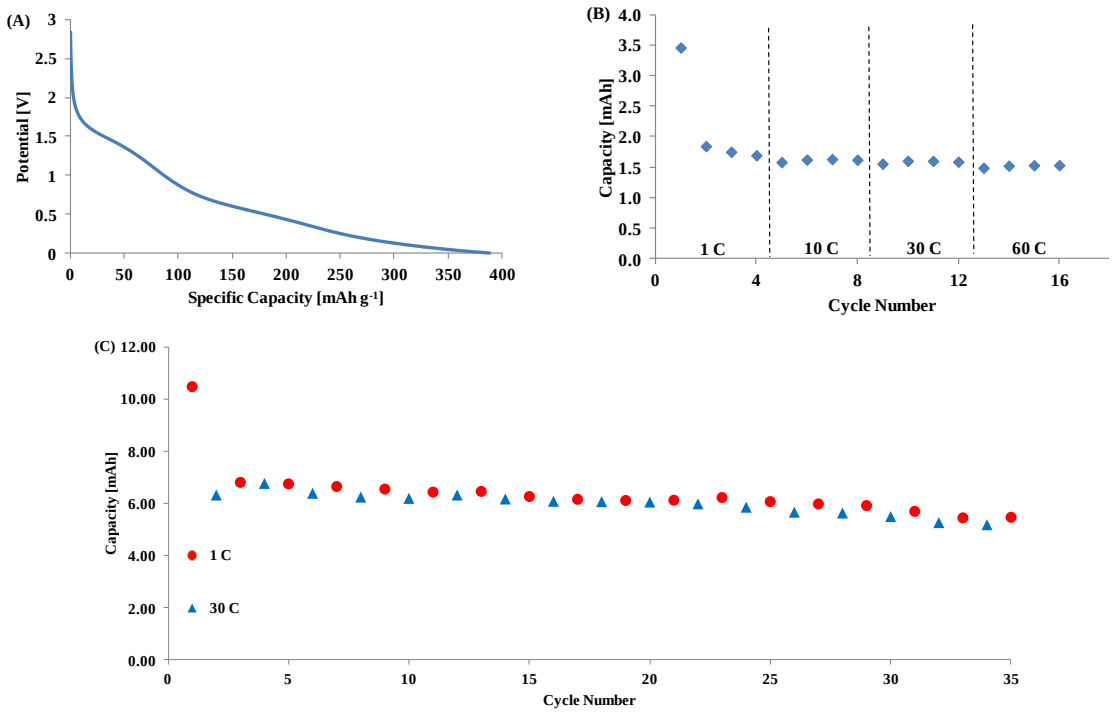

Figure 5.15: Electrochemical characterization of the NiSn electrodes: (A) discharge profile of a 90-layer electrode at 1 C, (B) capacity of a 90-layer electrode charged at various rates and discharged at 1 C, and (C) stack of three 90-layer electrodes cycled by charging at alternating rates and discharged at constant rate

5.6 Modeling of the Fabricated Electrodes

To determine if the models are able to predict the experimental data successfully, electrodes were fabricated, which possess similar dimensions to the optimum electrodes found via diffusion-limited models described in the previous section. The experimental results obtained from these electrodes are demonstrated in Figure 5.15.B. According to these models, the optimum NiSn-based electrode built on a footprint of 1 cm^2 with a total thickness of 300 µm, which can be charged in one minute with a negligible forfeit in its capacity, consists of 90 layers, and features an active material thickness and interlayer spacing of 0.2 µm and 1.4 µm, respectively. The theoretical capacity of such an electrode was found to be approximately 1.47 mAh, which is quite close to the experimental value of 1.65 mAh.

Figure 5.16 shows the comparison of the modeling and experimental results in terms of capacity retention. Since the electrodes are designed to deliver 100% of their capacity at charging rates of up to 60 C, a decrease in the capacity retention is not observed in the model predictions up to this point.

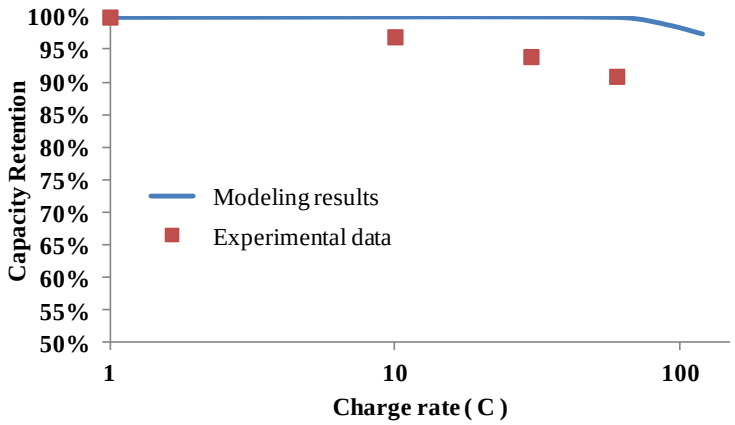

Figure 5.16: Theoretical capacity retention vs. experimental data of a 90-layer electrode with a 0.2-µm-thick active material at various charge rates

Although the fabricated electrodes were shown to exhibit high capacity retention (~91%) when charged at rates as high as 60 C, the measured capacity retention is still less than what the model predicted. One potential cause for the deviations from the theoretical results at high charging rates may be a result of a non-uniform active material film thickness. The SEM image shown in Figure 5.5.B confirms the roughness of the NiSn deposits, which also affects the structural Ni layers by transferring the wavy patterns to the subsequently deposited layers. Unlike the relatively conformal $Ni(OH)_2$ films demonstrated in the previous chapter, the SEM images of the sidewalls of the multilayer electrodes, indicate significant variations in the thickness of the NiSn film on each Ni layer ranging from 0.1 μm to 0.5 μm. Regions of the electrode with a thicker active material film are expected to require longer charge times.

Another possible reason for the deviations from the theoretical model may be related to the model assumption that the diffusion coefficient is constant throughout the charging process. It is well known that the diffusivity is also a function of the state of charge (i.e., amount of Li ions within the active material) of the electrode, which is not taken into account when modeling the optimum electrodes for Li-ion batteries. It was shown in Table 5.2 that even an order of magnitude change in the diffusion coefficient has a substantial impact on the optimum dimensions of the electrode. As the Li ion concentration within the active material increases, the diffusion coefficient is ideally expected to decrease. Therefore, an accurate knowledge of the diffusion coefficient is a necessity for a successful model.

5.7 Conclusions

This chapter described the design, fabrication, and characterization of MEMS-enabled electrodes with high-power capabilities utilized in Li-ion batteries. The active materials that were investigated include MnO_2, NiO, and NiSn. These materials were successfully incorporated into the anchor-supported, metallic multilayer structures and

demonstrated high performance in terms of power delivery at high charge rates. Among the tested materials, NiSn was found to be the most promising candidate for use in Li-ion batteries due to its high capacity retention at high charging rates, as well as outstanding cycling stability.

In this chapter, a novel multilayer fabrication approach was introduced that was not reported previously. This fabrication approach is based on a triple-bath robotic electroplating setup, enabling the concurrent electrodeposition of the active material (NiSn) along with the structural Ni layers and sacrificial Cu layers. As a result, the total fabrication duration was significantly reduced by eliminating the need for the processing step which involves the electrodeposition of the active material. This approach also ensured the formation of a relatively conformal active material film on each Ni layer, which otherwise would have to be realized via relatively complicated pulse plating techniques.

Diffusion-limited models that were introduced in the previous chapter have also been utilized in this chapter to optimize the liquid- and solid-state ion transport path lengths for the electrodes with high-power capabilities by determining the optimum active material thickness, as well as the inter-layer spacing within the multilayer electrode. The models were used to make projections about the performance of the ideal electrodes. It was concluded that to realize electrodes with high power density, the number of layers in a given volume of the multilayer structure should be maximized, which can be achieved by minimizing both the individual backbone layer thickness and the active material film thickness, as well as the gap between the adjacent etching holes.

The projected capacity for an electrode with a total thickness of 300 μm was found to be in good agreement with the experimental values. However, the experimental data showed some deviations from the predicted values in terms of the capacity delivery at high charge rates, which were postulated to originate from the assumptions of smooth active material films and constant diffusion coefficients throughout the charging process.

Nevertheless, the models can still be used as an approximation for designing the electrodes.

The Ragone plots shown in Figures 5.17 and 5.18 help visualize the contributions provided by the NiSn electrodes reported in this chapter in terms of gravimetric and volumetric power and energy densities, respectively. These values for a 90-layer electrode were calculated from both experimental and theoretical data, and compared to the existing energy storage systems shown in Figures 5.17 and 5.18. The points A and B in these two figures refer to the performance values of the current fabricated and modeled electrodes, respectively. The latter electrode features a Ni layer thickness of 0.1 µm, a NiSn film thickness of 0.1 µm, an inter-layer spacing of 2.1 µm, and a total thickness of 300 µm. As in the case of the $Ni(OH)_2$ electrodes, both experimentally and theoretically, a much more significant contribution is demonstrated in terms of the volumetric power and energy densities, as can be seen from Figure 5.18. This suggests that the approaches reported herein can be potentially utilized to fabricate electrodes for high-performance Li-ion batteries.

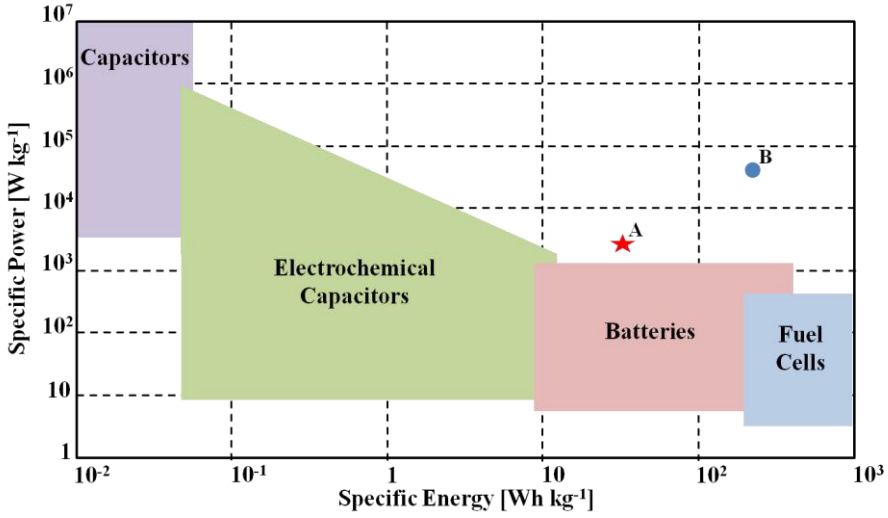

Figure 5.17: Ragone plot comparing the gravimetric power and energy densities of a 90-layer NiSn electrode (point A) and the modeled electrode with the optimized dimensions (point B) to the existing energy storage systems

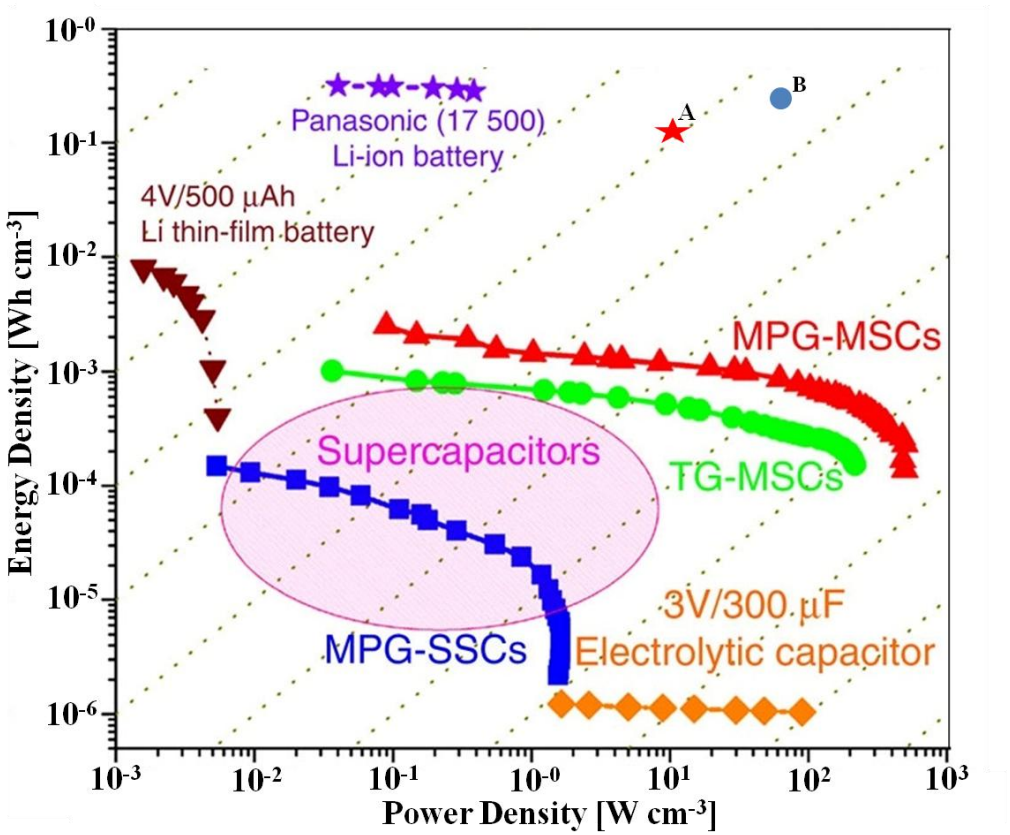

Figure 5.18: Ragone plot comparing the volumetric power and energy densities of a 90-layer NiSn electrode (point A) and the modeled electrode with the optimized dimensions (point B) to the existing energy storage systems

5.8 References

[1] T. B. Reddy, *Linden's Handbook of Batteries* vol. 4: McGraw-Hill New York, 2011.

[2] G. Pistoia, *Lithium Batteries: New Materials, Developments, and Perspectives* vol. 5: Elsevier Science Ltd, 1994.

[3] F. Cheng, J. Liang, Z. Tao, and J. Chen, "Functional materials for rechargeable batteries," *Advanced Materials,* vol. 23, pp. 1695-1715, 2011.

[4] G.-A. Nazri and G. Pistoia, *Lithium batteries: science and technology*: Springer Science & Business, 2008.

[5] C. K. Chan, H. Peng, G. Liu, K. McIlwrath, X. F. Zhang, R. A. Huggins*, et al.*, "High-performance lithium battery anodes using silicon nanowires," *Nature Nanotechnology,* vol. 3, pp. 31-35, 2008.

[6] H. C. Shin and M. Liu, "Three-dimensional porous copper–tin alloy electrodes for rechargeable lithium batteries," *Advanced Functional Materials,* vol. 15, pp. 582-586, 2005.

[7] O. Crosnier, T. Brousse, and D. Schleich, "Tin based alloys for lithium ion batteries," *Ionics,* vol. 5, pp. 311-315, 1999.

[8] C. Johnson, J. Vaughey, M. Thackeray, T. Sarakonsri, S. Hackney, L. Fransson, *et al.*, "Electrochemistry and in-situ X-ray diffraction of InSb in lithium batteries," *Electrochemistry Communications,* vol. 2, pp. 595-600, 2000.

[9] L. M. Fransson, J. Vaughey, R. Benedek, K. Edström, J. O. Thomas, and M. Thackeray, "Phase transitions in lithiated Cu_2Sb anodes for lithium batteries: an in situ X-ray diffraction study," *Electrochemistry Communications,* vol. 3, pp. 317-323, 2001.

[10] M.-K. Song, S. Park, F. M. Alamgir, J. Cho, and M. Liu, "Nanostructured electrodes for lithium-ion and lithium-air batteries: the latest developments, challenges, and perspectives," *Materials Science and Engineering: R: Reports,* vol. 72, pp. 203-252, 2011.

[11] J. H. Pikul, H. G. Zhang, J. Cho, P. V. Braun, and W. P. King, "High-power lithium ion microbatteries from interdigitated three-dimensional bicontinuous nanoporous electrodes," *Nature Communications,* vol. 4, p. 1732, 2013.

[12] P. V. Braun, J. Cho, J. H. Pikul, W. P. King, and H. Zhang, "High power rechargeable batteries," *Current Opinion in Solid State and Materials Science,* vol. 16, pp. 186-198, 2012.

[13] H. Zhang, X. Yu, and P. V. Braun, "Three-dimensional bicontinuous ultrafast-charge and-discharge bulk battery electrodes," *Nature Nanotechnology,* vol. 6, pp. 277-281, 2011.

[14] F. Croce, A. d'Epifanio, J. Hassoun, A. Deptula, T. Olczac, and B. Scrosati, "A novel concept for the synthesis of an improved LiFePO4 lithium battery cathode," *Electrochemical and Solid-State Letters,* vol. 5, pp. A47-A50, 2002.

[15] Y. Wang, Y. Wang, E. Hosono, K. Wang, and H. Zhou, "The design of a $LiFePO_4$/carbon nanocomposite with a core–shell structure and its synthesis by an in situ polymerization restriction method," *Angewandte Chemie International Edition,* vol. 47, pp. 7461-7465, 2008.

[16] X. L. Wu, L. Y. Jiang, F. F. Cao, Y. G. Guo, and L. J. Wan, "$LiFePO_4$ nanoparticles embedded in a nanoporous carbon matrix: superior cathode material for electrochemical energy-storage devices," *Advanced Materials,* vol. 21, pp. 2710-2714, 2009.

[17] S.-Y. Chung, J. T. Bloking, and Y.-M. Chiang, "Electronically conductive phospho-olivines as lithium storage electrodes," *Nature Materials,* vol. 1, pp. 123-128, 2002.

[18] M. Park, X. Zhang, M. Chung, G. B. Less, and A. M. Sastry, "A review of conduction phenomena in Li-ion batteries," *Journal of Power Sources,* vol. 195, pp. 7904-7929, 2010.

[19] D. Liu, B. B. Garcia, Q. Zhang, Q. Guo, Y. Zhang, S. Sepehri, *et al.*, "Mesoporous hydrous manganese dioxide nanowall arrays with large lithium ion energy storage capacities," *Advanced Functional Materials,* vol. 19, pp. 1015-1023, 2009.

[20] K. Nishikawa, K. Dokko, K. Kinoshita, S.-W. Woo, and K. Kanamura, "Three-dimensionally ordered macroporous Ni–Sn anode for lithium batteries," *Journal of Power Sources,* vol. 189, pp. 726-729, 2009.

[21] F.-s. Ke, L. Huang, H.-h. Jiang, H.-b. Wei, F.-z. Yang, and S.-g. Sun, "Fabrication and properties of three-dimensional macroporous Sn–Ni alloy electrodes of high preferential (110) orientation for lithium ion batteries," *Electrochemistry Communications,* vol. 9, pp. 228-232, 2007.

[22] S. Atlung, K. West, and T. Jacobsen, "Dynamic aspects of solid solution cathodes for electrochemical power sources," *Journal of The Electrochemical Society,* vol. 126, pp. 1311-1321, 1979.

[23] J. P. Fellner and S. S. Sandhu, "Diffusion-limited model for a lithium/polymer battery," *Electrochimica Acta,* vol. 43, pp. 1607-1613, 1998.

[24] H. Mukaibo, T. Momma, M. Mohamedi, and T. Osaka, "Structural and morphological modifications of a nanosized 62 atom percent Sn-Ni thin film anode during reaction with lithium," *Journal of the Electrochemical Society,* vol. 152, pp. A560-A565, 2005.

[25] J. Hassoun, S. Panero, P. Simon, P. L. Taberna, and B. Scrosati, "High-Rate, Long-Life Ni–Sn Nanostructured Electrodes for Lithium-Ion Batteries," *Advanced Materials,* vol. 19, pp. 1632-1635, 2007.

[26] M. Winter and J. O. Besenhard, "Electrochemical lithiation of tin and tin-based intermetallics and composites," *Electrochimica Acta,* vol. 45, pp. 31-50, 1999.

[27] S.-I. Lee, U.-H. Jung, Y.-S. Kim, M.-H. Kim, D.-J. Ahn, and H.-S. Chun, "A study of electrochemical kinetics of lithium ion in organic electrolytes," *Korean Journal of Chemical Engineering,* vol. 19, pp. 638-644, 2002.

[28] F. Cheng, J. Zhao, W. Song, C. Li, H. Ma, J. Chen, *et al.*, "Facile controlled synthesis of MnO2 nanostructures of novel shapes and their application in batteries," *Inorganic Chemistry,* vol. 45, pp. 2038-2044, 2006.

[29] A. Kumar Rai, L. Tuan Anh, C.-J. Park, and J. Kim, "Electrochemical study of NiO nanoparticles electrode for application in rechargeable lithium-ion batteries," *Ceramics International,* vol. 39, pp. 6611-6618, 2013.

[30] I. R. Kottegoda, N. H. Idris, L. Lu, J.-Z. Wang, and H.-K. Liu, "Synthesis and characterization of graphene–nickel oxide nanostructures for fast charge–discharge application," *Electrochimica Acta,* vol. 56, pp. 5815-5822, 2011.

[31] M.-S. Wu and Y.-P. Lin, "Monodispersed macroporous architecture of nickel-oxide film as an anode material for thin-film lithium-ion batteries," *Electrochimica Acta,* vol. 56, pp. 2068-2073, 2011.

[32] H.-R. Jung, E.-J. Kim, Y. J. Park, and H.-C. Shin, "Nickel–tin foam with nanostructured walls for rechargeable lithium battery," *Journal of Power Sources,* vol. 196, pp. 5122-5127, 2011.

CHAPTER 6

MEMS-ENABLED ELECTROCHEMICAL CAPACITORS

6.1 Background and Motivation

In addition to the batteries reported thus far in this work, the rationally designed and deterministically engineered, MEMS-enabled, 3D structures, including both lateral and vertical high-aspect-ratio architectures, were also utilized as current collectors for electrochemical capacitors. The resultant electrochemical capacitors were designed to exhibit battery-like performance by delivering significant amount of energy without compromising their high-power capabilities.

As described in the first chapter, capacitors can be distinguished by their charge storage mechanisms, leading to 3 major classes of capacitors: (1) conventional electrostatic capacitors that solely rely on the accumulation of the opposite charges on the surfaces of two electrodes sandwiching a dielectric material, (2) electrolytic capacitors utilizing an electrolyte between the dielectric material and the electrode, and (3) electrochemical capacitors (also called electric double-layer capacitors, supercapacitors, or ultracapacitors) that rely on double-layer capacitance and/or pseudocapacitance phenomena. The focus in this chapter will be on the electrochemical capacitors only.

Electrochemical capacitors are high-power energy storage devices that narrow the application gap between conventional electrostatic capacitors and batteries, as shown in the Ragone plot (Figure 1.1). Similar to their electrostatic counterparts, they exhibit rapid charge and discharge capabilities, as well as a high degree of reversibility in repetitive charge/discharge cycles. They also possess the ability to store substantially more energy per unit mass or volume than the electrostatic capacitors. Because of these attributes, electrochemical capacitors are recognized as promising next-generation energy storage devices and have been widely utilized in various applications ranging from portable electronic devices, as well as autonomous microsystems, to electrical vehicles [1].

Energy storage in electrochemical capacitors relies on two mechanisms: (1) energy is electrostatically stored via separated charges in a Helmholtz double-layer that forms at the interface between a conductive electrode surface and an electrolyte; and (2) energy is electrochemically stored via a phenomenon called pseudocapacitance which involves reversible Faradaic charge transfer between the surface of the electrode and the electrolyte. Faradaic charge transfer in the pseudocapacitive materials can further be classified in three categories: (1) reversible surface adsorption of H^+ or metal ions from the electrolyte; (2) redox reactions that involve the ions in the electrolyte; and (3) reversible intercalation/deintercalation in polymers [2]. The former two are primarily surface reactions and thus, they mainly rely on surface area, whereas the latter one is more of a bulk process and less dependent on the surface area. Depending on the type of the electrode, either the first or both of the charge storage mechanisms can be observed in an electrochemical capacitor.

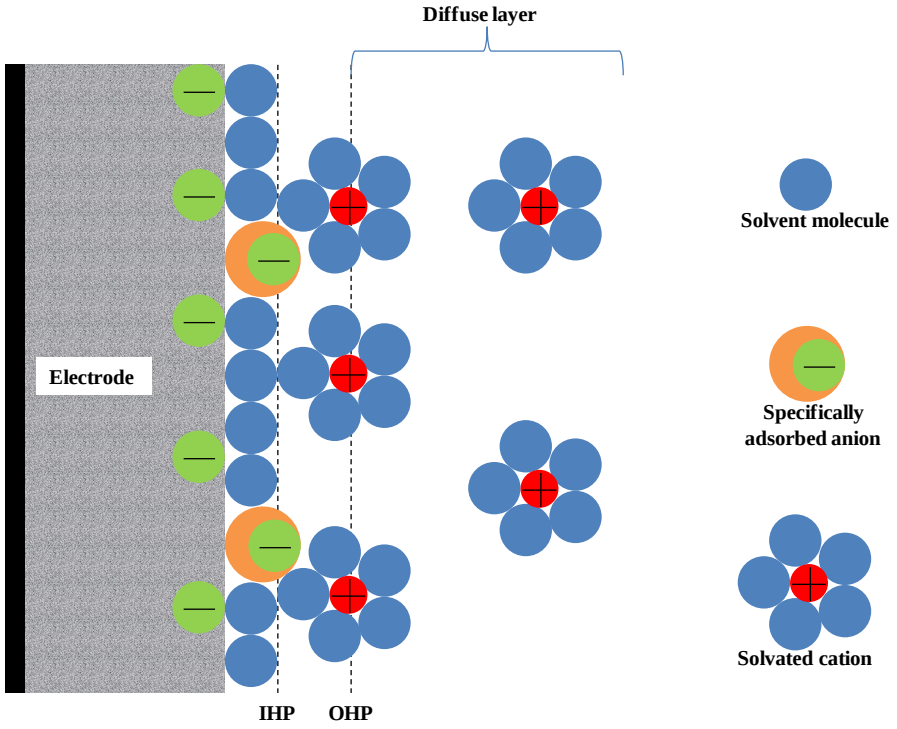

Figure 6.1: Schematic representation of the double-layer region on the electrode [3]

All of the aforementioned charge storage mechanisms take place within the electrical double layer on the electrode surface, which is shown in Figure 6.1 [3]. The solution side of the double layer consists of two layers. The innermost one that is closest to the electrode is called Helmholtz layer. This layer contains the solvent molecules and on some occasions, specifically adsorbed ions which contribute to the pseudocapacitance of the electrode. The plane that crosses the centers of the specifically adsorbed ions is called the inner Helmholtz plane (IHP).

As shown in Figure 6.1, solvated ions can only approach the electrode to a certain distance. These ions can only undergo electrostatic interactions with the electrode and hence, they are defined as nonspecifically adsorbed ions [3]. The plane that crosses the centers of these nearest solvated ions is called outer Helmholtz plane (OHP). The outermost layer that extends from the OHP into the bulk electrolyte is called diffuse layer where the nonspecifically adsorbed ions are distributed.

In recent years, considerable effort has been devoted to the development of electrochemical capacitors and significant improvements have been achieved through developing new active materials, altering the morphology of the existing materials, and implementing high-surface-area structures that serve as current collectors utilizing thin films of the existing materials [1].

The classification of the electrochemical capacitors can be performed based on various criteria including the active material, type of the electrolyte, and cell design [4]. The cell design is not the main concern for this study. Therefore, the focus herein will be on the former two.

6.1.1 Classes of Electrodes

There are three main types of active materials associated with electrochemical capacitor electrodes: (1) carbon-based, (2) polymer-based, and (3) metal-oxide based materials.

6.1.1.1 Carbon-based Electrochemical Capacitors

Carbon has been reported to be the most commonly used material for electrodes and most of the commercially available electrochemical capacitors today are carbon-based [5]. The reasons behind the frequent usage of carbon are its cost-effectiveness, abundance, ease of processing, chemical stability, high specific surface area, wide range of operating temperature, and good electronic conductivity [6]. The predominant energy storage mechanism in carbon-based electrodes involves the charges stored within an electrochemical double-layer that forms at the interface between the electrode and the electrolyte, rather than charges delivered to the bulk material [1]. Some contribution from the surface functional groups on activated carbons can also be observed which results in a 5-10% increase in the total capacitance. Hence, the key element that determines the capacitance (i.e., the energy) of the electrode in this particular type of electrochemical capacitors is the specific surface area. In addition, the pore-size distribution is also a similarly vital feature of the carbon electrodes, as the size of the pores plays an important role in determining the accessible surface area of the electrode for the ions in the electrolyte. High-surface-area structures made of carbon in the form of powders, fibers, nanotubes, and aerogels have been shown to exhibit a specific surface area of up to 3000 $m^2 g^{-1}$ [7]. Specific capacitance values ranging from 10 to 160 F g^{-1} have been enabled by using organic electrolytes [7]. Switching to aqueous electrolytes resulted in an increase in the specific capacitance up to 208 F g^{-1} [6]. Carbon-based electrochemical capacitors along with other types of electrodes with notable capacitances are tabulated in Table 6.1.

6.1.1.2 Polymer-based Electrochemical Capacitors

Considerable research has been conducted regarding the use of electronically conductive polymers as electrodes for electrochemical capacitors [1]. Some of the most commonly used polymers for electrochemical capacitor applications include polyaniline (PANI), polythiophene (PTh), polypyrrol (PPy) and their derivatives [1]. The energy storage mechanism in polymer-based capacitors primarily relies on the

pseudocapacitance of the electronically conductive polymer electrode, which stems from the fast reversible oxidation and reduction processes involving π-conjugated polymer chains [6, 8]. During the oxidation process, doping of the ions into the polymer backbone takes place and during the reduction, the ions are released back into the electrolyte [9]. Hence, unlike the other types of electrochemical capacitor electrodes, the charging and discharging occur throughout the bulk volume of the polymer film, rather than on the surface. This enables high levels of specific capacitance as shown in Table 6.1. The main shortcoming of this mechanism, however, is the volumetric changes that occur in the polymer electrodes during the doping and release processes of the ions which leads to poor cycling stability [10]. To mitigate the stability issue and also to further improve the specific capacitance, hybridized electrode configurations and composite electrodes have also been utilized [1]. Table 6.1 summarizes some of the polymer-based electrodes with distinguished performances.

6.1.1.3 Metal oxide-based Electrochemical Capacitors

Metal oxides are advantageous over the previously mentioned types of electrode materials since they offer higher energy density and better electrochemical stability than the carbon-based and polymer-based electrodes, respectively. Intrinsically, metal oxides possess high specific capacitance. This high specific capacitance stems from the fact that the charge storage mechanism in metal oxides does not only rely on electrochemical double-layer, but also on the reversible Faradaic reactions between the electrode materials and ions within a certain potential range [1]. In order for a metal oxide to serve as an electrode, three requirements need to be met: (1) the metal oxide must be electronically conductive; (2) the metal should exhibit at least two oxidation states and these states should coexist within the potential range of the electrolyte without any phase change comprising irreversible modifications of the electrode morphology; and (3) the metal oxide lattice should be able to undergo intercalation and deintercalation of H^+ during the oxidation and reduction processes, respectively, enabling a reversible

conversion between O^{2-} and OH^- [1]. Most commonly studied metal oxides to date include ruthenium oxide (RuO_2), manganese oxide (MnO_2), nickel oxide ($NiO/Ni(OH)_2$), cobalt oxide ($Co_3O_4/Co(OH)_2$), vanadium oxide (V_2O_5), and their composites. Some of the metal oxide-based electrodes with remarkable specific capacitance are listed in Table 6.1.

Table 6.1: Selected types of materials for electrochemical capacitors

Electrode Type	Electrode Material	Electrolyte Type	Potential (V)	Specific Capacitance ($F\ g^{-1}$)	Reference
Carbon-based	Meso/macroporous carbon	Aqueous	0.8	130	[11]
	Carbon aerogels	Organic	3.0	160	[12]
	C_{60}-loaded AC fiber	Aqueous	1.0	172	[13]
	Mesoporous carbon	Aqueous	0.9	180	[14]
	AC fiber cloth	Aqueous	1.0	208	[15]
Polymer-based	Ppy-MCNTs	Aqueous	1.0	427	[16]
	Ppy-65 wt% carbon	Aqueous	1.0	433	[17]
	Ppy-MnO_2	Aqueous	1.0	620	[18]
	PANI-Ti	Aqueous	1.0	740	[19]
	MPANI/CNTs	Aqueous	0.9	1030	[20]
Metal oxide-based	Cobalt-nickel oxides/CNTs	Aqueous	1.0	569	[21]
	$Ni(OH)_2$	Aqueous	0.8	578	[22]
	RuO_2	Aqueous	1.0	650	[23]
	RuO_2/carbon	Aqueous	0.8	1000	[24]
	Amorphous $Ru_{1-y}Cr_yO_2/TiO_2$	Aqueous	0.9	1272	[25]

6.1.2 Classes of Electrolytes

There are three major classes of electrolytes used in electrochemical capacitors: (1) aqueous electrolytes, (2) organic electrolytes, and (3) ionic liquids.

6.1.2.1 Aqueous Electrolytes

Aqueous electrolytes are one of the most commonly used class of electrolytes for electrochemical capacitors. One reason for the widespread use of these electrolytes is that they enable higher capacitance than the organic electrolytes which is speculated to result from the possibility of higher ionic concentrations and smaller ionic radii of the ions [1]. Higher concentration and smaller ion radius lead to higher number of ions per given electrode surface area and thus, more charge storage on the electrode surface. Another advantage associated with the aqueous electrolytes is the ease of handling when compared to organic electrolytes, which require processing under strictly controlled ambient conditions. In addition, aqueous materials are composed of relatively inexpensive compounds, resulting in a reduction of the total fabrication cost. Some examples of most commonly used aqueous electrolytes include potassium hydroxide (KOH), sodium hydroxide (NaOH), sulfuric acid (H_2SO_4), and sodium sulfate (Na_2SO_4).

The main disadvantage associated with aqueous electrolytes is the narrow operation voltage window. The potential range is mainly determined by the thermodynamic stability of the electrolyte (i.e., the electrolysis potential in the case of aqueous electrolytes is ~1.2 V). This value corresponds to less than half of the applicable potential in the case of organic electrolytes. While capacitance is an important factor determining the amount of stored energy (E) in the electrochemical capacitor, it is also known that the energy and power (P) of an electrochemical capacitor is proportional to the square of the potential built up across the electrodes of the cell as shown in Equations 6.1 and 6.2:

$$E = \frac{C \cdot V^2}{2} \quad (6.1)$$

$$P = \frac{V^2}{4 \cdot R_s} \quad (6.2)$$

where C, V, and R_s stand for capacitance, potential, and equivalent inner resistance of the electrochemical capacitor, respectively [1]. These equations confirm that the potential can be a significant limitation for aqueous electrolytes in terms of enhanced energy and power density. Therefore, the use of organic electrolytes has been encountered explored recently in studies comprising electrochemical capacitors with high energy densities [1].

6.1.2.2 Organic Electrolytes

Organic electrolytes are another frequently used class of electrolytes found in commercial electrochemical capacitors. The main advantage associated with the organic electrolytes is their higher achievable potential. This potential can be as high as 3.5 V, which is nearly three times time potential enabled by the aqueous electrolytes [1]. As can be deduced from Equation 6.1, a three-fold increase in the potential enables a nine-fold increase in the energy density. Therefore, organic electrolytes are generally preferred for high energy applications. However, the electrical resistivity of the organic electrolytes is at least an order of magnitude higher than the aqueous ones, resulting in higher internal resistance and thus, limited power capability as can be seen in Equation 6.2 [5]. Also, some of the organic electrolytes contain toxic, flammable, and relatively expensive solvents such as acetonitrile and tetrahydrofuran, limiting their use for certain applications.

6.1.2.3 Ionic Liquids

Another class of electrolytes that has recently attracted attention for electrochemical capacitors is ionic liquids, which can be defined as salts that are in the liquid state at temperatures below 100 °C, or even at room temperatures [1]. They have been reported to have a wide range of thermodynamic stability potential, which can be as

high as 6 V, rendering them as promising candidates for high energy applications [1]. However, some fundamental electrochemical aspects pertaining to energy storage mechanism of ionic liquids are yet to be understood in more detail [26]. Hence, their usage in electrochemical capacitors is quite limited. Some of the ionic liquids studied for electrochemical capacitor applications include imidazolium, pyrrolidinium, and aliphatic quaternary ammonium salts.

6.2 NiO- and $Ni(OH)_2$-based Electrodes

Thin and conformal deposition of the active material onto the rather complex 3D backbone structures is an essential part of the fabrication process of electrochemical energy storage systems because of the aforementioned reasons pertaining to resistances encountered during diffusion and conduction processes. Recent advances in deposition technologies offered subtle techniques to mitigate the conformal coating issues. Sputtering and evaporation have been shown to yield excellent coverage on 2D structures, yet they fail to demonstrate the same capability on 3D architectures. Chemical vapor deposition (CVD) offers a better conformality in 3D geometries, but even better results have been obtained via atomic layer deposition (ALD).

ALD is one of the most advanced techniques for conformal deposition and frequently used to achieve conformal coatings of the active materials. However, there are some shortcomings of this technique such as its high capital cost, slow throughput, and more importantly, lack of necessary precursors to deposit the desired material. Therefore, the focus in this study has been on electrochemical deposition. This choice of deposition technique automatically eliminates the utilization of most of the carbon-based and polymer-based electrode materials. Hence, metal oxides have become the material of interest for the fabrication of the MEMS-enabled electrodes.

Among the numerous metal oxides, $Ni(OH)_2$ was selected as a well-studied example of active material for electrochemical capacitor applications. Factors such as its

high theoretical specific capacitance, cost-effectiveness, easy synthesis, well-defined electrochemical redox activity, environmentally benign nature, and availability in various morphologies have rendered $Ni(OH)_2$ a promising candidate for electrochemical capacitor applications. In addition to these factors, our capability of incorporating $Ni(OH)_2$ in the battery electrodes as demonstrated in Chapter 4, has also played an important role in selecting this particular chemistry.

There are numerous studies in the literature involving $Ni(OH)_2$-based electrochemical capacitors [22, 27-37]. Some of these studies are summarized in Table 6.2. Chemical precipitation and electrodeposition are two most-commonly used techniques to deposit $Ni(OH)_2$. However, the latter method provides better control over the dimensions of the deposits. Therefore, electrodeposition was preferred for the deposition of the active material. The exact same technique as described in Chapter 4.4 was utilized to deposit the $Ni(OH)_2$ and the reasons behind this choice can be found in the same chapter.

Another common metal oxide possessing pseudocapacitive properties is nickel oxide (NiO) and studies comprising electrochemical capacitors based on this material are summarized in Table 6.3. NiO can simply be obtained by calcination of $Ni(OH)_2$ at high temperatures following the reaction given in Equation 6.3. Since the conversion from $Ni(OH)_2$ to NiO is simple, it was also tested as an active material in this study.

$$Ni(OH)_2 \rightarrow NiO + H_2O \tag{6.3}$$

Table 6.2: Performance of various $Ni(OH)_2$-based electrochemical capacitors

Deposition Technique	Specific Capacitance	Power Capability	Cycling Stability	Reference
$Ni(OH)_2$/AC composite via chemical precipitation	314.5 F g^{-1} at 2 mV s^{-1}	From 2 to 8 mV s^{-1}: 87% retention	-	[27]
Cathodic electrodeposition	578 F g^{-1} at 0.5 A g^{-1}	-	400 cycles: 95.5% retention	[22]
Electrodeposition on Ni foam	3152 F g^{-1} at 4 A g^{-1}	From 4 to 16 A g^{-1}: 9% retention	300 cycles: 52% retention	[28]
Chemical precipitation	1715 F g^{-1} at 5 mV s^{-1}	From 5 to 100 mV s^{-1}: 60% retention	2000 cycles: 77.9% retention	[29]
Cathodic electrodeposition	457 F g^{-1} at 10 mV s^{-1}	-	-	[30]
$Ni(OH)_2$/graphene composite via chemical precipitation	1735 F g^{-1} at 1 mV s^{-1}	From 1 to 50 mV s^{-1}: 30% retention	3000 cycles: 94.3% retention	[31]
High-potential electrochemical deposition	2188 F g^{-1} at 1 mV s^{-1}	From 1 to 20 mV s^{-1}: 57% retention	10000 cycles: 76% retention	[32]
$Ni(OH)_2$/graphene composite via chemical precipitation	1247 F g^{-1} at 5 mV s^{-1}	From 5 to 40 mV s^{-1}: 63% retention	2000 cycles: 95% retention	[33]
Chemical precipitation	282 F g^{-1} at 0.3 A g^{-1}	-	-	[34]
Repeated immersion	1300 F g^{-1} at 1 mV s^{-1}	From 1 to 5 mV s^{-1}: 68% retention	200 cycles: 95% retention	[35]
$Ni(OH)_2$/graphite composite via hydrothermal reaction	166 F g^{-1} at 0.5 A g^{-1}	From 0.5 to 10 A g^{-1}: 67% retention	1000 cycles: 65% retention	[36]
$Ni(OH)_2$/graphene composite via in situ crystallization	1953.6 F g^{-1} at 2 mV s^{-1}	From 2 to 20 mV s^{-1}: 44% retention	500 cycles: 94% retention	[37]

Table 6.3: Performance comparison of various NiO-based electrochemical capacitors

Deposition Technique	Specific Capacitance	Power Capability	Cycling Stability	Reference
Cathodic electrodeposition and calcination at 300 ^{o}C	59 F g^{-1} at 20 mV s^{-1}	From 0.063 to 32 mA cm^{-2}: 93% retention	600 cycles: negligible degradation	[38]
Cathodic electrodeposition and calcination at 300 ^{o}C	142 F g^{-1} at 20 mV s^{-1}	-	-	[39]
Chemical precipitation and calcination at 250 ^{o}C	124 F g^{-1} at 0.1 A g^{-1}	-	-	[40]
Potentiodynamic deposition via CV and calcination at 300 ^{o}C	138 F g^{-1} at 100 mV s^{-1}	From 100 to 500 mV s^{-1}: 60% retention	1000 cycles: 92% retention	[41]
Anodic electrodeposition and calcination at 300 ^{o}C	167.3 F g^{-1} at 1 A g^{-1}	From 1 to 16.5 A g^{-1}: 93.6% retention	5000 cycles: 87.5% retention	[42]
Electrophoretic deposition and calcination at 300 ^{o}C	112 F g^{-1} at 10 mV s^{-1}	From 10 to 500 mV s^{-1}: 72% retention	5000 cycles: 90% retention	[43]
Chemical precipitation and calcination at 250 ^{o}C	597.4 F g^{-1} at 0.3 A g^{-1}	From 0.3 to 5 A g^{-1}: 63% retention	-	[34]
Carbon-NiO core-shell composites	988.7 F g^{-1} at 0.5 A g^{-1}	From 0.5 to 3.0 A g^{-1}: 89% retention	1000 cycles: 90.7% retention	[44]
Chemical precipitation and calcination at 300 ^{o}C	286.7 F g^{-1} at 1 A g^{-1}	From 1 to 10 A g^{-1}: 68% retention	730 cycles: 88.5% retention	[45]
NiO/EG composites via chemical precipitation and calcination at 400 ^{o}C	510 F g^{-1} at 0.1 A g^{-1}	From 0.1 to 1 A g^{-1}: 82% retention	500 cycles: 95% retention	[46]
Hydrothermal synthesis and calcination at 300 ^{o}C	137.7 F g^{-1} at 0.2 A g^{-1}	From 0.2 to 2.0 A g^{-1}: 81% retention	950 cycles: 92% retention	[47]
NiO/CNT composites via chemical precipitation and calcination at 300 ^{o}C	523 F g^{-1} at 5 mA cm^{-2}	From 2 to 20 mA cm^{-2}: 90% retention	-	[48]

6.3 Fabrication of the Electrodes

Two different approaches involving multilayer structures have been adopted for the fabrication of MEMS-enabled electrochemical capacitors: (1) structures in the form of lateral high-aspect-ratio parallel plates similar to the ones demonstrated as battery electrodes in the previous chapters; and (2) structures in the form of vertical high-aspect-ratio concentric cylinders. For the former one, $Ni(OH)_2$ was utilized as the active material whereas the latter one involves NiO-based electrochemical systems.

6.3.1 Lateral high-aspect-ratio parallel plates

The fabrication process for the lateral high-aspect-ratio current collectors can be seen in Figure 6.2. The only part that differs from the previous process described in Chapter 4.3 is that Ni was utilized as the sacrificial material rather than Cu.

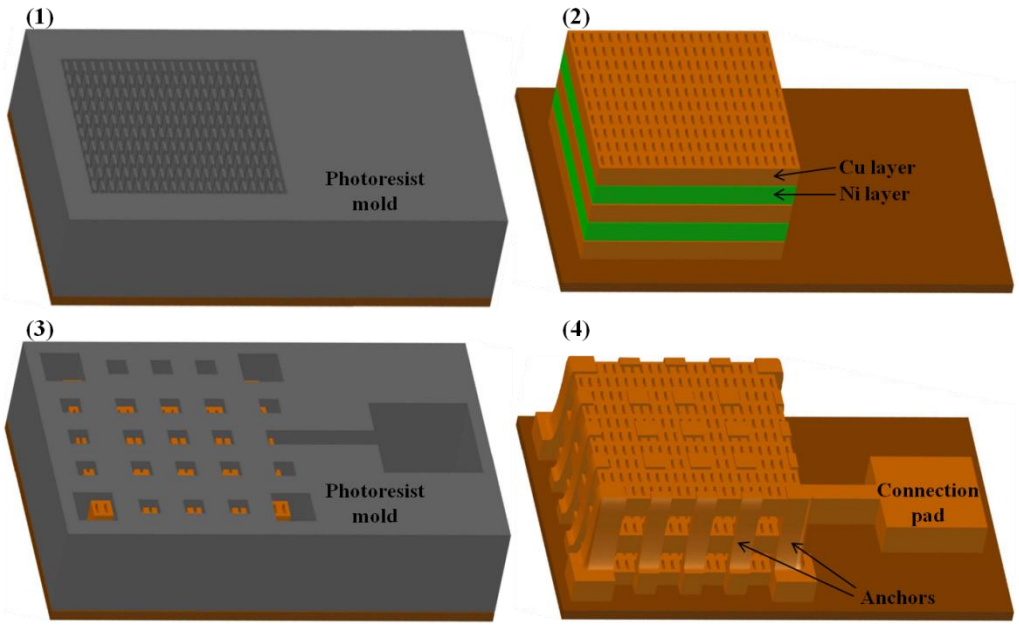

Figure 6.2: Fabrication sequence for the lateral high-aspect-ratio parallel plate current collectors: (1) deposition of the photoresist molds, (2) robotically-assisted sequential electroplating of Cu and Ni layers, (3) deposition of the second photoresist mold, and (4) electroplating of the Cu anchors along with the connection pad and selective removal of the Ni layers

Following the electroplating of the Cu anchors onto the specific regions of the multilayer structure, Ni layers were etched electrochemically by use of the corrosion potential difference between Cu and Ni in 0.1 M H_2SO_4 solution as described in Chapter 2.3.2, leaving a Cu backbone behind. An optical image of the Cu current collector can be seen in Figure 6.3. The primary reason for fabricating Cu-based current collectors instead of Ni as before was to demonstrate the capability of etching Ni selectively over Cu. Additionally, the surface area of the Cu structures was able to be measured by utilizing the underpotential deposition (UPD) of thallium (Tl), which was also briefly mentioned in Chapter 2.4.1.

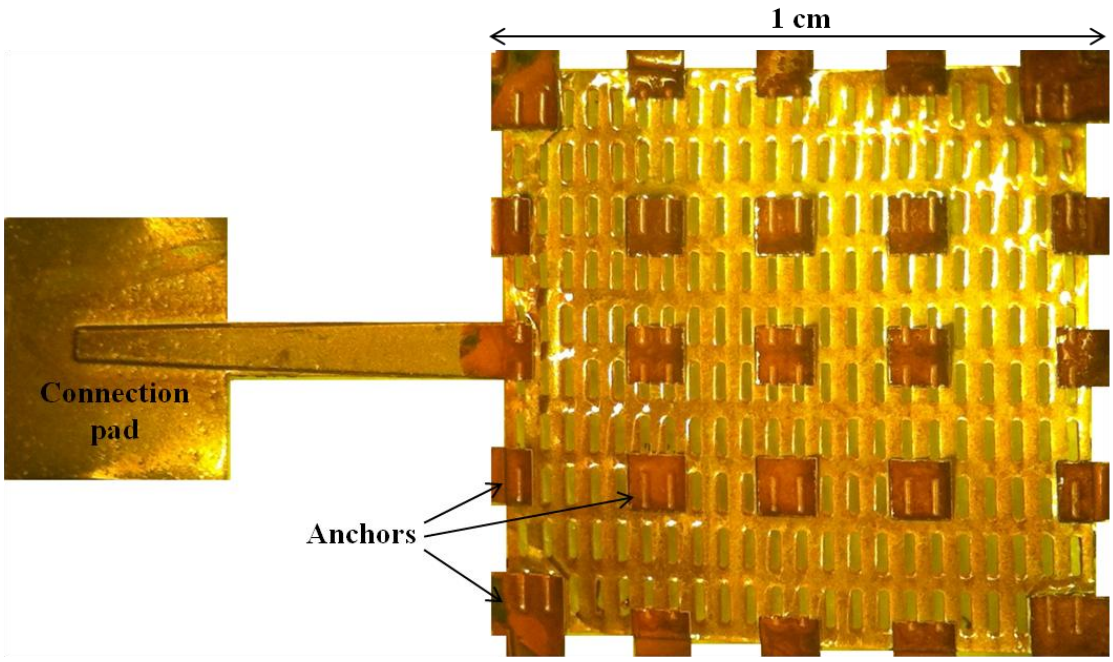

Figure 6.3: Top view of a multilayer Cu current collector

6.3.1.1 Surface Area Characterization

To determine the electrochemically accessible surface area of the resultant multilayer Cu structures, UPD was utilized as a cost-effective and relatively fast characterization technique. To our knowledge, this is the first utilization of this technique

for the measurement of the surface area of relatively complex, 3D Cu electrodes. UPD enables a precise and reproducible surface area modification through formation of a monolayer on the electrode surface using the cations in specific electrolytes [49]. This phenomenon is only possible when there is a potential difference between bulk deposition and deposition of the first monolayer on the substrate. For the study reported herein, the formation of a Tl monolayer was selected as a probe of the electrochemically accessible surface area of the multilayer Cu current collectors [50-52].

To form a Tl monolayer, the potential of the Cu electrode was set to a value slightly greater than the potential for the bulk Tl deposition. After the monolayer formation, the potential was increased to a value anodic of the UPD process to oxidatively strip the Tl monolayer from the surface of the Cu electrode. During this stripping process, the charge transfer was carefully monitored and recorded. Since the amount of the charge transferred is proportional to the number of Tl atoms removed from the surface of the electrode, the surface area was able to be determined easily.

To validate the use of the UPD application to determine the electrochemically accessible surface area, a polycrystalline Cu electrode with known surface area of 0.25 cm^2 was prepared by sputter deposition and tested in a solution made up of 0.5 M sodium sulfate (Na_2SO_4) and 2.5 mM thallium sulfate (Tl_2SO_4). The tests involved running a cyclic voltammetry (CV) scan in a three-electrode-cell configuration where Pt and Ag/AgCl were utilized as counter and reference electrodes, respectively. The CV profile of Tl on the Cu electrode is presented in Figure 6.4.A. The point c_1 (-0.50 V) can be noticed which refers to a reduction peak associated with the Tl monolayer formation. This is in good agreement with the previously reported value of -0.49 V [51]. The anodic peak at a_1 (-0.44 V) refers to the desorption of the Tl monolayer from the surface of the Cu electrode. Bulk deposition of Tl, on the other hand, initiates after the second cathodic peak, c_2 (-0.7 V), which has the corresponding anodic desorption peak at a_2 (-0.69 V).

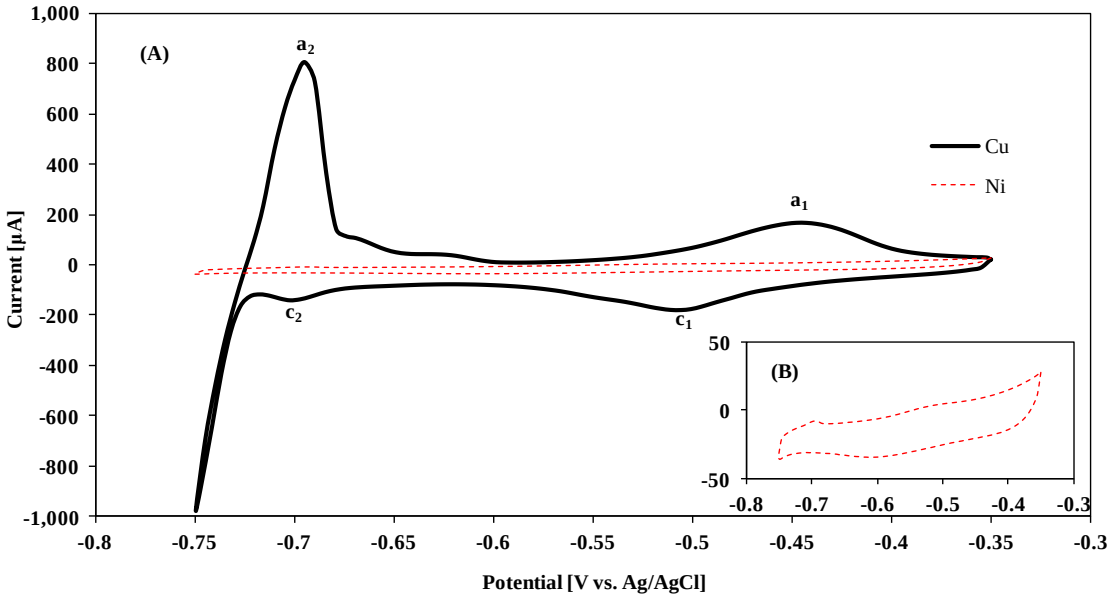

Figure 6.4: CV profiles of Tl on Cu and Ni electrodes: (A) comparison of the Cu and Ni electrodes of the same surface area and (B) enlarged view of the Ni electrode only

Once the CV tests on the Cu electrode were completed, a Ni electrode was prepared by electroplating a 0.5-µm-thick Ni film on the Cu electrode with the same dimensions and surface area of 0.25 cm^2. The same CV tests were repeated for the Ni electrode and as can be seen in Figure 6.4.A, as well as in the enlarged profile of the Ni electrode in Figure 6.4.B, no corresponding current peak for the formation of the Tl monolayer was observed in the given potential range. This finding indicates that if residual Ni is left in the multilayer 3D structure because of incomplete etching, it will not interfere with the surface area measurements of the Cu structure.

To further confirm that the UPD of Tl on the Cu surface occurs at the first cathodic peak, c_1, several chronoamperometric experiments were carried out. First, the potential of the Cu electrode was first set to -0.65 V for 30 seconds and then increased to -0.4 V. The amount of charge transferred during this potential increase was estimated by integrating the area under the chronoamperometric curve. It was calculated to be 111 µC cm^{-2} which is nearly identical to the reported quantity of charge density of 112 µC cm^{-2} in

the literature, necessary to form a monolayer of Tl on a polycrystalline Cu electrode surface [51]. Then, the time for the applied potential of -0.65 V was increased from 30 to 120 seconds and no significant change was recorded in the quantity of the stripped charge. This was an indication that 30 seconds is sufficient to form a Tl monolayer on the polycrystalline Cu surface. It also supported that no bulk deposition of Tl took place at that potential, which otherwise would have led to an increase in the quantity of the stripped charge, since the amount would be proportional to the duration of the applied potential. However, when the applied potential was brought to below the second cathodic peak c_2 even for a very short amount of time (e.g., 10 seconds), a drastic increase was observed in the quantity of the stripped charge, suggesting bulk deposition.

Another validation experiment was sought to determine the change in the effective surface area of the electrode without modifying its geometric area. This was done by thickening the sputter-deposited Cu electrodes through electroplating of additional 1-μm-thick Cu film, which increased the surface roughness. To have a better representation of the actual multilayer Cu electrodes, the same electroplating conditions and setups were utilized for the electrodeposition of that additional Cu layer. After repeating the same UPD experiments for these electrodes, an average total charge density of 132 μC cm^{-2} was determined. A surface roughness factor of 1.18 was found by dividing 132 μC cm^{-2} by the theoretical value associated with the formation of a Tl monolayer on a polycrystalline Cu surface (112 μC cm^{-2}).

One last set of experiments was performed to check whether UPD could reflect the change in the surface area of the electrode appropriately. Three more Cu electrodes with varying surface areas of 0.50, 1.00, and 1.25 cm^2 were fabricated in the same fashion as the aforementioned one with the surface area of 0.25 cm^2. The same UPD experiments were conducted using all of the electrodes, and the amount of the total charge stripped from each one was plotted with respect to the surface area of the electrodes. The schematic illustration of the electrodes, as well as the resulting calibration

plot can be seen in Figure 6.5.A and 6.5.B, respectively. A linear relationship was observed between the surface area and the amount of charge stripped, supporting the utilization of the UPD approach for determining the surface area of the Cu electrodes.

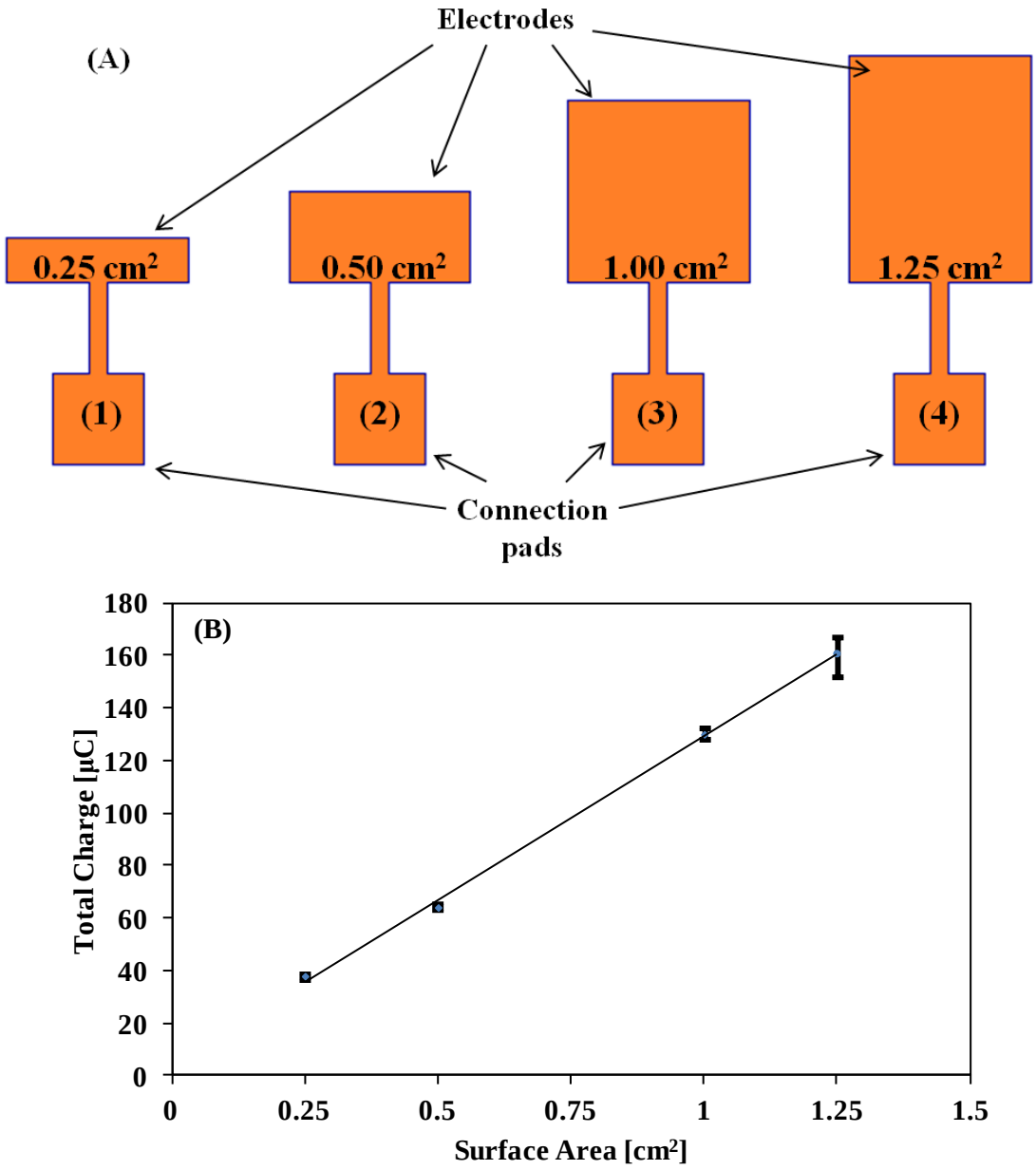

Figure 6.5: (A) Schematic illustration of the electrodes with various surface areas used in the UPD calibration experiments and (B) calibration plot showing the total charge stripped vs. the surface area of the electrodes

Following the fabrication of a 25-layer Cu current collector, UPD experiments were performed to determine the total accessible surface area of this structure. After three consecutive UPD runs, an average total charge of 5527 μC was measured for the anodic stripping of the Tl monolayer. Dividing by the charge density required to remove a complete Tl monolayer (112 μC cm^{-2}), the effective surface area was calculated to be 49.3 cm^2. By design, one side of each layer of the laminated current collector has a geometric surface area of 0.8 cm^2. Considering that 25 layers have both their top and bottom sides exposed following the complete removal of the Ni layers, the total theoretical exposed surface area of a 25-layer Cu current collector equals 40 cm^2 (25 x 2 x 0.8 cm^2), neglecting the area of the several-μm-thick side walls. Assuming that the surface roughness factor of 1.18 obtained on the test electrodes used for the calibration of the UPD method is a reliable estimate of the roughness on each layer in the multilayer Cu structure, then the predicted effective surface area becomes 47.2 cm^2. If this assumption holds, the difference between the measured and calculated surface area of 2.1 cm^2 most likely results from the surface area of the anchors and the sidewalls of each layer on the perimeter, as well as inside the etching holes.

6.3.1.2 Active Material Deposition

The final step in the fabrication process of the electrodes involves the electrodeposition of the $Ni(OH)_2$ film onto the 3D Cu current collector. The details of this active material deposition can be found in Chapter 4. However, it was observed that the adhesion between Cu and $Ni(OH)_2$ was not as strong as the adhesion between Ni and $Ni(OH)_2$. Achieving a conformal coating of the active material on the Cu surface was found to be quite challenging. Also, the active material was observed to flake off over the course of the performance tests.

To avoid these issues, a thin layer of Ni was electroplated onto the Cu current collector prior to the deposition of the active material. This Ni film not only provided better adhesion and thus, better cycling stability for the $Ni(OH)_2$, but also prevented the

Cu backbone from exposure to the alkaline electrolyte, inhibiting potential side reactions and electrode degradation. For the confirmation of the maximum and conformal surface coverage after each deposition step, cyclic voltammetry (CV) analysis was performed using a three-electrode-cell configuration in a 1 M KOH solution. Pt and Ag/AgCl were used as counter and reference electrodes, respectively, and the CV runs were performed at a scan rate of 10 mV s^{-1}.

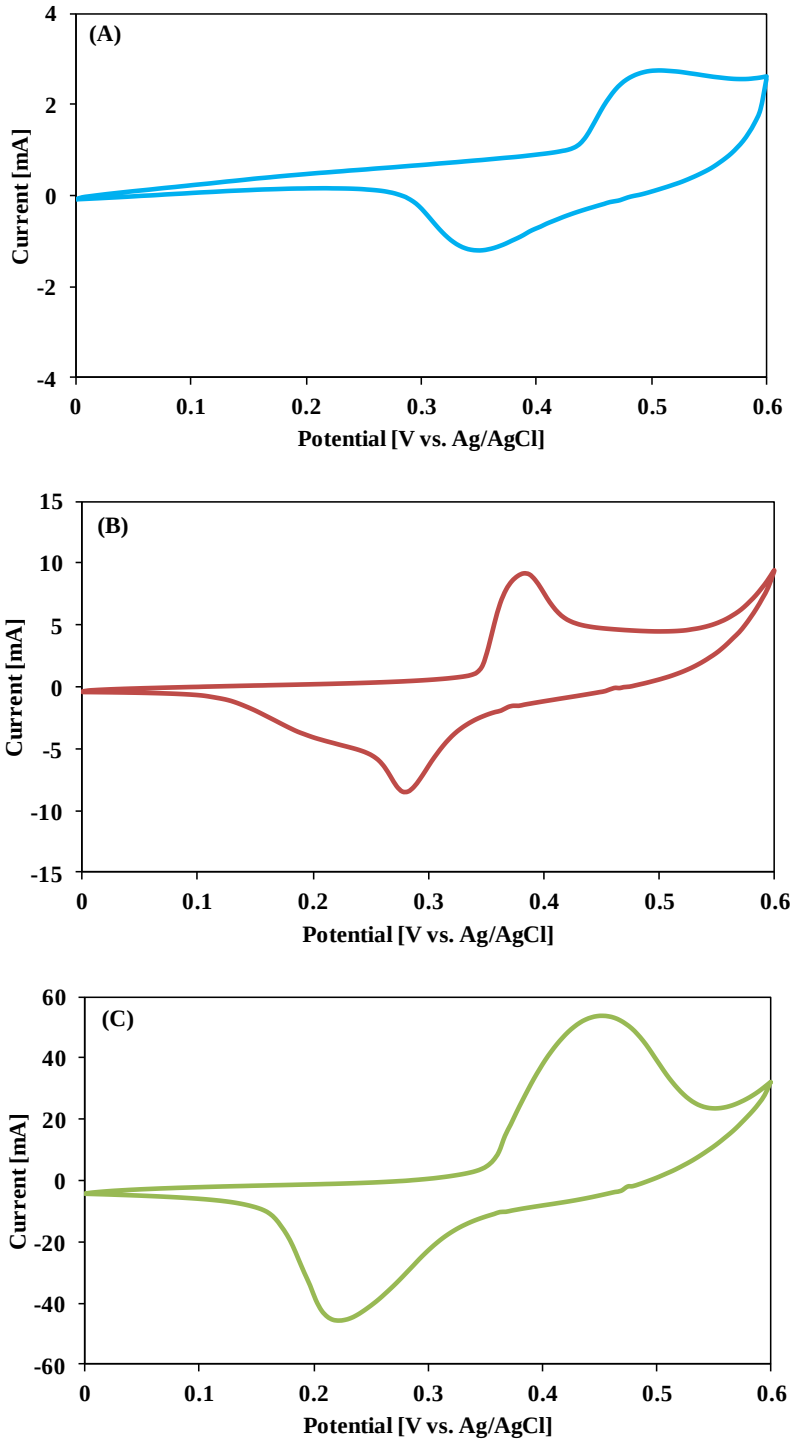

Figure 6.6: CV profiles of the electrodes in 1 M KOH solution: (A) bare Cu electrode, (B) Ni-coated Cu electrode, and (C) $Ni(OH)_2$ electrode

Figure 6.6 illustrates the CV profiles of the blank electrode (Cu only), Ni-coated electrode, and the final electrode after $Ni(OH)_2$ deposition. A significant shift in the anodic and cathodic peaks was observed following the Ni electroplating onto the bare Cu electrode, indicating a predominant existence of the Ni coating. Similarly, $Ni(OH)_2$ deposition resulted in a unique CV profile, suggesting a nearly complete surface coverage.

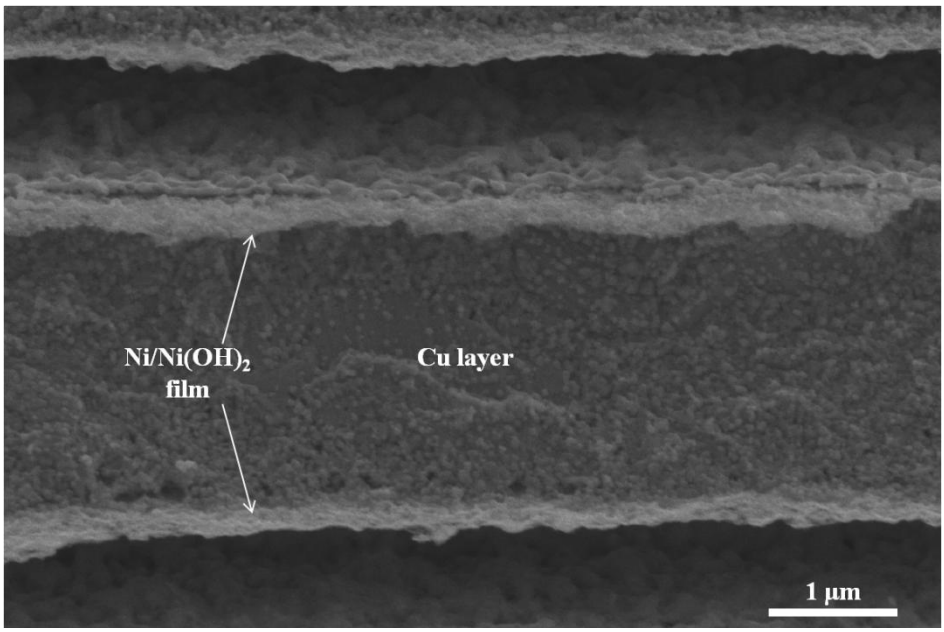

Figure 6.7: Cross-sectional view of a Cu layer sandwiched between $Ni/Ni(OH)_2$ films

The conformal coating of the Ni and $Ni(OH)_2$ layers was also confirmed visually by taking the SEM images of the cross-section of the multilayer electrode. To achieve this, the electrode was partially immersed in concentrated HNO_3 solution for a couple of seconds. The cross-sectional view of a Cu layer with a thin film of $Ni/Ni(OH)_2$ on both sides can be seen in Figure 6.7. Unlike battery applications described in Chapters 3, 4, and 5, only a thin layer of the active material is desired for supercapacitor electrodes. Figure 6.7 shows that a thin and conformal layer of approximately 0.1 µm was electrodeposited onto the individual layers of the multilayer, Ni-coated Cu backbone.

6.3.1 Vertical High-Aspect-Ratio Concentric Cylinders

The conceptual rendering of the fabrication process for the vertical high-aspect-ratio concentric cylinder electrodes is illustrated in Figure 6.8 [53]. The process, along with its benefits was briefly explained in Chapter 2.12. Here, more details will be given concerning the preparation of the SU-8 pillars, as well as both the mechanical and chemical etching processes. The details about robotically assisted sequential electroplating process and the active material deposition process can be found in Chapter 4.3.

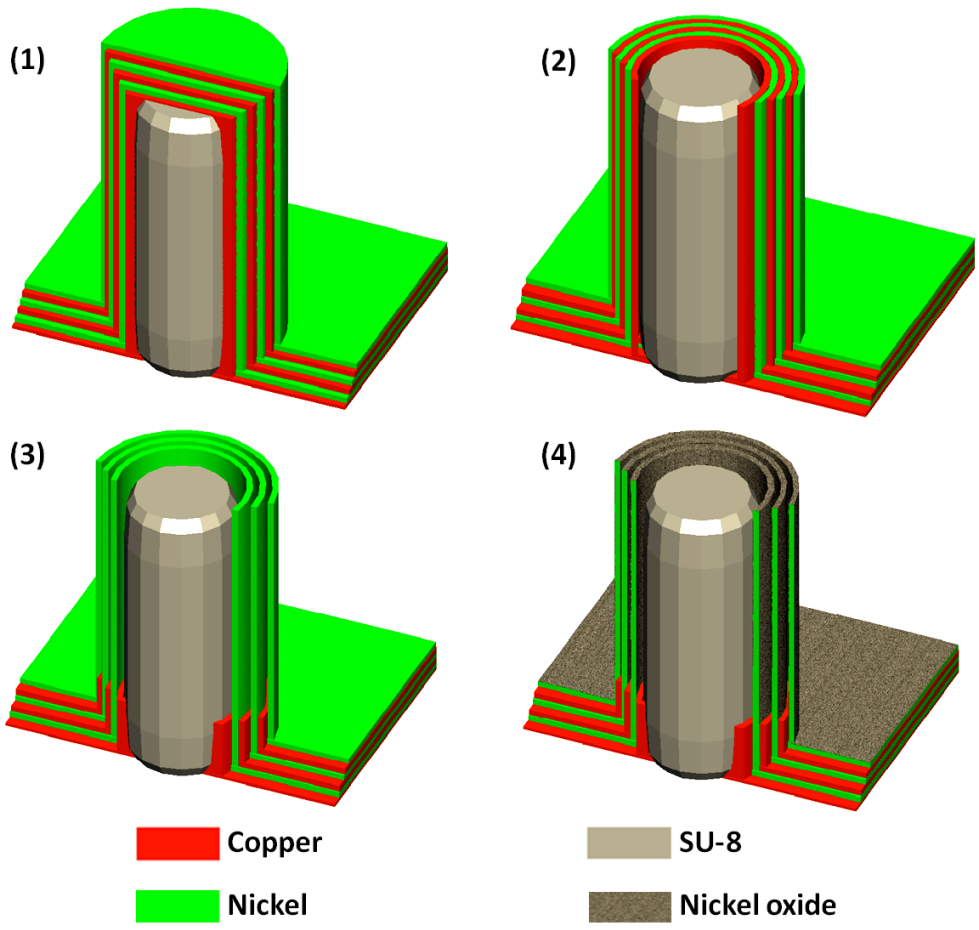

Figure 6.8: Conceptual rendering illustrating the cross-sectional view of the vertical high-aspect-ratio concentric cylinder electrodes: (1) sequential electrodeposition of Ni and Cu layers onto the metalized SU-8 pillars, (2) polishing of the pillars from the top surface, (3) selective etching of the Cu layers, and (4) active material formation

The very first step in the fabrication sequence of the electrode is the formation of the high-aspect-ratio SU-8 pillar arrays that will support the multilayer electrodes. These high-aspect-ratio pillars were enabled by adopting a thick SU-8 coating process with an approximate thickness of 1000 μm and h-line (405 nm) UV exposure method, coupled with backside exposure [54]. As a mask, an array of holes with a diameter of 100 μm was patterned on chromium (Cr)-coated glass to form the patterns for the SU-8 pillars. A thick SU-8 photoresist (SU-8 2025, MicroChem Inc.) film with an areal mass of 124 mg/cm^2 was dispensed onto the Cr-patterned glass substrate. For the pre-exposure bake process, the substrate coated with SU-8 was placed on the leveled hotplate. The temperature of the hotplate was slowly ramped up to 95 °C at a rate of 200 °C hr^{-1} and held for 15 hours. Due to the long duration of the pre-exposure bake and the decrease in the viscosity of the SU-8 with increasing temperature, leveling of the hot plate becomes particularly important to prevent uneven thickness distribution across the film and in some cases, overflow of the SU-8 from the substrate. After 15 hours, the hotplate was slowly cooled down to room temperature at 200 °C hr^{-1}.

Following the pre-exposure bake, UV exposure was carried out using a backside exposure scheme in which the sample was exposed through the glass with patterned Cr layer. The intensity and wavelength of the UV light were set to 35 mW cm^2 and 405 nm, respectively. A total exposure dose of 18 J was applied. During the exposure, a 0.22 inch-thick acrylic board (G11, Professional Plastics, Inc.) was utilized as a UV filter in order to block exposure wavelengths shorter than 400 nm. Upon completion of the exposure, the sample was let to rest for 30 minutes prior to the post-exposure bake. A post-exposure bake of one hour was performed on a hotplate at 95 ^oC by applying ramp-up and ramp-down rates of 200 ^oC hr^{-1}. Following the post-exposure bake, the SU-8 was developed in propylene glycol methyl ether acetate (PGMEA) solution for approximately 45 minutes.

During the development process, the sample was placed with its photoresist-coated side facing down and was slightly elevated from the bottom of the container using

clips attached to the corners of the substrate. Therefore, the unexposed regions of the SU-8 film were able to sink to the bottom of the container without inhibiting the mass transfer of fresh solution to the photoresist. Due to concern for the mechanical stability of the resulting high-aspect-ratio pillars, no agitation was utilized during the development process. After the development process, the sample was carefully rinsed using fresh PGMEA solution and DI water. A drying process was performed by carefully applying a cotton-based wipe (Texwipe) to soak up the excess water from between the pillars. Scanning electron microscope (SEM) images of the resulting high-aspect-ratio pillar arrays can be seen in Figure 6.9. These images were obtained by using variable pressure (VP) SEM, which enables imaging of the non-conductive samples without the need for coating them with a conductive layer. Under high vacuum conditions, non-conductive samples tend to charge, which prohibits adequate imaging.

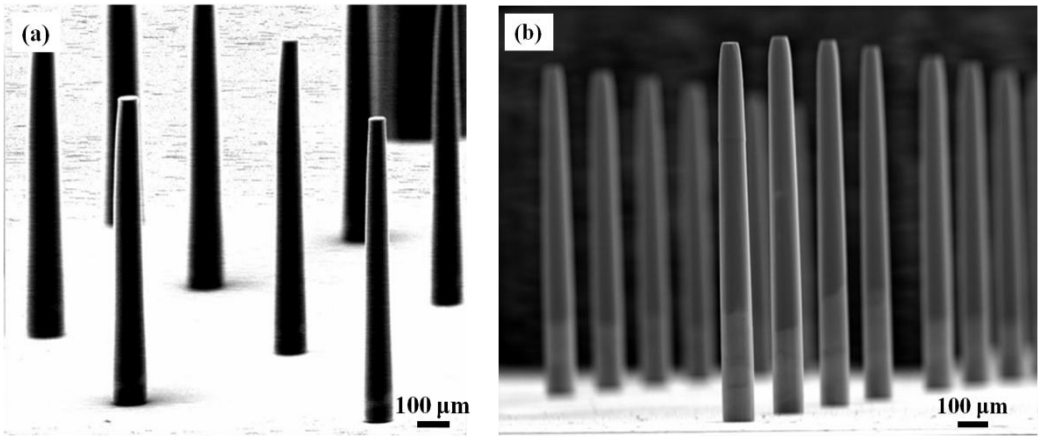

Figure 6.9: High-aspect ratio SU-8 pillars with two different aspect ratios: (a) 10:1 and (b) 20:1

In the next step of the fabrication process, DC sputtering was performed to metalize the high-aspect-ratio SU-8 pillar arrays shown in Figure 6.9. Ti and Cu seed layers were sputtered for 5 and 10 minutes, respectively, under 100% Ar at 6 mTorr. A surface profiler was utilized to determine the thickness values for the sputtered Ti and Cu

layers, which were found to be 200 and 800 nm, respectively. As mentioned in the previous chapters, the initial Ti layer serves as the adhesion promoter between the photoresist and the subsequent Cu layer. To ensure perfect metal coverage, the aforementioned charging phenomenon of the photoresist was utilized of by the high-vacuum SEM. Charging enables the detection of the unmetalized regions quite easily and and aids in the determination the optimum sputtering conditions.

Following the deposition of the seed layers, electroplating of the alternating Ni and Cu layers was carried out with the aforementioned robotic electroplating setup. 125 pairs of Ni/Cu layers were electrodeposited from their respective plating solutions. The plating conditions, including temperature, current density, bath type, anode materials, and their preparation, were the same as in the case of lateral high-aspect-ratio electrodes described in Chapters 4 and 5. Once the electroplating of alternating layers was completed, an additional, thick (35 - 40 μm) Ni layer was electroplated as the topmost layer in order to enhance the mechanical stability of the pillar array, which is quite crucial during the subsequent lapping step. The optical image of the array of pillars fabricated on a 1 cm^2 footprint area immediately after the electroplating process is shown in Figure 6.10.

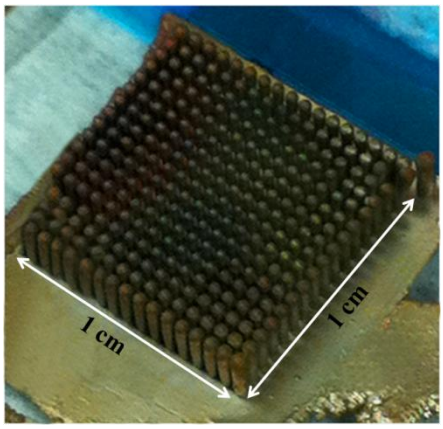

Figure 6.10: 17x17 array of SU-8 pillars coated with 125 pairs of Ni/Cu layers fabricated on a footprint of 1 cm^2

Upon the completion of the electroplating process, the metal-coated pillars were mechanically lapped from the topside using emery paper of various grades successively up to 600. Initially, a coarse lapping was carried out with a 120-grade emery paper. The main purpose of this coarse lapping was to remove the majority of the bulk Ni layer located on top of the pillars, which was electroplated in the very last step of the electroplating process. Then, higher grades of emery papers were utilized until all of the electroplated Ni and Cu layers on top of the SU-8 pillars were completely removed. This enabled the exposure of the interleaved Cu layers, as shown in the second step of the fabrication sequence given in Figure 6.8. To avoid excessive removal during the lapping process, the pillars were periodically observed under an optical microscope.

The mechanical polishing process concluded once the SU-8 cores in all of the pillars were completely exposed. The pillars were then cleaned using acetone, methanol, and IPA mixture and rinsed in DI water. Next, the samples were immersed in a concentrated nitric acid (HNO_3, 70%) solution for 15-20 seconds, and then again thoroughly rinsed with DI water. This step ensures a clean exposure of the layers from the topside by removal of the smeared Ni and Cu layers formed during the mechanical polishing process, as well as ensuring the removal of metal debris stuck between the pillars after the polishing. Optical images showing the top view of the resulting pillars can be seen in Figure 6.11. The enlarged view in Figure 6.11 helps the visualization of the individual layers around the pillar, which demonstrate a fingerprint-like pattern.

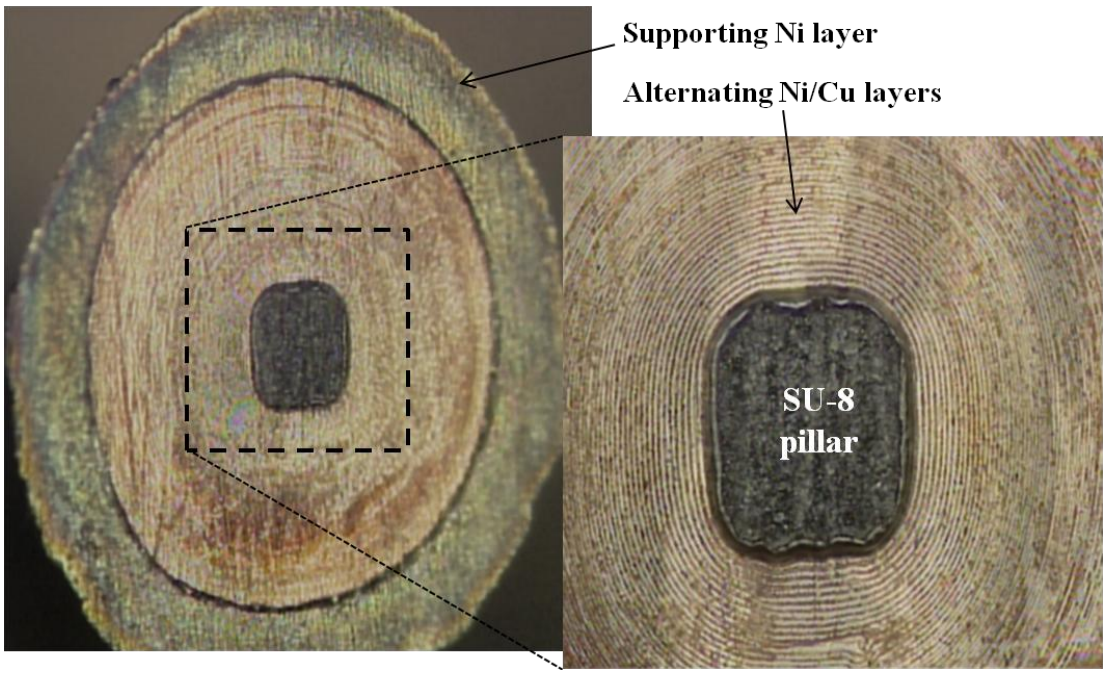

Figure 6.11: Top view of a multilayer pillar structure following the mechanical lapping process

Ideally, rectangular SU-8 pillars would yield a better utilization of the footprint area compared to their circular counterparts. As schematically illustrated in Figure 6.12, the radial growth would be expected to take place in accordance with the initial pattern. Therefore, starting with a rectangular pattern would, in theory, allow the coverage of the whole footprint area on the substrate. However, it was observed that regardless of the initial geometry of the SU-8 pillars, after the deposition of several pairs of Cu/Ni layers, the multilayer structure acquires a cylindrical geometry. This trend can also be seen in the optical images shown in Figure 6.11 where the core SU-8 pillars possesses a rectangular form while the ultimate multilayer structure exhibits a circular geometry. As the growth of these structures proceeded until two adjacent multilayer pillars came into contact and no more plating was able to be performed, dead spaces formed between four pillars as shown in Figure 6.12, reducing the utilization efficiency of the footprint area.

The reason for the deviation from the original rectangular geometry was postulated to result from the electric field being much stronger at the sharp corners of the

pillars than on the edges, and thus causing deposition rates to be higher in those regions. This issue might be overcome by performing the electrodeposition at lower current densities and keeping the plating durations much shorter. However, the resulting layers in that case would be much thinner and would most likely be not able to have the mechanical robustness necessary for support following the removal of the sacrificial layers.

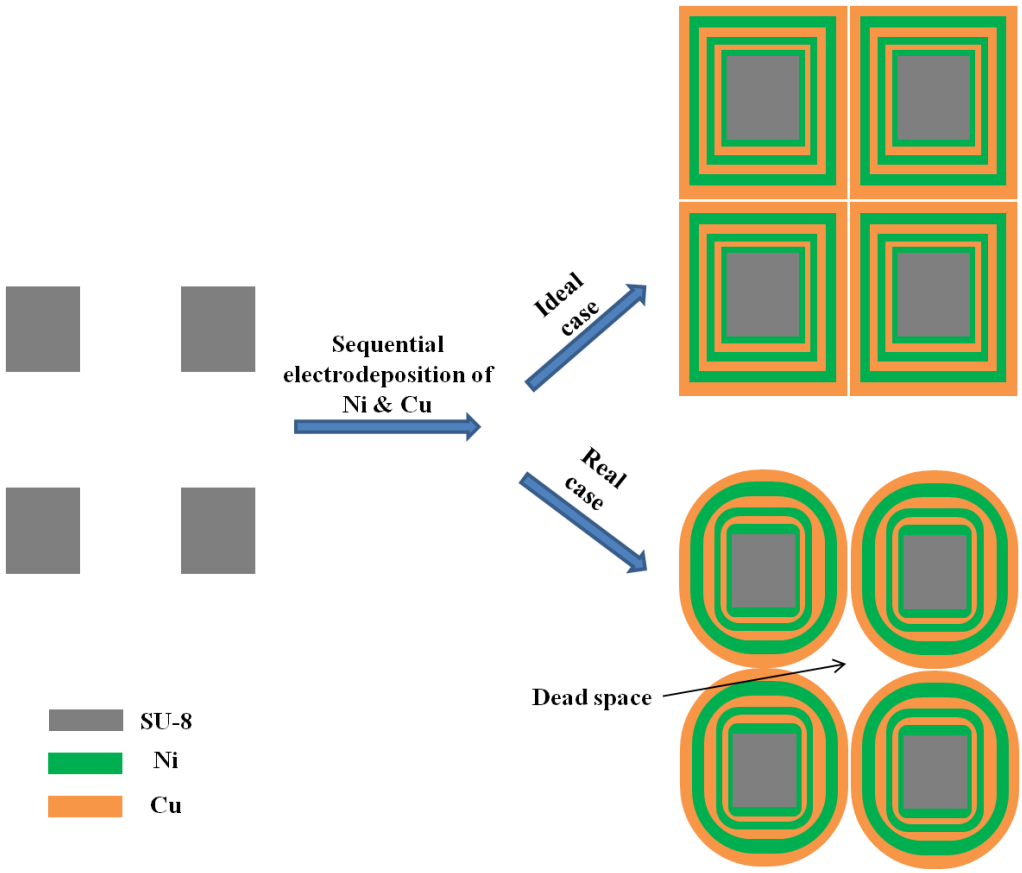

Figure 6.12: Conceptual rendering showing the top view of the growth pattern of the electrodeposited Cu and Ni layers on the rectangular SU-8 pillars: ideal case vs. real case

Following the mechanical polishing step, the structures were immersed in a selective Cu etching bath for 12 hours. The setup described in Chapter 2.3.1 was utilized where the sample was inverted and placed on a meshed plastic platform while the solution was being agitated slowly with the help of a Teflon-coated magnetic bar. The

sample was then placed in DI water for 30 minutes followed by immersion in IPA and methanol for 15 minutes each. As described earlier in Chapters 3.2.2, this process minimizes the interlayer surface tension forces and prevents the layers from collapsing. The etching process was finally completed by drying the samples in an oven at 65 ^{o}C for 30 minutes. The SEM image showing the top view of a pillar surrounded by the high-aspect-ratio concentric hollow cylinders in the resulting sample can be seen in Figure 6.13.

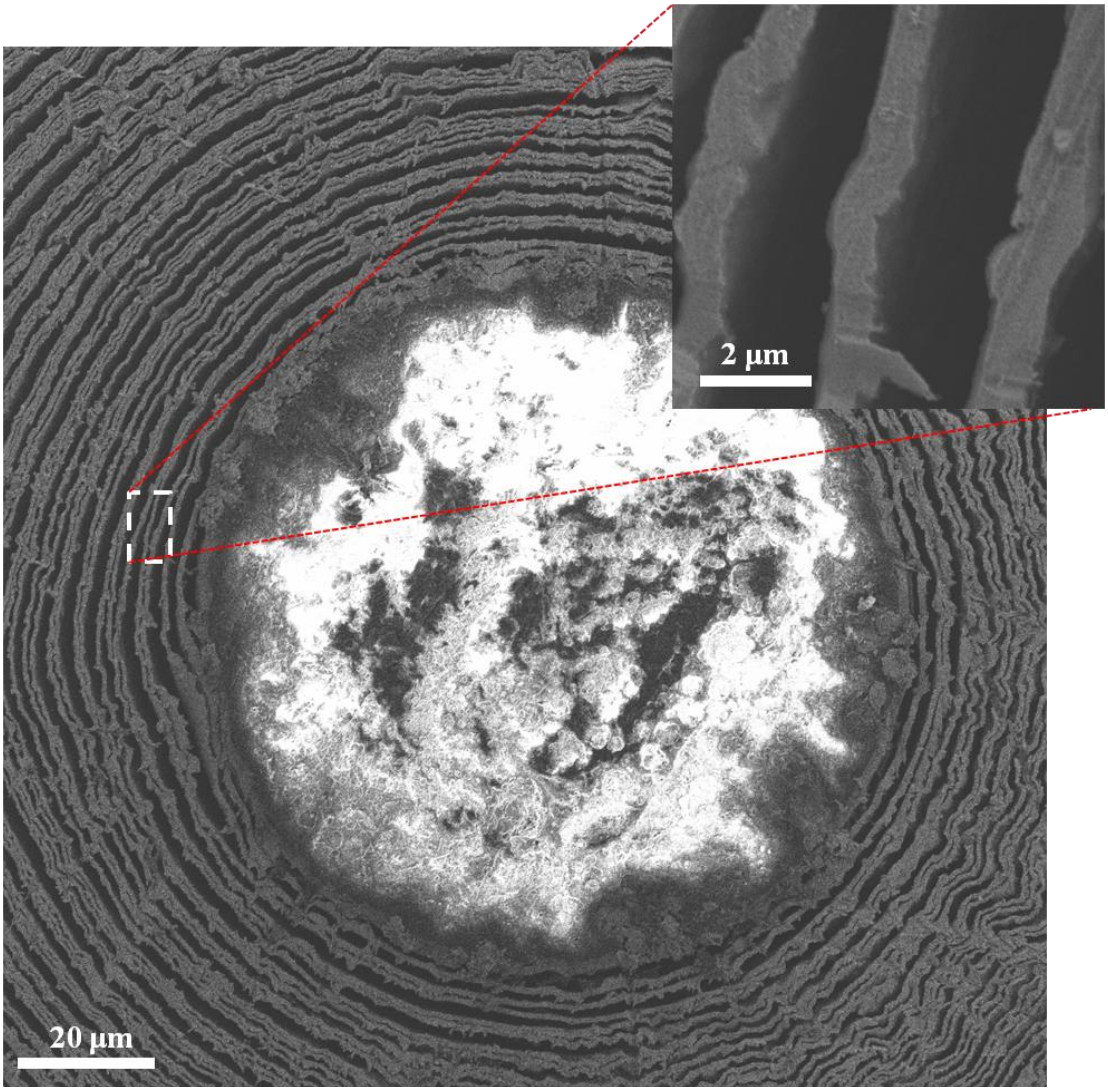

Figure 6.13: SEM image showing the top view of the multilayer pillar structure after the selective Cu etching step

To determine the exposed surface area, it was critical to ascertain the depth of the Cu etching from the top surface of the pillars. It was shown in Chapter 2.3.1 that the etching starts to advance in a non-uniform fashion if the diffusion path lengths are increased. In contrast to the lateral high-aspect-ratio structures where the etchant is able to attack the Cu layers from multiple points within the structure, high-aspect-ratio concentric cylinders allow only one access for the etchant which is from the top surface. Hence, the diffusion path lengths are drastically increased (> 400 μm).

The only way to visualize the advancement of the etching is by taking the cross-sectional images of the pillars. To do that, the sample was immersed in liquid epoxy under high vacuum. This high vacuum process promotes the diffusion of the polymer to the bottom of the hollow cylinders. Then, the sample was placed in the oven at 65 ^{o}C for 2 hours to accelerate the curing of the epoxy. Following the curing process, the sample was mechanically lapped with a coarse sandpaper in the lateral direction, such that the cross-section of the pillars can be seen. The lapping continued until the core SU-8 pillar was reached.

Figure 6.14 shows the optical images of the cross-sections taken after the lateral lapping process. As a result of the distinctive color of the Cu layers, the 12-hour etching depth (~500 μm) was easily visualized. This corresponds to an etching rate of ~0.7 μm s^{-1}, which is very close to the estimated value in the case of lateral high-aspect-ratio structures.

As shown in the enlarged cross-sectional view in Figure 6.14, a fairly uniform etching profile was observed. A similar pattern was found in other multilayer pillars on the same sample, indicating an overall uniformity in the etching profile. This was postulated to result from the convective effects introduced by agitating the solution during the etching process.

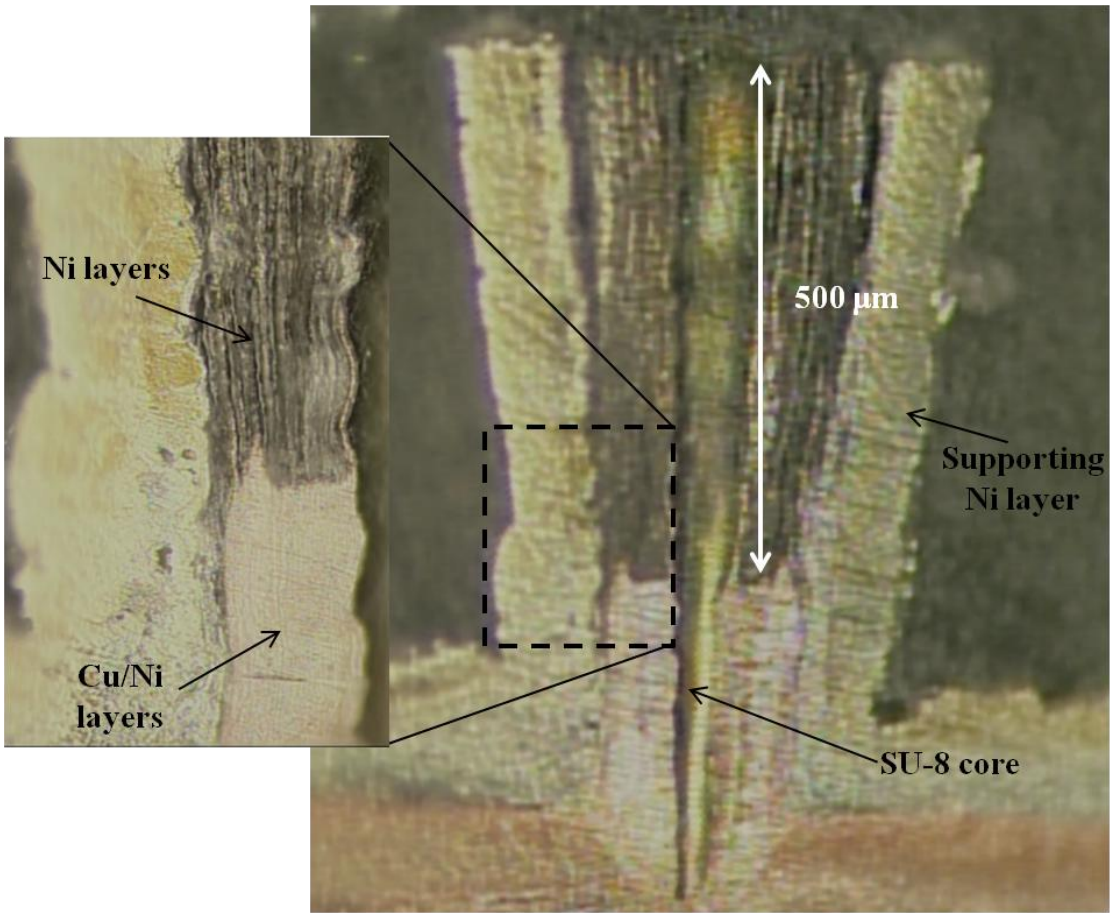

Figure 6.14: Cross-sectional view of a multilayer pillar after the etching process

The active material, $Ni(OH)_2$, was cathodically electrodeposited onto the Ni layers using pulse currents in a three-electrode-cell setup. The details of the electrodeposition process along with the reasons behind choosing particular deposition techniques can be found in Chapter 4.4.2. Prior to the deposition of the active material, the backside and the edges of the samples were coated with epoxy to enable a controlled deposition onto the pillars only.

Upon the completion of the $Ni(OH)_2$ deposition, the samples were placed in the oven to perform the calcination of the active material and finalize the formation of the NiO film as given in Equation 6.3. Several studies have confirmed that the optimum calcination temperature to achieve the highest capacitance is 300 °C [38, 39, 55]. Therefore, the sample was heated in air from room temperature to 300 °C at a rate of 5 °C

min^{-1}, maintained at 300 °C for two hours, and subsequently cooled to room temperature at the same rate, finalizing the fabrication process of the electrode.

6.4 Performance Characterization of the Electrodes

The characterization of the electrochemical performance of the $Ni(OH)_2$- and NiO-based electrodes was carried out in an alkaline electrolyte (1 M KOH) using a potentiostat (WaveDriver 10, Pine Instruments). For high power applications, the electrolyte concentration can be increased further to achieve a higher ionic conductivity at the expense of narrowed functional potential range of the electrode because of the reduced potential at which the oxygen formation occurs. Both of the electrodes were characterized in a three-electrode-cell configuration where Pt and Ag/AgCl served as counter and reference electrodes, respectively. Two electrodes will be discussed separately in the following sections.

6.4.1 $Ni(OH)_2$ Electrodes Based on Lateral High-Aspect-Ratio Parallel Plates

The capacitive behavior of the $Ni(OH)_2$-based electrode was first characterized by performing CV analysis. The electrodes were scanned between the potentials of 0.0 and 0.6 V at scan rates ranging from 5 to 25 mV s^{-1}. The resultant CV curves can be seen in Figure 6.15.A. The shape of these curves suggests a distinguished pseudocapacitive behavior from pure double-layer capacitance as in the case of carbon-based electrochemical capacitors, which ideally would have a rectangular CV profile. Two clear anodic and cathodic peaks in the profiles correspond to the reversible Faradaic reactions of $Ni(OH)_2$ taking place on the surface of the electrode:

$$Ni(OH)_2 + OH^- \leftrightarrow NiOOH + H_2O + e^- \quad (6.4)$$

The forward (charging) and reverse (discharging) reactions in Equation 6.4 refer to the anodic and cathodic peaks in the CV curves, respectively. These peaks exhibit a nearly perfect symmetry suggesting an excellent reversibility of the active material [32]. Increasing the scan rate from 5 to 25 mV s^{-1} results in the shift of the oxidation and reduction peaks to a more positive and negative potential values, respectively. This shift is mainly associated with the increase in the internal resistance of the electrode. However, it is also observed that there is no significant shape change of the CV curves with increasing scan rate as a result of the reduced equivalent series resistance and improved mass transfer, as well as excellent electron conduction [31].

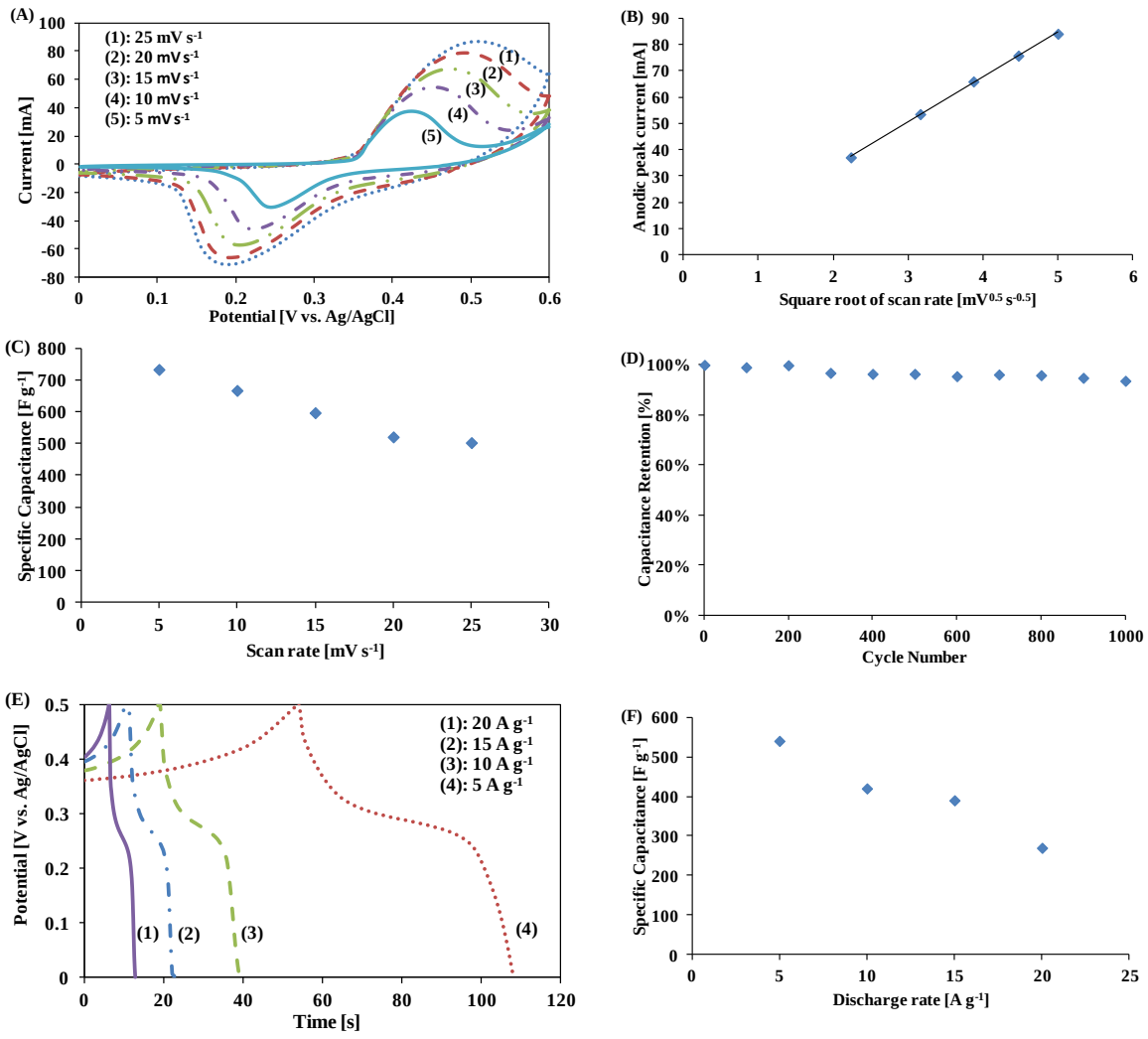

Figure 6.15: Electrochemical characterization of the $Ni(OH)_2$ electrodes based on lateral high-aspect-ratio structures: (A) CV profiles at various scan rates, (B) relationship between the anodic peak current and square root of scan rates, (C) specific capacitance obtained from CV profiles with respect to scan rates, (D) capacitance retention of the electrode at 20 mV s^{-1} for over 1000 cycles, (E) galvanostatic charge and discharge curves at various rates, and (F) specific capacitance obtained from galvanostatic discharge tests at various rates

To verify that the conformal deposition of the $Ni(OH)_2$ film onto the highly conductive Cu current collector can significantly enhance the kinetics, as well as the electrochemical utilization of $Ni(OH)_2$, the effect of scan rates, v, on the anodic peak currents, I_p, in the CV profiles of the electrode was also investigated as shown in Figure

6.15.B. The linear relationship between the anodic peak current (I_p) and the square root of the scan rate, ($v^{0.5}$) at all rates indicates that the redox reactions of $Ni(OH)_2$ in KOH solution is a diffusion-controlled process [56, 57].

The CV profiles given in Figure 6.15.A were also utilized to determine the specific capacitance, C_s (F g^{-1}), of the $Ni(OH)_2$ electrodes by calculating the area under the CV curves according to the following equation:

$$C_s = \frac{1}{m \cdot v \cdot (V_c - V_a)} \int_{V_a}^{V_c} I(V) dV \qquad (6.5)$$

where V_c, V_a, m, v, and I are the cathodic potential (V), anodic potential (V), total mass of the active material (g), scan rate (mV s^{-1}), and response current as a function of the applied potential (A), respectively. To be consistent with the previous studies from the literature involving $Ni(OH)_2$ as the active material for the electrochemical capacitors, V_c (0.0 V) and V_a (0.6 V) values were selected accordingly. The total mass m of the electrodeposited $Ni(OH)_2$ was measured using a high-precision microscale and found to be 1.8 mg. This value is in accordance with the theoretical value estimated from the correlation given in Chapter 4.4.2. By inserting this value into Equation 6.5, the specific capacitances of the electrodes were calculated to be 733, 667, 597, 521, and 503 F g^{-1} at scan rates of 5, 10, 15, 20, and 25 mV s^{-1}, respectively. As the scan rate was increased to 25 mV s^{-1}, the specific capacitance dropped to 503 F g^{-1}, corresponding to approximately 69% of the capacity at 5 mV s^{-1}. This remarkably high capacitance retention indicates an enhanced high-rate performance when compared to previously reported values in the literature [28, 29, 31, 33, 35, 37].

Furthermore, CV runs were also utilized to investigate the long-term stability of the $Ni(OH)_2$ electrode in KOH solution. As illustrated in Figure 6.15.D, more than 1000 CV cycles were performed at a relatively high scan rate of 20 mV s^{-1}, and the electrode

exhibited only ~6% degradation in its capacitance. This negligible degradation is an indication of excellent long-term stability of the electrode.

In addition to the CV experiments, galvanostatic charge and discharge tests were performed to analyze the electrochemical performance of the $Ni(OH)_2$ electrodes. Figure 6.15.E demonstrates the charge and discharge profiles of the electrode between the potentials of 0.0 and 0.5 V at relatively high current densities ranging from 5 to 20 A g^{-1}. The corresponding specific capacitance values at the discharge rates of 5, 10, 15, and 20 A g^{-1} were calculated to be 540, 420, 390, and 270 F g^{-1}, respectively, by using Equation 6.6.

$$C_s = \frac{I}{m \cdot v} \tag{6.6}$$

Figure 6.15.F demonstrates the relationship between the specific capacitance and the corresponding discharge rate. Increasing the current density from 5 to 20 A g^{-1} was observed to result in a decrease in the specific capacitance by approximately 50%, indicating again a relatively high retention in the capacitance.

To realize the contribution of the multilayer Cu backbone to the overall performance of the system quantitatively, same amount of $Ni(OH)_2$ (i.e., 1.8 mg) was electrodeposited on a single layer structure with the same footprint area as the multilayer one and its performance was compared to the multilayer electrode. CV runs performed on the single layer electrode at 20 mV s^{-1} revealed a specific capacitance of 6.1 F g^{-1} which corresponds to 1.2% of the value obtained with the multilayer electrode under the same conditions.

In addition to the specific capacitance, areal capacitance is also an important feature that needs to be calculated, since these energy storage systems are mainly considered for portable electronic devices which, particularly miniaturized versions, have

limited footprint area to place their energy source. High areal capacitance values of 1319 and 972 mF cm^{-2} were calculated from the CV data and galvanostatic discharge data, respectively.

Ragone plots that relate the specific power of the energy storage systems to their specific energy are a commonly used method to evaluate the performance of the electrochemical capacitors. The specific energy (E) and power (P) of an electrochemical capacitor can be calculated by using the Equations 6.7 and 6.8, respectively.

$$E = \frac{1}{2} \cdot C_s \cdot (\Delta V)^2 \quad (6.7)$$

$$P = \frac{E}{\Delta t} \quad (6.8)$$

The values obtained for both the CV data and the galvanostatic discharge data by using these equations are plotted as shown in Figure 6.16. Remarkably high specific energy of 25.2 Wh kg^{-1} was obtained at a significantly high power density of 3800 W kg^{-1}.

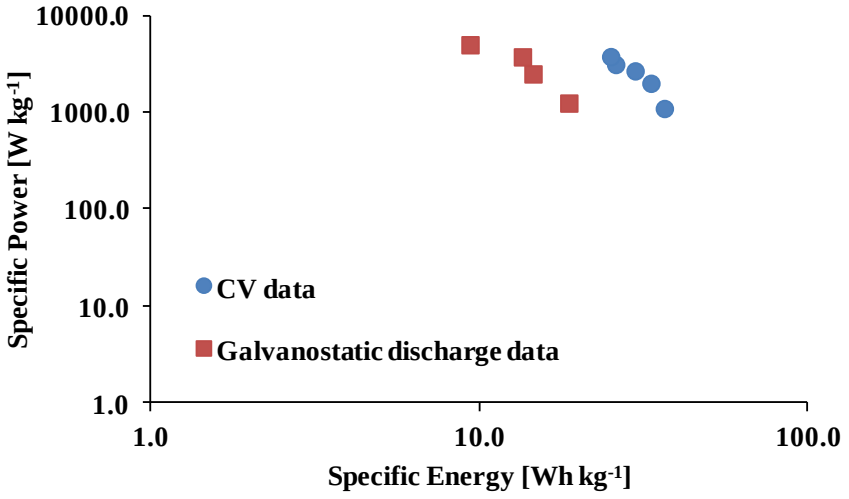

Figure 6.16: Ragone plot showing the relationship between the specific power and energy of a $Ni(OH)_2$-based electrochemical capacitor electrode

6.4.2 NiO Electrodes Based on Vertical High-Aspect-Ratio Concentric Cylinders

For the performance evaluation of the electrodes based on vertical high-aspect-ratio concentric cylinders, pillar arrays with 10x10 evenly spaced pillars on a 1 cm^2 footprint area were fabricated. The pillars had a total height of 1 mm. Prior to the electrochemical characterization, the samples were immersed in the KOH solution, and vacuum was applied to remove the air trapped in between the hollow cylinders and ensure a good contact between the electrode and the electrolyte.

To be consistent with the literature, the CV experiments were carried out between -0.2 and 0.4 V [43]. The scans were performed at 20 mV s^{-1}. For the demonstration of the degree of capacitance improvement provided by the multilayer pillar electrodes, a planar square Ni electrode with the same footprint area of 1 cm^2 was also tested along with the multilayer electrode. This provided a baseline to assess the improvement in the capacitance from 2D geometries to high surface area 3D architectures.

The CV profiles of the electrodes are shown in Figure 6.17. Prior to these profiles, 20 CV runs were carried out to ensure the stabilization of the electrodes. $Ni(OH)_2$-coated multilayer pillar electrode before the heat treatment is given in Figure 6.17.A. A cathodic peak can be seen around 0.27 V which is in agreement with the shape and the potential of earlier studies in the literature [40]. This result implies that the electrode surface was able to be successfully coated with $Ni(OH)_2$ film undergoing the redox reactions given in Equation 6.3.

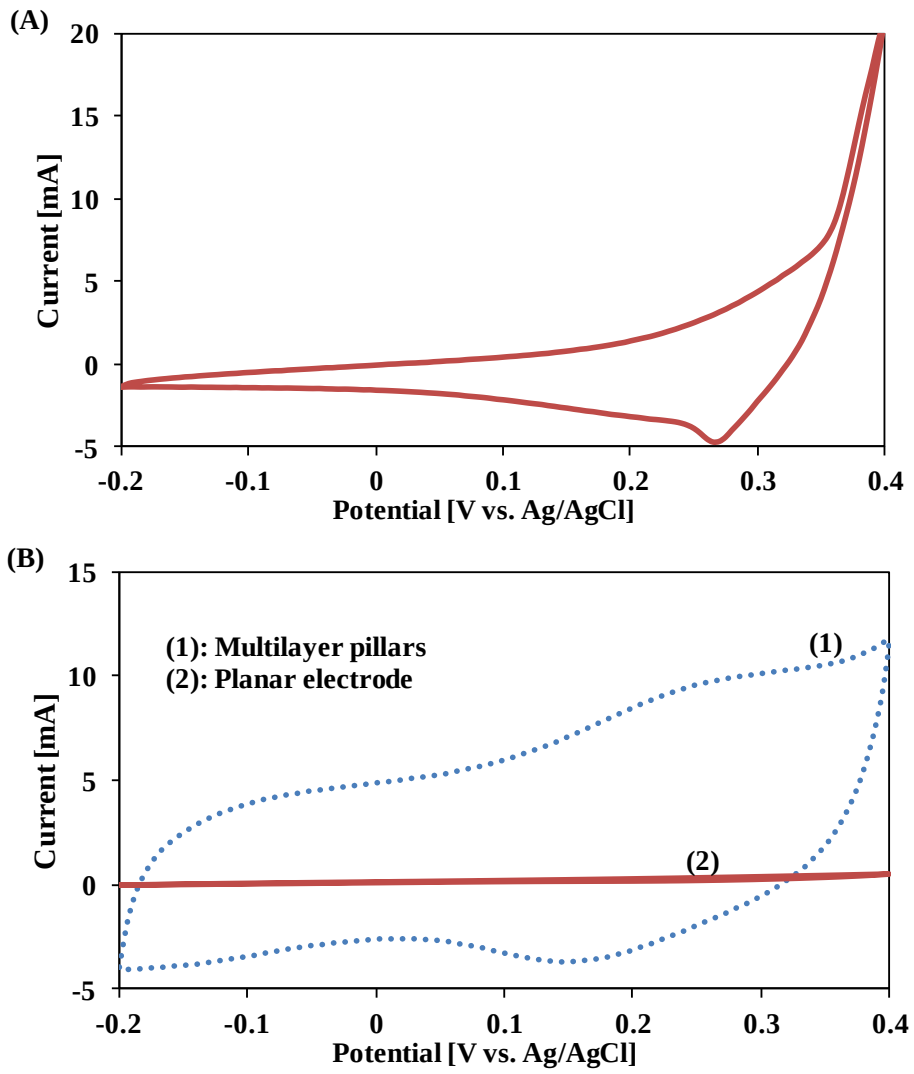

Figure 6.17: CV profiles at 20 mV s^{-1}: (A) CV of the multilayer pillar electrode after $Ni(OH)_2$ deposition and (B) CV profiles of the planar and multilayer pillar electrodes following the calcination of $Ni(OH)_2$ at 300 °C

The CV profiles of the plain and multilayer pillar electrode following the calcination at 300 °C can be seen in Figure 6.17.B. Areal capacitance of the electrodes was calculated by using Equation 6.5. For the multilayer pillar electrode, the capacitance was found to be 270 mF cm^2 at a scan rate of 20 mV s^{-1}. The planar electrode exhibited a capacitance of 11 mF cm^{-2}. This corresponds to a more than 25-fold improvement in the performance enabled by the multilayer pillar electrodes.

Measuring the mass of the active material was rather problematic due to the complications that took place during the calcination process. The complications mainly arose from the presence of the epoxy on the backside and the edges of the sample. When the sample was heated to 300 °C for 2 hours and then cooled, a net weight loss was observed which was postulated to originate primarily from the decomposition of the epoxy polymer. Some portion of this weight loss also may have resulted from the partial decomposition of SU-8 cores. Additional weight loss was also expected due to the dehydration of $Ni(OH)_2$ as shown in the calcination reaction in Equation 6.3. As a result, determination of the mass of NiO was quite challenging.

Nonetheless, the mass of the electrodeposited $Ni(OH)_2$ was able to be measured, as well as calculated using the correlation given in Chapter 4.4.2. It has been also reported in the literature that the mass of the electrochemically deposited $Ni(OH)_2$ film reduces to 60% of its initial value when heated to 300 °C or above [39]. Assuming that this holds in our experiments, the amount of NiO was calculated to be 4.8 mg, leading to a specific capacitance of 56 F g^{-1}, which is very close to a previously reported value of 59 F g^{-1} for NiO [38]. No significant change was observed in the specific capacitance following 400 more CV cycles.

6.5 Conclusions

In this chapter, it was demonstrated that the electrochemical capacitors involving electrodes based on rationally designed and deterministically engineered 3D architectures exhibit an improved performance. The resultant $Ni(OH)_2$ electrodes offered a relatively high specific and areal capacitances of 733 F g^{-1} and 1319 mF cm^{-2}, respectively, that were determined by CV runs at a scan rate of 5 mV s^{-1}. A remarkable power capability was demonstrated by delivering 69% of those capacitances at high scan rates of 25 mV s^{-1}. A similarly high capacitance delivery was also observed when performing galvanostatic charge and discharge experiments at rates as high as 20 A g^{-1}. The

electrodes also exhibited an excellent cycling stability with a capacitance retention of 94% following in excess of 1000 CV runs performed at a relatively high scan rate of 20 mV s^{-1}. These high specific power and energy values have been attributed to the presence of the 3D Cu backbone structure with minimal internal resistance and high surface area, both of which are highly desirable features for electrochemical energy storage systems in general.

Figure 6.18 shows the Ragone plot given in Chapter 1 and compares the performance of the electrochemical capacitors based on multilayer electrodes to the existing energy storage systems. The specific power and energy values obtained from the CV data and galvanostatic discharge data are labeled separately. As can be seen in Figure 6.18, in contrast to the previous accomplishments where capacitor-like battery performance was reported, the electrochemical capacitors discussed herein demonstrate a battery-like performance.

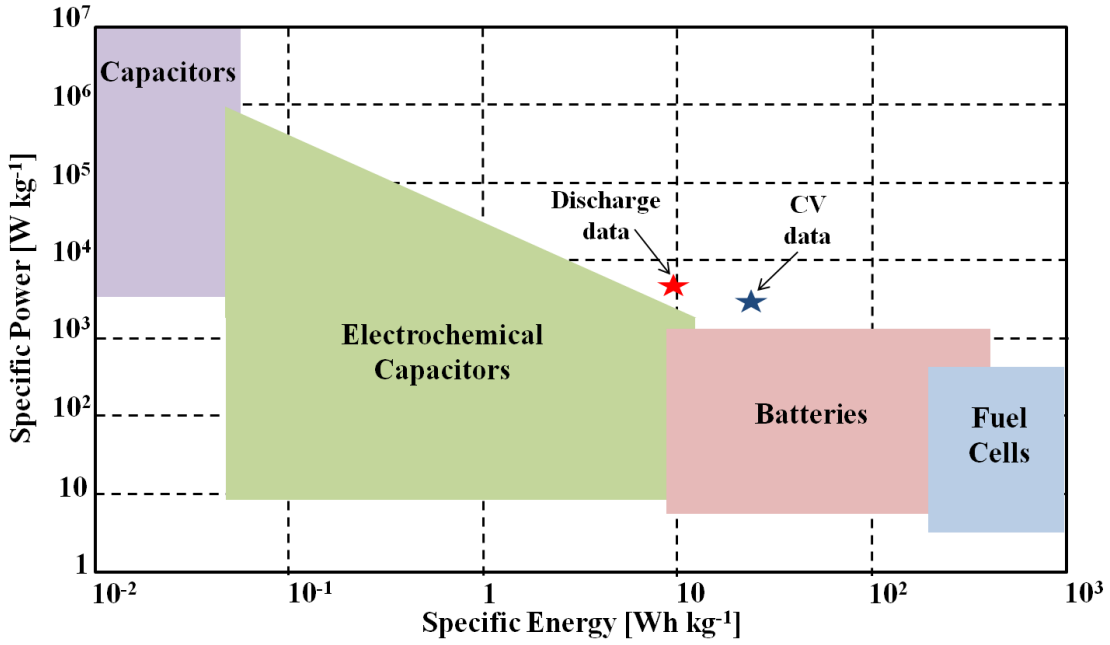

Figure 6.18: Ragone plot comparing the performance of the fabricated electrodes to the existing energy storage systems

In addition to the improvements pertaining to the electrochemical performance of the 3D electrodes, successful utilization of the straightforward and inexpensive electrochemical techniques was also demonstrated. One of these techniques involves selective electrochemical etching of Ni layers over Cu, enabling an alternative fabrication approach for the realization of 3D Cu architectures which was not reported previously. In addition, the use of UPD phenomenon for precisely determining the surface area of relatively complex 3D Cu structures was also successfully demonstrated as a simple, cost-effective, and reliable tool.

It was also shown that the alternative fabrication approach comprising vertical high-aspect-ratio concentric cylinder structures enables promising electrodes to be utilized in electrochemical capacitor applications. The fabricated electrodes were shown to possess excellent mechanical stability even at elevated temperatures and yielded relatively high areal capacitance values of 270 mF cm^{-2}, sufficiently high for certain autonomous microscale applications.

One main advantage associated with the use of vertical high-aspect-ratio pillars is that this approach allows mold-free fabrication of high surface area structures. In addition, higher utilization of the volume is possible due to the capability of fabricating ultrahigh-aspect-ratio pillars that can achieve thicknesses of more than 2 mm. In the case of lateral high-aspect-ratio multilayer structures, on the other hand, the total thickness of the structure is limited by the mold thickness (<1 mm). Both of these approaches open up the possibility for electrodes with even higher power and energy densities, by incorporating active materials with higher intrinsic capacitances (e.g., RuO_2).

6.6 References

[1] G. P. Wang, L. Zhang, and J. J. Zhang, "A review of electrode materials for electrochemical supercapacitors," *Chemical Society Reviews,* vol. 41, pp. 797-828, 2012.

[2] X. Zhao, B. M. Sanchez, P. J. Dobson, and P. S. Grant, "The role of nanomaterials in redox-based supercapacitors for next generation energy storage devices," *Nanoscale,* vol. 3, pp. 839-855, 2011.

[3] A. J. Bard and L. R. Faulkner, *Electrochemical methods: fundamentals and applications* vol. 2: Wiley New York, 1980.

[4] R. Kotz and M. Carlen, "Principles and applications of electrochemical capacitors," *Electrochimica Acta,* vol. 45, pp. 2483-2498, 2000.

[5] A. G. Pandolfo and A. F. Hollenkamp, "Carbon properties and their role in supercapacitors," *Journal of Power Sources,* vol. 157, pp. 11-27, Jun 2006.

[6] Y. Zhang, H. Feng, X. B. Wu, L. Z. Wang, A. Q. Zhang, T. C. Xia, *et al.*, "Progress of electrochemical capacitor electrode materials: A review," *International Journal of Hydrogen Energy,* vol. 34, pp. 4889-4899, Jun 2009.

[7] C. D. Lokhande, D. P. Dubal, and O. S. Joo, "Metal oxide thin film based supercapacitors," *Current Applied Physics,* vol. 11, pp. 255-270, May 2011.

[8] B. C. Kim, J. M. Ko, and G. G. Wallace, "A novel capacitor material based on Nafion-doped polypyrrole," *Journal of Power Sources,* vol. 177, pp. 665-668, Mar 2008.

[9] P. Sharma and T. S. Bhatti, "A review on electrochemical double-layer capacitors," *Energy Conversion and Management,* vol. 51, pp. 2901-2912, Dec 2010.

[10] E. Frackowiak, V. Khomenko, K. Jurewicz, K. Lota, and F. Beguin, "Supercapacitors based on conducting polymers/nanotubes composites," *Journal of Power Sources,* vol. 153, pp. 413-418, Feb 2006.

[11] Y. Zhao, M. B. Zheng, J. M. Cao, X. F. Ke, J. S. Liu, Y. P. Chen, *et al.*, "Easy synthesis of ordered meso/macroporous carbon monolith for use as electrode in electrochemical capacitors," *Materials Letters,* vol. 62, pp. 548-551, Feb 2008.

[12] B. Z. Fang and L. Binder, "Enhanced surface hydrophobisation for improved performance of carbon aerogel electrochemical capacitor," *Electrochimica Acta,* vol. 52, pp. 6916-6921, Aug 2007.

[13] K. Okajima, A. Ikeda, K. Kamoshita, and M. Sudoh, "High rate performance of highly dispersed C-60 on activated carbon capacitor," *Electrochimica Acta,* vol. 51, pp. 972-977, Nov 2005.

[14] W. Xing, S. Z. Qiao, R. G. Ding, F. Li, G. Q. Lu, Z. F. Yan, *et al.*, "Superior electric double layer capacitors using ordered mesoporous carbons," *Carbon,* vol. 44, pp. 216-224, Feb 2006.

[15] B. Xu, F. Wu, S. Chen, C. Z. Zhang, G. P. Cao, and Y. S. Yang, "Activated carbon fiber cloths as electrodes for high performance electric double layer capacitors," *Electrochimica Acta,* vol. 52, pp. 4595-4598, Mar 2007.

[16] Y. P. Fang, J. W. Liu, D. J. Yu, J. P. Wicksted, K. Kalkan, C. O. Topal, *et al.*, "Self-supported supercapacitor membranes: Polypyrrole-coated carbon nanotube networks enabled by pulsed electrodeposition," *Journal of Power Sources,* vol. 195, pp. 674-679, Jan 2010.

[17] H. F. An, Y. Wang, X. Y. Wang, L. P. Zheng, X. Y. Wang, L. H. Yi, *et al.*, "Polypyrrole/carbon aerogel composite materials for supercapacitor," *Journal of Power Sources,* vol. 195, pp. 6964-6969, Oct 2010.

[18] R. K. Sharma, A. C. Rastogi, and S. B. Desu, "Manganese oxide embedded polypyrrole nanocomposites for electrochemical supercapacitor," *Electrochimica Acta,* vol. 53, pp. 7690-7695, Nov 2008.

[19] S. H. Mujawar, S. B. Ambade, T. Battumur, R. B. Ambade, and S. H. Lee, "Electropolymerization of polyaniline on titanium oxide nanotubes for supercapacitor application," *Electrochimica Acta,* vol. 56, pp. 4462-4466, Apr 2011.

[20] H. Zhang, G. P. Cao, Z. Y. Wang, Y. S. Yang, Z. J. Shi, and Z. N. Gu, "Tube-covering-tube nanostructured polyaniline/carbon nanotube array composite electrode with high capacitance and superior rate performance as well as good cycling stability," *Electrochemistry Communications,* vol. 10, pp. 1056-1059, Jul 2008.

[21] Z. Fan, J. H. Chen, K. Z. Cui, F. Sun, Y. Xu, and Y. F. Kuang, "Preparation and capacitive properties of cobalt-nickel oxides/carbon nanotube composites," *Electrochimica Acta,* vol. 52, pp. 2959-2965, Feb 2007.

[22] D. D. Zhao, S. J. Bao, W. H. Zhou, and H. L. Li, "Preparation of hexagonal nanoporous nickel hydroxide film and its application for electrochemical capacitor," *Electrochemistry Communications,* vol. 9, pp. 869-874, May 2007.

[23] I. H. Kim and K. B. Kim, "Electrochemical characterization of hydrous ruthenium oxide thin-film electrodes for electrochemical capacitor applications," *Journal of the Electrochemical Society,* vol. 153, pp. A383-A389, 2006.

[24] N. A. Choudhury, A. K. Shukla, S. Sampath, and S. Pitchumani, "Cross-linked polymer hydrogel electrolytes for electrochemical capacitors," *Journal of the Electrochemical Society,* vol. 153, pp. A614-A620, 2006.

[25] B. Gao, X. G. Zhang, C. Z. Yuan, J. Li, and L. Yu, "Amorphous Ru1-yCryO2 loaded on TiO2 nanotubes for electrochemical capacitors," *Electrochimica Acta,* vol. 52, pp. 1028-1032, Nov 2006.

[26] M. Armand, F. Endres, D. R. MacFarlane, H. Ohno, and B. Scrosati, "Ionic-liquid materials for the electrochemical challenges of the future," *Nature Materials,* vol. 8, pp. 621-629, Aug 2009.

[27] Q. H. Huang, X. Y. Wang, J. Li, C. L. Dai, S. Gamboa, and P. J. Sebastian, "Nickel hydroxide/activated carbon composite electrodes for electrochemical capacitors," *Journal of Power Sources,* vol. 164, pp. 425-429, Jan 2007.

[28] G. W. Yang, C. L. Xu, and H. L. Li, "Electrodeposited nickel hydroxide on nickel foam with ultrahigh capacitance," *Chemical Communications,* pp. 6537-6539, 2008.

[29] H. Jiang, T. Zhao, C. Z. Li, and J. Ma, "Hierarchical self-assembly of ultrathin nickel hydroxide nanoflakes for high-performance supercapacitors," *Journal of Materials Chemistry,* vol. 21, pp. 3818-3823, 2011.

[30] R. D. Apostolova, Y. A. Tkachenko, O. V. Kolomoyets, and E. M. Shembel, "Thin-layer electrolytic nickel hydroxide Ni(OH)(2) in an electrochemical capacitor," *Surface Engineering and Applied Electrochemistry,* vol. 48, pp. 170-174, Mar 2012.

[31] J. Yan, Z. J. Fan, W. Sun, G. Q. Ning, T. Wei, Q. Zhang, *et al.*, "Advanced asymmetric supercapacitors based on Ni(OH)2/graphene and porous graphene electrodes with high energy density," *Advanced Functional Materials,* vol. 22, pp. 2632-2641, Jun 2012.

[32] H. B. Li, M. H. Yu, F. X. Wang, P. Liu, Y. Liang, J. Xiao, *et al.*, "Amorphous nickel hydroxide nanospheres with ultrahigh capacitance and energy density as electrochemical pseudocapacitor materials," *Nature Communications,* vol. 4, May 2013.

[33] Y. X. Xu, X. Q. Huang, Z. Y. Lin, X. Zhong, Y. Huang, and X. F. Duan, "One-step strategy to graphene/Ni(OH)(2) composite hydrogels as advanced three-dimensional supercapacitor electrode materials," *Nano Research,* vol. 6, pp. 65-76, Jan 2013.

[34] Q. Li, H. F. Ni, Y. Cai, X. Y. Cai, Y. J. Liu, G. Chen, *et al.*, "Preparation and supercapacitor application of the single crystal nickel hydroxide and oxide nanosheets," *Materials Research Bulletin,* vol. 48, pp. 3518-3526, Sep 2013.

[35] K. Wang, L. W. Li, and T. Z. Zhang, "Synthesis of nickel yydroxide and its electrochemical performances," *International Journal of Electrochemical Science*, vol. 8, pp. 6252-6257, May 2013.

[36] J. Y. Ji, L. L. Zhang, H. X. Ji, Y. Li, X. Zhao, X. Bai, *et al.*, "Nanoporous Ni(OH) thin film on 3D ultrathin-graphite foam for asymmetric supercapacitor," *ACS Nano*, vol. 7, pp. 6237-6243, Jul 2013.

[37] H. J. Yan, J. W. Bai, J. Wang, X. Y. Zhang, B. Wang, Q. Liu, *et al.*, "Graphene homogeneously anchored with Ni(OH)(2) nanoparticles as advanced supercapacitor electrodes," *Crystengcomm*, vol. 15, pp. 10007-10015, 2013.

[38] V. Srinivasan and J. W. Weidner, "An electrochemical route for making porous nickel oxide electrochemical capacitors," *Journal of the Electrochemical Society*, vol. 144, pp. L210-L213, Aug 1997.

[39] V. Srinivasan and J. W. Weidner, "Studies on the capacitance of nickel oxide films: Effect of heating temperature and electrolyte concentration," *Journal of the Electrochemical Society*, vol. 147, pp. 880-885, Mar 2000.

[40] W. Xing, F. Li, Z. F. Yan, and G. Q. Lu, "Synthesis and electrochemical properties of mesoporous nickel oxide," *Journal of Power Sources*, vol. 134, pp. 324-330, Aug 2004.

[41] K. R. Prasad and N. Miura, "Electrochemically deposited nanowhiskers of nickel oxide as a high-power pseudocapacitive electrode," *Applied Physics Letters*, vol. 85, pp. 4199-4201, Nov 2004.

[42] M. S. Wu, Y. A. Huang, C. H. Yang, and H. H. Jow, "Electrodeposition of nanoporous nickel oxide film for electrochemical capacitors," *International Journal of Hydrogen Energy*, vol. 32, pp. 4153-4159, Dec 2007.

[43] M. S. Wu, C. Y. Huang, and K. H. Lin, "Electrophoretic deposition of nickel oxide electrode for high-rate electrochemical capacitors," *Journal of Power Sources*, vol. 186, pp. 557-564, Jan 2009.

[44] L. Fan, L. Tang, H. F. Gong, Z. H. Yao, and R. Guo, "Carbon-nanoparticles encapsulated in hollow nickel oxides for supercapacitor application," *Journal of Materials Chemistry*, vol. 22, pp. 16376-16381, 2012.

[45] Z. H. Zhu, J. Ping, X. P. Huang, J. G. Hu, Q. Y. Chen, X. B. Ji, *et al.*, "Hexagonal nickel oxide nanoplate-based electrochemical supercapacitor," *Journal of Materials Science*, vol. 47, pp. 503-507, Jan 2012.

[46] J. Xu, X. F. Gu, J. Y. Cao, W. C. Wang, and Z. D. Chen, "Nickel oxide/expanded graphite nanocomposite electrodes for supercapacitor application," *Journal of Solid State Electrochemistry*, vol. 16, pp. 2667-2674, Aug 2012.

[47] Y. Z. Zheng, H. Y. Ding, and M. L. Zhang, "Preparation and electrochemical properties of nickel oxide as a supercapacitor electrode material," *Materials Research Bulletin,* vol. 44, pp. 403-407, Feb 2009.

[48] B. Gao, C. Z. Yuan, L. H. Su, L. Chen, and X. G. Zhang, "Nickel oxide coated on ultrasonically pretreated carbon nanotubes for supercapacitor," *Journal of Solid State Electrochemistry,* vol. 13, pp. 1251-1257, Aug 2009.

[49] E. Herrero, L. J. Buller, and H. D. Abruna, "Underpotential deposition at single crystal surfaces of Au, Pt, Ag and other materials," *Chemical Reviews,* vol. 101, pp. 1897-1930, 2001.

[50] E. Norkus, A. Vaškelis, and I. Stalnioniene, "Changes of the Cu electrode real surface area during the process of electroless copper plating," *Journal of Solid State Electrochemistry,* vol. 4, pp. 337-341, 2000.

[51] E. Norkus, A. Vaškelis, J. Jačiauskienė, I. Stalnionienė, and G. Stalnionis, "Obtaining of high surface roughness copper deposits by electroless plating technique," *Electrochimica acta,* vol. 51, pp. 3495-3499, 2006.

[52] A. Vaškelis, E. Norkus, and G. Stalnionis, "Effect of the Cu electrode formation conditions and surface nano-scale roughness on formaldehyde anodic oxidation," *Electrochimica Acta,* vol. 49, pp. 1613-1621, 2004.

[53] A. Armutlulu, J. Kim, M. Kim, S. Allen, and M. Allen, "Nickel-oxide-based supercapacitors with high aspect ratio concentric cylindrical electrodes," in *Solid-State Sensors, Actuators and Microsystems (Transducers & Eurosensors XXVII), 2013 Transducers & Eurosensors XXVII: The 17th International Conference on*, 2013, pp. 1480-1483.

[54] J. Kim, M. G. Allen, and Y. K. Yoon, "Computer-controlled dynamic mode multidirectional UV lithography for 3D microfabrication," *Journal of Micromechanics and Microengineering,* vol. 21, Mar 2011.

[55] K.-W. Nam, W.-S. Yoon, and K.-B. Kim, "X-ray absorption spectroscopy studies of nickel oxide thin film electrodes for supercapacitors," *Electrochimica Acta,* vol. 47, pp. 3201-3209, 2002.

[56] J. Yan, W. Sun, T. Wei, Q. Zhang, Z. Fan, and F. Wei, "Fabrication and electrochemical performances of hierarchical porous Ni (OH) 2 nanoflakes anchored on graphene sheets," *Journal of Materials Chemistry,* vol. 22, pp. 11494-11502, 2012.

[57] Y. Zhou, F. Hou, Z.-P. Wan, Y.-L. Tang, D.-M. Yang, S. Zhao, *et al.*, "Facile synthesis of Ni (OH) 2 nanoflakes on carbon nanotube films as flexible binder-free electrode for supercapacitors," *ECS Solid State Letters,* vol. 3, pp. M1-M4, 2014.

CHAPTER 7

CONCLUSIONS AND FUTURE WORK

7.1 Summary and Conclusions

The work reported herein focuses on the design, fabrication, and characterization of deterministically engineered, 3D, versatile structures to be used as high-performance electrodes in energy storage applications, including batteries and supercapacitors. These electrodes were realized by making use of electrochemical techniques and MEMS technologies. The resultant electrodes are based on highly laminated structures possessing precisely controlled characteristic dimensions, such as surface area, ionic diffusion and electronic conduction path lengths, that ultimately determine the energy storage performance of the electrode.

The enhanced performance of the electrodes was enabled by simultaneously minimizing the transport resistance of the ionic and electronic species during high charge and discharge rates, which was achieved by increasing the electrochemically accessible surface area of the electrode and reducing the diffusion and conduction path lengths for the ions and electrons, respectively. The fabrication approach, which allows this simultaneous minimization of the resistances, involves the sequential electrodeposition of relatively thin alternating layers of structural and sacrificial materials through a temporary mold by utilizing an automated robotic system. Following the removal of the sacrificial layers, the final structure with a large number of separate layers of the structural material was obtained. This resultant structure serves as a highly conductive current collector for the electrode which is formed by the conformal deposition of the electrochemically active material.

The first demonstration of the contribution of the MEMS-enabled multilayer structures to the improved power capabilities of the energy storage systems was a proof-

of-concept 3D Zn-air microbattery. For a set amount of Zn, these primary 3D batteries demonstrated a superior performance to their 2D thin-film counterparts in terms of energy density, particularly at high discharge rates. The underlying reason for this enhanced power capability is the highly conductive, multilayer backbone structure, which, not only provides an increased surface area for the electrode, but also maintains a consistent and continuous electrical access to the conformal Zn film on it with a minimal ohmic loss. The resultant electrodes featured energy densities up to 3 mWh cm^{-2}.

Another demonstration involved secondary battery chemistries, including $Ni(OH)_2$ and Li-ion systems, where rapid charging of the electrodes was performed, and the capacity retention was investigated. Both Li-ion and $Ni(OH)_2$ electrodes demonstrated remarkable power capability by delivering more than 50% of their capacities after ultra-fast charge rates of 60 C. In addition, the electrodes exhibited outstanding cycling stability when charged and discharge at high rates. With the use of a novel photoresist mold, highly laminated structures with thicknesses in the millimeter range were realized, providing areal capacities as high as 5.1 mAh cm^{-2}.

When designing the electrodes with high-power capabilities, diffusion-limited models were adopted to determine the optimum characteristic dimensions, including the active material thickness on each layer, the inter-layer spacing, and the distance between the adjacent etching holes of the multilayer structure. These models were validated experimentally and found to be more successful in predicting the performance of the $Ni(OH)_2$ electrodes as compared to the NiSn electrodes. The reasons for the deviations from the theoretical performance values in the case of the NiSn electrodes were postulated to be the inability to deposit as smooth active material films and the lack of a proper formula to accurately predict the change in the diffusion coefficient during the charging process. The models were also used to make projections concerning how much improvement could be achieved in terms of power and energy densities using this electrode design. It was found that the key to realizing electrodes with further enhanced

power performance (i.e., power density) is reducing the thickness of both the individual Ni layers and the active material film within the multilayer electrode, and thus, enabling deposition of higher number of layers. In particular, the gravimetric power and energy densities are highly dependent on the mass of the electrochemically inactive material (i.e., Ni backbone) within the electrode.

The multilayer fabrication approach was also proven successful for fabricating high-performance electrochemical capacitors, supporting the versatility of the technology. $Ni(OH)_2$-based supercapacitors demonstrated a relatively high areal capacitance of 1319 mF cm^{-2}. An excellent cycling stability with a capacity retention of 94% was reported following more than 1000 CV runs at a high scan rate of 20 mV s^{-1}. In addition to the conventional multilayer structures with laterally high aspect ratios, a new approach comprising vertical high-aspect-ratio concentric cylinder structures were introduced. This latter approach enabled the fabrication of high-surface-area electrodes with thicknesses exceeding 2 mm through a mold-free method and hence, allows higher utilization of the volume. By incorporating NiO as the active material, an areal capacitance of 270 mF cm^{-2} was measured.

The multilayer electrode concept introduced in this work addresses several aspects of electrochemical energy storage dynamics that are essential for improved performance. First, the high surface area provided by the highly laminated Ni structures enables a larger contact area between the electrode and electrolyte, resulting in increased number of active sites for the redox reactions. Second, the formation of a thin and conformal active material film on each layer renders a reduced ionic diffusion and electronic conduction path length. In this way, the power-limiting effect stemming from the use of active materials with relatively low conductivities (e.g., $Ni(OH)_2$, NiO, MnO_2) is significantly mitigated. Third, the highly conductive metallic backbone serving as a mechanically stable and electrochemically inert current collector exhibits minimized transport resistance for the electrons to and from the active material. Lastly, one of the

unique features of the multilayer approach is the scalability of the electrodes, i.e., the ability to increase the capacity of the electrodes further by simply increasing the number of layers in the structure without compromising neither the footprint area, nor the active material thickness. This attribute enables the realization of high-performance electrodes for a wide variety of applications, ranging from autonomous microsystems to macroscale portable electronics.

7.2 Suggestions for Future Work

Suggestions for future work involves two types of approaches: (1) improvement of the design and fabrication techniques reported in this work, and (2) developing new fabrication methods.

7.2.1 Realization of Structures with Higher Capacities and Energy Densities

As mentioned throughout the work, the total thickness of the fabricated structures is determined by the thickness of the photoresist mold used in the sequential electroplating process. To realize structures with higher number of laminations than what has been demonstrated so far, other types of molds can be sought that feature the following properties: (1) easily patternable, high-aspect-ratio structures with feature sizes on the order of microns; (2) good adhesion to the substrate; (3) high chemical resistance when exposed to corrosive plating solutions for extended periods of time; and (4) easily removable upon completion of the sequential electroplating process. However, it is not always easy to identify a mold that would satisfy all of the outlined requirements. Hence, instead of coming up with a new technology, modification of the existing fabrication approach may be considered.

The most challenging part in achieving thick photoresist molds is the fabrication of the pillar arrays that ultimately determine the dimensions and locations of the etching holes within the multilayer structures, as shown in Figure 7.1. This is primarily due to the

high aspect ratio of these pillars. In addition to the challenges in their fabrication process, these pillars need to be handled carefully until the plating process is initiated, since they are easily distorted. For these reasons, pillars are the limiting factors for achieving thicker structures, i.e., electrodes with higher number of laminations and thus, higher capacities.

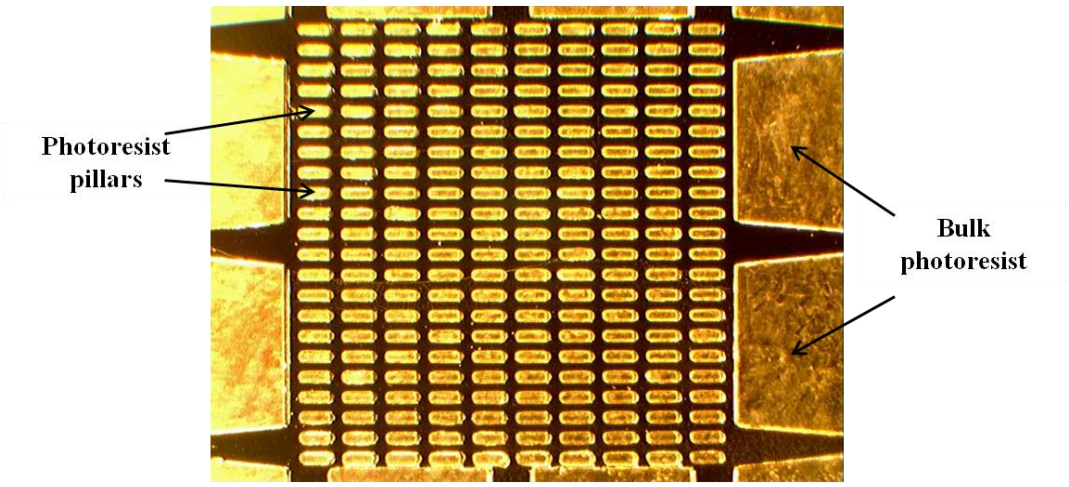

Figure 7.1: Optical image showing the top view of the photoresist mold

The bulk photoresist surrounding the multilayer structure (see Figure 7.1), on the other hand, exhibit much lower aspect ratios as compared to pillars and thus, can easily be fabricated even with thicknesses exceeding 1 mm. This bulk photoresist is also mechanically more stable as compared to the pillars, and hence, it is easier to handle. Hence, the fabrication process could be modified in a way that it only involves the bulk photoresist mold, and the etching holes could be created following the sequential electrodeposition. Therefore, laser micromachining techniques may be considered as an alternative method to create the etching holes.

Some preliminary work has been completed by sequentially electroplating planar Ni and Cu layers with a footprint of 1 cm^2. These multilayer structures were then ablated with the help of an IR laser as shown in Figure 7.2. It can be seen that the laser was able to ablate through the relatively thick metal structure. However, redeposition of the molten

metal during the ablation process blocked the cross-section of the holes and prevented the exposure of the individual layers. Figure 7.2.A shows the redeposited metal residues on the surface and the cross-section of the structure following the ablation process. This redeposition issue was easily overcome by immersing the samples briefly in concentrated nitric acid solutions. After the acid treatment, the individual layers became visible as shown in Figure 7.2.B. This process can further be optimized by modifying the ablation conditions and hole dimensions, enabling realization of electrodes with higher number of laminations.

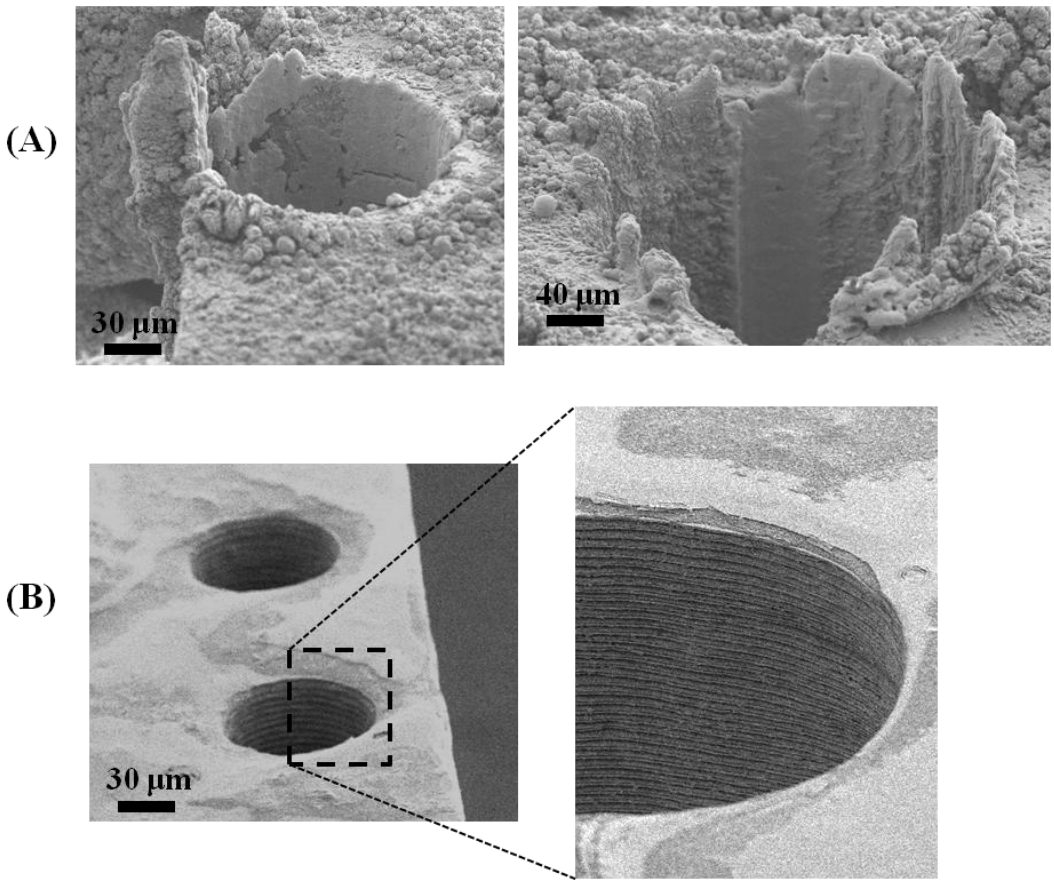

Figure 7.2: Etching holes formed via laser ablation process: (A) immediately after laser ablation, (B) following the acid treatment

Although increasing the number of layers results in higher areal capacities, the energy and power densities of the multilayer electrode with a given active material thickness are not a function of the number of laminations. In Chapters 4 and 5, it was shown for a given active material thickness on each layer, the gravimetric power and the energy density of the multilayer electrodes can be increased by minimizing the mass of the electrochemically inactive material (i.e., the Ni backbone), which can be achieved by reducing the thickness of the individual Ni layers. The same principles apply to volumetric power and energy densities as well.

Although the current techniques allow deposition of layers on the order of tens of nanometers, maintaining the mechanical integrity of the backbone structure in the subsequent fabrication steps (i.e., wet etching of the sacrificial layers and active material deposition) is the main limitation for reduced layer thickness. In the case of structures with submicron-thick individual layers, the wet etching process of the sacrificial layers, as well as the electrodeposition process of the active material were found to cause deformations in the backbone structure, which are postulated to stem from the capillary effects of the liquids the structures are exposed to during these processes.

One way of overcoming such deformations and hence, allowing the realization of structures with thinner individual layers is through redesigning the anchors that support the structure after the etching process. By narrowing the distance between the anchors on the sidewalls and by increasing the number of the etching holes to place extra anchors to support the structure from central regions, a better mechanical support can be created. Also, replacing the sacrificial layer with another material, which enables a less destructive removal (e.g., dry etching), may be considered as an alternative to achieving multilayer structures with thinner layers.

Another issue that needs to be resolved in order to achieve electrodes with better performance is improving the conformal deposition of the active material. This can be quite challenging, particularly if the spacing between the layers is reduced significantly,

as suggested by the modeling results for the optimized electrodes shown in Chapters 4 and 5. In this work, electrodeposition has been the preferred method to deposit the active material, mainly because of its cost-effectiveness and relatively simpler application process. However, other techniques, including atomic layer deposition (ALD) and chemical vapor deposition (CVD), are known to be quite useful in depositing conformal, nanoscale films onto complex 3D architectures. Through the development of appropriate precursors for the deposition of the active materials and optimization of the deposition conditions, these techniques can be incorporated into the current fabrication process for improved electrode performance.

7.2.2 3D Systems Based on Interdigitated Electrodes

Except for the case of Zn-air batteries discussed in Chapter 3, the multilayer electrodes were only tested as half cells in the secondary battery, as well as electrochemical capacitor applications. When dealing with half cells, no significant effort was given toward the minimization of the distance between the electrodes. However, for the realization of high-performance electrochemical systems, in addition to the diffusion path lengths of the solid-state ions and conduction path lengths of the electrons, the diffusion path lengths of the liquid-state ions need to be minimized as well. An effective way to achieve this is by minimizing the inter-electrode separation distance, which can be done through the fabrication of interdigitated electrodes.

Proof-of-concept structures were fabricated by utilizing laser micromachining techniques. Figure 7.3 shows the fabrication scheme of these interdigitated electrodes from the top view. Multilayer concentric pillars were first fabricated as described in Chapter 6. Thereafter, IR laser was used to cut the seed layer and electrically isolate half of the pillars (Electrode A) from the other half (Electrode B) in an interdigitated fashion as demonstrated in Figure 7.3.2. The inter-electrode separation is determined by the beam

size of the laser, which can be as small as tens of micrometers. The optical images of the resultant structures can be seen in Figure 7.4.

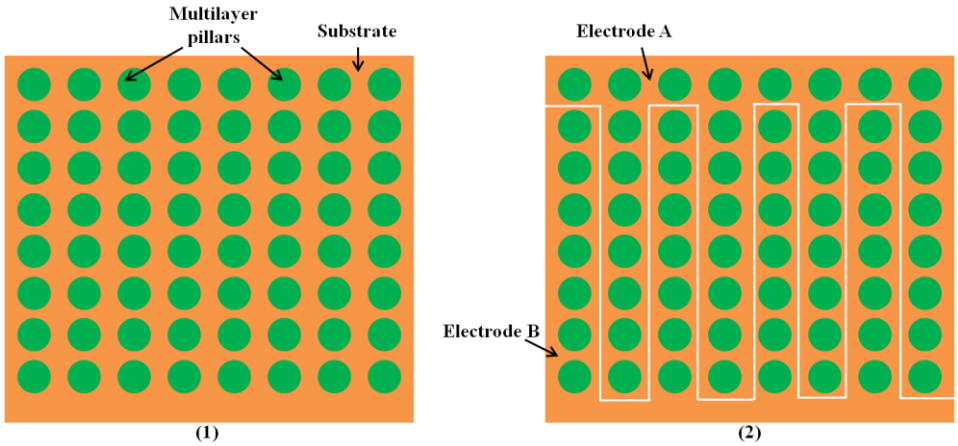

Figure 7.3: Conceptual rendering of the fabrication process for the interdigitated electrodes: (1) multilayer concentric pillars fabricated on a substrate, (2) separation of the electrodes with the IR laser

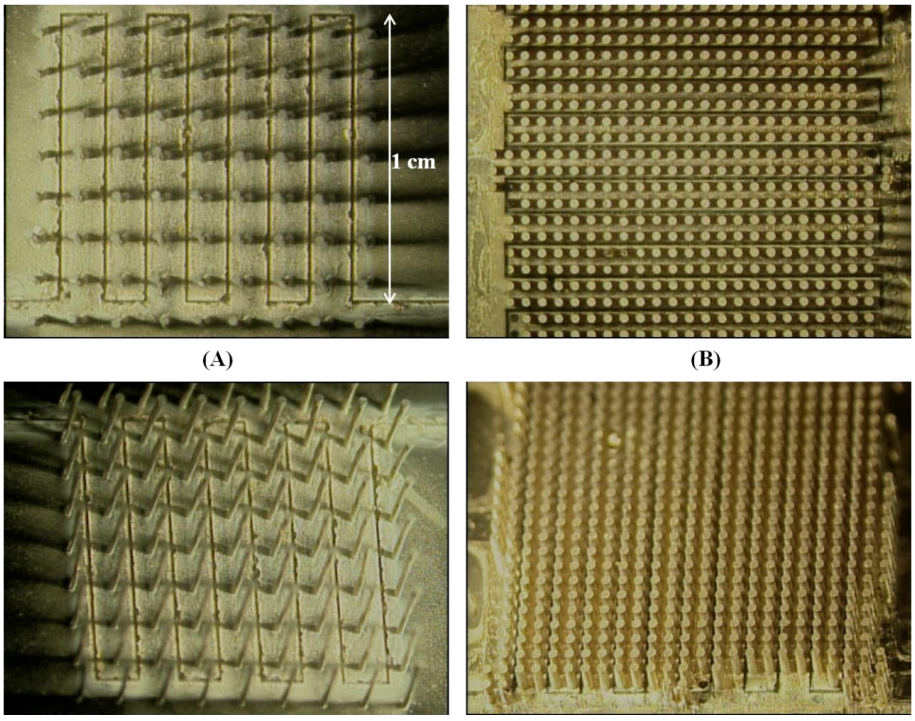

Figure 7.4: Laser-cut interdigitated electrodes based on vertical high-aspect-ratio concentric cylinders: (A) 9x9 pillar array on 1 cm^2 footprint, (B) 24x24 pillar array on 1 cm^2 footprint

A 9x9 pillar array fabricated on a footprint of 1 cm^2 can be seen in Figure 7.4.A. To enable higher energy density, the packing density of the pillars was increased significantly as shown in Figure 7.4.B. This interdigitated pillar system can be utilized to fabricate symmetric electrochemical capacitors. In addition to the pillar structures with vertically high aspect ratios, conventional multilayer electrodes with laterally high aspect ratios can also be fabricated via this method. Since the electrodes are electrically isolated, it is possible to deposit two different active materials on either electrode. To fabricate a 3D Li-ion battery based on interdigitated electrodes, for example, NiSn can be deposited onto one electrode as the anode material, while MnO_2 film is formed on the other electrode as the cathode material.

7.2.3 Incorporation of Alternative Active Materials

Three different active materials (i.e., MnO_2, NiO, and NiSn) were demonstrated for the Li-ion electrodes. Among these active materials, the best performance was obtained from the NiSn electrodes. The drawback of NiSn, however, is that forming a smooth layer with a uniform thickness is not that easy, particularly if the thickness needs to be more than several hundreds of nanometers. This results in the loss of control over the thickness of the active material film, which is against the premise of this work. To improve the quality of the NiSn deposits, alternative deposition baths can be sought. In the case of Cu deposits, it was demonstrated in Chapter 3 that the presence of certain additives can drastically improve the deposit quality. Additives with similar effects, or baths with completely different compositions may exist for NiSn deposition baths as well.

As was discussed in Chapter 5.1, there are a wide variety of active materials for Li-ion electrodes. Other potential active materials that are compatible with the fabrication process can be investigated to realize systems with better performance. For the

conventional fabrication approach, where the multilayer backbone is first fabricated and then the active material deposition is performed, the compatibility of the active material depends on whether or not the active material can be deposited onto the multilayer backbone in a conformal way. For the more recent approach that is based on the concurrent deposition of the active material along with the structural and sacrificial materials, the active material needs be resistant to both Ni and Cu plating solutions, as well as to the Cu etchant used in the final step. Other alloys of Sn (e.g., Cu_6Sn_5) are also known to be electrodepositable and demonstrated outstanding performance. Hence, they are worth investigating.

Silicon is reportedly one of the promising active materials for Li-ion systems due to its high specific capacity, which is even higher that the pure metallic Li [1]. Incorporation of Si into the multilayer structures can potentially result in a drastic improvement in the capacity of the electrodes. There are well-known techniques for the deposition of the Si, which mainly involve vacuum processes such as sputtering [2, 3]. More recently, there have been efforts to electroplate Si using non-aqueous solutions. A successful incorporation of the latter method would enable a unique fabrication approach for Si-based Li-ion electrodes.

7.2.4 Alternative Method for Vertical High-Aspect-Ratio Multilayer Structures

Vertical high-aspect-ratio concentric cylinders demonstrated in Chapter 6.3.1 undergo growth in both radial and vertical directions. Radial growth takes place around the pillars, and the layers formed in these regions are ultimately utilized as the scaffold for the electrode. Vertical growth, on the other hand, happens on the topside of the pillars, as well as on the surface of the substrate (i.e., bottom part of the pillars), as illustrated in Figure 2.13. The layers deposited onto the topside of the pillars are lapped completely so that the vertical layers are exposed to the etchant in the subsequent step. However, the layers formed on the surface of the substrate remain there throughout the

whole fabrication process. Since it is not possible for the etchant to diffuse laterally and remove the Cu layers, as can be seen in Figure 6.14, the layers formed on the bottom parts of the pillars do not contribute to the surface area of the electrode. In addition, they increase the total mass of the electrode and thus, reduce both the energy and power density.

An alternative fabrication approach, as shown in Figure 7.5 can prevent the formation of such unnecessary layers, and enable the realization of electrodes with larger surface area, as well as higher energy and power densities. The process starts with the selectively metalized, high-aspect-ratio SU-8 pillars or walls with non-conductive substrates placed on both sides. Next, the sequential electrodeposition of the alternating Ni and Cu layers is performed. The presence of the non-conductive substrates forces the metal growth to take place in radial direction only. Upon completion of the sequential deposition of the layers, one of the substrates is removed and a thick Ni layer is electroplated on one side. This is followed by the removal of the second substrate on the other side and selective etching of the Cu layers. In this approach, lapping step is eliminated, shortening the duration of the fabrication. Also, sacrificial Cu layers can be etched completely, resulting in substantially improved surface area. In addition to the energy storage applications, the resultant structures can also be utilized as channels in microfluidics applications.

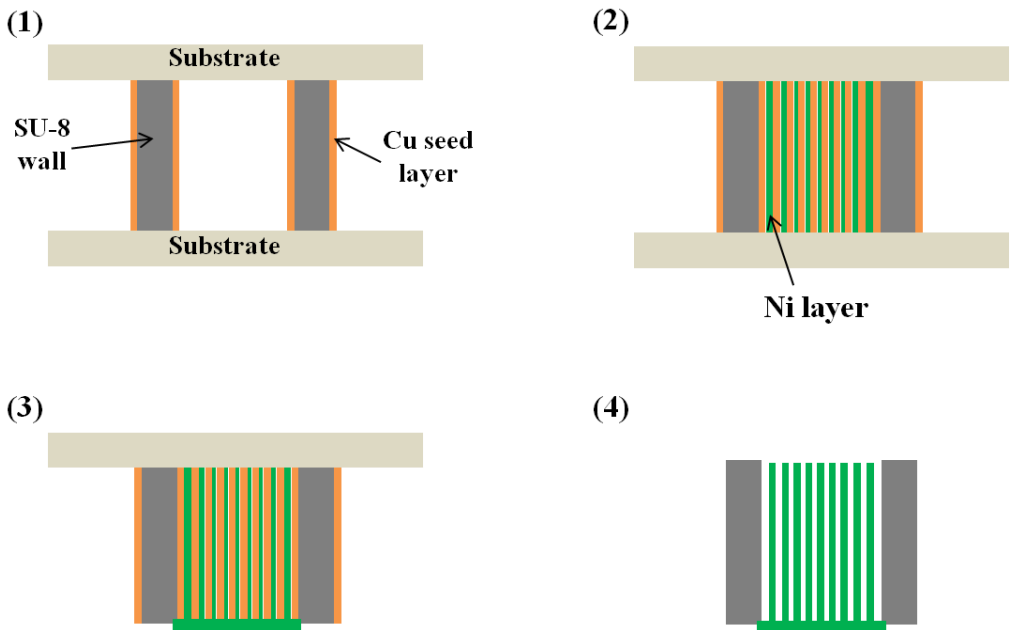

Figure 7.5: Fabrication scheme for the vertical high-aspect-ratio channels: (1) formation of channels composed of selectively metalized SU-8 walls sandwiched between two substares, (2) sequential electroplating of Ni and Cu layers, (3) removal of the substrate from one side and electroplating of Ni anchor, and (4) removal of the other substrate and selective etching of Cu layers

7.2.5 Comprehensive Modeling of the Electrodes

In Chapters 4 and 5, diffusion-limited models were utilized for determining the optimum values for the characteristic dimensions of the electrode. More comprehensive models can be adopted to predict the optimized characteristic dimensions of the electrode in a more precise way. In the case of Li-ion batteries, for example, a complete mathematical representation of the system can be achieved by including the equations describing the following phenomena: (1) mass transport of Li ions in the active material and electrolyte, (2) charge transport in the active material and electrolyte, and (3) energy transport in the whole cell. This comprehensive model would be able to predict the concentration distribution of Li ions, as well as the temperature distribution within the cell which may play a vital role in the performance of the system and has not been investigated in this work. Butler-Volmer-type kinetic expression can be utilized to

describe the charge transfer across the electrode/electrolyte interface. For describing the temperature variations throughout the cell, Arrhenius-type expressions can be assumed.

Furthermore, the mathematical model can be supported experimentally by performing electrochemical impedance spectroscopy (EIS). EIS can be utilized to evaluate the electrochemical kinetics and intrinsic resistance during the charge and discharge processes. This technique can also be used to determine the diffusion coefficient of the active material, which was shown to have a significant impact on the optimized dimensions in Chapter 5.4.

7.3 References

[1] C. K. Chan, H. Peng, G. Liu, K. McIlwrath, X. F. Zhang, R. A. Huggins, *et al.*, "High-performance lithium battery anodes using silicon nanowires," *Nature Nanotechnology,* vol. 3, pp. 31-35, 2008.

[2] S. C. Zhang, Z. J. Du, R. X. Lin, T. Jiang, G. R. Liu, X. M. Wu, *et al.*, "Nickel nanocone-array supported silicon anode for high-performance lithium-ion batteries," *Advanced Materials,* vol. 22, pp. 5378-+, Dec 2010.

[3] F. F. Cao, J. W. Deng, S. Xin, H. X. Ji, O. G. Schmidt, L. J. Wan, *et al.*, "Cu-Si nanocable arrays as high-rate anode materials for lithium-ion batteries," *Advanced Materials,* vol. 23, pp. 4415-+, Oct 2011.

APPENDIX A

MATLAB CODES

Code for the Modeling of the Active Material Thickness

```
function ActiveMaterial
m=0;
x=linspace(0,0.00004,20);
t=linspace(0,60,120);
u=pdepe(m,@system,@pdeic,@bc1,x,t);

display(u(120,:)/0.0192);
surf(x,t,u);
title('Surface plot of concentration');
xlabel('Distance (cm)');
ylabel('Time (s)');
zlabel('Concentration (mol/cm^3)');
end

function [c,b,s]=system(x,t,u,DuDx)
c=1;
b=(1*10^-10)*DuDx; %D*DuDx
s=0;
end

function u0=pdeic(x)
u0=0.0192; %initial concentration
end

function [pl,ql,pr,qr]=bc1(xl,ul,xr,ur,t)
pl=0;
ql=1;
pr=0.0012355/(96485*1); %i/(F*n), calculate the current accordingly
qr=1;
end
```

Code for the Modeling of the Inter-layer Spacing

```
function pdemodel
[pde_fig,ax]=pdeinit;
pdetool('appl_cb',10);
set(ax,'DataAspectRatio',[1 0.017499999999999998 1]);
set(ax,'PlotBoxAspectRatio',[85.714285714285722 57.142857142857146
2857.1428571428573]);
set(ax,'XLim',[-0.01 0.05]);
set(ax,'YLim',[-0.0001 0.0006]);
set(ax,'XTickMode','auto');
set(ax,'YTickMode','auto');

% Geometry description:
pderect([0 0.03 0.00014 0],'R1');
set(findobj(get(pde_fig,'Children'),'Tag','PDEEval'),'String','R1')

% Boundary conditions:
pdetool('changemode',0)
pdesetbd(4,...
'dir',...
1,...
'1',...
'0.001')
pdesetbd(3,...
'neu',...
1,...
'0',...
'-0.0006/96485')
pdesetbd(2,...
'dir',...
1,...
'1',...
'0.001')
pdesetbd(1,...
'neu',...
1,...
'0',...
'-0.0006/96485')

% Mesh generation:
setappdata(pde_fig,'Hgrad',1.3);
setappdata(pde_fig,'refinemethod','regular');
setappdata(pde_fig,'jiggle',char('on','mean',''));
setappdata(pde_fig,'MesherVersion','preR2013a');
pdetool('initmesh')
pdetool('refine')
pdetool('refine')
pdetool('jiggle')

% PDE coefficients:
pdeseteq(2,...
```

```
'0.00001',...
'0.0',...
'0',...
'1.0',...
'linspace(1,120,10)',...
'0.001',...
'0.0',...
'[0 100]')
setappdata(pde_fig,'currparam',...
['0.00001';...
'0      '])

% Solve parameters:
setappdata(pde_fig,'solveparam',...
char('0','1440','10','pdeadworst',...
'0.5','longest','0','1E-4','','fixed','Inf'))

% Plotflags and user data strings:
setappdata(pde_fig,'plotflags',[1 1 1 1 1 1 1 1 0 0 0 10 1 0 1 0 0 1]);
setappdata(pde_fig,'colstring','');
setappdata(pde_fig,'arrowstring','');
setappdata(pde_fig,'deformstring','');
setappdata(pde_fig,'heightstring','');

% Solve PDE:
pdetool('solve')
```

VITA

ANDAC ARMUTLULU

Andac Armutlulu was born and raised in Istanbul, Turkey. He received both his B.S. and M.S. degrees in Chemical Engineering from Bogazici University (Istanbul, Turkey) in 2007 and 2009, respectively. His M.S. thesis was on the simulation of allosteric interactions in proteins. He joined the MicroSensors and MicroActuators (MSMA) group in October 2009, and has since been pursuing his Ph.D. degree in the School of Chemical and Biomolecular Engineering at the Georgia Institute of Technology, co-advised by both Dr. Sue Ann Bidstrup Allen and Dr. Mark G. Allen. His research interests include applied electrochemistry, micro- and nanofabrication technologies, energy storage systems, and biodegradable power sources.